
The University Of Sheffield.

# Magnetic Nanoparticles for Drug / Gene Delivery

**By:**

Wenxing Song

A thesis submitted to the University of Sheffield for the degree of Doctor of Philosophy

The University of Sheffield

The Department of Chemical and Biological Engineering

October 2018

# Abstract

Although various drugs have been developed to treat different diseases such as cancer, the therapeutic effects of many drugs have been limited by their undesirable properties such as poor solubility, poor bioactivity, rapid clearance in blood and non-specific distribution. Nanoparticles as carriers have received more and more attention in the last two decades due to their ability of overcoming these obstacles and enhancing the therapeutic efficiency of the conventional drugs. In this thesis, various kinds of nanoparticles were developed aiming at improving the therapeutic efficiency and targeted delivery of anti-cancer drug and gene.

Curcumin is a promising anti-cancer drug but its applications in cancer therapy are limited due to its poor solubility, short half-life and low bioavailability. In this thesis, magnetic-polymer core-shell nanoparticles based on non-toxic, biocompatible and biodegradable polymers such as silk fibroin, alginate and chitosan were prepared and optimized to improve the uptake efficiency and cell growth inhibition effect of curcumin towards cancer cells. The size, zeta potential, surface morphology, drug loading / release profile, *in vitro* uptake and growth inhibition effect to cancer and normal cells of these curcumin loaded nanoparticles were investigated. The results indicated that the curcumin loaded particles exhibited enhanced uptake efficiency and growth inhibition effect on MDA-MB-231 cancer cells compared with free curcumin. Higher uptake efficiency and cytotoxicity to MDA-MB-231 cells than normal human dermal fibroblast cells were observed, suggesting they have specific effects against cancer cells. Moreover, *in vitro* targeted delivery of curcumin to specific areas of cells was achieved with the presence of an external magnetic field, suggesting these magnetic nanoparticles are promising for targeted delivery of drugs to desired sites applying

magnetic forces.

Apart from drug delivery the applications of magnetic nanoparticles in gene delivery was also investigated. Polyethyleneimine is one of the most efficient non-viral transfection agents for gene delivery due to its high cationic charge density. In this thesis, silk fibroin was selected to fabricate magnetic-silk / polyethyleneimine core-shell nanoparticles and silk-polyethyleneimine nanoparticles for the transfection of an anticancer gene (c-myc antisense oligodeoxynucleotides) into MDA-MB-231 breast cancer cells and human dermal fibroblast cells. The results illustrated that the cytotoxicity of magnetic-silk / polyethyleneimine core-shell nanoparticles was significantly lower than polyethyleneimine coated magnetic nanoparticles which is widely studied as a gene delivery carrier. The magnetic-silk / polyethyleneimine core-shell nanoparticles were capable of delivering c-myc antisense oligodeoxynucleotides into MDA-MB-231 cells and significantly inhibiting the cell growth. Employing magnetic-silk / polyethyleneimine core-shell nanoparticles, high uptake efficiency of c-myc antisense oligodeoxynucleotides was achieved within 20 min via magnetofection. In addition, magnetic-silk / polyethyleneimine core-shell nanoparticles exhibited higher cytotoxic effect against MDA-MB-231 breast cancer cells than normal human dermal fibroblast. Moreover, *in vitro* targeted delivery of oligodeoxynucleotides can be achieved using magnetic-silk / polyethyleneimine core-shell nanoparticles under a magnetic field.

# Acknowledgement

I would like to thank my supervisor Dr Xiubo Zhao for inspiring and supporting me during my PhD study with lots of professional suggestions and help.

I want to thank my parents for financially and mentally supporting my PhD.

Also, I would like to thank Dr David A. Gregory who provided lots of great suggestions on my research and thesis writing.

I also want to thank my colleagues, Dharana S Jayawardane, Yu Zhang, Silvia Cirillo, Roja Hadianamrei, Weizhen Sun, Ana Jimenez Franco, Mhd Anas Tomeh and Piyush Kumar for their assistance with my work.

Furthermore, I would like to thank Dr Munitta Muthana for her support and allowing me to work in her lab. Her PhD student Haider AL-Janabi also helped me a lot during my work.

My friends, Dr Richard J. Archer, Dr Xing Su, Wei Li and Yaoxun Wang also helped me lots with my research work and life in Sheffield.

Finally, I want to thank the CBE department for providing facilities for my PhD work.

# Publications

**[1] The published paper:**

Song, W.; Muthana, M.; Mukherjee, J.; Falconer, R. J.; Biggs, C. A.; Zhao, X., Magnetic-Silk Core-Shell Nanoparticles as Potential Carriers for Targeted Delivery of Curcumin into Human Breast Cancer Cells. ACS Biomaterials Science & Engineering 2017, 3 (6), 1027-1038.

**[2] The paper draft based on Chapter 4 with the title:**

'Preparation of Magnetic Alginate / Chitosan Layer-by-Layer Nanoparticles as Potential Carriers for Targeted Delivery of Curcumin into Human Breast Cancer Cells.'

**[3] The paper draft based on Chapter 5 with the title:**

'Magnetic-Silk Fibroin / Polyethyleneimine Core-Shel Nanoparticles as Potential Carriers for Cell Transfection.'

# Table of Contents

# List of Figures

# 1. Introduction

## 1.1. Drug delivery systems

### 1.1.1. Nanocarriers improve therapeutic effect of conventional drugs

Although various drugs have been developed to treat different diseases such as cancer, the therapeutic effects of many drugs have been limited by their undesirable properties such as poor solubility, poor stability, poor bioactivity, rapid clearance in blood and non-specific distribution [1-2]. Therefore, to overcome these obstacles and enhance the therapeutic efficiency of the conventional drugs, nanocarriers are being developed [2]. For instance, the poor solubility of hydrophobic drugs such as curcumin (CUR) can be improved by nanocarriers. CUR is a Food and Drug Administration (FDA) approved medicine [3] and has been largely employed for medical applications attributed to its anti-oxidant [4-6], anti-inflammatory [7-9], wound healing [10-11] and anti-bacterial [12-13] activities. Recent research also indicated that CUR demonstrated impressive anti-cancer properties [14-17]. It has been reported that CUR showed the ability to inhibit the carcinogenesis in various cell lines including breast, colon and gastric cancer cells, which made it promising for cancer therapy [16]. However, despite all the promising properties, the solubility of CUR is very poor in aqueous solution, leading to its poor bioavailability and limited therapeutic effect for cancer treatment [18-20]. By encapsulating CUR in nanocarriers, including lipid based nanoparticles [21-25], polymer nanoparticles [26-32] and inorganic nanoparticles [33], the solubility and bioavailability of CUR have been improved and enhanced therapeutic effect can be achieved. The poor pharmacokinetics (PK) of some anti-cancer drugs is one of the greatest obstacles of their therapeutic effects [2]. The rapid clearance of drugs or

drug loaded nanoparticles in the bloodstream is mainly promoted by protein adsorption [34]. The adsorbed proteins on the surface of drugs or nanoparticles tend to facilitate the opsonisation of therapeutic agents and promote their aggregation. The majority of opsonised drugs or particles can be eliminated by a receptor-mediated mechanism within a few minutes [34]. The rapid clearance and short half-life of anti-cancer drugs such as doxorubicin (DOX) normally results in the necessity of increased injection dose or injection frequency to reach the efficacious responses [35]. However, increasing the dose of toxic anti-cancer drugs may cause undesired side effects to the human body or healthy tissue and should be avoided. Encapsulation of the drugs into nanocarriers, which are designed to provide protection to the encapsulated cargo generally will lead to an increased half-life and enhanced therapeutic effect of drugs [35]. For example, Harivardhan *et al*. compared the pharmacokinetics of free DOX and DOX loaded poly(butyl cyanoacrylate) nanoparticles after they were injected into albino rats [36]. The results indicated that most of the free injected DOX was rapidly cleared within 2 h, where total clearance was after 8 hours. On the other hand, DOX loaded poly(butyl cyanoacrylate) nanoparticles showed a significantly longer elimination time [36]. Modification of nanocarriers can be made to further improve the PK of drug loaded carriers. For example, it has been reported that the coating or incorporation of poly(ethylene glycol) (PEG) into nanoparticles can decrease the drug clearance by immune recognition [2]. Gabizon *et al*. investigated the PK of DOX loaded liposomes containing polyethylene glycol-derivatized distearoylphosphatidylethanolamine (PEG / DSPE) in rodents and dogs and found that the plasma concentrations of DOX in animals treated with PEG / DSPE-containing liposomes were significantly higher than those without PEG / DSPE [37].

Another major obstacle of the therapeutic effect of free drugs is their undesired biodistribution (BD) [35]. Conventional free drugs especially small molecular forms are distributed non-specifically in the

body in which they will not only reach tumour sites but also healthy tissue [1]. The nonspecific accumulation of drugs in healthy tissue both lowers the drug concentration at tumour sites, limiting the anti-cancer effect and increases the risk of undesired side effects to healthy tissue [1]. Increasing the drug dose to obtain a higher drug concentration at tumour sites provides a better therapeutic effect for cancer treatment. However, with this approach, drug concentrations are also greatly increased in the healthy tissue, increasing the toxicity effect, thus causing stronger side effects. By using nanocarriers, the problem of poor biodistribution can be minimised, due to the enhanced permeability and retention (EPR) effects [2].

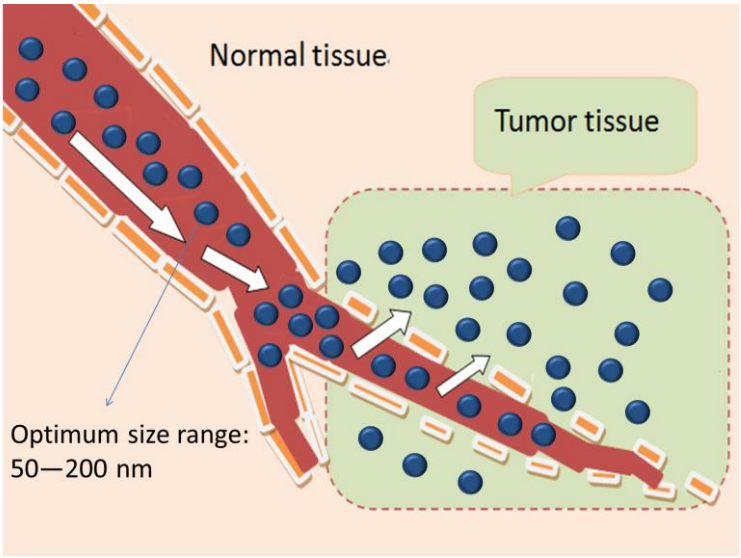


Fig. 1.1 Schematic representation of drug delivery by nanocarriers. The accumulation of the drug at tumour sites is promoted by the EPR effect. Anti-cancer drug loaded nanocarriers extravasate from the blood through gaps in vascular endothelial cells and accumulate in tumour sites, but not in normal tissue.

As shown in Fig. 1.1, in the tumour sites of the human body, blood vessels are remodelled to enable leukocyte extravasation, thus increasing the vascular permeability and enabling the extravasation and accumulation of nanocarriers at tumour sites [2]. As the tumour grows the original blood vessels are incapable to supply enough nutrients and oxygen to supply the tissue and thus signal molecules such as cytokines are released resulting in the formation of new blood vessels at the tumour sites, a

process known as angiogenesis [2]. Unlike blood vessels in normal tissue which possess tightly arranged endothelial cells, the angiogenic blood vessels possess large gaps between endothelial cells, which tend to further promote the extravasation of drug loaded nanocarriers and the accumulation of these carriers at the tumour sites [2]. Therefore, nanocarriers within the appropriate size range cannot pass through the gaps in normal blood vessels, but can largely extravasate from blood vessels in tumour tissue [2]. Since the extravasation of nanocarriers into tumour sites via the EPR effect is a size dependent process, it is important to investigate the suitable size range of carriers for drug delivery. For the efficient delivery of drugs to the cancer sites, the optimum size range of drug carriers is generally accepted to be about 50 - 200 nm [38]. Particles with a size less than 50 nm will easily extravasate through the discontinuous endothelium of liver, spleen and bone marrow, and are less likely to be accumulated at the desired sites. On the other hand, particles with diameters larger than 200 nm may not pass through the porous vasculature of the tumour to reach the tumour site and will be eliminated more easily by the immune system [38]. It is worth noting that the EPR effect is not the only factor to alter the targeted accumulation of carriers [2]. The circulation time of carriers, degree of tumour vascularization and the degree of angiogenesis can also affect their accumulation at tumour sites [2]. Normally, a longer half-life results in a higher accumulation of carriers at tumour sites; tumours with less vascularization lead to less accumulated carriers; small pre-angiogenic tumours tend to accumulate carriers poorly [2]. Moreover, ligand modified nanocarriers containing drugs can bind to specific receptors on the surface of cancer cells before entering the cells, thus achieving targeted drug delivery [2].

In summary, the therapeutic effect of many conventional drugs is limited by their poor solubility, undesirable PK and BD. The nonspecific distribution of free drugs leads to the undesired accumulation of drugs in healthy tissue which will result in increased toxicity and undesired side

effects. The deployment of nanocarriers can overcome these problems by targeted delivering drugs to tumour sites via the EPR effect and providing protection to avoid rapid clearance [1].

### 1.1.2. Properties of nanocarriers affecting drug delivery

As previously mentioned in Section 1.1.1, nanocarriers can be employed to improve the PK and BD of drugs to obtain an enhanced therapeutic effect. Normally, if the release rate of the encapsulated drug from carriers is very low, then the PK and BD of the encapsulated drug are the same as the PK and BD of drug carriers [2]. On the other hand, if the drug is rapidly released, the PK and BD of the encapsulated drug will be similar to that of free drug [2]. In most of drug delivery applications, the release rate of drugs is altered to achieve a sustained slow release to avoid rapid clearance and high injection frequency. Therefore, it is required for drug carriers to possess desirable PK and BD such as long circulation half-life, capable of accumulating at the tumour sites via the EPR effect. Conventional non-modified nanocarriers are generally rapidly cleared from the blood stream by the reticuloendothelial system (RES), which is an immune system including organs such as the liver and spleen [39]. Therefore, in order to develop nanocarriers suitable for targeted delivery, it is important to investigate the properties of carriers that affect their performance in the process of targeted delivery. Recent studies indicated a few crucial properties of nanocarriers that play important roles in targeted drug delivery including particle size, surface charge and hydrophobicity [1-2, 35].

#### 1.1.2.1. The effect of nanoparticle size

One of the advantages of nanoparticles is their tuneable size [1]. As mentioned in Section 1.1.1 nanocarriers can accumulate in tumour tissues by taking the advantage of the EPR effect [2]. For effective accumulation, the size of nanocarriers should be within a size range of 50-200 nm. Smaller carriers (< 50 nm) are more likely to leak through the gaps of endothelial cells in the liver or spleen and larger carriers (>200) are more difficult to extravasate from the discontinuous blood vessels in tumour tissue [38]. Particle size also plays an important role in altering the circulation time of carriers in blood [34]. As previously mentioned in Section 1.1.1, the key factor in the clearance of nanocarriers by RES is protein adsorption. The adsorption of proteins on the surface of nanocarriers leads not only to the aggregation of the carriers but also their opsonisation, marking them for clearance by phagocytic cells in RES organs [34]. Larger particles (> 200 nm) are reported more likely to be captured by phagocytic cells in the RES such as liver and spleen [34-35]. For example, Fang *et al*. compared protein adsorption and phagocytic uptake of PEG-PHDCA (poly methoxypolyethylene glycol cyanoacrylate-co-n-hexadecyl cyanoacrylate) nanoparticles of three sizes: 80, 170 and 240 nm after incubation with serum for 2 h [40].The results indicated that protein adsorption was 6%, 23% and 34% respectively for the sizes. The blood clearance of large particles was twice as fast as that of small nanoparticles [40].

#### 1.1.2.2. The effect of nanoparticle surface charge

The surface charge of nanocarriers can significantly affect their circulation half-life, cellular uptake efficiency as well as BD in the drug delivery process. It was previously reported that particles with positively charged amino groups on their surface are more likely to be cleared by phagocytic cells than particles with negatively charged sulfate, hydroxyl and carboxyl groups on their surface [34]. This

can be attributed to the electrostatic interactions between particles and cell surfaces. Positive nanoparticles tend to adsorb on negatively charged cell surfaces, therefore increasing their chance to be internalized by cells.

For some applications, such as gene transfection which requires the condensation of negative DNA, passing through the cell membrane, escaping from the endosome and delivering the DNA to cell nucleus, positive nanocarriers such as polyethyleneimine or chitosan nanoparticles have been used [41-45]. However, positive surface charge on carriers can also increase their chance of protein adsorption causing rapid clearance by the RES ad well as nonspecific uptake [34]. In contrast, negative particles show a lower chance of nonspecific uptake and clearance by RES [34]. Yamamoto *et al*. compared the BD of neutral Tyr- PEG / PDLLA and negative Tyr-Glu-PEG / PDLLA micelles in mice and found that the anionic micelles exhibited a 10 times lower distribution into the liver and spleen than the neutral ones 4 h after injection than neutral micelles [46]. This indicates that the electrostatic repulsion between negative carriers and the negative cell surfaces reduced their nonspecific cellular uptake, strongly suggesting that the surface charge of nanocarriers is an important factor affecting their circulation half-life and BD [34]. From this, one can infer that altering the surface charge of nanocarriers can result in a better control of circulation time and nanocarrier distribution for the desired applications.

#### 1.1.2.3. The effect of hydrophobicity

The surface hydrophobicity of nanocarriers is also an important factor that affects their circulation half-life and distribution [1]. Serum proteins are more likely to adsorb onto particles with a higher hydrophobicity, thus highly hydrophobic nanocarriers have a greater chance to be cleared by macrophages [1]. Gessner *et al*. compared the protein adsorption on latex particles with varying

surface hydrophobicity after incubation in human plasma for 5 min at 37°C [47]. The data showed that with decreasing hydrophobicity, protein adsorption decreased. Therefore, in order to achieve prolonged circulation time in the blood stream, nanocarriers should ideally possess hydrophilic surface [1]. A common method to provide carriers with a hydrophilic surface is coating with PEG, a hydrophilic polymer [2].

In summary, in order to improve the circulation half-life and BD of encapsulated drug, nanocarriers need to be carefully engineered to possess suitable properties such as appropriate size range, surface charge and hydrophobicity. Further to the targeted delivery of drugs via the EPR effect, another method known as magnetic targeting, that usually used to enhance accumulation of magnetic nanocarriers at the target cells, can provide more specific delivery of drugs [1, 48]. In this thesis, $Fe_3O_4$ magnetic nanoparticles are employed to fabricate magnetic core-shell nanoparticles for targeted drug delivery. The mechanism and properties of drug delivery by magnetic nanoparticles are discussed in the following Section 1.1.3.

### 1.1.3. Magnetic nanoparticles for drug delivery

Magnetic nanoparticles (MNPs) are a kind of nanomagnetic material with small particle size, large surface area, magnetic response and superparamagnetism [49]. MNPs are widely employed in magnetic resonance imaging (MRI), magnetic hyperthermia and drug delivery due to their magnetic property [49]. For the application of drug delivery, MNPs are usually employed in the form of superparamagnetic magnetic nanoparticles of a particle size smaller than 30 nm [50]. $Fe_3O_4$ and γ-$Fe_2O_3$ are the most frequently used superparamagnetic iron oxide nanoparticles (SPIONs) and both materials are ferromagnetic in larger sizes [50]. However, when their size is decreased to below 30 nm, they become superparamagnetic instead of permanent magnetic, which means that MNPs

can be affected by an external magnetic field but do not get attracted to each other [50]. The superparamagnetism property of SPIONs decreases their risk of aggregation in solution, thus making them promising as drug carriers [50]. Iron oxide based MNPs are suitable for medical applications such as drug delivery because the human body contains a large amount of natural occurring iron, meaning that iron oxide nanoparticles are biocompatible and can be metabolized by the human body [50]. Further to this, MNPs can be used to deliver drugs to desired sites with the help of an external magnetic force.

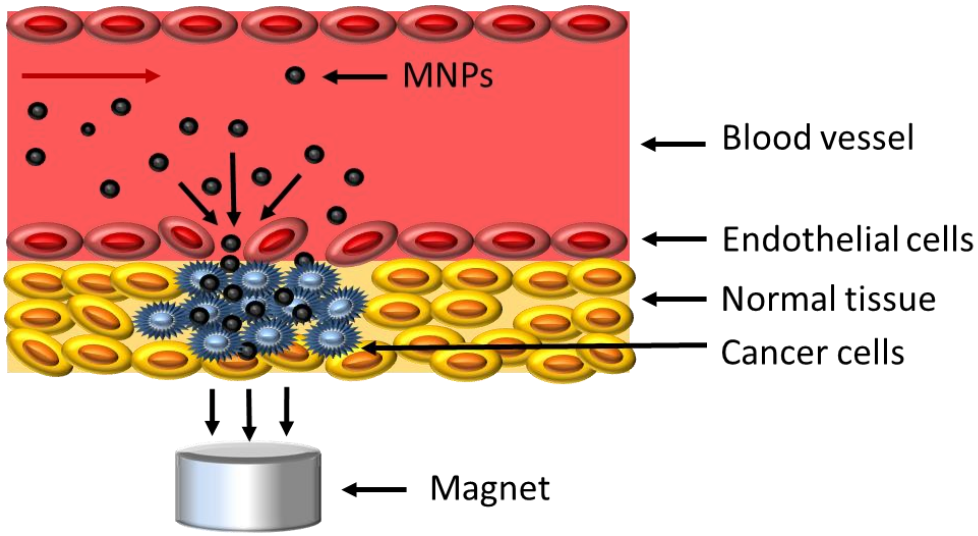


Fig. 1.2. Schematic representation of targeted delivery of MNPs with the presence of an external magnetic field.

The mechanism of targeted delivery of MNPs under a magnetic field is shown in Fig. 1.2. MNPs are used in targeted delivery of drugs to cancer cells, the anti-cancer drugs are encapsulated in the carrier or coated on its surface [51]. MNPs can pass through the gaps between endothelial cells in the blood vessels in tumour tissue to reach the cancer cells via the EPR effect [51-52]. External magnetic fields can be used to facilitate their extravasation from blood vessels and accumulation at the desired tumour sites [51-52]. Once accumulated, drugs are either released from the carriers or internalized by cancer cells along with the carriers [51]. Therefore, targeted delivery and located

accumulation of drugs can be achieved, helping to reduce the undesired accumulation of drugs within healthy tissue and enhancing the therapeutic effect against cancer cells. The effect of MNP accumulation depends on the intensity of the magnetic field, rate of blood flow, surface characteristics of magnetic carriers and the location of tumour tissue [51]. For tumours located deep inside the human body, magnetic targeting more difficult to achieve due to the magnetic force being dependent on the inverse square of the MNP-magnet distance [53]. In order to counter this problem a magnet would need to be implanted near the tumour tissue [53].

Drug delivery via magnetic carriers includes several advantages such as (1): the targeting process can be visualized by MRI; (2): external magnetic fields can provide additional means for directed accumulation at tumour sites, thus possessing a higher specificity against cancer cells; (3) in an alternating magnetic field, MNPs can be employed as mediators for magnetic hyperthermia [48, 52]. Due to their outstanding properties, MNPs are believed to be very promising as drug carriers and research has been conducted to explore their applications in the field of drug delivery [48].

The application of magnetic carriers for drug delivery was first conducted in the year 1978 by Widder *et al*., who reported the targeted delivery of DOX by magnetic albumin microspheres in animal models [54]. This concept was then further developed in 1980s when several groups reported the employment of magnetic microspheres for drug delivery [55-57]. However, these carriers used in early research were micro-sized. As discussed in Section 1.1.2.1, large particles are more likely to be eliminated by the RES and may not pass through the gaps in tumour blood vessels via the EPR effect, therefore, nano-sized magnetic carriers are desirable. The first usage of nano-sized magnetic carriers in animal models was reported by Lübbe *et al*. in 1996, who employed epirubicin loaded MNPs in first phase I clinical trials [58]. From then onwards, various strategies have been used to prepare MNPs with improved properties and their application in the field of biomedical

engineering was expanded [48]. For example, Tian *et al*. prepared the silk fibroin coated MNPs containing DOX for the targeted delivery of DOX in mice [59]. Their results indicated that a significantly higher amount of DOX accumulated at the tumour sites when magnetic carriers were used (with an external magnetic field provided) in comparison to nonmagnetic carriers.

However, despite various advantages of MNPs as mentioned above, there are drawbacks limiting their applications. One of the major drawbacks is their instability in aqueous solution [60]. $Fe_3O_4$ MNPs are more active than their bulk materials due to their high surface to volume ratio, thus are more likely react in aqueous solution [60]. After injection into the human body, reactive oxygen species (ROS) may be generated from the surface of MNP by enzymatic degradation [50]. Once ROS accumulates in the human body, consequences such as damage to cellular proteins, enzymes, lipids, and nucleic acids can occur, leading to apoptosis of healthy cells [50]. Therefore, it is essential to coat the magnetic cores in order to avoid the leaching of toxic components [60]. Apart from providing a shell to protect the magnetic cores from corrosion, surface coating made from e.g. polymers can be used to provide the MNPs with different applications. Coating of silk fibroin can provide a polymer matrix for enhanced drug loading and controllable drug release [28, 59]. Coating polyethyleneimine onto $Fe_3O_4$ MNPs surfaces enables the magnetofection of DNA [61]. Another example is the coating of alginate / chitosan polymers onto the surface of $Fe_3O_4$ MNPs, enabling enzyme immobilization [62].

In this thesis, the three naturally occurring polymers (silk fibroin, alginate and chitosan) are used for the surface coating of $Fe_3O_4$ MNPs for controlled release of curcumin. They were chosen due to their excellent properties such as low toxicity, good biocompatibility and biodegradability.

### 1.1.4. Properties of polymers investigated in this project

#### 1.1.4.1. Silk fibroin

In recent years, silk fibroin obtained from the silkworm *bombyx mori* has been widely studied to develop various biomaterials such as micro / nanoparticles, mats, films, scaffolds and gels for applications such as drug delivery and tissue engineering due to its excellent properties such as high biocompatibility, tuneable biodegradability, robust mechanical performance and ease of process [63-66].

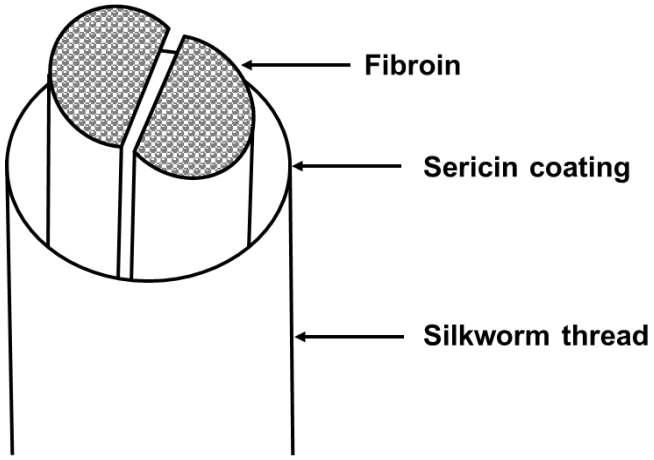


Fig. 1.3. Schematic representation of the structure of silk.

The structure of silk is shown in Fig. 1.3. Naturally produced silk fibres consist of two parallel silk fibroins are surrounded by sericin [63]. There is approximately 75% silk fibroin (SF) which is a fibrous protein and 25% sericin which is an amorphous protein [64, 67]. The semi-crystalline structure of SF provides silk with stiffness and strength while sericin plays the role of a linker to keep the integrity of fibres [64, 66]. Through a process known as degumming, sericin can be removed from SF and dissolved in boiling $Na_2CO_3$ solution [64]. SF is composed of a light (L) chain (26 kDa) and a heavy (H) chain (390 kDa), which are linked by a single disulphide bond between Cys-c20 of the H chain and Cys-172 of the L chain [64, 67]. P25, which is a glycoprotein (25 kDa), also acts as a linker to

non-covalently link the H and L chains [64]. The ratio of H chain, L chain and P25 is 6:6:1 in SF [64]. The amino acids in SF from *bombyx mori* mainly consist of alanine (Ala) (30%), glycine (Gly) (43%) and serine (Ser) (12%) [68]. The hydrophobic domains of the H chain consist of repetitive hexapeptides of Gly-Ala-Gly-Ala-Gly-Ser and dipeptides of Gly-Ala, Gly-Ser and Gly-Tyr (tyrosine), which form stable anti-parallel β-sheet crystallites [63]. On the other hand, the amino acid sequences in L chains are not repetitive, which makes the L chain less hydrophobic and more elastic [63]. The crystal structures of SF including mainly random coil rich silk I and β-sheet rich silk II [63]. Moreover, another crystal structure of SF (silk III) with a hexagonal packing of silk molecules in a left handed threefold helical chain conformation was also observed in films of the air / water interface of SF solutions [69].

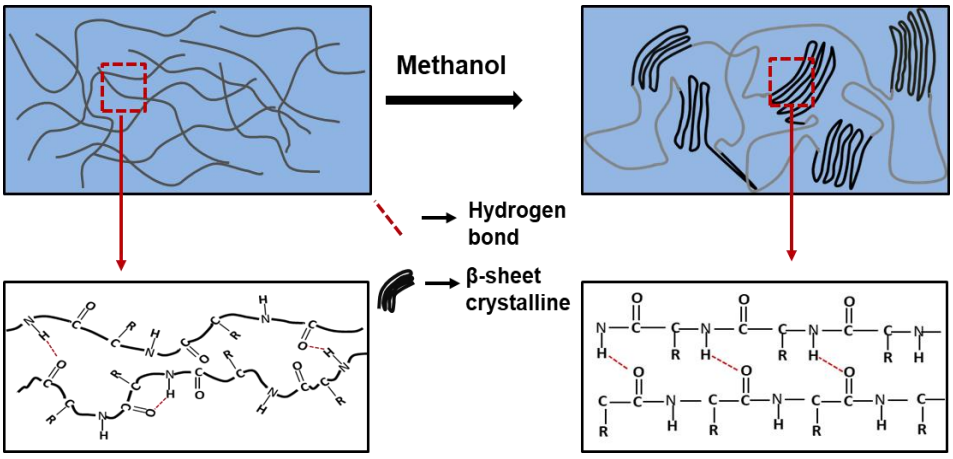


Fig. 1.4. Schematic representation of silk I structure converted to silk II.

As shown in Fig. 1.4, silk I structure is metastable, soluble in water as random coils and α-helixes. On the other hand, silk II structure is rich in β-sheet, stable and insoluble in water [70]. Silk I structure can be easily converted to silk II structure by adding methanol or potassium phosphate [63-64, 71]. The strong hydrogen bonds between adjacent segments of the anti-parallel β-sheet structure in silk II makes it insoluble in water and thus provides a favourable materials for the fabrication of SF biomaterials [63].

Kundu *et al*. investigated the drug release profile of vascular endothelial growth factor (VEGF)

loaded SF nanoparticles (150-170 nm) and found that sustained release of VEGF lasted over three weeks [72]. Bessa *et al*. prepared the Bone morphogenetic proteins (BMPs) encapsulated SF microparticles (from 500 nm to 3 μm) and reported that sustained release of BMPs for two weeks was observed [73]. Further to this, Chen *et al*. fabricated paclitaxel loaded SF nanoparticles 270-520 nm in diameter and reported a sustained release of the drug for 2 weeks [74]. Wen *et al*. successfully loaded enhanced green fluorescent protein (EGFP) in SF microspheres (30-60 μm) at a high encapsulation efficiency of 95% and achieved a burst release free and sustained release for 50 days. All these researches indicate that SF is a promising material for the fabrication of drug carriers [75].

As previously discussed in Section 1.1.2.1, the size of drug carriers needs to be carefully engineered to improve circulation half-life and BD of loaded drug. Therefore, various methods have been developed for the fabrication of SF particles with appropriate size ranges. Cao *et al*. fabricated SF particles with sizes ranging from 200 nm to 1.5 μ m by adding predefined amounts of ethanol into SF solutions and incubation of the mixtures in a freezer (at temperatures between -5 to -40℃) [76]. The size of particles could be controlled by altering the concentration of SF, amount of ethanol used and the temperature of the freezer [76]. A major advantage of this method is the simple production process coupled by ease of particle size control. However, the organic solvent residue in resultant particles may bring potential risk in their drug delivery applications due to toxicity [28].

Imsombut *et al*. fabricated SF microspheres by adding SF solution dropwise into ethyl acetate under continuous stirring to create a W / O emulsion system in which the silk solution acted as the water phase and ethyl acetate as oil phase [77]. The SF microspheres could be fabricated in the emulsion system and collected by centrifugation, washing with ethyl acetate and drying in a vacuum oven at room temperature for 4 h [77]. This method possesses the advantage of fabricating smooth and

completely spherical shaped particles but its major drawbacks are difficulty to process and to remove the emulsion agent.

An aqueous based method has been reported by Wang *et al*. to fabricate silk nano / microspheres (300 nm-2 μm) [78]. Firstly, SF solution and polyvinyl alcohol (PVA) were blended and air-dried to produce silk / PVA blend films. These films were then dissolved in water and centrifuged to remove PVA [78]. The PVA network enables the fabrication of regular and smooth SF particles but the process is slow and complicated [63].

In contrast, the fabrication of SF particles via a salting-out method is significantly simpler [63]. Lammel *et al*. fabricated SF particles by adding SF solution into potassium phosphate solution followed by incubation in a freezer at -20 ℃ for 2 h [79]. the size of resulting SF particles ranged between 500 nm to 2 μm depending on the SF concentration and the ionic strength of the potassium phosphate solution [79]. Apart from being a simple process, this method possesses several other advantages including the absence of organic solvents, low cost and safe operation. However, the size of SF particles (500 nm - 2μm) prepared by this method is far from the optimum size range (50 - 200 nm) of nanocarriers for drug delivery applications [38].

#### 1.1.4.2. Chitosan

Chitosan (CHI) is a polysaccharide which is normally prepared by the deacetylation of chitin which is a naturally derived, nontoxic, biocompatible and low-cost polysaccharide [80]. Chitin can be easily obtained from the environment because it wildly exists in shells of crabs or shrimps and can be used as a biomaterial to fabricate artificial fibres for wound dressing or coupled with chitosan to make tablets for drug delivery [81]. However, the applications of chitin are limited compared with chitosan mainly because chitin is a hydrophobic polysaccharide which is insoluble in aqueous

solution [81].

Unlike chitin, CHI is soluble in acidic solutions such as acetic acid and formic acid, which makes it easier to process CHI for the fabrication of many biomaterials [81]. The different solubility of chitin and CHI results from their differences in structure. As shown in Fig. 1.5, CHI is composed of N-acetyl-D-glucosamine and D glucosamine in which the primary amino groups of CHI result from the deacetylation of chitin [81-82].

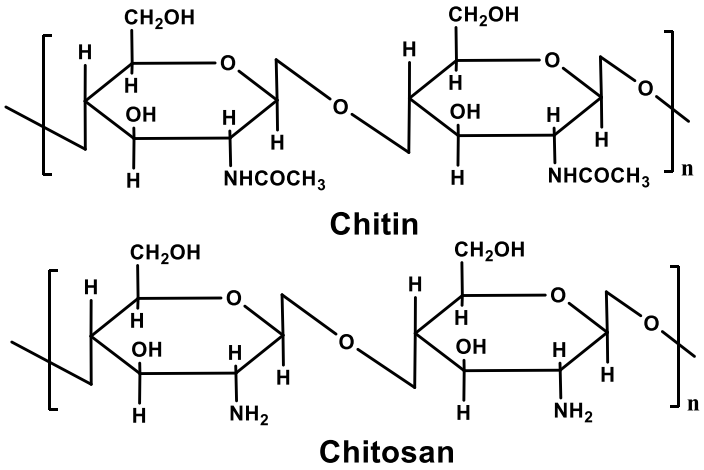


Fig. 1.5. Chemical structure of chitin and chitosan.

The primary amino groups of CHI are responsible for the solubility of CHI. Under acidic conditions, amino groups of CHI interact with protons, which leads to the protonation of the CHI structure [80]. Therefore, the CHI chains will carry cationic charges which will increase the electrostatic repulsion between CHI chains and keep them stable and soluble in water. This is the reason why CHI is usually dissolved in 1% (v/v) acetic solution [80].

In neutral and alkaline solutions, the protons associated with CHI amino groups tend to dissociate from amino groups, which lead to the neutralization of CHI chains and the reduction of the cationic charges and the electrostatic repulsion between CHI chains [32]. In this case, the electrostatic repulsion will be insufficient to keep CHI chains from interacting with each other and thus resulting

in the reduced solubility of CHI [32]. This mechanism has been confirmed by many previous reports [32, 83-84]. For instance, López *et al.* fabricated CHI coated iron oxide nanoparticles and investigated their stability and zeta potential at different pH conditions [83]. They found at a pH value lower than 3, the zeta potential of particles was larger than +40 mV, suggesting protonation of CHI. With increasing pH, the zeta potential decreased, indicating that CHI chains were undergoing deprotonation. At pH 11 the surface charge of particles reached ~0 mV and a large amount of precipitate could be observed.

The pH-dependent zeta potential of CHI makes it a unique material among natural derived polymers [85]. The positive charge of CHI provides advantages for many applications including wound dressing, tissue engineering, gene delivery and drug delivery [85]. For instance, by utilizing the pH dependent solubility property of CHI, particles for drug delivery can be made [80].

Particles can be fabricated by adding acidic CHI solution into alkali solution such as sodium hydroxide or sodium hydroxide / methanol with an air nozzle to induce precipitations [80]. The size of the particles can be controlled by altering the nozzle diameter or the air pressure [80]. The drawback of this method is the introduction of hash environment from high concentration of alkaline solutions.

Another way to make CHI particles is an emulsion cross-linking method [80]. In this method, cross-linking agents are used to react with CHI. The amino groups in CHI can interact with aldehyde groups from cross-linking agents to form a cross-linked network. The reaction generally occurs in a water / oil emulsion system in which CHI is dissolved in the aqueous phase surrounded by oil phase [86]. With this method, the CHI particles size can be controlled by altering the aqueous droplet size [80]. However, this method possesses a few drawbacks e.g. difficulty to process and the requirement of introduction of cross-linking agents [80].

Using an ionic gelation method these problems can be overcome [87]. Advantages of this method are

easy fabrication and avoiding the use of toxic cross-linking agents, this therefore can avoid the risk of organic solvents interacting with active drugs and allows the loading of sensitive molecules [80, 88]. Fabrication of CHI particles with this method depends on the interaction between positive amino groups from CHI and negative phosphate ions from tripolyphosphate (TPP) which is a polyanion [88]. In this method, CHI is first dissolved in acidic solution where its amino groups are protonated to possess positive charges. Next, the CHI solution is added dropwise to TPP solution with consistent stirring. In the mixed solution, cationic amino groups will interact with the anionic phosphates, which lead to the ionic gelation of CHI and the formation of CHI particles [80]. Although this method possesses many advantages, there is one drawback associated with CHI particles fabricated with this method, which is the poor mechanic strength of these particles [80].

The previously mentioned characteristics together with low toxicity, good biodegradability and biocompatibility make CHI a promising material for the fabrication of drug carriers [80]. It has been reported that the LD50 of CHI in laboratory mice is 16 g/kg, which is close to sugar or salt [80]. When in living tissues, CHI does not cause allergic reactions and can be degraded to non-toxic amino sugars that can be absorbed by the human body [80]. Moreover, CHI possess antimicrobial properties and can absorb toxic metals such as mercury and cadmium [80].

Moreover, CHI particles possess a few advantages as drug carriers such as controlled release property, mucoadhesive character, transfection enhancing property and permeation enhancing property [80, 85]. These advantages are associated with the cationic amino group property of CHI. For example, CHI based carriers are excellent choices for the sustained release of anionic drugs [85]. Normally, sustained release of drug depend on electrostatic interactions mediated retardation is a frequently used strategy for drug delivery if the desired release profile cannot be obtained by simple dissolution, diffusion, erosion or membrane control [85]. Thus CHI particles can be used for the

release of anionic drugs such as naproxen [89] and curcumin [29, 32, 90] to achieve prolonged drug release. Apart from this, coupled with anionic polymers such as alginate or carrageenan, CHI can be used to produce stable complexes from which encapsulated drugs can be sustained released via a diffusion or erosion process [91]. The mucoadhesive character of CHI particles, which is achieved via the electrostatic interactions between positive amino groups from CHI and the negative substructures in the mucus gel layers, can help to increase their residual time at the site of absorption [80,85]. Moreover, the transfection enhancing property, which can improve the uptake of DNA based drugs and the permeation enhancing property of CHI based carriers are also based on the positive charges of CHI [85].

#### 1.1.4.3. Alginate

Alginate is a naturally obtained anionic polysaccharide extracted from brown seaweed [92-94]. Hydrogels of alginate can be fabricated in different ways and they possess structures similar to the extracellular environment of living tissues [93]. In addition to this, alginate possesses a few desirable properties such as good biocompatibility, low cost, low cytotoxicity and a mild synthesis process during gelation [92-94]. Thus, alginate is a promising material for various applications including wound dressing, delivery of drugs and tissue engineering [92-94]. As wound dressings, alginate matrixes can help to maintain a physiologically moist environment and minimize the microbial infection of the wound, which contributes positively to wound healing [93-94]. As drug carriers, the release rate of active materials such as small molecular drugs or macromolecular proteins from alginate hydrogels can be controlled by altering the cross-linking methods and cross-linking agents [93, 95-97]. As tissue engineering materials, alginate hydrogels can be used for the delivery of cells to the wounded sites, providing a space for new tissue to form and giving control over the structure and function of the

engineered tissue [93, 98].

Alginate consists of two monomeric units: (1-4)-linked β - D-mannuronate (M) and α -L-guluronate (G) residues [93]. As shown in Fig. 1.6, the structure of alginate is made up of the blocks of consecutive G residues, M residues and alternating M-G residues [93]. Alginate originating from different sources possess different percentages of M and G residues and their sequences [93].

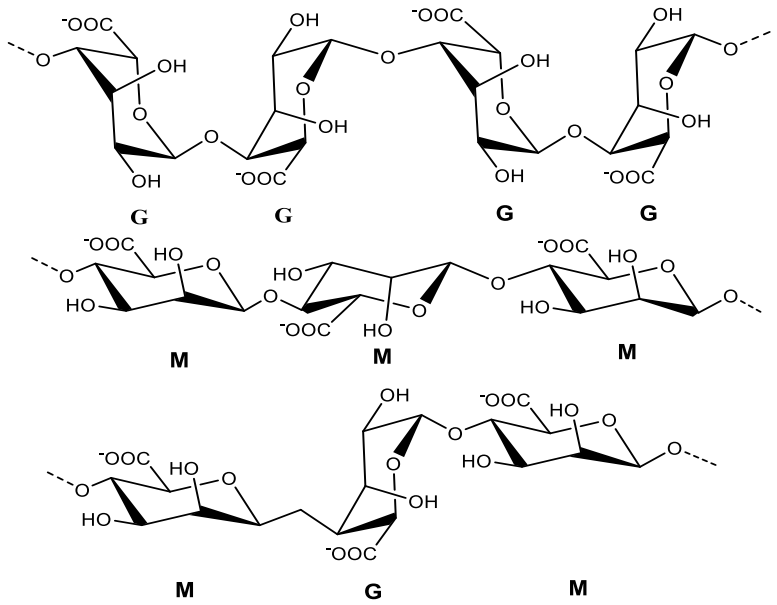


Fig. 1.6. Chemical structures of G block, M block and alternating G-M block in alginate.

M and G residues have different properties. For example, only G blocks in alginate are believed to be capable of cross-linking with divalent cations such as $Ca^{2+}$ and $Ba^{2+}$ to generate hydrogels [93]. The process of fabricating alginate hydrogels with divalent cations is the most common method [93]. When the divalent cations (e.g. $Ca^{2+}$) are introduced to an alginate solution, they are believed to bind to the G blocks in alginate chains via the electrostatic interactions between carboxyl groups and cations [93]. Therefore two G blocks on two adjacent alginate chains bind to cations and form a 'diamond shaped hole' consisting of a hydrophilic cavity that binds the cations by multicoordination [92]. As shown in Fig. 1.7, this process leads to formation of the alginate network in the shape of an 'egg-box' [92]. The physical properties of the resulted hydrogels can be affected by the ratio of G and

M residues, their sequences, G block length and molecular weight [93]. Normally, the longer the G block length and the higher the molecular weight, the stronger the mechanical properties for alginate hydrogels are [93]. In addition, alginate hydrogels with higher amount of G residues exhibit a higher structural strength compared to the hydrogels with lower G residue content [94].

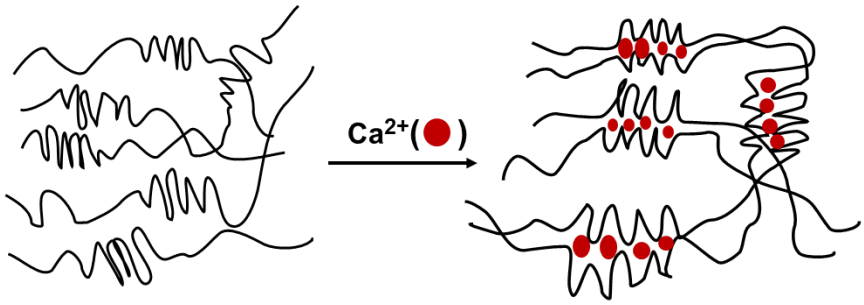


Fig. 1.7. Preparation of alginate hydrogel via $Ca^{2+}$ cross-linking resulting in the 'egg-box' shaped network.

Apart from ionic cross-linking, alginate hydrogels can also be fabricated via altering the pH of the alginate solution [92]. The disassociation constants ($pK_a$) of M and G residues are 3.38 and 3.65 respectively [92]. Therefore alginate is soluble in water at neutral environment due to the deprotonation of carboxyl groups on alginate chains and exhibit negative charge across a wide range of pH [92, 99]. The solubility of alginate solution decreases with decreasing pH and becomes insoluble around pH 3-3.5 as carboxyl groups of alginate chains are protonated and form hydrogen bonds which results in the formation of alginate acid hydrogels [93]. The rate at which the pH changes can be used to form different types of alginate acid hydrogels [100]. When the pH is rapidly decreased, alginate polymers tend to precipitate and form aggregates [100]. On the other hand, if the pH is reduced slowly and steady, continuous alginate acid bulk gels can be prepared [100]. Similar to ionic cross-linked hydrogels, the mechanical strength of alginate acid hydrogels is improved with increasing G block content in the alginate chains [101].

## 1.2. Gene delivery systems

### 1.2.1. Gene therapy

The mutation or deletion of human genes can result in disorders in metabolic pathways, receptor functions or protein structure and function, which will result in various diseases including cancer [102]. Researchers found that by transferring a corrected or completed copy of the mutant or deleted gene into human cells, the gene-related diseases can be controlled or cured [103]. By delivering genomic materials into certain cells to correct the disordered cell behaviour or provide the cells with desired functions, many diseases can be cured, this process is known as gene therapy [104]. The concept of gene therapy was first investigated in the early 1970s [105] and the first gene transfer in humans was conducted in 1989 on tumour-infiltrating lymphocytes [106]. In 1990, the first gene therapy was conducted to treat patients with severe combined immunodeficiency defects [107]. During the last two decades, it has been used to treat many inherited and acquired diseases such as cancer, Parkinson's disease, AIDS, cardiovascular diseases and cystic fibrosis [67, 108]. Therefore, gene therapy is believed to be a promising technique for treating many human diseases caused by genetic problems [67, 109].

However, the efficient application of gene therapy for curing diseases is still limited due to several biological barriers that must be overcome [108]. For example, (1) the negatively charged phosphate backbone of DNA repels it from negatively charged cell surfaces, due to the electrostatic repulsion [110]; (2) the length of a DNA strand can be $10^5$ times the length of a cell, which makes it very difficult to enter cells without being packed into a highly condensed structure [110-112]; (3) naked DNA can easily be degraded by extra-cellar nucleases [110]. What is more, the transgenes must be targeted delivered to the nucleus of cells for the correct gene expression, which is difficult for the gene itself

[108]. Therefore, in order to deliver the transgenes into the cell nucleus and to avoid gene degradation, sophisticated gene delivery systems are necessary [113-114].

Apart from ensuring the delivery of transgenes to desired site of cells, a perfect gene delivery system is expected to possess several features: (1) it will not interact with vascular endothelial cells and blood components [115]; (2) it will not be taken up by RES [116]; (3) the size of the vector should be small enough to pass through the cell membrane for the final approaching of the cell nucleus [117].

Various gene delivery systems have been developed for efficient gene delivery within the last three decades [118]. Viral vectors are one of the most widely used vectors in gene therapy due to their high efficiency in delivering genes and ability in ensuring long term expression [119]. However, the application of a viral delivery system is limited by its inherent drawbacks such as high toxicity, the risk of causing an immune response, high cost, difficulty to prepare and limited capacity for genes [108]. Therefore, non-viral gene delivery systems that possess advantages of low cost and lower toxicities have been developed as an alternative choice [108]. Both viral and non-viral vectors are reviewed in following sections.

### 1.2.2. Viral gene delivery systems

Viral vectors refer to vectors prepared from viruses. Viruses are capable of passing through cell membranes and delivering their own genetic materials to the nucleus of the host cells [120]. After entering the host cell, viruses can use the cellular machinery of the host cells to replicate and express their own genetic materials before they spread to other cells [120]. In order to be used as a gene delivery vector, the pathogenic part of the genetic materials of a virus must be removed and replaced by the desired gene [121]. Meanwhile, the nonpathogenic structures of the virus must be retained to ensure its ability of infecting the cells [120]. The prepared virus without pathogenic genes is called a viral vector [121]. So far, viral vectors are one of the most used vectors for the transfection of genes due to their high transfection efficiency *in vivo* [122]. Although as a successful gene delivery system, viral vectors possess several serious drawbacks that cannot be ignored: (1) viral vectors may cause serious immune responses in the human body [122]; (2) it is very difficult and expensive to prepare viral vectors in large quantities [123]; (3) the size of gene that can be carried by viral victors is limited [123]. Some of most frequently used viral vectors including retrovirus vectors, adenovirus vectors and adeno-associated vectors are listed in following sections.

#### 1.2.2.1. Retrovirus vectors

Retroviruses possess the genome of 7-10 kb which consists of four gene regions known as *gag*, *pro*, *pol* and *env* [124]. These four gene regions are in charge of capsid proteins, viral protease, integrase and viral reverse transcriptase respectively [124]. The life cycle of retrovirus is shown in Fig. 1.8. Once bound to the host cell receptor, the conformation of the glycoprotein of retrovirus will be changed, which causes the fusion of their retroviral envelope with the membrane of the host cell [124].

Meanwhile, the single stranded RNA of the retrovirus will be released into the cytoplasm and will be reverse transcribed to a double stranded DNA proviral genome [124]. The DNA will then interact with the virial integrase to form a pre-integration complex which will be delivered to reach the nuclear membrane [124]. When mitosis occurs, the nuclear membrane becomes disrupted and enables the internalization of complex to nucleus [124]. After entering nucleus, the proviral genome will be integrated randomly to the host chromosomal genome by the viral integrase and the viral genes will be expressed by the host cellular machinery [124].

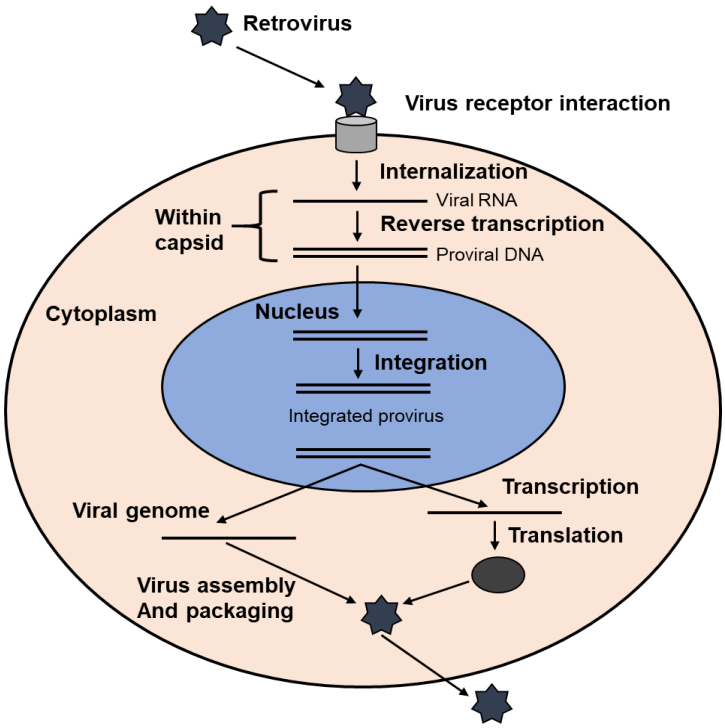


Fig. 1.8. Schematic representation of the retrovirus life cycle.

To prepare the retroviruses as gene delivery vectors, all the retroviral genes must be deleted and replaced with therapeutic genes or other desired genes [124]. After the retroviral gene deletion, the infected host cells will not express viral proteins but will be capable of expressing the therapeutic genes [124].

As one of the most frequently used viral vectors, retrovirus possess several advantages such as the inability to express any viral proteins, which can avoid immune responses, capability of stably

transduce dividing cells and capable of long term transgenes expression for over two years [125]. On the other hand, the disadvantages of retrovirus vectors include their low capacity for therapeutic genes, the random insertion into the host genome, which may result in the activation of oncogenes or the inactivation of tumour suppressor genes, low efficiency *in vivo* and the inability to transduce non-dividing cells [124].

#### 1.2.2.2. Adenovirus vectors

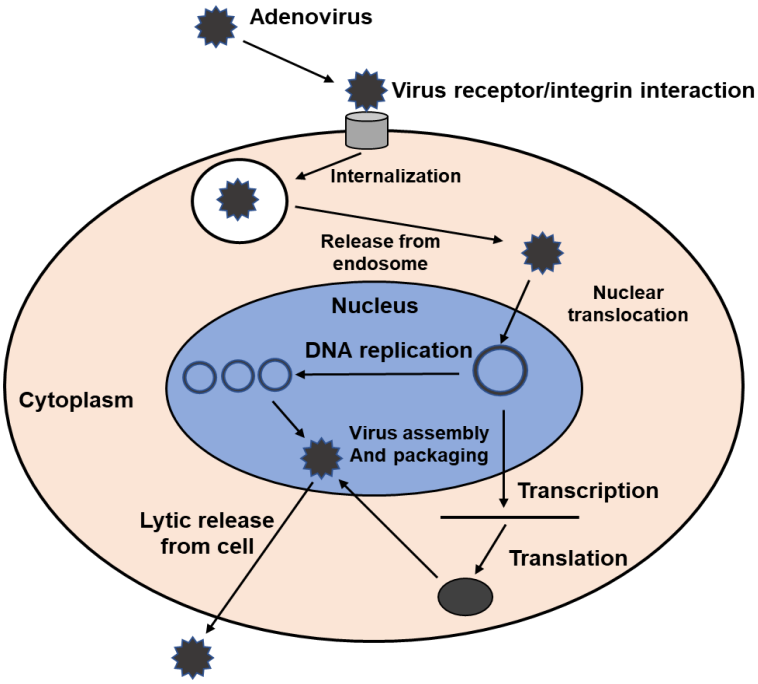


Fig. 1.9 Schematic representation of the adenovirus life cycle.

Adenoviruses are double stranded DNA viruses and can cause several mild human infections such as respiratory tract infections and gastroenteritis [124]. Adenoviruses are capable of efficiently infecting many cell types including dividing and non-dividing cells, which makes the adenovirus developed vectors capable of transferring both cell types [118, 124]. The length of adenovirus genome is 36 kb which makes it possible to pack large therapeutic genes after the deletion of its own DNA [124, 126]. As shown in Fig. 1.9, the infection of adenoviruses to a host cell is started from the interactions

between the virus fibre knob protein and the adenovirus receptor on surface of the cell [124]. After the initial attachment, the adenovirus virion will be internalized by the host cell through endocytosis and then packed in the endosome [124]. In the acidic environment of endosome, the conformation of adenoviruses virion capsid proteins tend to change which results in the release of the capsid into cytoplasm from where the capsid is delivered to the cell nucleus [124]. After entering the cell nucleus the adenovirus genome will be released and start the process of replication and transcription without integrating into the host cell genome [118, 124].

Adenovirus vectors can be prepared by the deletion of the E1 region and the replacement of E1 region with therapeutic genes [124]. The adenovirus vectors possess several advantages including: (1) the ability to infect various cell types including dividing and non-dividing cells [127]; (2) a large transgene capacity [124]; (3) a high gene transfer efficiency [124]; (4) and the DNA of adenoviruses not integrating into the genome of host cells, therefore reducing the risk on activation of oncogenes or the inactivation of tumour suppressor genes [124]. Despite these advantages, there are some disadvantages that restrict the applications of adenovirus vectors [118]. For example, the gene expression time of adenovirus vectors is very short [118, 124]. Another main drawback of adenovirus vectors is that they have a high risk of causing an immune response and some other bad side effects in humans [118, 124].

#### 1.2.2.3. Adeno-associated vectors

Adeno-associated vectors are similar to adenovirus vectors in some respects but possess lower risks to human health, because they do not cause any human diseases [128]. Adeno-associated viruses possess a short single stranded DNA which can integrate to a specific location on human chromosome 19 [118]. The life cycle of the adeno-associated virus is shown in Fig. 1.10. Unlike

retrovirus and adenovirus, the adeno-associated virus is incapable of replicating without the presence of a helper virus such as an adenovirus or herpes simplex virus [124]. This feature makes the preparation of recombinant adeno-associated vectors become relatively complex. To replicate the vectors, helper viruses are needed for the infection, which result in the contamination of helper viruses in the resulting adeno-associated vector solution [124]. In order to prepare purified vectors, a purification step is required during the production process [124].

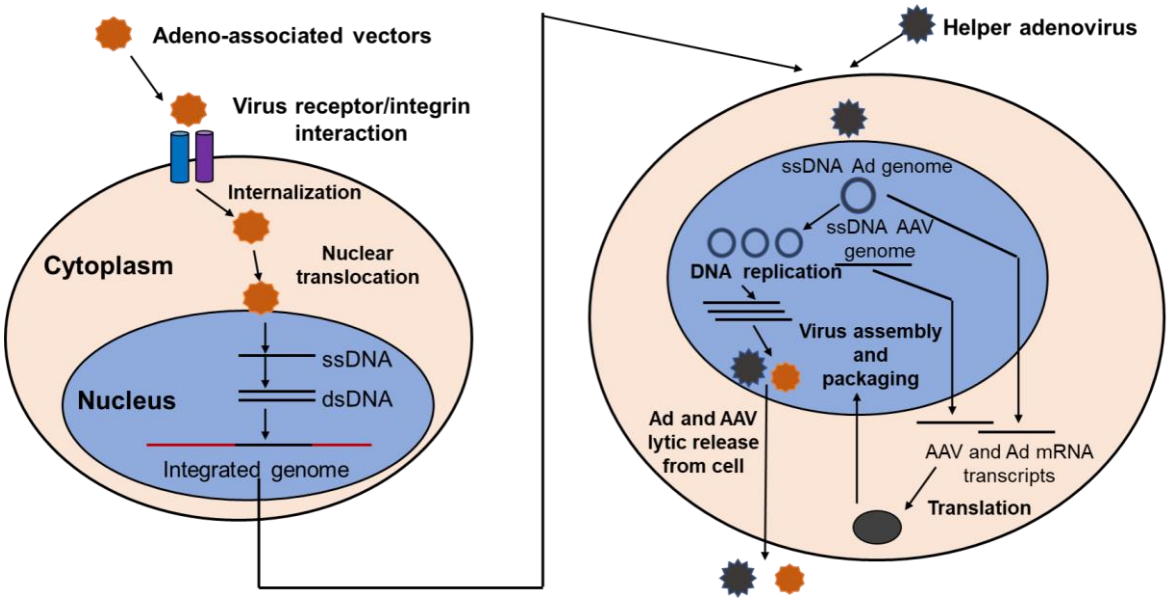


Fig. 1.10. Schematic representation of the adeno-associated virus life cycle.

Apart from the difficulty in vector production, another main drawback of adeno-associated vectors is their limited gene capacity (4.7 kb) [124]. Despite their drawbacks, adeno-associated vectors possess some advantages that cannot be ignored. Firstly, as all the viral genes are deleted from adeno-associated viruses, the resulting vectors are believed to be substantially safer to other vectors and are therefore not likely to cause any disease or immune response [124]. Further to this, due to the integration of the vectors to the specific site of human chromosome 19, long-term transgene expression can be obtained [118, 124].

### 1.2.3. Non-viral gene delivery systems

As reviewed above (Section 1.2.2), though viral vectors are widely used for gene delivery owning to their high efficiency and long term transgene express, their drawbacks such as the risk of causing serious immune responses, high toxicity and foreign gene insertion, which may cause mutations, have raised concerns for their usage in humans [114]. Further to this, viral vectors are difficult to prepare, expensive and have limited transgenes capacity [114]. All these drawbacks have brought various challenges to the application of viral vectors. Therefore, different non-viral vectors have been developed as alternatives [114]. Synthetic or natural materials are used to design and fabricate non-viral vectors. Therefore, non-viral vectors usually possess reduced toxicity and immune response risks compared to viral vectors [129]. What is more, chemical based non-viral vectors can be designed to enable transfection in specific cells and tissue [129]. Although the lower transfection efficiency and relatively short term transgene expression remains challenging for the application of non-viral gene delivery methods, they are expected to have a strong future [129].

#### 1.2.3.1. Cationic Lipid vectors

It was first reported in 1987 that N-[1-(2,3-dioleyloxy)propyl]-N,N,N-trimethylammonium chloride is capable of transferring DNA into cells. Since then, various cationic lipid vectors have been developed [114]. The structure of lipid vectors can be divided into three sections: (1) a positively charged hydrophilic head, which is in charge of the interaction with nucleic acids; (2) a hydrophobic tail and (3) a linker group that connects the head and tail groups (see Fig. 1.11) [130].

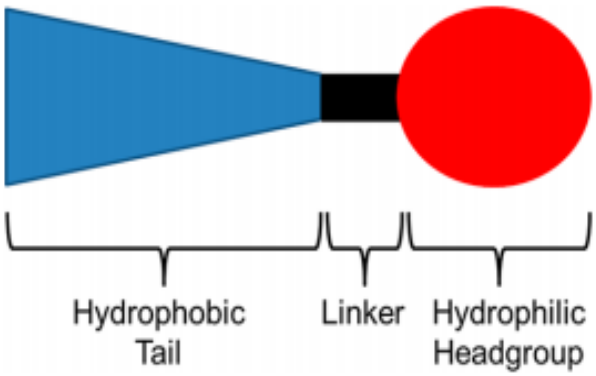


Fig. 1.11. Schematic representation of cationic lipid vectors.

In the early generations the most commonly used hydrophilic heads are primary, secondary and tertiary amines but new cationic lipid vectors have been developed using guanidino, imidazole, pyridinium and phosphorus for head groups [129-130]. The hydrophobic tail groups are usually made of aliphatic chains and cholesterol linked to the hydrophilic head group by ether, ester or amide bonds [114].

As shown in Fig. 1.12, the transfection of DNA by lipid vectors is a complex process which involves: (1) the preparation of DNA-lipid complexes; (2) internalization by cells through endocytosis and encapsulation by endosome; (3) escape from endosome and enter cytoplasm; (4) DNA imported into nucleus [131]. DNA-lipid complexes can be spontaneously formed by mixing DNA with lipids. When mixed with DNA, the positively charged head group of lipid victors will interact with negatively charged DNA through electrostatic attractions and the DNA will be condensed to form small particles. In the following process of lipid rearrangement, DNA is covered by lipids and DNA-lipid complexes are formed, known as lipoplexes [114]. Since the negatively charged DNA is covered by positively charged lipids, lipoplexes are able to interact with the negatively charged cell membranes [129]. After approaching the cell membranes, lipoplexes are readily taken up by cells through endocytosis [131].

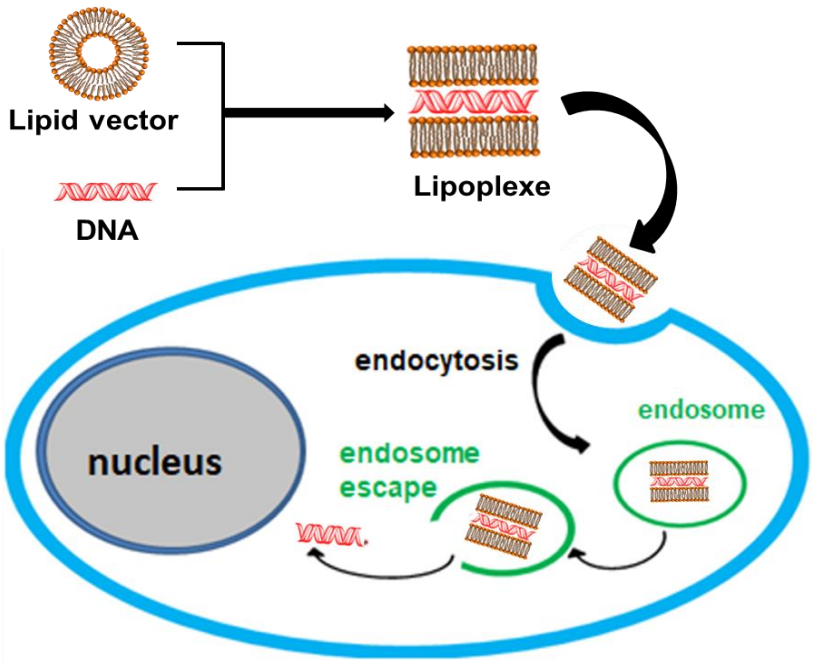


Fig. 1.12. Schematic representation of the cationic lipidmediated DNA transfection.

It was initially believed that the fusion between lipoplexes and cell membranes was the main means for the internalization of lipoplexes, but new evidence may suggest that it is a proteoglycan mediated interaction process [131]. After the initial internalization, DNA must escape the endosome to avoid being degraded by lysosomes and to reach cell nucleus, where the transgenes can be expressed [114]. Therefore, cationic lipid mediated endosome escape is a crucial process in lipid-based transfection. The process of releasing DNA from the endosome into the cytoplasm based on the destabilization of endosome membrane by the cationic lipids [131]. As shown in Fig. 1.13 four steps are involved in endosome escaping [132]. (1) Lipoplexes internalized by cells via endocytosis and encapsulated in an endosome [132]. (2) A flip-flop that faces the cytoplasm is then created as a result of the electrostatic attractions between cationic lipids from lipoplexes and anionic lipids from the endosome membrane [132]. (3) The anionic lipids then diffuse into the complex and form charge-neutralized ion pairs with the cationic lipids [132]. (4) The complex is collapsed and the DNA is released into the cytoplasm [132]. DNA that has been released from the endosomes needs to be imported into the nucleus for its expression. However, the detailed process of the internalization

of DNA into nucleus is currently not clear. It has been suggested that mitosis is required for DNA to enter the cell nucleus [131].

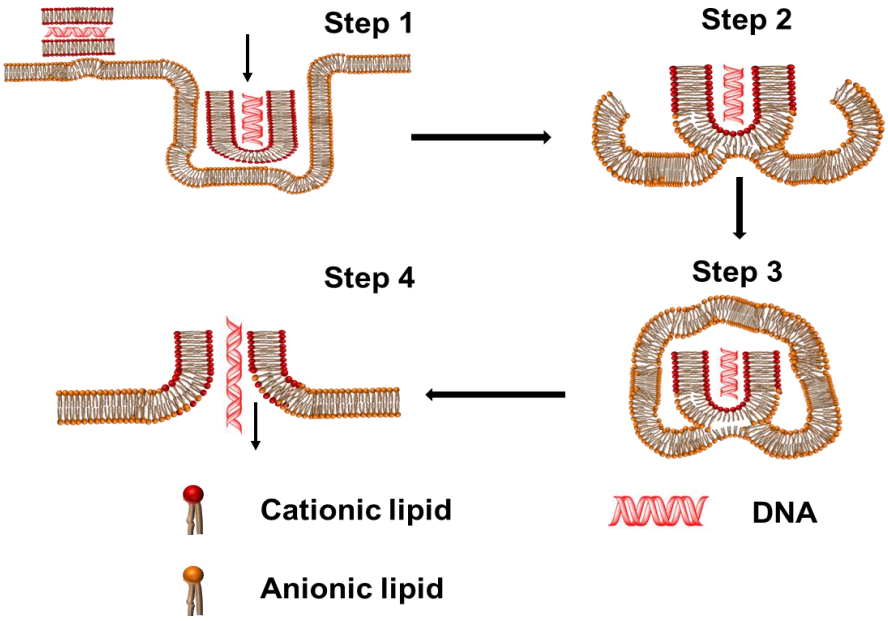


Fig. 1.13. Schematic representation of lipid mediated DNA escaping from endosome.

Good transfection efficiencies can be achieved by cationic-lipids-mediated transfections in cell culture, in the absence of serum. However, their performances are usually not satisfactory when transfection is conducted in cell cultures and *in vivo* with serum present [133]. This phenomenon is associated with the positive charge of lipoplexes. When used *in vivo*, lipoplexes will interact with negative serum components in blood which results in the formation of large aggregates. These aggregates may accumulate to block microvasculatures and can be rapidly eliminated, which lead to the short circulation half-life of cationic lipoplexes [129]. The rapid clearance of lipoplexes in blood tends to reduce their transfection efficiency and limit their applications *in vivo* [129]. In addition, another negative side effect associated with the electrostatic interaction between positively charged lipoplexes and negatively charged serum molecules is the toxicity in transfection [114]. Upon cationic lipids mediated transfection *in vivo*, negative serum proteins tend to adsorb on the surface of

lipoplexes and act as opsonins to trigger the uptake of the aggregates by RES, leading to toxic responses [114].

To overcome these problems, various strategies have been used [129]. For example, hydrophilic, neutral polymers such as PEG have been used to cover the surfaces of lipoplexes. Once coated with PEG, the excess positive charge of lipoplexes is reduced, which tends to decrease the electrostatic attraction between the lipoplexes and the negative components in blood [129]. As a result, circulation time of lipoplexes is prolonged and the risk of causing serious immune response is reduced [129]. Although increased circulation time is expected to increase the amount of lipoplexes that can interact with targeted cells which in turn increase the transfection efficiency, it is worth to note that the PEG coating can, on the other hand, lead to a dose dependent inhibition on the overall transfection efficiency since it can block the intimate interactions between cell membranes and lipoplexes [114]. Therefore, PEG-lipid complexes with different hydrocarbon lengths haven been developed to adjust the time of PEG-lipid association with lipoplexes [114].

Helper lipids such as dioleoylphosphatidylethanolamine (DOPE) and cholesterol can also be employed to reduce lipoplexes toxicity and increase transfection efficiency. Application of DOPE in cationic lipid systems has been reported to be capable of facilitating the escape of transgenes from endosomes by the means of promoting the membrane fusion between lipoplexes and the endosomal membrane [114]. As a result, the cationic lipid mediated transfection efficiency can be promoted. Moreover, with promoted endosomal escape provided by DOPE the lipid / DNA charge ratio required to reach the maximal transfection efficiency is reduced, which in turn reduces the toxicity of lipoplexes [129]. Although proven to be an effective helper lipid for transfection *in vitro* without the presence of serum, DOPE shows adverse effects on transfection. This is because DOPE lipoplexes tend to fall apart in presence of blood components [134]. Cholesterol, on the other

hand, has been reported to be a better helper lipid in the presence of serum. Cholesterol can stabilize the lipoplexes in blood against the serum components and provide better transfection efficiency [129].

In summary, cationic lipids possess advantages such as simple preparation and can be cheaply engineered for targeted transfection. On the other hand, their disadvantages are their high toxicities and low transfection efficiency [129].

#### 1.2.3.2. Cationic polymer vectors

Cationic polymers, synthesized or naturally derived, have been widely used as gene carriers [129]. After mixing with DNA, cationic polymers tend to condense DNA molecules to form nano-sized complexes which are called polyplexes [129]. One of the major advantages of polyplexes is their higher stability compared to lipoplexes [129]. Poly-L-lysine is one of the first synthetic polymers that has been employed as a gene transfection carrier since 1987 [135]. Since then, various cationic polymers have been developed for gene delivery both *in vitro* and *in vivo* [129]. Among them, polyethyleneimine is one of the most frequently used and most effective cationic polymers for gene transfection due to its high density of primary, secondary, and tertiary amine groups [129]. The process of PEI mediated gene transfection is shown in Fig. 1.14.

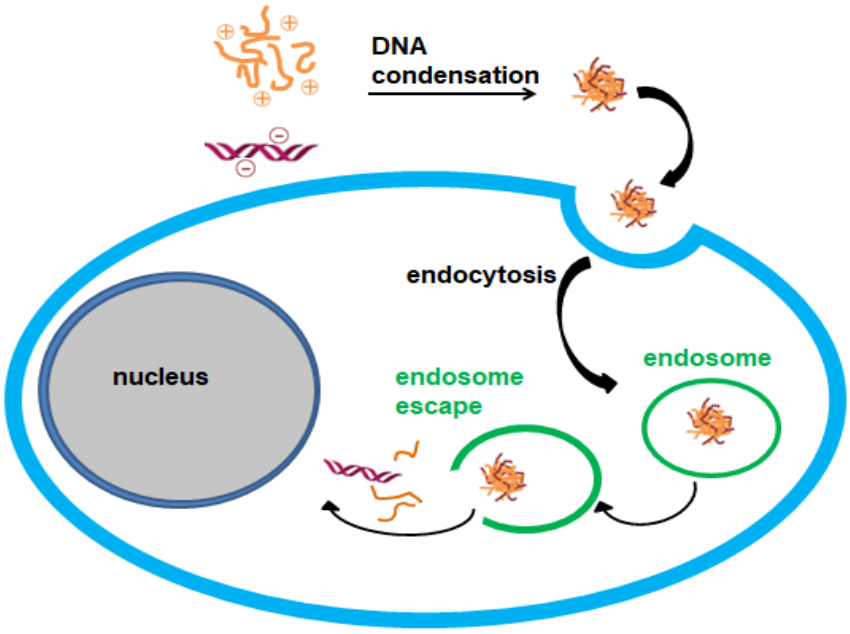


Fig. 1.14. Schematic representation of PEI mediated gene transfection.

PEI is capable of complexing with DNA to form polyplexes due to its high cationic charge density at physiological pH [42]. The resulting PEI / DNA polyplexes are then concentrated at the cell surface via the electrostatic attractions between the positive polyplexes and negative cell membranes [61]. The polyplexes are then internalized by cells through endocytosis and encapsulated in endosomes [61]. After being encapsulated in endosomes, macromolecules normally will be transported into lysosomes where they will be degraded [129]. In order to prevent the degradation of DNA in lysosomes, the endosome-lysosome process must be intercepted [129]. PEI is known to be capable of protecting DNA from been degraded in lysosomes through the 'proton sponge effect' [61]. The majority of the amine groups in PEI are non-protonated at physiological pH [61]. In endosomes, these non-protonated amine groups will absorb protons at the low pH environment, which results in the protonation of these amine groups and the accumulation of protons in endosomes [61]. Chloride ions, as counterions, are also internalized by endosomes and cause increased osmotic pressure, which in turn leads to the disruption of endosomes and the release of polyplexes to cytoplasm [61]. Moreover, the protonated amine groups in endosomes will buffer the endosome pH, slowing down

the acidification process which is essential for endosome-lysosome transition [114]. Therefore, PEI can protect the DNA from being degraded in lysosomes. Eventually, DNA is transported to cell nucleus for expression.

Despite the promising functions of PEI during gene transfection, its applications are continuously limited by its persistent problems such as strong cytotoxicity and relatively low *in vitro* and *in vivo* transfection efficiency [42]. The cytotoxicity and transfection efficiency of PEI is reported to be structure and molecular weight dependent [114]. There are two types of structures observed for PEIs: branched and linear [114]. The structures of branched PEI (BPEI) and linear PEI (LPEI) are shown in Fig. 1.15. Both BPEI and LPEI have shown good gene transfection capabilities *in vitro* but moderate transfection efficiency *in vivo* [114]. Both PEIs possess molecular weight dependent transfection efficiency and cytotoxicity [114]. The optimal molecular weight for transfection is 25 KDa for BPEI and 22 KDa for LPEI [114]. Higher molecular weight is associated with higher transfection efficiency but also greater cytotoxicity [114]. PEI with a molecular weight of 2 KDa or less is nontoxic however it shows no effect for transfection [114]. When the molecular weight is higher than 25 K, PEI is still active for transfection but exhibits a much higher cytotoxicity [114]. Upon adding to cell cultures, LPEI polyplexes exhibit higher gene expression to cells than BPEI polyplexes [114]. This phenomenon is most likely because LPEI polyplexes are not as condensed as BPEI polyplexes and more readily release DNA into the cells [114]. It has also been reported that LPEI polyplexes tend to enter the cell nucleus more rapidly [114]. Moreover, LPEI is reported to be less toxic to cells compared to BPEI [114].

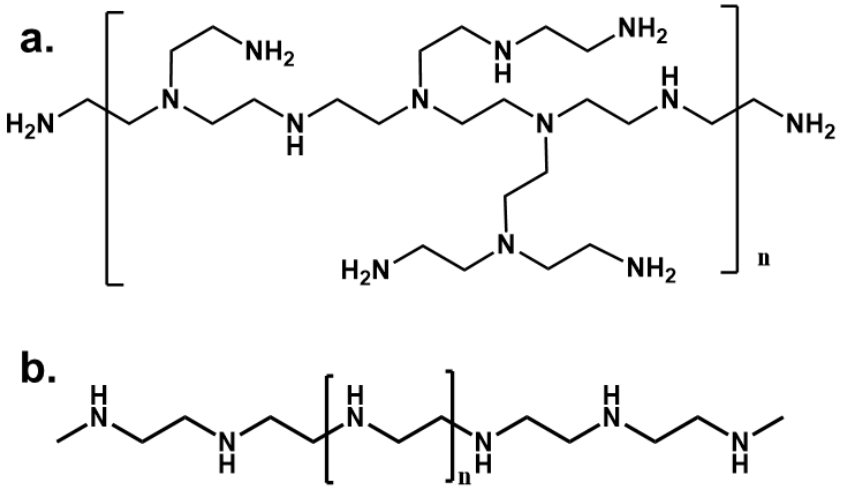


Fig. 1.15. Schematic representation of the chemical structures of BPEI (a) and LPEI (b).

Although BPEI exhibits higher toxicity and a lower transfection efficiency than LPEI, it is capable of condensing DNA more tightly and forming smaller and more stable nanoparticles [129]. Normally, when mixed with DNA, BPEI can form particles with the size of a few hundred nanometers, while LPEI tends to form much larger particles with sizes at the micrometer scale [41].

A hypothesis on the mechanism of the cytotoxicity of PEI is that it results from the high cationic charge density of PEI [45, 136-138]. Free PEI molecules can interact with negative substances in blood such as serum proteins or red blood cells, forming aggregates which can adhere to tissue surfaces and cause significant cell damages [136]. PEI can also interact with proteins inside the cell to interfere critical intracellular processes which can lead to serious toxic effects [44]. Therefore, reduction of PEI surface charge is expected to be capable of reducing the cytotoxicity of PEI mediated polyplexes. In fact, many researches aimed at reducing the cationic charges of PEI have been done through conjugating nontoxic polymers or proteins on PEI or directly coating the polyplexes with nontoxic materials [114]. The resulting PEI derivatives showed less cytotoxicity to cells [114]. For example, in the research of Xue *et al.,* hexadecylated polyethyleneimine polymers complexed with siRNA were encapsulated by negative lipids, the surface charge of encapsulated complex was decreased as

well as the cytotoxicity compared to un-encapsulated PEI complexes [139]. Liu *et al.* designed ASF (*Antheraea pernyi* silk fibroin) / PEI / DNA ternary complexes by coating negatively charged ASF onto the surface of PEI / DNA complexes [140]. The coating of ASF resulted in fewer surface charges for the complexes and higher viability for cells transfected with ASF / PEI / DNA ternary complexes compared with cells treated with PEI / DNA complexes. Ogris *et al.* compared the *in vitro* and *in vivo* properties of PEI / DNA polyplexes with PEGylated PEI / DNA polyplexes and indicated that PEGylation of the polyplexes significantly reduced the binding of serum protein, leading to a prolonged circulation of PEGylated polyplexes in blood [141].

Although reduction of cationic charge of PEI based polyplexes can reduce their cytotoxicity effect to cells, it is worth to note that too much elimination of the positive charge can also lead to loss of transfection efficiencies [114]. It is suggested that the coating / binding of PEI on the surface of nanoparticles may also modulate its cytotoxicity [136]. For instance, after gold nanoparticles are coated with PEI, the resulting hybrid transfection carrier exhibited significantly lower cytotoxicity than PEI [136]. Apart from gold nanoparticles, it is found that by coating PEI on surface of $Fe_3O_4$ nanoparticles, magnetic nanoparticle-PEI (MNP-PEI) victors can be fabricated for efficient gene delivery through magnetofection [67]. While applying magnetofection, an external magnetic field can be used to improve the transfection efficiencies via rapidly concentrates the magnetic vectors on the surface of cells [142]. Moreover, it has been reported that the cytotoxicity of MNP-PEI victors are significantly lower than PEI [143].

#### 1.2.3.3. Magnetofection

One of the major drawbacks of non-viral vectors including the most efficient transfection polymer (PEI) is their relatively low *in vitro* and *in vivo* transfection efficiency compared to viral vectors [144].

This drawback is mainly due to the fact that their delivery process is limited by the time that required for the gene loaded vectors to accumulate on cell surfaces, which is a diffusion dependent process [144]. Therefore, rapid accumulation of the vectors on the surface of cells or target tissue is desired for the improvement of the transfection efficiency [144] .

Magnetic particles have therefore been developed to rapidly concentrate genes at the target sites under a magnetic field [145]. The first practice of employing magnetic carriers to deliver nucleic acids was conducted in 1996, however with little experimental evidence [146]. The first accounts in the scientific literature have been conference abstracts by Mah *et al.* [147] and Plank *et al.* [148] in 2000. The first full paper on concentrating vectors at desired sites was reported by Hughes *et al.* in 2001 [149]. Since then, various magnetic vectors were developed for the delivery of genes to target cells, this method is referred to as magnetofection [145].

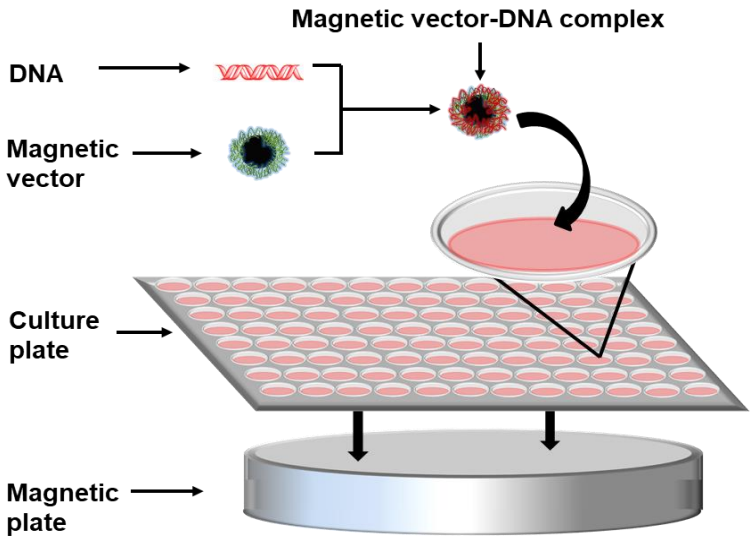


Fig. 1.16. Schematic representation of the principle of magnetofection. [144].

The principle of magnetofection is shown in Fig. 1.16. Firstly, magnetic vectors are fabricated by coating MNPs with cationic materials e.g. PEI. The resulting magnetic vectors are then mixed with naked DNA to form magnetic vector-DNA complexes via electrostatic attraction between DNA and vectors. Next, the magnetic complexes are added to cell cultures and a magnetic plate is placed

under the cell culture plate to provide a downward magnetic force. With the help of this magnetic force, the magnetic complexes will rapidly concentrate on cell surfaces to overcome the diffusion barrier, which in turn will result in enhanced internalization of the magnetic complexes and improved transfection efficiency [144].

Magnetofection exhibits advantages of much faster transfection than non-magnetofection method. For example, Mykhaylyk *et al.* have investigated the transfection performance of magnetic and non-magnetic complexes exposed to a magnetic field, their result indicated that the magnetic complexes can be rapidly focused onto the surface of target cells and the consequently transfection efficiencies can be 1,000-fold higher than the transfections conducted with non-magnetic vectors [150]. Kro¨tz *et al*. have reported that magnetic particle-ODN complexes were transfected into 84% human umbilical vein endothelial cells within 15 min when exposed to a magnetic field, non-magnetofection methods, in contrast, required 24 h. [151]. Also, it is worth to note that the mechanism of gene delivery from the cell surface into cells via magnetofection is the same as non-magnetofection [145]. In another word, the external magnetic forces do not appear to draw the magnetic complexes into cells, instead, the improved gene transfection efficiency is due to the rapid sedimentation of complexes on the cell surface within a few minutes [145].

## 1.3. Thesis plan

In summary, the above sections showed that nanocarriers can significantly facilitate the internalization of drugs and genes into cells. Materials used for the fabrication of nanocarriers must be carefully selected and generally nontoxic, biocompatible and biodegradable polymers are especially favoured so the resulting nanocarriers can avoid been rapidly cleared by the human immune system. In addition, the size and surface charge of the resulting nanocarriers can largely affect their half-life, biodistribution and internalization effect in a drug / gene delivery process. Further to this, the deployment of magnetic nanoparticles can provide nanocarriers with the ability to target desired sites under a magnetic field. Based on this information, my project aims at the design and preparation of nanocarriers with suitable size, surface charge, biocompatible coating materials and magnetic cores for the application of drug / gene delivery.

The first experimental Chapter (Chapter 3) is focused on the fabrication of magnetic-silk core-shell nanoparticles via the salting-out method. In the conventional salting-out methods SF particles are prepared by potassium phosphate [152]. However, the size of the resulting SF particles being around 500-1200 nm is significantly larger than the optimum size range of 50-200 nm for cancer therapy [38]. Therefore, a different salt (sodium phosphate) was selected for the preparation of SF particles. According to the 'Hofmeister Series'：

$$NH_4^+ > Cs^+ > Rb^+ > K^+ > Na^+ > Li^+ > Ca^{2+} > Mg^{2+}$$

the larger and less charged cations (cations to the left) are most effective at protein salting out, while the divalent cations (cations to the right) can lead to increased protein solubility [153]. Thus, the employment of sodium phosphate is expected to be capable of preparing SF particles with smaller sizes compared to those prepared by potassium phosphate. Magnetic-silk core-shell nanoparticles

will be prepared using sodium phosphate, and the effect of the SF concentration, salt concentration and pH of the salt solution of the resulting particle size will be explored.

In Chapter 4, instead of using only one polymer (e.g. SF) as the coating material, negatively charged sodium alginate and positively charged chitosan are layer-by-layer coated on MNPs to fabricate magnetic alginate/chitosan layer-by-layer nanoparticles for drug delivery. Alginate and chitosan are both commonly used polymers for drug delivery due to their excellent biocompatibility, biodegradability and nontoxicity [82]. The electrostatic attraction between alginate and chitosan enables them to be layer-by-layer coated onto MNPs to construct particles with different amounts of coating layers. This method provides a simple way to control the size and surface charge of the resulting particles. The number of the coated layers and the outermost layer of polymers is expected to be capable of controlling the loading and release profile of drugs dependent on their electrostatic interactions with the drug.

As mentioned in Section 1.2.3.2, PEI is one of the most frequently used and most effective cationic polymers for gene transfection due to its high density of amine groups [129]. However, the application of PEI is limited by its strong cytotoxicity, which can lead to low *in vitro* and *in vivo* transfection efficiencies [42]. The cytotoxicity of PEI is believed to be due to its high positive charge density [45, 136-138]. Free PEI molecules can interact with negatively charged substances such as serum proteins or even red blood cells to form aggregates, which can adhere to tissue surfaces and cause significant cell damage [136]. Therefore, in Chapter 5, negatively charged, nontoxic, biocompatible SF is mixed with PEI to prepare SF-PEI nanoparticles and magnetic SF / PEI core-shell nanoparticles. It is expected that SF can reduce the overall surface charge of the resulting nanoparticles which can lead to the reduction of their cytotoxicity.

# 2. Materials and Methods

## 2.1. Materials

*Bombyx mori* silk was obtained from Jiangsu, P.R. China. $Na_2CO_3$ (11552) was purchased from Alfa Aesar. Curcumin (C8069) was purchased from LKT Laboratories. Paraformaldehyde (sc-253236A) was purchased from Chem Cruz®. $K_2HPO_4$ (BP363), $KH_2PO_4$ (BP362), $CaCl_2$ (C1016), $Na_2HPO_4$ (S7907), $NaH_2PO_4$ (S8282), ammonium hydroxide (221228) DMSO (Dimethyl sulfoxide, D5879), Rhodamine B isothiocyanate (R1755), Sodium alginate (w201502), $Ca(OH)_2$ (21181), DMSO (Dimethyl sulfoxide, D5879) and Polyethyleneimine (branched, 408727) were purchased from SIGMA-ALDRICH. Roswell Park Memorial Institute (RPMI) 1640 Medium (BE 12-167F), PBS (Dulbecco's Phosphate Buffered Saline, BE17-512F), Penicillin 5.000 U/ml-Streptomycin 5.000 U/ml (DE17-603E), L-Glutamine (17-605F) were purchased from Lonza®. $NaHCO_3$ (A17005), Chitosan (349051000), Iron (II) chloride tetrahydrate (44939), Iron (III) chloride hexahydrate (44944), Foetal Bovine Serum (FBS,10500064), Texas Red®-X Phalloidin (T7471), Alexa Fluor® 568 phalloidin (A12380), Oligofectamine (12252011), MTT (M6494) assay and DAPI (4′, 6-Diamidino-2-phenylindole dihydrochloride, D1306) were purchased from Thermo Fisher Scientific. MDA-MB-231 cells (Human Caucasian Breast Adenocarcinoma cells) were purchased from ECACC. Ultra-High Quality (UHQ) water was prepared using PURELAB Classic (ELGA). HDF cells were provided by the Sheffield RNAi screening facility. Single-stranded human c-myc antisense oligodeoxynucleotides (5′-AAC-GTT-GAG-GGG-CAT-3′, with and without 5′-FAM (carboxyfluorescein- 5-succimidyl ester) labelled) were purchased from Eurogentec Ltd. (UK) and were HPLC purified.

## 2.2. Methods

### 2.2.1. Particle preparation and drug release

#### 2.2.1.1. Preparation of silk fibroin (SF) solution

Silk fibroin solutions were prepared based on the protocol previously reported [154]. Silk fibres were boiled for 30 min in a solution of 0.02 M $Na_2CO_3$ and then rinsed 3 times with DI water to remove sericins. The resultant material was degummed silk fibroin. Then the degummed silk fibroin was dried overnight in a drying oven at 60°C before added into a ternary system ($CaCl_2$ / Ethanol / water at molar ratio of 1: 2: 8) and heated to keep the system temperature at 75°C for 3 h. The solid silk fibroin was observed dissolved in the solution within 30 min. Next, the silk fibroin solution was dialysed in a cellulose dialysis tube (12 KDa cut off) against DI water for 3 days, during which DI water was replaced at least 5 times per day. The resulting solution was centrifuged twice at 10,000 g to remove the impurities before stored in the refrigerator at 4 °C.

#### 2.2.1.2. Preparation of magnetic nanoparticles (MNPs)

4 g iron (III) chloride hexahydrate and 4.5 g iron (II) chloride tetrahydrate were each dissolved in 150 ml DI water and degassed with nitrogen for 30 min to remove the oxygen in the solutions. The solutions were then mixed in a 500 ml round-bottom flask and 15 ml of ammonium hydroxide was added under vigorous stirring in a nitrogen atmosphere at room temperature for 2 h. The magnetic nanoparticles (MNPs) were collected with strong Neodymium magnets and washed at least 5 times with DI water to remove any impurity. The particles were then washed with ethanol and dried over night at room temperature and stored for future usage.

#### 2.2.1.3. Preparation of silk fibroin particles (SFPs)

The fabrication of SF particles is based on the protocol reported by Lammel *et al*.[79] and modified for the present experiments. Briefly, SF solutions with different concentrations (0.1-12 mg/ml) were added to potassium phosphate or sodium phosphate solutions (ionic strength: 1.25 M, pH 8) in a volume ratio of 1:5 followed by storing the as-prepared mixtures in the refrigerator for 2 h at -20 °C. The resulting particles were unfrozen and centrifuged at 20,000 g for 15 min before being re-dispersed and washed three times in UHQ water. To investigate the effect of phosphate ionic strength on SF particle size, sodium / potassium phosphate solutions with ionic strength from 0.6 to 2 M were mixed with SF solutions (5 mg/ml). The effect of sodium phosphate pH on the secondary structure of SF particles was also studied by producing SFPs with sodium phosphate solutions at pH 4, 7 and 9. Secondary structures of SFPs were investigated with Fourier transform infrared (FTIR) spectroscopy.

#### 2.2.1.4. Preparation of magnetic silk fibroin particles (MSPs)

MNPs were dispersed in sodium phosphate (1.25 M, pH 8) solution to reach the concentration of 0.1 mg/ml. The MNP-salt mixture was then blended with SF (0.5 - 10 mg/ml) solutions to produce particles according to the process mentioned in Section 2.2.1.3 and the resulting MSPs were collected using Neodymium magnets. Sodium phosphate solutions with different pH values were also mixed with SF solution (5 mg/ml) to investigate the effect of pH on MSP size.

#### 2.2.1.5. Preparation of curcumin loaded magnetic silk fibroin particles (CMSPs)

Curcumin (CUR) was dissolved in DMSO with a concentration of 100 mg/ml CUR DMSO solution. 1 mg MNPs and different amount of CRU DMSO solutions (with CUR weight equal to 10%, 30%, 60%

and 90% of total SF used) were added to 10 ml sodium phosphate (1.25 M, pH 8) solution. To investigate the effect of pH on CMSP size, zeta potential and CUR release rate, sodium phosphate solutions with pH value 4, 7, 8 and 9 were used (while the CUR usage was 10 %). The prepared mixture was then blended with 2 ml SF solution (5 mg/ml) and stored at -20 °C for 2h. The CMSPs were then unfrozen and the supernatant was analysed to determine residual CUR concentration using UV-Vis spectrometry (JENWAY 6715, Bibby Scientific, UK). Standard calibration curves for CUR in sodium phosphate and PBS were used. Concentration of particles was determined by weighing dried particles from 1 ml solution. Encapsulation and loading efficiencies were determined by Eq. (2.1) and (2.2) below:

$$Encapsulation\ efficiency\ (w/w\,\%) = \frac{amount\ of\ CUR\ in\ particles}{CUR\ initially\ added} \quad (2.1)$$

$$Loading\ efficiency\ (w/w\,\%) = \frac{amount\ of\ CUR\ in\ particles}{amount\ of\ particles} \quad (2.2)$$

#### 2.2.1.6. Preparation of magnetic alginate particles (MAPs)

Magnetic alginate nanoparticles (MAPs) were prepared based on the procedure described by Liu *et al*. [62]. 20 ml of ethanol and 10 ml of DI water was mixed into a beaker and 0.25 g of MNPs were suspended in the prepared mixture. Next 40 ml of sodium alginate (SA) solution (20 mg/ml) was added to the beaker upon which the mixture was sonicated for 10 min to allow full homogenous dispersion of MNPs in the suspension. The resultant mixture was vigorously stirred for 30 min at room temperature. Following, 128 ml of $Ca(OH)_2$ solution (0.74 mg/ml) was added into the suspension and stirred for 1 h before 16 ml of $NaHCO_3$ solution (10 mg/ml) was added. The suspension was then stirred for a further 12 h at room temperature and the resulting MAPs were collected with strong Neodymium magnets washing thoroughly with ethanol and water to remove excess salts. Finally, purified MAPs were suspended in DI water before been used for the

layer-by-layer process.

#### 2.2.1.7. Preparation of magnetic alginate / chitosan layer-by-layer particles (MACPs)

The preparation of Magnetic alginate / chitosan layer-by-layer nanoparticles (MACPs) was based on the layer-by-layer self-assembly of sodium alginate (SA) and chitosan (CHI) on MAPs. Chitosan solution (10 mg/ml) was prepared in 1% (v/v) acetic acid aqueous solution. The first layer was deposited by adding 1 g of MAPs into 100 ml of the chitosan solution under vigorous stirring for 20 min at room temperature. The resultant MA / CHI particles were collected with a Neodymium magnet and the excess CHI was removed by washing the particles several times with DI water. The next SA layer was deposited by adding the previously prepared MA / CHI particles into 100 ml of SA solution (10 mg/ml) under vigorous stirring for 20 min thus forming MA / CHI / SA particles. For each layer the previously described purification process was used. Particles with more layers were fabricated by alternatively coating positively charged CHI and negatively charged SA on MACPs until the desired number of layers was obtained.

#### 2.2.1.8. Preparation of curcumin loaded magnetic alginate / chitosan layer-by-layer particles (CMACPs)

20 ml of CUR DMSO solution (7.5 mg/ml) was added into 30 ml of DI water to prepare the CUR mixture (3 mg/ml). Then 30 mg of MACPs were added into 20 ml of the CUR mixture and stirred for 24 h. The resultant Curcumin loaded Magnetic alginate / chitosan layer-by-layer nanoparticles (CMACPs) were collected with a Neodymium magnet and washed three times with DI water. The supernatants were collected and analysed with a UV-Vis spectrometry (JENWAY 6715, Bibby Scientific, UK) to determine the concentration of residual CUR. The CMACPs were dispersed in 5 ml of DI water and the concentration of these particles was determined by weighing dried particles

from 1 ml solution. Encapsulation and loading efficiencies were determined by Eq. (2.1), and Eq. (2.2).

#### 2.2.1.9. Preparation of silk fibroin-polyethyleneimine particles (SPPs)

SF solution (5 mg/ml) and polyethyleneimine (PEI) solution (5 mg/ml) were mixed at different volume ratios (1:9, 1:3, 1:1, 3:1 and 9:1) to prepare SF/PEI mixtures. 2 ml of SF/PEI mixtures were then added to 10 ml of sodium phosphate solutions with an ionic strength of 1.25 M at pH 8. The prepared solutions were kept at room temperature (20 °C) for 6 h to allow the formation of particles. The resultant solution was then centrifuged at 20,000 g for 15 min to collect the SPPs. The particles were washed several times with DI water to remove excess salts before further characterizations. SF and PEI particles were prepared using the same method as controls.

#### 2.2.1.10. Preparation of magnetic silk fibroin / polyethyleneimine particles (MSPPs)

5 mg of MNPs were dispersed in 50 ml of sodium phosphate solution to prepare a MNP-salt mixture. 2 ml of SF/PEI mixtures (5 mg/ml) at different SF/PEI concentration ratios (1:9, 1:3, 1:1, 3:1 and 9:1) were then blended with 10 ml of MNP-salt mixtures and the resulting solutions were kept at room temperature (20 °C) for 6 h to allow the formation of MSPPs. The particles were then washed and collected with Neodymium magnets. Magnetic SF and magnetic PEI particles were prepared by the same method as controls.

#### 2.2.1.11. Preparation of magnetic-silk / polyethyleneimine nanoparticles-cmyc antisense oligodeoxynucleotide (MSPP-ODN) complexes

MSPP-ODN complexes were prepared by mixing the MSPP solutions with cmyc antisense oligodeoxynucleotide (ODN) solutions. An ODN aqueous solution of 0.2 mg/ml was prepared.

MSPPs were dispersed in DI water to obtain MSPP solutions at different concentrations (0.2, 1.2, 2.4, 5, 10, 20 mg/ml). 100 µl of prepared ODN solution was then added to 100 µl MSPP solutions and mixed under gentle shaking until a homogenous dispersion was achieved. Finally, the mixed solution was incubated for 30 min at room temperature. The ODN concentration in the mixed solution described above was fixed at 0.1 mg/ml and the MSPP concentrations were varied from 0.1 to 10 mg/ml to achieve different MSPP/ODN mass ratios (1:1, 6:1, 12:1, 25:1, 50:1, 100:1). MSPP/ODN mixed solutions with higher concentrations of ODN (1 or 2 mg/ml) and MSPPs (12 or 24 mg/ml) were also prepared with similar process. The prepared dispersions were diluted in PBS before added into cell cultures.

#### 2.2.1.12. Release of curcumin from curcumin loaded magnetic alginate / chitosan layer-by-layer nanoparticles

5 mg of CMSPs or CMACPs were suspended in 5 ml PBS buffer (pH 7.4) in vials and incubated at 37 °C under constant agitation (200 rpm). The particles were collected with strong Neodymium magnets at pre-determined time points and the supernatants were carefully removed before re-dispersing the particles in 5 ml fresh PBS. The CUR concentrations of the supernatants were analysed using UV-Vis-spectrometry and the percentage of cumulative CUR release was plotted as a function of incubation time.

### 2.2.2. Characterization

#### 2.2.2.1. Particle size and zeta potential analysis

The particle size and zeta potential of SFPs, MSPs, CMSPs, SPPs and MSPPs were carried out by a Dynamic light scattering analyser (DLS) (NanoBrook 90 plus Pals Particle size Analyzer, Brookhaven Instrument, NY, USA). Particles were dispersed in DI water in a cuvette before placed in the sample cell. A diode laser with wavelength of 660 nm was used. All samples were washed several times and dispersed in DI water prior to measurements. Refractive indexes of 1.331 for water and 1.540 for particles were employed for the calculation of particle size. All experiments were conducted at a measurement temperature of 18 °C using a circulation bath. Three batches of samples were prepared and analysed.

The particle size of MACPs and CMACPs were analysed by a nanoparticle tracking analysis (NTA, Nanosight LM10, UK). Particles were dispersed in sodium phosphate solution (10mM, pH7) and injected into the scattering cell of a NTA where their motion was analysed and average size was calculated. The zeta potential measurement of particles was carried out by a Dynamic light scattering analyser (DLS) (NanoBrook 90 plus Pals Particle size Analyzer, Brookhaven Instrument, NY, USA). Particles were washed several times and dispersed in DI water (pH adjusted to 7 with NaOH and HCl) or 10 mM sodium phosphate buffer (pH 7) prior to zeta potential measurements.

#### 2.2.2.2. Fourier transform infrared spectroscopy

Fourier transform infrared spectroscopy (FTIR) analysis of SFPs was conducted with Fourier Transform Infrared Spectrophotometer (IR Prestige-21, Shimadzu, UK). SFPs were washed three times with UHQ water and allowed to air dry on the diamond attenuated total reflectance (ATR)

attachment (ATR apparatus, Pike Technologies, USA) of the spectrophotometer. The range of wave numbers was set from 4000 to 400 $cm^{-1}$ and the spectrum was read using the Happ-Genzel apodisation function over 64 scans with a resolution of 4 $cm^{-1}$. The amide I region (1575 - 1750 $cm^{-1}$) was investigated to determine the secondary structure of SF protein. The spectral processing was conducted with the software IR solution provided within the FTIR instrument.

FTIR analysis of MAPs and MACPs was conducted with the Spectrum 100 spectrophotometer (PerkinElmer, USA). Particles were washed three times with DI water and dried in an oven at 60 °C for 24 hours before being placed on the diamond attenuated total reflectance (ATR) accessory and compressed. The wavenumber region was set from 4000 to 600 $cm^{-1}$ with a resolution of 1 $cm^{-1}$. The spectral processing was conducted with the software (IRPal 10) provided within the FTIR instrument.

#### 2.2.2.3. Atomic Force Microscopy analysis

The size and morphology of particles was characterised using Atomic Force Microscopy (AFM) (Dimension Icon with ScanAsyst, Bruker Corporation, U.S.A). Particle suspensions were dropped on mica substrates and air dried before being placed on the sample stage. AFM measurements were conducted using SCANASYST-AIR tips and PeakForce Tapping mode. The data was analysed with NanoScope Analysis 1.5 software.

#### 2.2.2.4. Transmission electron microscopy analysis

Particles were dispersed in DI water at the concentration of 0.1 mg/ml. The dispersions were then dropped onto TEM copper grids and incubated at room temperature for 30 s. Excess solution on grids was then removed with filter paper, by gently dapping the edge and allowing excess liquid to

be absorbed prior to TEM imaging (Tecnai G2 Spirit, FEI, USA). An acceleration voltage of 80 kV was used and images were recorded using a Gatan Orius SC1000B bottom mounted digital camera and analysed in Gatan Digital Micrograph software (version 3.9.1).

#### 2.2.2.5. *In vitro* cytotoxicity assay

**SFPs, MSPs, CMSPs:** MDA-MB-231 cells were cultured in RPMI medium supplemented with 10 % Foetal Bovine Serum (FBS), 1 % Penicillin / Streptomycin and 1 % L-Glutamine at 37 °C and 5 % $CO_2$. The cytotoxicity of SFPs, MSPs and CMSPs against MDA-MB-231 cells was investigated by the MTT assay. The cells were seeded in 96 - well plates at a density of $5 \times 10^3$ cells per well before incubation for 24 h to allow cells to attach to the plates. Cells were then incubated with SFPs, MSPs, CMSPs (30 % CUR usage) and free CUR (amount equal to the CUR content in CMSPs) at preselected concentrations respectively. After 3 days incubation, 50 µl of 3 mg/ml MTT was added to each well and incubated at 37 °C for 3 hours followed by removing the supernatants and adding 200 µl DMSO. A plate reader (FLUOstar galaxy, BMG LABTECH, Germany) was used to measure the absorbance of each well including control wells containing only cells at 570 nm. The relative cell viability was determined by comparing the absorbance with control wells.

**MACPs and CMACPs:** MDA-MB-231 or HDF cells were seeded into 96-well plates with 200 µl medium at a density of $5 \times 10^3$ cells per well and incubated overnight at 37 °C under 5% $CO_2$ atmosphere. Then the mediums were removed and replaced with 200 µl free CUR medium solution, MACPs or CMACPs dispersion (CUR content in the particles is equivalent to the dosage of free CUR) to reach the final CUR concentration of 0.5, 1.5, 5, 15, 30 µg/ml. After 48 h of incubation, 50 µl of 3 mg/ml MTT was added to each well and incubated at 37 °C for 3 hours followed by removing the supernatants and adding 200 µl DMSO. The absorbance of each well was measured at 570 nm

with a plate reader (FLUOstar galaxy, BMG LABTECH, Germany).

**SPPs, MSPPs, SPP-ODN and MSPP-ODN**: MDA-MB-231 or HDF cells were seeded into 96-well plates with 200 µl of complete RPMI medium (supplemented with 10% Foetal Bovine Serum (FBS) and 1% L-Glutamine) at a density of $5 \times 10^3$ cells per well and incubated overnight at 37 °C under 5% $CO_2$ atmosphere. The medium was then removed, and the cells were washed twice with PBS buffer before being replaced with 180 µl serum-free medium. 20 µl of SPP-ODN or MSPP-ODN complex dispersions with different particle/ODN mass ratios were added into each well. SPP or MSPP solutions (20 µl) with equivalent amount of particles used for complexation with ODNs were added into wells. ODN solutions were also used as negative controls with dosages equivalent to the amount of ODNs used in complexes. Cells were incubated for 4 h initially being exposed to a magnetic field for 20 min. The serum-free medium was then removed and replaced with 200 µl complete medium and cells were cultured to a final duration of 3 days. Then 50 µl of MTT reagent (3 mg/ml) was added into each well and cells were cultured for another 3 h until the purple precipitate was visible. The medium was then removed and 200 µl of DMSO was added into each well before placing plates on a shaker until purple precipitates in wells were fully dissolved. The absorbance of each well was measured at 570 nm with a plate reader (FLUOstar galaxy, BMG LABTECH, Germany).

#### 2.2.2.6. Cellular uptake assays

**SFPs, MSPs and CMSPs:** SF was labelled with Rhodamine B isothiocyanate (Ex 543 nm, Em 580 nm) before used for the fabrication of SFPs, MSPs and CMSPs fabrication. MDA-MB-231 cells were seeded in 6-well plates with $3 \times 10^5$ cells per well and incubated overnight at 37 °C under 5% $CO_2$ atmosphere before incubation with Rhodamine B labelled SFPs, MSPs and CMSPs (30% CUR

usage) at particle concentrations in medium from 3 -100 μg/ml. After 24 h, the cells were harvested with trypsin and washed twice with PBS to remove free particles. The intracellular fluorescence of Rhodamine B and CUR was determined using a flow cytometer (FACS Calibur, BD Biosciences, USA) to investigate the particle and CUR uptake.

**CMACPs:** CUR medium solutions were prepared by adding CUR dissolved in DMSO (50 mg/ml) dropwise into medium to obtain different final CUR concentrations (0.5, 1.5, 5, 15, 30 μg/ml). CMACPs were dispersed in medium to reach the final CUR concentrations equivalent to those of CUR medium solutions. MDA-MB-231 and HDF cells were seeded in 6-well plates at a density of 3 × $10^5$ cells per well and incubated overnight at 37 °C and 5% $CO_2$. Then the mediums were removed and replaced with 2 ml CUR medium solutions or CMACPs medium solutions and incubated for a further 24 h. After this, the cells were harvested with trypsin and washed twice with PBS to remove any free CUR or CMACPs. The resultant cells were collected and analysed with the BD™ LSR II flow cytometer (BD Biosciences, USA) to investigate the cells CUR uptake.

**SPP-ODN and MSPP-ODN complexes:** MDA-MB-231 and HDF cells were seeded in 6-well plates at a density of 5 ×$10^5$ cells per well with complete medium and incubated overnight at 37 °C and 5% $CO_2$. The cell culture mediums were removed, and cells were washed twice with PBS before incubation with serum-free medium. SPP-ODN or MSPP-ODN complexes were added into different wells and incubated for 5, 20 min or 1, 4, 24 h with and without initial exposure to a magnetic field for 5 or 20 min (the maximum exposure time is 20 min). ODNs were added as a negative control. Oligofectamine-ODN was used as a positive control with a standard incubation time for 4 h in serum-free medium. After incubation, cells were washed twice with PBS buffer before further incubation in the complete medium to a final duration of 24 h (the total incubation time is fixed at 24 h). The resulting cells were harvested with trypsin and analysed with the BD™ LSR II flow

cytometer (BD Biosciences, USA) to investigate the ODN uptake.

#### 2.2.2.7. Fluorescence microscopic images and magnetically targeted delivery assay

**CMSPs:** To obtain fluorescence microscopic images of cellular uptake, MDA-MB-231 cells were incubated on the cover slips in 12-well plates at a concentration of $1\times 10^5$ cells per well and incubated with CMSPs (30% CUR usage) at 37 °C and 5 % $CO_2$ for 3 h. Cells were washed three times with PBS to remove non-specifically adsorbed particles or CUR before fixation with 4 % paraformaldehyde at room temperature for 30 min. The fixed cells were stained with 3 µl 1% Texas Red®-X Phalloidin (Ex 591 nm, Em 608 nm) for 1 h and washed twice with PBS followed by staining with DAPI (Ex 358 nm, Em 461 nm) for 30 min. Finally, cells washed twice with PBS ready for fluorescent microscope (AF6000, Leica, Germany). Fluorescence images of DAPI, Texas Red and CUR (Ex 340 nm, Em 530 nm [155]) stained cells were captured using different channels. All images were captured and analyzed with LAS AF Lite software (Leica, version 2.6.3).

**CMACPs:** MDA-MB-231 cells were seeded in glass bottom dishes (Nunc™, Thermo Scientific, diameter 35 mm) at a density of $3\times10^5$ cells per dish and incubated for overnight to allow the settlement. Free CUR and CMACPs were added into cell cultures to reach a final CUR concentration of 5 µg/ml and incubated for 4 h. Magnetically targeted delivery was conducted by initially placing a Neodymium magnet under one edge of the dish for the first 15 min during incubation. Cells were then washed twice with PBS buffer and fixed with 4 % paraformaldehyde. The fixed cells were stained with Alexa Fluor 568 Phalloidin and DAPI for 1 h. The confocal fluorescence images of cellular uptake of CUR were observed with an Inverted Zeiss LSM 510 NLO microscope (Zeiss, Germany) and analysed with LSM Image Browser software version 4.2.0.121.

**SPP-ODN and MSPP-ODN:** MDA-MB-231 cells were seeded into 6-well plates (with 2 coverslips in

each well) at a density of $3\times10^5$ cells per well with complete medium. After 24 h, cells were washed twice with PBS buffer before incubation in serum-free medium. Cells were incubated with naked ODNs, Oligofectamine-ODN, SPP-ODN and MSPP-ODN complexes for 4 h. The magnetically targeted delivery was conducted by placing a circular neodymium magnet under one of the coverslips in each well for 20 min at the start of incubation. After initial incubation, cells were washed twice with PBS buffer to remove free ODNs and transfection complexes followed by a further incubation in complete medium to a total incubation time of 24 h. The cells were then washed twice with PBS and fixed with 4% paraformaldehyde. The fixed cells were stained with Alexa Fluor 568 Phalloidin and DAPI for 1 h. The confocal fluorescence images of cellular uptake of ODNs were observed with an Inverted Zeiss LSM 510 NLO microscope (Zeiss, Germany) and analysed with LSM Image Browser software (version 4.2.0.121).

## 2.3. Techniques

### 2.3.1. Dynamic light scattering

Dynamic light scattering (DLS) is used to investigate the size and zeta potential of particles.

#### 2.3.1.1. Particle size analyzation

DLS is a powerful technique commonly used to determine particle size and distribution in suspensions [156]. The measurement is based on the detection of the Brownian motion of particles. When particles are dispersed in a solution, they undergo a constant random movement known as Brownian motion [156]. The Brownian motion rates of these particles are related to their sizes and larger particles move slower in solution. DLS can detect and analyse the motion performance of these particles and calculate their size. The schematic representation of a DLS apparatus is shown in Fig. 2.1.

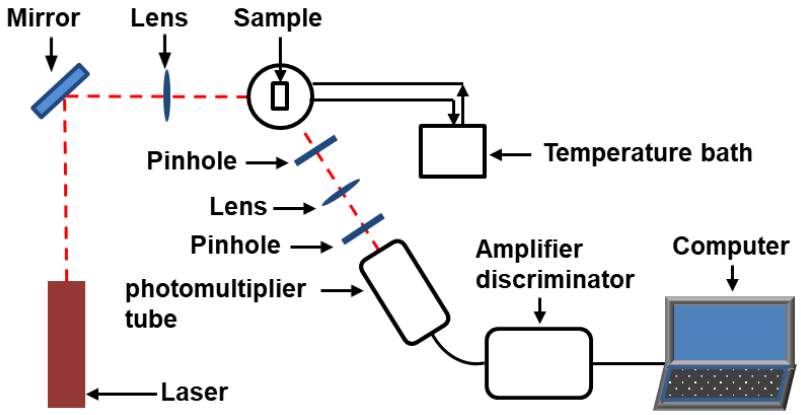


Fig. 2.1. Schematic diagram of DLS analysing particle size.

As shown in Fig. 2.1, a laser is focused on the sample and strikes the particles in the suspension, leading to scattered light in all directions. The scattered light is then collected by the photomultiplier tube (PMT) and the output of the PMT is digitized and sent to the autocorrelator [156]. If all the

particles stay stationary in the solution, the intensity of scattered light will remain stationary as well [156]. However, as mentioned above, particles are undergoing constant Brownian motion which will cause either constructive or destructive interference of the scattered light [156]. Therefore, the intensity of scattered light fluctuates and can be detected by DLS to determine the time autocorrelation function $G_t$:

$$1 + \gamma(G_t)^2 = \frac{<I_t><I_0>}{<I_0><I_0>} \tag{2.3}$$

where $\gamma$ is a constant determined by experimental setup and $I_0$, $I_t$ is the scatter light intensity at the start of experiment and at time *t*. It can be expected that $I_t$ is related to the position of particles which can be related to the rate of their Brownian motion [156]. Therefore, $G_t$ can be used to calculate the particle size. For dilute and monodispersed suspensions of nanoparticles, $G_t$ is determined by the self-diffusion coefficient ($D_t$) of particles and the length of the scattering vector $q$ shown as:

$$G_t = \exp(-q^2 D_t) \tag{2.4}$$

In Eq. (2.4), $q$ depends on the scattering angle $\theta$ and the wavelength λ of the light in the scattering medium shown as:

$$q = (\frac{4\pi}{\lambda}) \sin(\theta/2) \tag{2.5}$$

Since $G_t$ is given by DLS, from Eq. (2.4) and (2.5), the self-diffusion coefficient $D_t$ can be obtained. For spherical particles in a dilute dispersion, $D_t$ is related the particle radius $R$ shown as:

$$D_t = k_B T/6\pi\eta R \tag{2.6}$$

where $k_B$ is Boltzmann's constant, *T* is the thermodynamic temperature and *η* is the suspension

medium viscosity [156]. Combining all the equations above the radius of spherical particles can be obtained. It is important to note that the solvation layer is also included in the calculated radius.

For non-spherical particles the radius calculated from the equations above is called the hydrodynamic radius which is not equal to the geometrical radius of the particles, size of solvent molecules or other molecules moving with the particles are included in the hydrodynamic radius. The shape of the particles can also affect the hydrodynamic radius. In most measurements, particles are not monodispersed, and they therefore have different diffusion coefficients $D_t$, thus the autocorrelation function is given as:

$$G_t = \sum_i A_i \ exp(-q^2 D_{it}) \tag{2.7}$$

"Where $A_i$ is a weighting factor of a certain fraction of particles in the solution and is proportional to the scattered light intensity [156]." $D_{it}$ is the diffusion coefficient for each faction of particles. Therefore, the autocorrelation function has become a sum of exponentials contributed by particles with different $D_{it}$ that size related to different particle sizes. Cumulant method can be used to solve this equation and calculate the size distribution of the particles [156].

#### 2.3.1.2. Zeta potential measurements

The zeta potential (ZP) of particles is measured by the electrophoretic light scattering in conjunction with DLS [157]. The ZP is the difference in potential between the electric double layer of a particle and the dispersant around them [157]. If particles possess net charges on their surfaces are dispersed in a solvent. The ions with opposite charges to the particle surface charge will be attracted to the surface of the particles and form an ion layer called 'Stern layer' [157]. Outside the Stern layer, the electrostatic effects caused by the particle surface charges decreases as the increase of the distance of a point

from the Stern layer [157]. Therefore both same and opposite charged ions are grow beyond the Stern layer [157]. These ions and the ions in Stern layer together form the electric double layer (EDL) as shown in Fig. 2.2 [157]. When placed in an electric field, the particles move toward the opposite electrode [157]. Part of the diffuse layer moves with the particle, therefore a hypothetical plane, called slipping plane, is determined and acts as the interface between the moving particles and dispersant around it during electrophoresis. The ZP of the particles is the potential at the slipping plane [157].

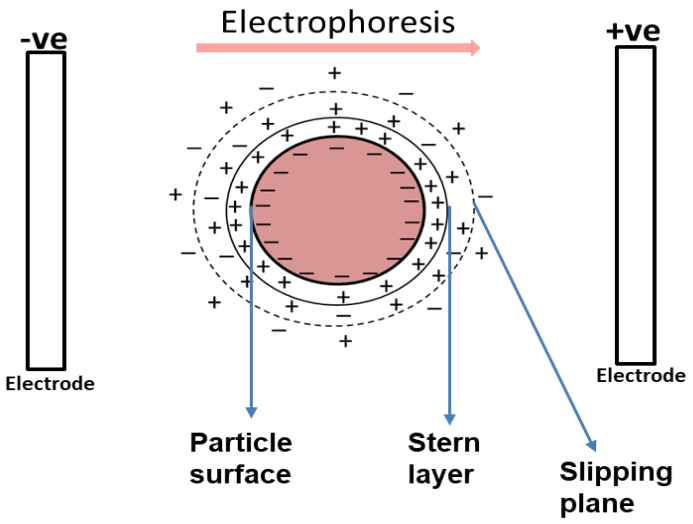


Fig. 2.2. Schematic representation of the EDL on the surface of a negatively charged particle. Ions with opposite charges are attracted to the surface of the particle and a strongly adhered layer (Stern layer) is formed. A diffuse layer consisting of both positive and negative ions is developed outside of the Stern layer. During electrophoresis the particle and its EDL moves towards the electrode of opposite charge. The slipping plane becomes the interface between the particle and dispersant.

To determine the ZP, a technique called electrophoretic light scattering is used as shown in Fig. 2.3. A laser is focused on the sample and once it hits the particles, scattered light is generated which possess light frequency different from that of the original laser [157]. The shift of frequency is proportional to the velocity of particles moving toward the electrodes [157]. Fig. 2.3 illustrates that the laser beam is divided into two beams in which one is used to strike the sample and the other is used as the reference beam. The scattered light from the sample is collected and combined with the

reference beam to determine the shift of light frequency [157]. Thus the velocity of particles can be determined from the frequency shift and in turn determine the ZP [157].

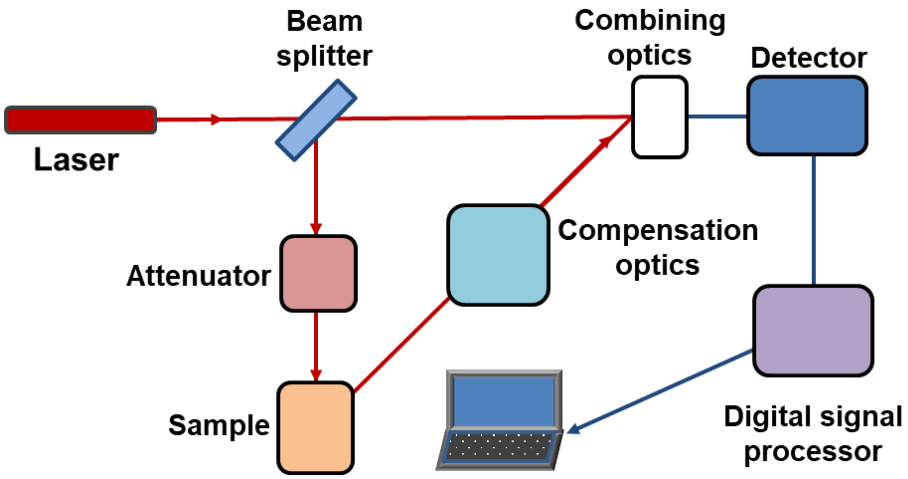


Fig. 2.3. Schematic representation of the instrumentation of ZP measurement by electrophoretic light scattering [157].

### 2.3.2. Nanoparticle tracking analysis

#### 2.3.2.1. Working principle of nanoparticle tracking analysis

Nanoparticle tracking analysis (NTA) was another method to analyse the size of particles. Similar to DLS, the analysis of particle size by NTA is also based on determining the Brownian motion of particles. However, a different strategy is used to do this. Fig. 2.4 shows the principle of analysing particle size with an NTA instrument. As shown in Fig. 2.4, a laser is guided to a glass prism through which it is introduced into the sample (dilute suspensions of particles in liquid). After passing through the glass prism, the laser is refracted at a low angle and then enters the sample, which results in the illumination of the particles in the sample [158]. Scattered light is generated when the laser hits the particles. The scattered light from particles in the sample can be collected by a microscope fixed with a video camera. In this way, the particles can be visualized and a video

recording the motion of the particles is taken, which is then analysed by the NTA software [158]. In the video, the particles are detected and their Brownian motion is tracked on a frame-by-frame basis and used to obtain particle sizes by Eq. (2.8)

$$< x, y >^2 = \frac{T_t k_b}{3\pi\eta d_h} \tag{2.8}$$

where $<x,y>^2$ is the mean squared displacement of particles, $k_b$ is Boltzmann's constant, $T$ is the thermodynamic temperature of the solvent, $\eta$ is the suspension medium viscosity, t is the sampling time and $d_h$ is the hydrodynamic diameter [158].

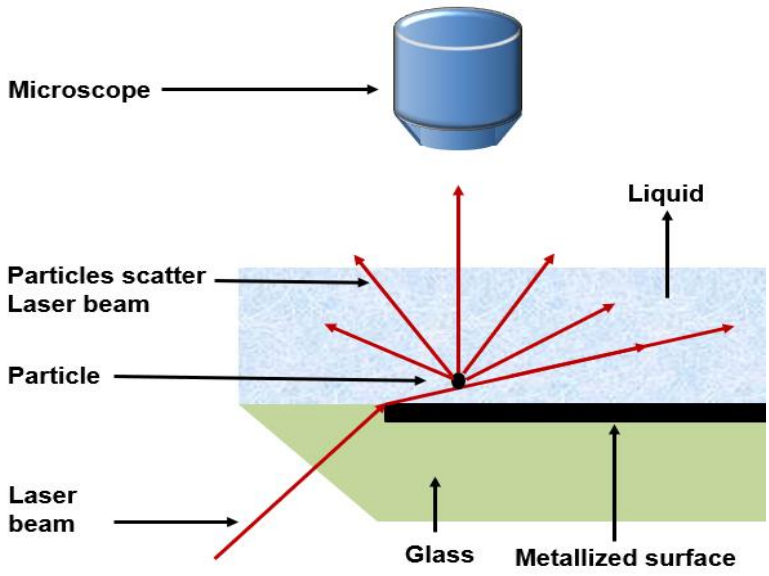


Fig. 2.4. Schematic representation of an NTA instrument configuration.

### 2.3.2.2. Comparing NTA with DLS

DLS is a powerful technique for particle sizing and it has the advantage of rapid analysis and ease of operation. However, a drawback of DLS is that it tends to bias larger particles. In DLS the particle size is determined by analysing the fluctuations of total scattered light from all the particles in

sample [159]. However, the total scattered light is not equally contributed by each particle [159]. In fact, larger particles will provide higher light intensities because the intensity of the scattered light is proportional to the sixth power of the diameter of particles [159]. Therefore, DLS is more sensitive to the larger particles in samples and results in a bias to larger particles. On the other hand, NTA determines the particle size by tracking the movement of individual particles visualized on the screen, which allows better resolution of particle sizes and there is no intensity bias towards larger particles [159].

### 2.3.3. Atomic force microscopy

In this thesis atomic force microscopy (AFM) was used to investigate the size, shape and surface topography of particles. An AFM can scan samples in *x*, *y* and *z* directions therefore capable of providing 3D representations of the surface of the samples.

#### 2.3.3.1. Principle of AFM

The principle of an AFM is shown in Fig. 2.5, a very sharp probe tip is mounted on a cantilever which scans over the sample [160]. When the tip is moved to a position close enough to the sample surface, the force between the tip and the surface of the sample will cause the deflection of the cantilever [160]. A laser is reflected off the top of the cantilever and detected by a position sensitive photodetector. Therefore, the deflection profile of the cantilever can be obtained by analysing the movement of laser position [160].

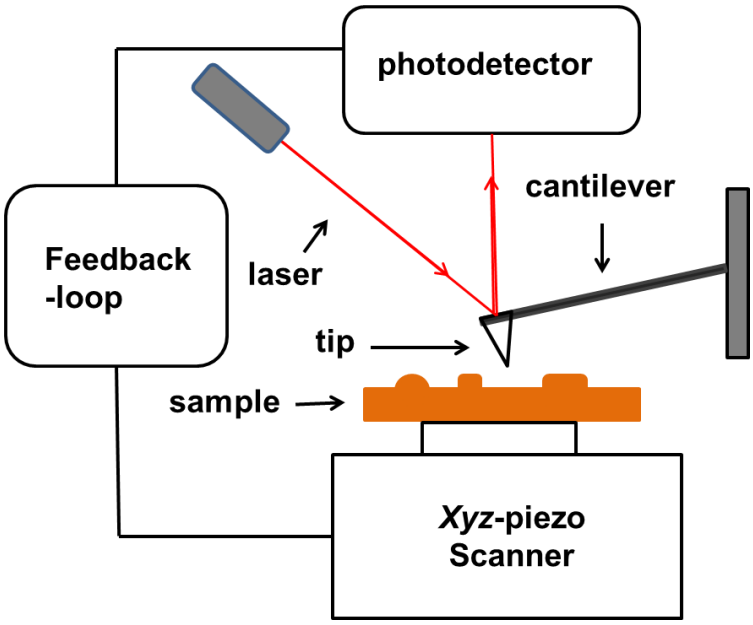


Fig. 2.5. Schematic representation of the basic principle of AFM. A sharp probing tip is mounted on a cantilever. The cantilever deflected by the force between tip and the sample. The deflections can be monitored by a photodetector and the feedback loop is used to keep the deflection constant.

The deflection of the cantilever is related to the force between the probe tip and the sample surface, while the force is related to the distance between tip and sample following Hook's Law:

$$F = -kx \tag{2.9}$$

where *F* is the force between sample and probe tip, *k* is the spring constant of the cantilever and *x* is the deflection of the cantilever [160].

There are two basic modes for the scanning of samples in AFM, known as the contact mode and tapping mode [161]. In contact mode, the probe tip is close enough to the sample surface to generate a repulsive force between the tip and surface of sample. Then the tip is dragged over the sample surface and the deflection or the position of laser hit on the photodetector is kept constant by adjusting the height of sample with the *XYZ*-piezo scanner and the feedback loop [161]. Thus, the height information of the sample surface can be obtained. However, since the probe tip is very close to the sample surface, contact mode has a drawback that cantilever is easily attracted to the sample

surface, due to the capillary condensation [161]. To overcome this problem, tapping mode was developed.

In the tapping mode, the cantilever is oscillated at a fixed frequency and the tip is made to contact the surface of the sample on each oscillation [161]. The frequency and amplitude of the cantilever oscillation is constant if there is no interaction between the probe tip and the sample surface. However, when the tip moves close to the sample surface, a force is generated from the interaction between tip and sample surface [161]. This causes the amplitude of the cantilever to change, which is detected by the photodetector. Via the feedback loop the height of cantilever is altered to keep the cantilever amplitude constant [161].

#### 2.3.3.2. Factors to note in AFM

AFM artefacts in its images that do not indicate the actual surface information of the sample and can be generated due to intrinsic limitations of AFM. Therefore, it is important to recognize and avoid the artefacts during AFM operation. For example, Fig. 2.6 shows artefacts that can be caused by tips.

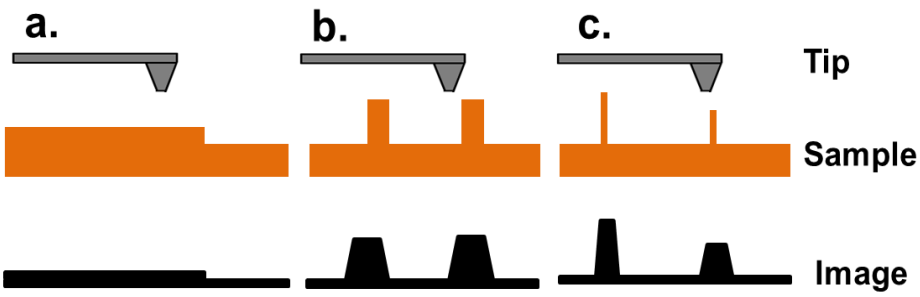


Fig. 2.6. Three types of situations, when tips scan sample surfaces. a) The objects on sample surface are significantly larger than the tip. b) The size of tip is comparable to the size of objects. c) Objects are significantly smaller than the tip [162].

A probe tip should be significantly smaller than the objects on sample surface to be able to determine accurate morphology of the sample [162]. Blunt tips or tips attached with materials from

sample can lead to poor AFM images. As shown in Fig. 2.6a, the radius of the tip is significantly smaller than the objects and there are no objects on sample surface can touch the side walls of the tip [162]. Therefore, accurate information of the sample surface can be obtained. When the size of the tip is comparable to the sample objects as shown in Fig. 2.6b, the tip cannot scan every place in the 'well', thus the resulting image shows the sidewalls of the tip instead of the accurate shape of the objects [162]. In an extreme case, as shown in Fig. 2.6c, the radius of the tip is significantly larger than the size of objects on the sample surface. Thus, the resulting image can only show the shape of the tip. The tip-related artefacts may result from the selection of wrong tips or the tips are contaminated by sample materials attached on them [162]. In this case, a fresh tip is required [162].

### 2.3.4. Transmission electron microscopy

Transmission electron microscopy (TEM) was used to analyse the size, shape and inner structure of $Fe_3O_4$ / Polymer (silk fibroin, alginate or chitosan) core-shell nanoparticles. TEM is a powerful technique to investigate the details of small samples such as subcellular structures. The principle of TEM is similar to optical microscopes but instead of using photons to detect samples, electrons are used in TEM [163-164]. Since the wavelength of electrons is much smaller than the wavelength of light, much higher magnifications can be obtained by TEM than optical microscopes [163]. Therefore, significantly more detailed information, even small as a single atom, can be obtained by TEM [163]. The working principle of a TEM instrument is illustrated in Fig. 2.7. Firstly, an electron beam is created by the electron source and then reaches the condenser lenses where it is focused to a small, thin coherent beam. The final size range of the electrons strikes the sample can be controlled by adjusting the condenser lenses. After passing through the condenser lenses, the electron beam

passes through a condenser aperture where it is restricted and the high angle electrons are removed [163]. Next, the restricted electron beam from condenser aperture strikes the specimen where the electrons interact with the sample and are divided into three electron types: (1) transmitted electrons, (2) elastically scattered electrons and (3) inelastically scattered electrons [163]. The amount of transmitted electrons is dependent on the properties of materials such as thickness, density, electron transparency and composition [163]. Normally, more electrons will be allowed to pass through a low-density or thin materials compared to thick and dense materials [163]. After passing through the specimen, the transmitted electrons strike the objective lens and are then focused into an image on the fluorescent screen. The objective aperture can block out high-angle diffracted electrons to enhance the contrast. The projector lens can be used to enlarge the electron beam onto the fluorescent (phosphor) screen where light is generated [163-164].

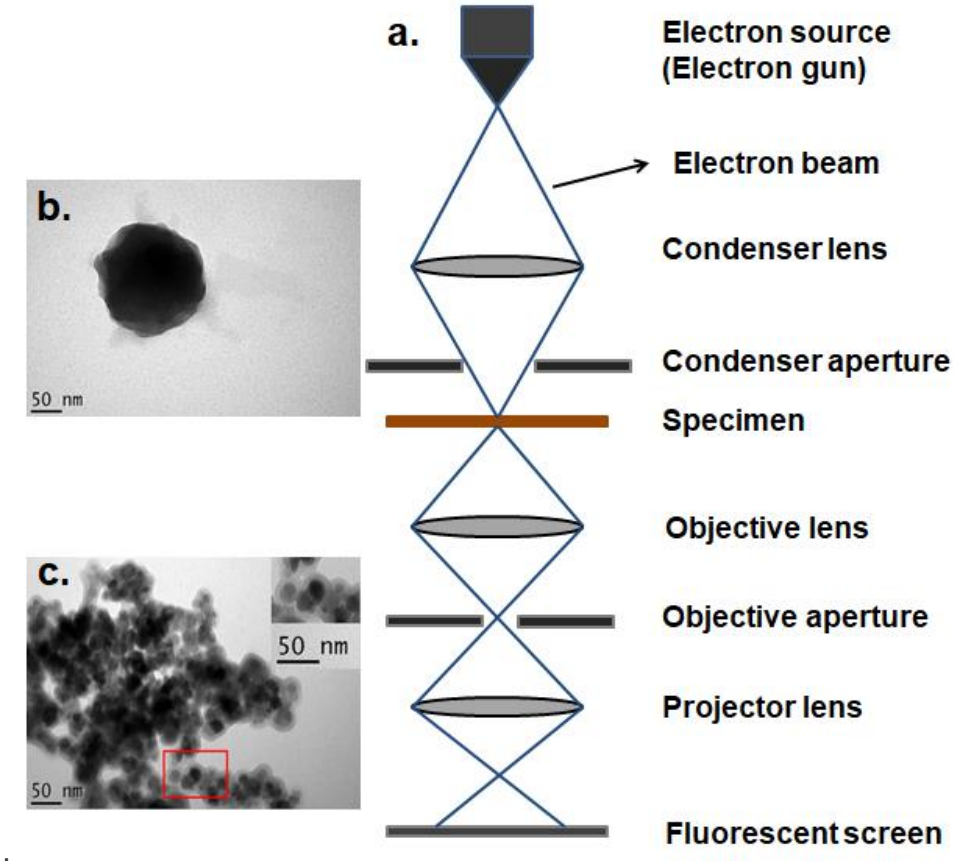


Fig. 2.7. Schematic representation of the working principle of TEM (a). TEM images of SF-PEI (polymer) nanoparticles (b) and $Fe_3O_4$ – SF / PEI core-shell nanoparticles(c).

Therefore, the electron signal is converted to a light image that can be used to analyse the detailed structure of the sample. The darker areas of the image represent areas where fewer electrons have been transmitted, those areas are denser than the lighter areas. For example, Fig. 2.7 shows the TEM image of SF-PEI polymer nanoparticles. The darker area in the middle of the image represents the thick polymer material of SF-PEI where less electrons have been transmitted, while the lighter areas around represent arears where more electrons have passed through. The detailed structure of a nonuniform material can also be determined by TEM. As shown in Fig. 2.7c, the darker areas in the image represent the presence of $Fe_3O_4$ particles and the surrounding lighter areas represent the presence of less dense polymers of SF-PEI nanoparticles.

Since electrons can only transmit through very thin materials, the specimen must be carefully prepared to provide a thin film, which allows the transmission of sufficient electrons [163]. In this project, the specimens of particles are prepared by dropping particle dispersion onto the grid with incubation at room temperature for 30 s. Excess solution on grids was then removed with filter paper, by gently dapping the edge and allowing excess liquid to be absorbed prior to transmission electron microscope (TEM) imaging. It is very important in the process to keep the particle dispersion at low concentrations to avoid excess thicknesses. On the other hand, if the particle concentration was too low, it is difficult to find enough particles for analysis.

### 2.3.5. MTT assay

In this thesis, the MTT (3-[4,5-dimethylthiazol-2-yl]-2,5 diphenyl tetrazolium bromide) assay was used to measure the viability of cells after treatment with free drugs, drug loaded nanoparticles or blank particles. Thus, the cytotoxicity of different materials toward cancer or normal cells could be determined.

#### 2.3.5.1. Principle of MTT

The principle of the MTT assay is based on the fact that MTT can be reduced to insoluble purple formazan crystals by mitochondrial succinate dehydrogenase. Since the mitochondrial activity is constant for most viable cells, the increase or decrease of viable cell numbers is linearly related to the mitochondrial activity [165]. The activity of mitochondria can be estimated by the level of MTT converted into formazan, which is soluble in DMSO and the optical density (OD) of formazan /

DMSO solution, which is related to its concentration, can then be measured by a plate reader [165]. Therefore, the difference on the number of viable cells in each well can be determined by measuring their OD values. In an application of measuring the cytotoxicity of a drug towards the cells, the decreased OD value represents the decreased mitochondrial activity that reflects the decreased number of viable cells [165]. Therefore, the inhibition of a drug to cells can be determined by comparing the OD values of wells with the drug treated cells and those with the untreated cells.

#### 2.3.5.2. Procedure of MTT

**Plate setup:** cells are generally plated in a 96-well plate with culture medium and are incubated for overnight to allow the settlement of cells. In the plate, blank wells (without cells and drugs), control wells (with cells but without drugs) and experimental wells (with cells and drugs) must be contained [165].


Fig. 2.8. Schematic representation of Part of a 96-well plate after formazan crystalsare fully dissolved. (a) Blank control wells. (b) Untreated control wells. (c) Drug treated experimental wells.

An example of blank control wells, untreated control wells and drug treated experimental wells is

shown in Fig. 2.8, in which blank control wells contain only medium; untreated control wells contain same amount of cells as experimental wells but are not exposed to drugs; experimental wells contain cells and medium and treated with drug at different concentrations [165]. If a drug shows absorbance at the wavelength that can affect the OD value of formazan, the additional control wells (without cells) that contain the drug are required. The outer wells surround the plate cannot be used for the experiment because they can evaporate more rapidly than the inner wells. Normally, PBS is used to fill the outer wells to minimize the evaporation of the plate.

**Drug incubation:** Drugs of desired concentrations are added to the experimental wells. Equivalent amounts of solvent of drug solutions is added to the untreated control wells. The cells are then incubated for certain periods (normally 1-4 days) to determine the optimum effect of drugs to the cells [165].

**MTT incubation:** after the appropriate incubation time, MTT solutions are added to the 96-well plate followed with an incubation for 3-6 h at 37°C in a $CO_2$ incubator [165].

**Formazan dissolution & viability calculation:** the supernatant in each well is carefully removed and DMSO is added. The plate is then placed on a shake bed where it undergoes a mild agitation to allow the full dissolution of formazan. The OD value of each well can then be measured by a plate reader. In order to determine the viability of each well, the average OD value of blank control wells is subtracted from that of untreated control wells and experimental wells. The viability of cells in an experimental well is calculated by (mean OD of experimental wells - mean OD of blank control wells) / (mean OD of untreated control wells - mean OD of blank wells) [165].

### 2.3.6. Flow cytometry

Flow cytometry is a powerful technique that can be used to simultaneously obtain multiple physical characteristics of a single cell such as size and granularity (internal complexity) in a short period of time [166]. Therefore, this technique is widely employed for manly applications such as immunophenotyping of peripheral blood cells, analysis of apoptosis and detection of cytokines [166].

#### 2.3.6.1. Principle of flow cytometry

The successful process of analysing cells by a flow cytometry is based on focusing the cell suspension into a tiny stream allowing the analyzation of one cell at a time. This process is conducted by the device shown in Fig. 2.9 a. When the cell suspension is injected into the flow chamber, it is focused by the surrounding sheath fluid to form a tiny stream located in the core of sheath fluid.

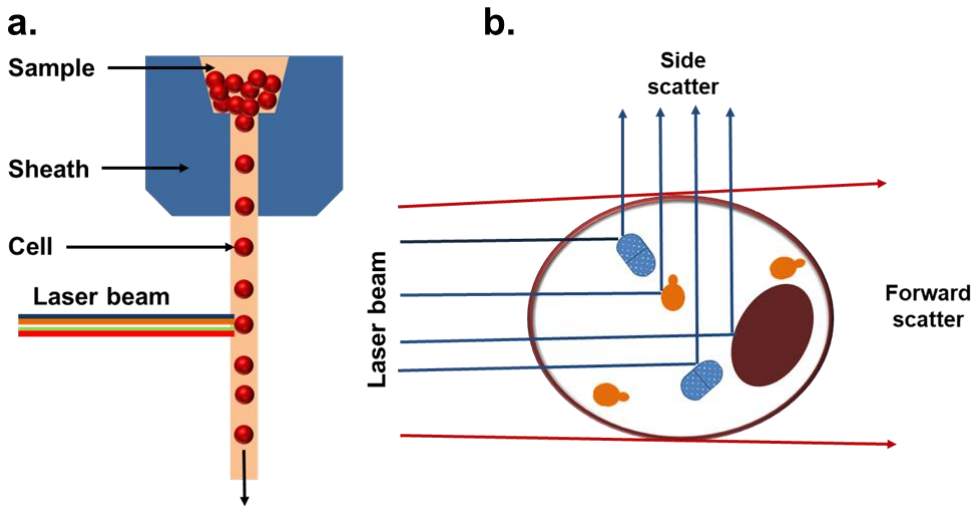


Fig. 2.9. Schematic representation of the working principle of a flow cytometer (a) and light scattering (b).

The pressure of the cell suspension stream is always greater than the pressure of sheath fluid, thus making the cells align in a single file fashion through the laser beam [166]. The flow rate of cell

suspension to the laser beam can be controlled by altering its pressure for different purpose of analysis [166].

When the laser beam strikes a cell, lights is scattered. There are two kinds of light scattering called forward scatter (FSC) and side scatter, as shown in Fig. 2.9b. The FSC is measured along the path of the laser beam and the SSC is measured perpendicular to the laser beam. The light scattering can be affected by the cell membrane, size, shape, surface morphology and internal complexity [166]. For FSC, it is proportional to the surface and size of cells and suitable for the application of immunophenotyping [166]. On the other hand, SSC is proportional to the granularity (internal complexity) of cells such as nucleus, mitochondria and particles internalized by cells [166]. Fluorescent light generated from antibodies or dyes can be measured at the same angle as SSC. By combining FSC and SSC, information of cell types and populations can be obtained [166]. The fluorochromes in cells can be excited by the laser beam and the emission light is collected by a series of lenses, and a series of optical mirrors and filters are used to separate the collected light and direct those with specified wavelength to suitable optical detectors [166].

The scattered light is collected and then transformed to voltages by photodetectors [166]. There are two types of photodetectors: photodiodes (PDs) and photomultiplier tubes (PMTs). as shown in Fig. 2.10, PDs detect the stronger light signals, which is generated from FSC. PMTs can be used to detect the weaker signals generated by SSC due to higher sensitivity of PMTs compared to PDs [166]. The light signals detected by PDs and PMTs are converted to a proportional number of electrons to generate an electrical current which then travels to the amplifiers and converted to voltage pulse (see Fig. 2.10) [166].

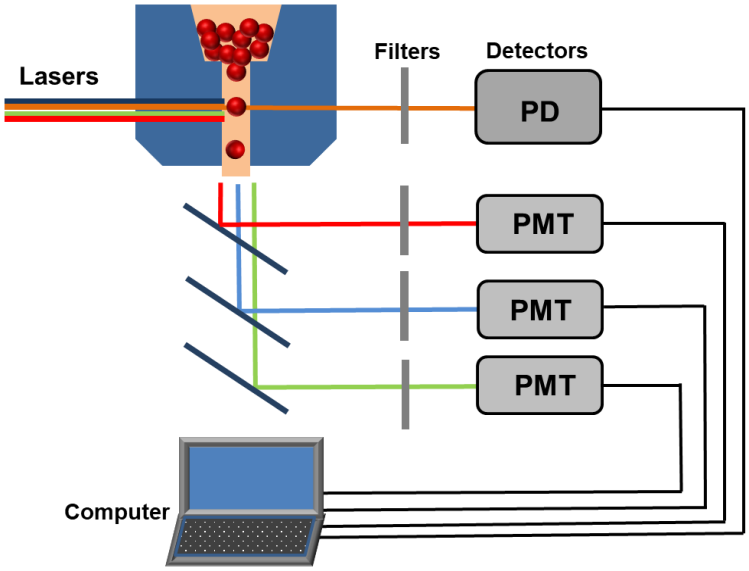


Fig. 2.10. Schematic representation of the signal detectionand processing by a flow cytometer.

When a cell strikes the center of the laser beam, the maximum amount of scatter or fluorescence is generated. After the cell leaves the laser beam, the voltage pulse decreases to the baseline [166]. Therefore, the information of each cell can be obtained in the form of voltage pulse which needs to be converted into a digital data that can be displayed as plots for analysis [166].

### 2.3.7. Fluorescence microscopy

Fluorescence microscope is used to visually determine the uptake of drugs or genes by the cancer cells and their location within the cells. The principles of conventional fluorescence microscopy and confocal fluorescence microscopy are reviewed in the following sections.

#### 2.3.7.1. Conventional fluorescence microscopy

The principle of confocal fluorescence microscopes is developed based on conventional fluorescence microscopes [167]. Thus it is helpful to understand the mechanism of the conventional

fluorescence microscopes for the study of the confocal fluorescence microscope [168]. Fig. 2.11 shows the schematic representation of a fluorescence microscope. Multiple excitation lights are generated from the light source and only the excitation light with selected wavelength can pass through the excitation filter to reach the dichroic mirror. The dichroic mirrors possess the unique property of reflecting light with wavelength shorter than a certain value but passing those with wavelength longer than that [167]. Therefore, the selected excitation light that possess short wavelength (with higher energy) is reflected to the objective from where it is focused onto the sample.

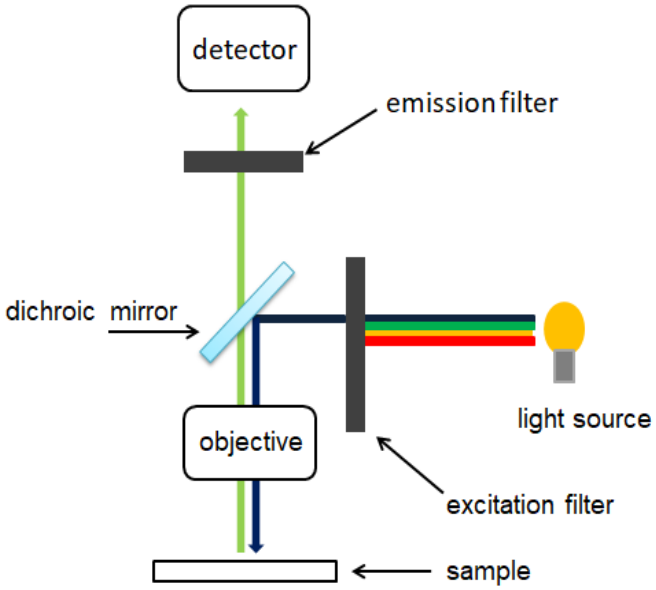


Fig. 2.11. Schematic diagram of a fluorescence microscopy. Emission light is emitted by the excitation light focused on the sample and then focused to the detector by the objective.

Upon reaching the sample, some molecules in the sample can absorb the energy from photons from excitation light at the right wavelength and become unstable. Part of the absorbed energy can be lost by these molecules and photons with less energy is emitted. The emission light is then guided to the dichroic mirror by the objective. An additional emission filter is employed to prevent the light with unselected wavelength from reaching the detector [169].

#### 2.3.7.2. Confocal fluorescence microscopy

In conventional fluorescence microscopy, the whole region of the sample is illuminated and all the emission light (from focal point or not) is collected by detector, thereby obscuring the image of the point we want to see [167]. Confocal microscopy is developed to reduce this effect. The principle of confocal fluorescence microscopy is shown in Fig. 2.12. A laser is reflected by the dichroic mirror to the objective where it is focused onto the sample. The sample is excited and fluorescent light is generated and guided by the objective to pass though the dichroic mirror. The light (blue lines in Fig. 2.12) from the focal point (the point we want to see) on the focal plane will be focused to another focal point on the other side of the objective system. The yellow lines in Fig. 2.12 represent the light from another point in the sample which is away from the focal point and it is not focused to the focal point to the left side of objective system. Unlike in conventional fluorescent microscopes, in a confocal fluorescent microscope, all the light from the sample must go through a pinhole before it can finally reach the detector. The pinhole is placed at the same point as the focal point. As a result, the light (blue) form the focal point in the sample and focused to the other focal point at the other side of the objective and pass through the pinhole to be detected. On the other hand, the light (yellow) form another point on the sample is out of focus, thus most of the light (yellow) is blocked and the image of yellow point is significantly attenuated compared to the image of blue point (focal point) [167]. In this way, the background haze is significantly reduced by confocal microscopy. Since the objective lens forms an image at the focal point where the pinhole is placed, those two points are celled conjugate points and the pinhole is called confocal pinhole [167].

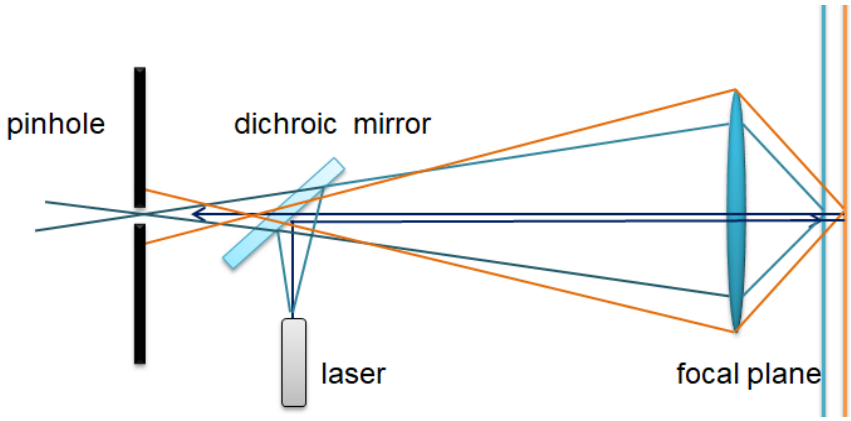


Fig. 2.12. Schematic representation of the principle of confocal microscopy. The light from the focal point on the focal plane is allowed to pass through the pinhole while most of the light from other point is blocked.

However, in confocal microscopy, only one point is imaged at one time. In order to obtain the whole image, a point-by-point illumination of the sample is required. The setup is shown in Fig. 2.13. Excitation light is provided by the laser and reflected by the dichroic mirror to a serial of scanning mirrors which can be rotated to scan the laser across the sample [167]. The emission light generated from the sample is then guided by the same mirrors and focused by objectives to pass through the pinhole and finally reach the detector [167]. Since the image of the sample is obtained via the point-by-point illumination, the complete image can only be obtained by building up the image one pixel at a time [167].

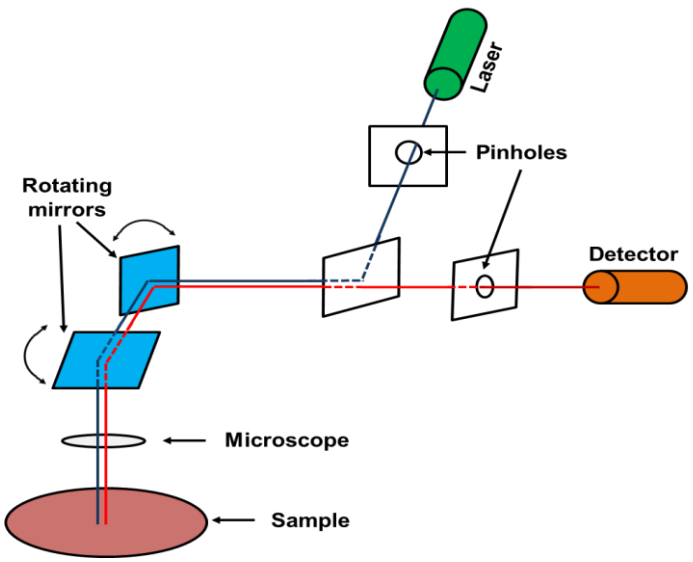


Fig. 2.13. Schematic representation of the basic setup of a confocal microscope.

### 2.3.8. Fourier-transform infrared spectroscopy

Fourier-transform infrared spectroscopy (FTIR) is used to investigate the structure and composition of particles. FTIR is a powerful technique to obtain infrared spectrum of solid, liquid or gas materials.

#### 2.3.8.1. Principle of FTIR

When infrared radiation come into contact with a sample, some molecules can selectively absorb the radiation with a specific wavelength, which leads to a change in the dipole moment of these molecules. The vibration energy of the sample molecules is then increased from ground state to an excited state. The frequency and intensity of the absorption peaks is related to the unique vibration properties of the molecules [170-171]. Therefore, the structural information of these molecules can be obtained by analysing their infrared spectrum [170]. It is important to note that homo-nuclear diatomic molecules such as $N_2$ and $O_2$ are not appropriate for infrared spectroscopy because their vibration and rotation cannot cause dipole changes [171]. Apart from those molecules Infrared absorption spectroscopy is suitable for most molecules and is capable of analysing gases, solids and liquid samples. If there is only one species to be analysed, a conventional species-specific spectrometer can be used, in which the radiation with a narrow wavelength is employed.[171] For samples containing different components, FTIR which employ infrared radiation with large range of wavelength need to be used [171].

For FTIR, the radiation beam generated by the source strikes the interferometer where it is divided to two radiation beams. These beams travel through different path and re-combined before reaching the detector. The radiation signal is then converted to a digital signal by a computer.

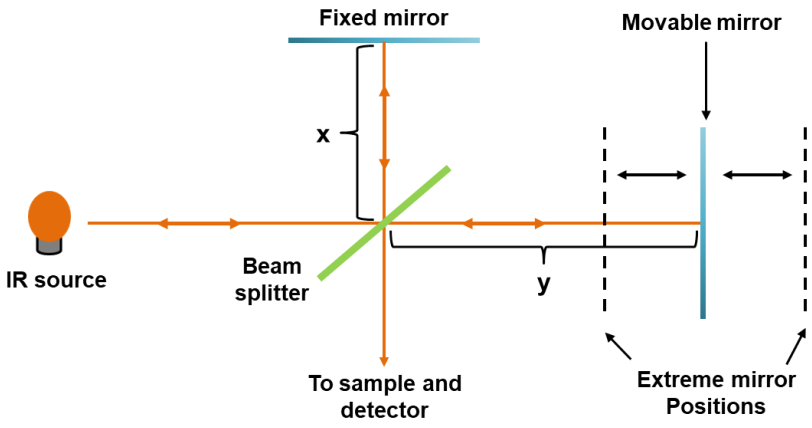


Fig. 2.14. Schematic representation of the principle of a Michelson interferometer.

The key component in FTIR is Michelson interferometer which serves the purpose of providing the interference beam that possesses path distance dependent intensity. The principle of a Michelson interferometer is shown in Fig. 2.14. The infrared radiation emitted from radiation source strike onto the beam splitter from which half of the radiation is transmitted to a movable mirror that moves between two extreme positions at constant speed [171]. The other half of the original radiation is reflected to a fixed mirror and goes back to the beam splitter along with the transmitted radiation that also reflected back from the movable mirror [171]. These two beams then recombine at the beam splitter where interference between beams occurs [171].

Assuming the distance between the beam splitter and the fixed mirror is x and the distance between the beam splitter and movable mirror is *y*, the optical path difference (retardation $\delta$) of these two beams is 2(*x*-*y*). If *x*=*y*, then the optical path difference equates 2(*x*-*y*) =0. Therefore, these two beams are perfectly in phase and will interfere constructively in the beam splitter. As a result, all radiation from the radiation source will reach the detector [171]. On the other hand, if the movable mirror is moved forward for a distance equivalent to quarter of the wavelength ( $\frac{1}{4}\lambda$) of the original beam, then the optical path difference is $\frac{1}{2}\lambda$ which will result in a destructive interference and no light will reach the detector [171]. If the movable mirror is moved forward for a distance of $\frac{1}{2}\lambda$, the

optical path difference will be $\lambda$ which means another constructive interference pattern is obtained. Therefore, when the movable mirror is constantly moved, a cosine curve (interferogram) of light intensity as a function of optical path difference can be obtained [171].

The frequency of the cosine wave is related to the frequency of wavelength of the line source and the amplitude is related to the intensity of line source [171]. If another line source is added and both reach the interferometer at the same time, the resultant interferogram will be the sum of two individual line sources. In a similar way, if a broad band source is used, the resultant interferogram will be the sum of curves generated by different radiation with identical frequency and intensity. By converting the optical path difference to wavenumber and the relative light intensity to absorbance or transmittance, a FTIR spectrum can be obtained which illustrates the absorbance of an unidentified sample at different wavenumbers and this information can be used to determine the component of the sample.

# 3. Magnetic-Silk Core-Shell Nanoparticles as Potential Carriers for Targeted Delivery of Curcumin into Human Breast Cancer Cells


## Abstract

Curcumin is a promising anti-cancer drug but its applications in cancer therapy are limited due to its poor solubility, short half-life and low bioavailability. In this Chapter, a curcumin loaded magnetic silk fibroin core-shell nanoparticle system is presented for sustained release of curcumin into breast cancer cells. Curcumin loaded magnetic silk fibroin core-shell nanoparticles were fabricated by a simple salting-out method using sodium phosphate with magnetic nanoparticles. The size, zeta potential, encapsulation / loading efficiency and curcumin release rate were controlled and optimised by regulating silk fibroin concentration, pH value of the phosphate solution and curcumin usage. Curcumin loaded magnetic silk fibroin core-shell nanoparticles showed enhanced cytotoxicity and higher cellular uptake in the human Caucasian breast adenocarcinoma cell line (MDA-MB-231cells) evidenced by MTT and cellular uptake assays. In addition, silk fibroin nanoparticles and magnetic silk fibroin nanoparticles without CUR loaded were used as controls. The particles prepared using sodium phosphate showed significantly smaller diameter (90-350 nm) compared with those prepared using potassium phosphate, which possess a diameter range of 500-1200 nm. These smaller particles are superior for biomedical applications since smaller particles (50-200 nm) are desired for cell internalization. In addition, the magnetic cores inside the particles provide possibility of using an external magnet for cancer targeting.



**Keywords**: Silk, Magnetic nanoparticles, Drug delivery, Cancer, Curcumin

**Abbreviations:**

SF: silk fibroin; CUR: curcumin; MNPs: magnetic nanoparticles;

SFPs: Silk fibroin nanoparticles;

MSPs: Magnetic silk fibroin core-shell nanoparticles

CMSPs: CUR loaded magnetic silk fibroin core-shell nanoparticles

## 3.1. Introduction

Curcumin (CUR) is the main component of turmeric which is extracted from the root of *Curcuma longa* native to Southeast Asia [172]. It is considered a pharmacologically safe drug [173] and has been widely used in medicine due to its anti-oxidant [4-6], anti-inflammatory [7-9], wound healing [10-11] and anti-bacterial [12-13] properties. Also, CUR has been widely used to fight against cisplatin-resistant cancer cells and decrease its unwanted side effects [14]. Moreover, it has also been found that CUR may modulate markers of High-density lipoprotein (HDL) function and subsequently improve conditions in which HDL is dysfunctional [174]. Recent research revealed that CUR also possess anti-cancer properties on multiple cell lines via its effects on the regulation of cellular growth and apoptosis [15-17] which makes it a promising drug for cancer therapy. However, due to its poor solubility in aqueous solution [18-19], short half-life in the body and low bioavailability after oral administration [175-177], the accumulation and uptake of CUR at the disease area by itself is very poor. Therefore, the applications of CUR as an anti-cancer drug have been significantly limited [19, 175-176, 178]. To overcome these obstacles, various strategies including the development of liposome [23], phospholipid [21], adjuvants [179] and nanoparticle carriers [22] for CUR delivery have been conducted. However, most of these drug delivery systems lack the ability of tumour targeting, which makes the accumulation of drugs at tumour sites limited. Thus, a drug delivery system which is capable of not

only improving the availability, cell uptake and half-life of CUR, but can also deliver it to disease sites is desired. In this report, we present the fabrication of CUR loaded magnetic silk fibroin core-shell nanoparticles (CMSPs) for the delivery of CUR into breast cancer cells.

Silk fibroin (SF) protein from cocoons of *Bombyx mori* is an FDA approved, natural derived material and has been widely used to form various biomaterials including SF gels, sponges and films for different medical applications [64]. It has also been demonstrated that SF is an extremely promising material for drug delivery systems due to its excellent biocompatibility [180], tuneable biodegradability [181] and easy processing [64]. An increasing number of strategies including capillary-microdot technique [182], desolvation method [72-74, 183], supercritical fluid technologies [184] and salting-out method [79] have been developed to fabricate SF based nanoparticles that can load and release model drugs. For example, Gupta *et al*. have fabricated CUR loaded SF nanoparticles (<100 nm) with the capillary-microdot technique [182]. However, preparation of SF nanoparticles (SFPs) with this method is difficult to process and the yield is relatively low. Kundu *et al.* have prepared SFPs (150 - 170 nm) with the desolvation method by adding SF solutions into dimethyl sulfoxide (DMSO) [72]. Nevertheless, the organic solvent residue in these SFPs is still difficult to avoid. Zhao *et al*. have prepared smaller SFPs (~ 50 nm) using solution-enhanced dispersion by $CO_2$[184]. However, the processing of this method is complicated and the cost is high. Lammel *et al*. have developed a salting-out method for the preparation of SFPs (500 - 1200 nm) by adding SF solution into potassium phosphate solutions [79]. This method possesses several advantages such as low cost, simplicity and safe operation, avoiding the use of toxic solvents and easy to maintain protein activities. However, the size of SF particles prepared with this approach is relatively large, which means their circulation time in blood will be shorter and are more likely to be entrapped within the liver and spleen [35].

Targeted drug delivery using magnetic carriers and an external magnetic field focused on the tumour areas has been reported as a promising strategy, which possesses advantages such as visualize the targeting process, rapid targeting and potential of being heated in a magnetic field to promote drug release as well as avoiding complicated chemical modification of targeting ligands on the surface of nanocarriers [48]. Therefore, the combination of magnetic nanoparticles (MNPs) and SF become a promising strategy for targeted drug delivery. Recently, Tian and co-workers successfully prepared Doxorubicin (DOX) loaded magnetic silk fibroin nanoparticles (DMSPs) using the potassium phosphate salting-out method. The as-prepared DMSPs were proved capable of delivering the drug to the tumour site with the help of an external magnetic field [59]. Nevertheless, targeted delivery of CUR using magnetic silk fibroin particles (MSPs), and the use of sodium phosphate to make smaller SFPs, to the best of our knowledge, has not yet been reported. It has been observed in our result that SFPs fabricated using sodium phosphate possess much smaller particle sizes (90 – 300 nm) compared with those fabricated with potassium phosphate, which normally possess the size over 500 nm. Since the particle size and performance of SFPs produced using sodium phosphate is significantly different from those fabricated using potassium phosphate and the properties of these particles have not yet been studied. It is important to investigate the size, zeta potential, secondary structure, CUR loading / release efficiency of SFPs and CMSPs prepared using sodium phosphate. On the other hand, it is expected that CUR will easily be encapsulated or adsorbed on the water-insoluble SFPs or CMSPs due to the strong hydrophobic interaction between hydrophobic CUR and the water-insoluble silk-II structure formed during the salting-out process. High encapsulation and loading efficiency of CUR in SFPs and CMSPs are also expectable, which is desired for a drug delivery system. Therefore, in this experiment, CMSPs were prepared with the salting-out method using sodium phosphate instead of potassium phosphate to

prepare smaller SFPs. The particle properties including size, zeta potential and CUR loading / release efficiency were investigated. In addition, how processing parameters such as pH value of sodium phosphate solution affect those properties were also studied. The cytotoxicity and cellular uptake performance of CMSPs was investigated using MDA-MB-231 (human breast adenocarcinoma) cells.

## 3.2. Results and discussion

### 3.2.1. Controlling the size and secondary structures of silk fibroin nanoparticles

Desolvation and salting-out are two common methods for the fabrication of SF particles [185]. While the desolvation method [186] is capable of making relatively smaller SFPs (< 200 nm), toxic organic solvents such as ethanol, methanol or acetone have to be introduced in the process, which may increase the toxicity to cells. On the other hand, SF particles can be prepared by the salting-out method without organic solvents involved. In the process of salting-out, SF protein chains will first form micellar-like structures in a salt solution due to the enhancement of hydrophobic interactions. The particulate globules will then be formed with the micelles by further hydrophobic interactions [79]. In this paper, the salting-out method was used for the fabrication of SF particles. To investigate the effect of SF concentration and different salts on the size of SF nanoparticle, SF solutions with various concentrations (0.1-12 mg/ml) were added to 1.25 M sodium or potassium phosphate solutions (pH 8) and kept at - 20 °C for 2 h. The as-prepared particles were measured with dynamic light scattering (DLS). As shown in Fig. 3.1a, when using potassium phosphate, increasing SF concentrations from 0.1 to 12 mg/ml, resulted in the change of particle mean diameter from 0.62 to 2.12 μm which is very similar to the result reported by Lammel and co-workers [79]. However, the sizes of the particles are bigger than the desired size for drug delivery. For example, it has been

reported that nanoparticles in the range of 100 - 200 nm can extravasate through vascular fenestrations of tumours and escape filtration by liver and spleen [35].

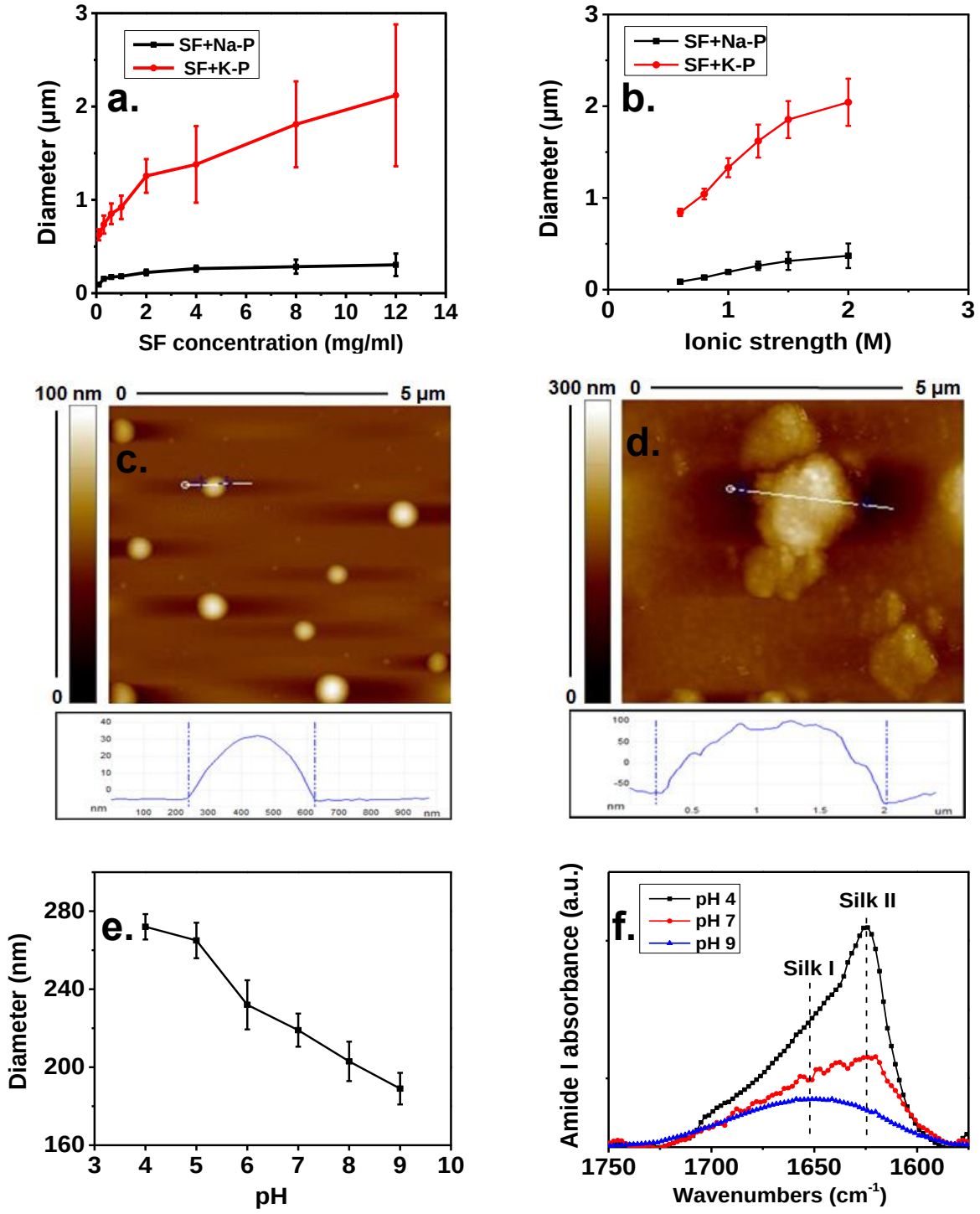


Fig. 3.1. Effects of SF concentration, salt, ionic strength and solution pH to the particle size and protein secondary structure. Particle diameter as a function of SF concentration when adding SF (concentration from 0.1-12 mg/ml) solutions to sodium phosphate (Na-P) and potassium phosphate (K-P) solutions (both at ionic

strength 1.25 M, pH 8) at the volume ratio of 1:5 (a). Diameter of SFPs fabricated with K-P or Na-P as a function of their ionic strength (b). (The SF concentration was fixed at 5 mg/ml). AFM images of particles fabricated by adding silk fibroin solution (12 mg/ml) in to Na-P (c) and K-P (d) both solutions are at ionic strength 1.25 M and pH 8. Diameter of SFPs fabricated with Na-P as a function of the pH of Na-P solutions (e). The SF concentration was fixed at 5 mg/ml. FTIR spectra of particles produced by salting out by 1.25 M Na-P at different pH values (f). The results are shown in mean ± SD, $n \geq 3$. It was found from the above results that the use of Na-P, lower ionic strength and higher pH of solution provides smaller SFPs.

Nanoparticles with diameter ~100 nm are long-lasting in circulation, as the size increased to 150 nm and larger, more and more nanoparticles become entrapped in the liver and spleen [35]. Therefore, it is likely that lots of these SF nanoparticles with diameters over 600 nm will be filtered by the liver and spleen instead of reaching the tumour site once injected into human body. In contrast, those fabricated with sodium phosphate showed much smaller sizes (90 - 300 nm) and narrower size distributions (Fig. 3.1a). Therefore, it provides a method to prepare SFPs with more appropriate sizes for drug delivery without involving organic solvent.

To explain the difference in nanoparticle size crated using sodium phosphate and potassium phosphate, we need to first determine the reason why SF polypeptides are stable in aqueous solution. Since the isoelectric point (pI) of SF is 4.53 and its surface charge becomes more and more negative by increasing the pH above the pI [79]. SF is negatively charged in aqueous solution (pH 7). The net charge on the surface of SF thus prevents them from aggregating via electrostatic repulsion [187]. Therefore, to eliminate the polypeptide-polypeptide repulsion of SF for their aggregation, counterions must be introduced. Here, the counterions are sodium and potassium ions. When SF solutions are mixed with sodium or potassium phosphate solutions, the cations can adsorb onto the negatively charged SF surface which results in the decrease of the overall SF net charge, resulting in aggregation. The difference in the adsorption behaviour of sodium and

potassium ions is expected to be responsible for the different aggregation results of SF. When added to water, the negative side of water molecule (oxygen) will be attracted to the cations (sodium and potassium ions) and the positive side of water (hydrogen) to negatively charged phosphate ions [188]. As a result, ion-water shell structures are created with ions surrounded by shells of water molecules, which are celled hydrated ions. Since sodium and potassium ions possess the same charge while the ion radius of sodium is smaller than potassium, sodium ions have a higher charge density compared to potassium ions. Therefore, sodium ions exhibit a stronger affinity towards water compared to potassium ions, which also results in a larger radius of hydrated sodium ions (see Fig. 3.2a) [189].

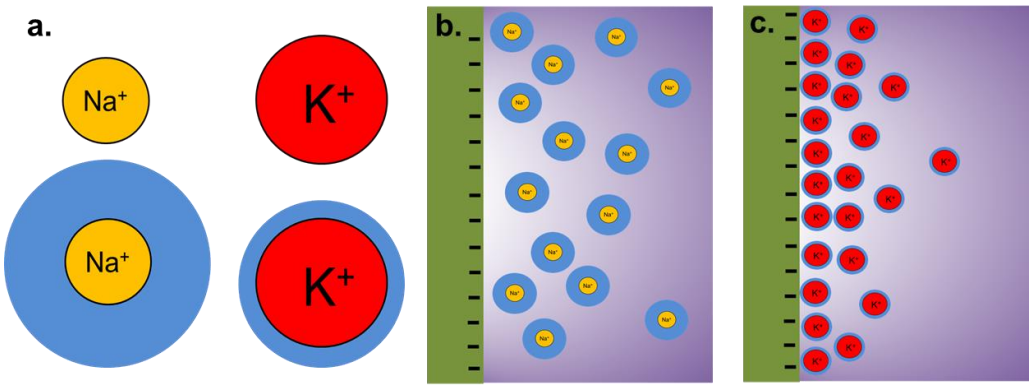


Fig. 3.2. Schematic representation of the ion radius and hydrated ion radius of sodium and potassium ions (a). the adsorption of hydrated sodium (b) and potassium (c) ions onto hydrophobic SF surfaces.

According to the law of matching water affinities (LMWA), cations tend to contact and form stable ion pairs with anions with the same affinity to water [190]. Which means, strongly hydrated cations are more likely to contact with strongly hydrated anions instead of weakly hydrated anions. Therefore, sodium ions may more readily be adsorbed to the strongly hydrated groups such as $COO^-$ from SF polypeptide than potassium ions do, while potassium ion are more readily to adsorb to the negative sides of backbones such as C=O. It can be assumed that sodium ions are more hydrophilic than

potassium ions and tend to stay closer to the bulk of water molecules while potassium ions tend to stay closer to SF backbones. Therefore, during the process of salting out, sodium ions are more readily adsorbed to more hydrophilic and strongly hydrated sites of SF than potassium ions. However, when it comes to more hydrophilic and less hydrated sites, potassium ions are more readily to be adsorbed. Then it can be assumed that there are more weakly hydrated sites in SF than the strongly hydrated ones and the salting out property of SF is dominated by the weakly hydrated and less hydrophilic parts. In this case, potassium ions can be more effectively adsorbed onto SF to reduce its overall net charge and induce aggregation.

It might be easier to explain the above process by assuming the SF polypeptides are small, uniform and hydrophobic (more hydrophobic than water) particles with negatively charged surfaces (as shown in Fig. 3.2b&c). Then the salting out process is to eliminate their surface charges by adsorption of counterions (sodium / potassium) to their surface. In this case, strongly hydrated sodium ions prefer to stay close to the bulk of water due to their higher infinity with water, while weakly hydrated potassium ions prefer to stay close to hydrophobic SF surface and away from the bulk. Therefore, potassium ions can more effectively bind to SF surfaces and reduce their surface charge to facilitate aggregation.

Apart from the different adsorption behaviours of sodium and potassium ions, their different hydration behaviour may also responsible for their difference in aggregation. As shown in Fig. 3.2b&c, once hydrated cations are adsorbed on SF surfaces, water molecules from hydrated cations are also located surround SF surfaces. As a result, a layer of tightly bound water molecules is produced on SF surfaces which may provide protection against direct contacting between SF polypeptides. Since the hydrated sodium ions possess more water molecules than hydrated potassium ions, SF that has hydrated sodium ions adsorbed is expected to possess a thicker water

bound layer (Fig. 3.2b) than SF adsorbed with hydrated potassium ions (Fig. 3.2c) [191]. Therefore, more hydrated sodium ions exhibit a lower salting out efficiency compared to less hydrated potassium ions, in this case resulting in smaller SF particles fabricated using sodium phosphate to potassium phosphate.

The effect of ionic strength on the size of the particles has also been investigated. Fig. 3.1b illustrates the diameter of SFPs fabricated with sodium or potassium phosphate as a function of the ionic strength of the salts. Below 0.6 M ionic strength, particles in both salt solutions can hardly be detected. Therefore, the lowest ionic strength to form particles is assumed to be 0.6 M. This finding is consistent with the previous literature [79]. Increased ionic strength resulted in larger particles for both cases, which is assumed to be a result of enhanced denaturation of silk fibroin and aggregation of smaller SF nanoparticles. It is also clear that at the same ionic strength, particles fabricated with potassium phosphate are much larger than those fabricated with sodium phosphate. AFM images of SF nanoparticles fabricated by adding SF solution (12 mg/ml) into sodium or potassium phosphate solution (1.25 M, pH 8) are shown in Fig. 3.1c&d. Particles formed using sodium phosphate are much smaller (380 nm) and smoother, while particles formed by potassium phosphate are larger (1800 nm) in size and have a rough surface that may result from the aggregation of smaller particles. Therefore, by using different phosphate solutions or adjusting their ionic strength, SFPs with a large range of diameters (90 nm - 2.2 μm) can be prepared, which provides more options on designing SFPs for different applications.

The solution pH can also affect particle size. Fig. 3.1e shows the diameter of SFPs fabricated with sodium phosphate as a function of pH, the ionic strength of solutions was fixed at 1.25 M. From pH 4 to 9, the size of particles decreased gradually. The isoelectric point (pI) of silk fibroin is 4.53 [79], at

which pH the net charge of SF is close to 0 and thus tend to aggregate due to the increased inter-molecular interaction [79]. At pH higher than the pI, the net charges of SF are negative and the charge density tends to increase as pH increases. As a result, the increased repulsion resulted in smaller SF nanoparticles and prevented further aggregation.

To investigate the effect of pH values on SF secondary structures, FTIR analysis was carried out and the results are shown in Fig. 3.1f. Absorption band in the frequency range of 1616 - 1637 cm-1 represents the β-sheet rich silk-II form while those in the frequency range from 1636 - 1655 $cm^{-1}$ represent the random coil and α-helix rich silk I form [192]. In an α-helix structure, hydrogen bonds are formed between the N-H groups and C=O groups within the same strand. On the other hand, in a β-sheet structure, hydrogen bonds are formed between adjacent peptide strands, which can bring strands to interact with each other to form insoluble aggregates [63]. Therefore, the silk II structure is more hydrophobic than the silk I structure. As revealed in Fig. 3.1f, the secondary structure of SFPs contains more silk II structure, and is more hydrophobic, at pH 4 compared to a less hydrophobic silk I-rich structure at pH 9. These results explain the change on SF nanoparticle size at different pH values, more hydrophobic particles have larger tendency to gather and form bigger aggregates. Furthermore, this phenomenon is very useful in manipulating drug loading, for example, increasing the loading efficiency of hydrophobic drugs on particles by using more hydrophobic particles.

### 3.2.2. Controlling the size and Zeta potential of magnetic silk fibroin nanoparticles and curcumin loaded magnetic silk fibroin core-shell nanoparticles

Magnetic $Fe_3O_4$ nanoparticles (MNPs) with diameter 10 - 30 nm were introduced to SFPs by adding MNPs into sodium phosphate solutions (1.25 M, pH 8) before mixed with SF solutions. As shown in Fig. 3.3, as-prepared magnetic-SF core-shell particles (MSPs) can be rapidly collected with the help of an external magnetic force from a Neodymium magnet, which can be potentially used for the targeted delivery of particles to desired tissue sites under external magnetic forces [59].

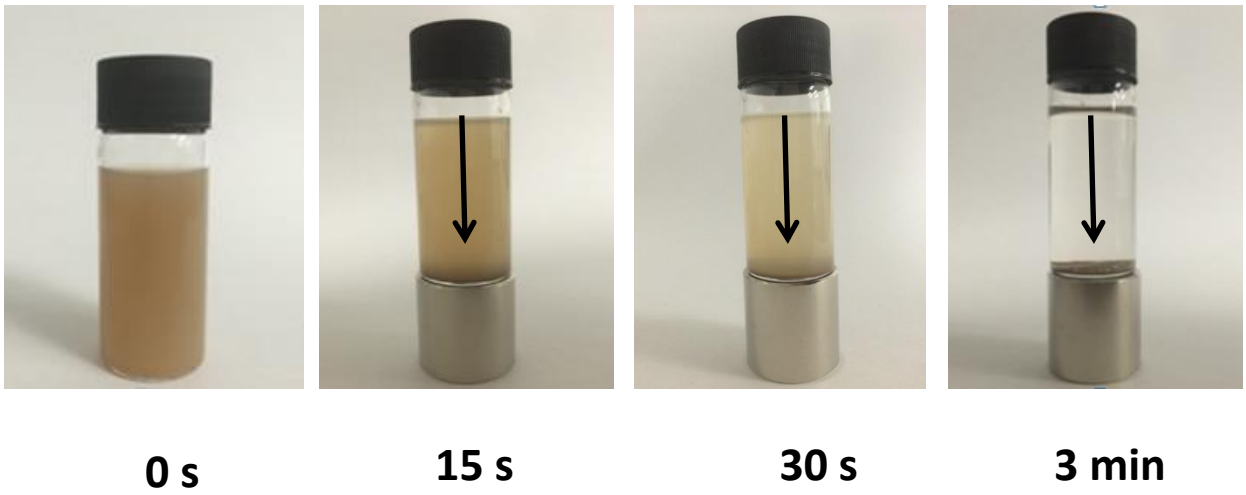


Fig. 3.3. MSPs can be rapidly collected with a Neodymium magnet (pull force 25 Kg, 25.4 mm Diameter x 30 mm thick) within 3 min.

The size of as-prepared MSPs can be manipulated by changing SF concentration or pH values of sodium phosphate used. Fig. 3.4a illustrated the diameter of MSPs as a function of SF concentrations. The addition of MNPs did not change the particle size of SFPs. Instead, the particles size remained within the range of 100 - 250 nm. This result is in agreement with the work of Tian *et al*. who have reported that, when using potassium phosphate, the addition of MNPs can dramatically decrease the particle size of SFPs from 1.4 μm to 130 - 210 nm [59]. Fig. 3.4b showed

the effect of sodium phosphate pH on MSP diameter. It is clear that both SF concentration and sodium phosphate pH affect MSP size similarly as they affect SF particle size (Fig. 3.1a&e), which suggests the property of MSPs is dominated by the SF structures coated on the MNPs. It can be assumed that when the MSPs were prepared in a pH 9 solution, the SF coating became more negatively charged and less hydrophobic, which tend to increase the repulsion and decrease the hydrophobic interaction among MSPs and eventually fabricate smaller particles. Therefore, the size of MSPs can be controlled by altering the pH value of salt solution used in the process.

CMSPs were fabricated by adding CUR and MNPs into sodium phosphate solution (1.25 M, pH 8) followed by adding SF solution (5 mg/ml) into the mixture. As shown in Fig. 3.4c, increasing the amount of CUR (with weight equivalent to the percentages of the weight of SF used) resulted in the increased diameter of CMSPs, indicating the drug loading into the particles. The Zeta potential of the CMSPs with different CUR loading was measured. As shown in Fig. 3.4e, higher CUR usages resulted in less charge densities, which lead to weaker repulsive interactions and therefore, larger particles. The same reason can also be used to explain the effect of pH value on CMSP size. As shown in Fig. 3.4d, CMSP diameter decreases with the increase of sodium phosphate pH value. Meanwhile, Fig. 3.4f illustrated that higher pH values correspond to higher charge densities. Thus, we may conclude that the property of CMSPs is also dominated by its SF content, therefore, higher pH value correspond to higher charge densities and smaller particles.

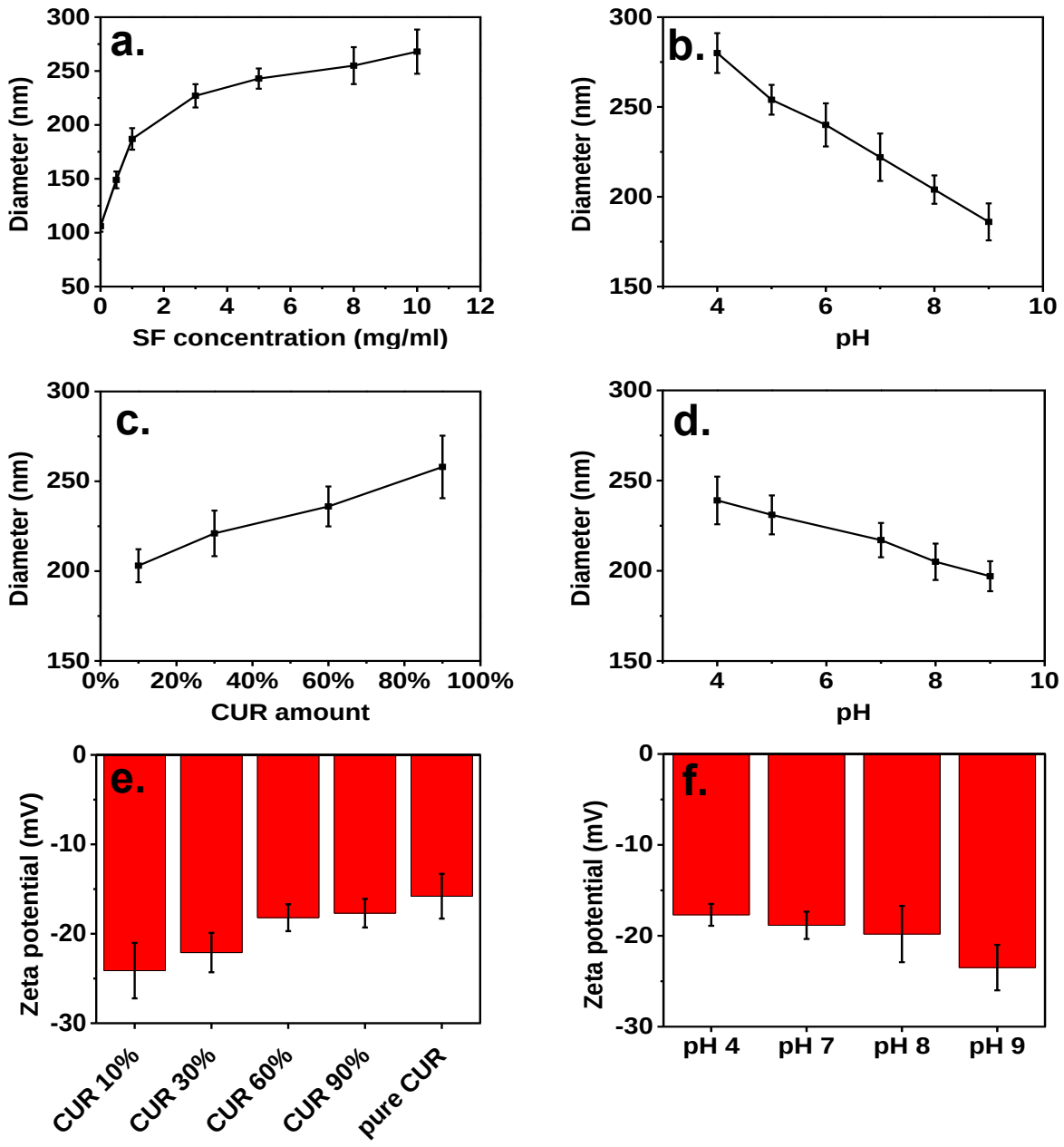


Fig. 3.4.The effects of SF concentration, solution pH, and CUR amount to the particle size and zeta potential of MSPs and CMSPs. The effect of SF concentrations to the diameter of MSPs fabricated by sodium phosphate solutions (a) (ionic strength: 1.25 M, pH 8). The effect of sodium phosphate solution pH to the diameter of MSPs (b) (SF concentration: 5 mg/ml, sodium phosphate ionic strength: 1.25M). The effect of CUR amount to the diameter (c) and Zeta potential (e) of CMSPs, which were fabricated by adding different amounts of CUR (with weight equivalent to the percentages of SF used) to sodium phosphate solutions before SF solutions (5 mg/ml) and MNPs were added to the mixed solution. The effect of sodium phosphate solution pH to the diameter (d) and Zeta potential (f) of CMSPs (SF concentration: 5 mg/ml, CUR amount: 10% of SF used). The results are shown in mean ± SD, $n \geq 4$. It was found that the size and Zeta potential of

MSPs and CMSPs can be controlled by altering the SF concentration, solution pH and the amount of CUR used in the fabrication process.

Pure CUR is negatively charged as shown in Fig. 3.4e, the surface charge property of CUR is attributed its chemical structure. The IUPAC nomenclature of CUR is (1E,6E)-1,7-bis(4-hydroxy-3-methoxyphenyl)-1,6-heptadiene-3,5-dione and its chemical structure is shown in Fig. 3.5. CUR is composed of two aromatic rings that are connected by a seven carbon linker (α,β-unsaturated β-diketone moiety) [193]. A methoxy and a phenolic hydroxyl group are contained in each aromatic ring at the ortho position. A keto-enol tautomerism exists in diketones group, leading to two different forms of CUR (enol form and keto form). The enol form is more stable than the keto form in solution phase and gas phase because the structure is composed of three planar groups inter connected via two double bonds. Since the carbon atoms in the aromatic ring are $sp^2$-hybridized and left their π electrons to delocalized in the molecular orbitals extend all over the ring, the atoms in the aromatic ring are on the same plane and the ring is conjugated. Apart from the aromatic group, the seven-carbon linker in a CUR molecule (enol form) consists of double bonds separated by single bonds, therefore, the linker is also conjugated. Combining the linker and two aromatic rings, the conjugation is extended and the π electron cloud is all along the CUR molecule [193-194]. Because of the conjugated structure of CUR, the hydroxyl groups (one enolic hydroxyl group and two phenolic hydroxyl groups) in CUR possess protons that can be ionized. A long pair on the oxygen atom can overlap with the delocalized π electrons on the CUR molecule, which leads to the extension of the delocalization of π electrons to the oxygen atom. Once a proton is lost, the negative charge from the oxygen atom will delocalize around the π system and the resulting anion is stabilized. Therefore, CUR molecules exhibit weak acidity in aqueous solution and the resulted CUR ions are negatively charged.

There are three different $pK_a$ values for the three hydroxyl groups in CUR. The identification of $pK_a$ is shown in Eq. (3.3) - (3.5):

$$HA \leftrightharpoons H^+ + A^- \tag{3.3}$$

$$K_a = \frac{[H^+][A^-]}{[HA]} \tag{3.4}$$

$$pK_a = -log_{10}(K_a) \tag{3.5}$$

Where *HA* represents an acid, $H^+$ represents a hydrogen ion, $K_a$ is the acid dissociation constant, $pK_a$ is the negative base 10 logarithm of $K_a$ [195]. The smaller the $pK_a$ value, the higher the hydrogen ion concentration is in solution and therefore the stronger the acid is [195]. The enolic proton has been reported as the most acidic one among the three protons in CUR and it has a $pK_{a1}$ value of 7.8, as shown in Fig. 3.5. The phenolic protons are slightly weaker in acidity and have $pK_{a2}$ and $pK_{a3}$ of 8.5 and 9.0 respectively [196].

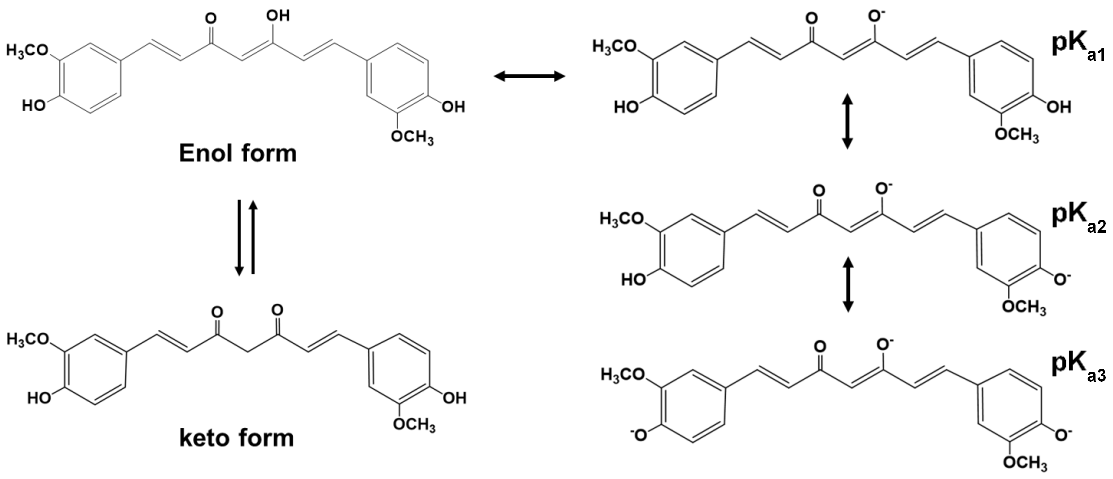


Fig. 3.5. Chemical structure of CUR and the ionization of CUR (Enol form).

To reveal the morphology of the particles before and after the CUR loading, AFM and TEM experiments have been carried out. AFM images of MSPs and CMSPs are shown in Fig. 3.6a&b respectively. Spherical particles with a smooth surface were observed for MSPs, very similar to the

morphology of the SFPs (Fig. 3.1c). The diameter of the particles is around 250 nm, consistent with the data measured by DLS in Fig. 3.4a. In contrast, the surface of CMSPs appears to be rougher, indicating the loading of CUR into the particles. Presumably, the loading of CUR into the particles makes the particles more hydrophobic; therefore, the particles were dehydrated. Fig. 3.6c&d showed the TEM images of MSPs and CMSPs respectively. These images indicate clearly that both MSPs and CMSPs are formed by multiple magnetic cores covered by SF or SF / CUR shells, which is in agreement with the work by Tian *et al* [59]. The insets in Fig. 3.6c&d are the enlarged images from the red boxes. It can be seen from the enlarged images that the black magnetic cores are surrounded by SF shells. A number of smaller core-shell particles (~ 30 nm) aggregate to form a bigger particle (~ 250 nm).

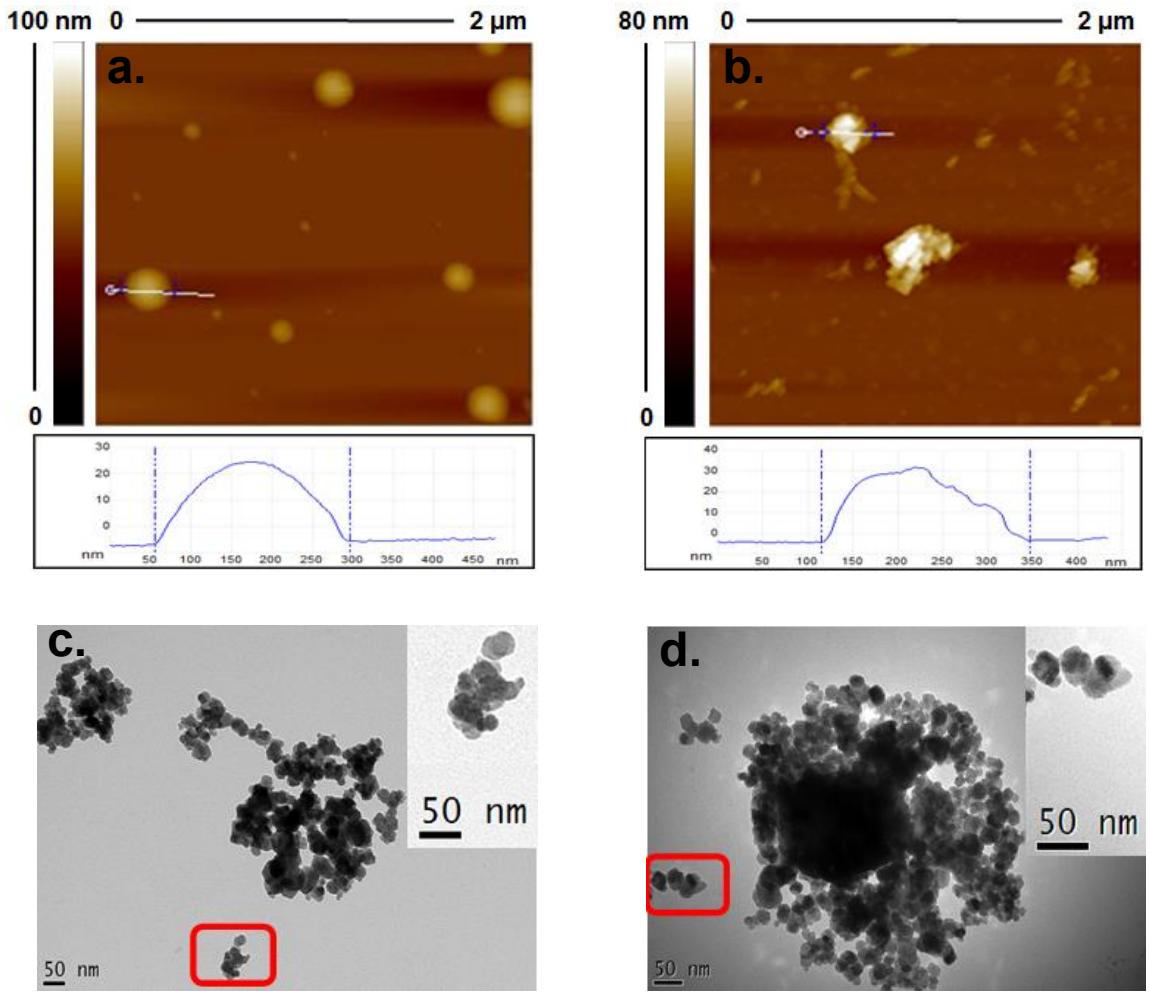


Fig. 3.6. AFM and TEM images of the MSPs and CMSPs. AFM (a) and TEM (b) images of MSPs (SF: 5 mg/ml, ionic strength of sodium phosphate: 1.25 M, pH 8). AFM (b) and TEM (d) images of CMSPs (SF: 5 mg/ml, ionic strength of sodium phosphate: 1.25 M, pH 8, CUR amount: 10% of SF used). Inserts are the enlarged images of from the red boxes.

### 3.2.3. Controlling loading and release of curcumin

To investigate the loading and release property of CMSPs, diverse amounts of CUR were loaded into CMSPs and the effect of sodium phosphate pH values was also investigated. Fig. 3.7a illustrated the effect of CUR amount on encapsulation of CUR. The pH of sodium phosphate solution was fixed at 8 in this experiment. It can be seen that more than 97% of CUR has been encapsulated regardless of the amount of CUR used. Loading efficiency of CUR into these particles increased from ~ 10% to ~ 80% with the increasing amount of CUR used as shown in Fig. 3.7c. The encapsulation and loading efficiency of CUR in CMSPs is remarkably high given the fact that the typical loading efficiency for hydrophobic compound loading in protein nanoparticles is around 5% [197-201]. This phenomenon could owe to the strong hydrophobic interaction between hydrophobic CUR and the water-insoluble silk-II structure formed during the salting-out process. The results has shown significant improvement in loading efficiency (up to 80%) compared with 6% found for curcumin-loading into silk fibroin (SF) / poly(L-lactic acid-co-e-caprolactone) (P(LLA-CL)) nanofibrous scaffolds [202], 12% for the silk / curcumin nanoparticles fabricated in supercritical $CO_2$ [27], 15% for the SF nanoparticles reported by Li *et al*. [203], 30% for the silk / curcumin nanoparticles produced by desolvation method [204], as well as 10% loading efficiency for the paclitaxel loaded silk fibroin nanoparticles [205]. The lower loading efficiency in SF nanoparticles via desolvation method was due to the fact that CUR tend to dissolve in organic solvent instead of adsorb on SF nanoparticles. However, for loading via slating-out method, the hydrophobic CUR was either encapsulated in or adsorbed on the water-insoluble SF nanoparticles instead of suspend in the aqueous solution. Therefore, the loading of CUR in SF nanoparticles via salting-out method is more suitable for the fabrication of high CUR-loading efficiency SF nanoparticles, which is desired for the drug delivery systems.

Another desired capability of a drug carrier is to be able to control the release of drug and normally a longer releasing period is desired. To investigate the release profile of the CMSPs with different encapsulation and loading efficiencies, 5 mg of each type of particles were dispersed in 5 ml PBS (pH 7.4) and incubated at 37 °C with shaking (200 rpm). The CUR concentrations in solution were measured at different time scales and the cumulative CUR release curves are shown in Fig. 3.7e. Although CMSPs with 10% CUR loading released more in terms of percentage (12.4% drug released in 20 days) of loaded CUR than others during the releasing period, the total amount of released CUR is still less than other (30%, 60% and 90% CUR loaded) particles. The drug release rate for CMSPs with 10% CUR loading stays at a higher slope for the first 14 days and gradually level off, while for other particles, the release rates are still at steady slopes. The higher accumulative release rate was due to the low CUR loading [206].

During the whole period of CUR releasing, the release was progressive without obvious burst release, which indicates that the CUR was homogeneously dispersed in the CMSPs. This release profile was also in agreement with the work by Xie *et al*. that the inconspicuous burst release was due to the poor water-solubility of CUR [27]. The release profile of CUR from SF matrix can be described as a three-step process; firstly, the initial diffusion resulted from desorption of CUR from the particle surface, then water penetrates into the matrix and the inner drugs are released. Finally, the degradation of SF releases the remaining encapsulated drug [207]. Since the burst release of CUR is limited by its poor solubility, the CUR release can be assumed that depend on the solubility, diffusion and biodegradation of the SF matrix. It has been reported that the change of SF structure can lead to a different release profile of CUR [208]. Xie *et al*. found that silk I structure of SF nanofibrous become more water-insoluble when exposed to ethanol vapour, and the ethanol vapour treated SF carriers showed a lower CUR release rate than the no-treated ones [27]. Li *et al*. have

prepared CUR loaded SF nanoparticles by desolvation method, the resulted SF carriers have released only ~ 5% of loaded CUR and nearly stopped releasing after around 3 days [203]. This low CUR release amount and short release period can be explained by the fact that water-insoluble β-sheet structures were formed after the SF have been treated with ethanol [186], thus the hydrophobic CUR tend to remain in hydrophobic SF matrix, weakening the CUR diffusion. It should be noted that our release profile last 20 days with up to 12% release of the CUR which is significant better than the literature which normally last only one week [27, 203-204].

Because the structure of SF particles can be controlled by using salt solution with different pH values, we have observed the loading / release profiles of CMSPs prepared at different pH values. Fig. 3.7b&d illustrated the encapsulation and loading efficiencies of CUR in MSPs fabricated using sodium phosphate solutions with different pH values. It can be seen that MSPs fabricated by sodium phosphate solutions with pH 4 - 8 have similar CUR encapsulation (over 97%) and loading (over 10.5%) efficiencies, however, those using pH 9 solution showed noticeably less encapsulation (76%) and loading (8.4%) efficiencies than others. Considering the results shown in Fig. 3.1f that SFPs fabricated with pH 9 sodium phosphate solutions have more silk-I content than those fabricated in lower pH values, it is suspected that the secondary structure of SF significantly affects the ability of MSPs in absorbing CUR and the less hydrophobic silk-I content is less capable of capturing CUR. Therefore, the CUR loading efficiency of CMSPs via salting-out method can be controlled by altering the pH of salt solution. Fig. 3.7f showed the cumulative CUR release of CMSPs fabricated using sodium phosphate with different pH values. CMSPs fabricated in pH 4 have released more CUR than those fabricated at higher pH values. This is because the CUR loading was carried out at pH 4 while SF was more hydrophobic and the release was carried out at pH 7.4, at which pH the SF become less hydrophobic therefore facilitate the release of the

hydrophobic CUR. Therefore, the release of CUR depends on the charge and structure of SF which can be controlled during the salting-out process. These results suggest that CMSPs possess many desired properties such as high encapsulation / loading efficiency and controllable release profile, which makes it a promising system for drug delivery.

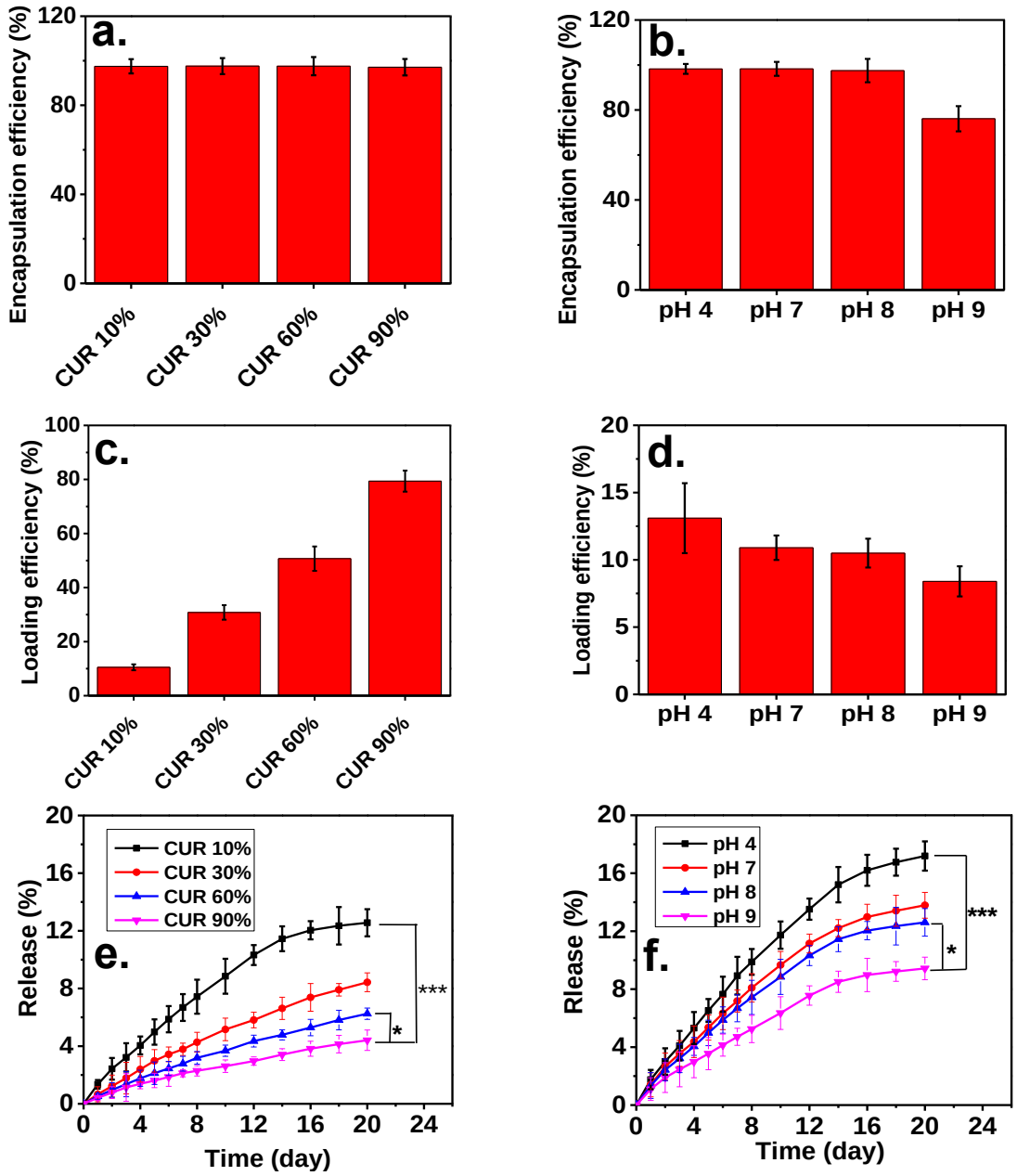


Fig. 3.7. Drug leading and release profiles of the CMSPs. Encapsulation efficiency of CMSPs fabricated with various CUR amounts in terms of the amount of SF used (a) (pH 8) and various pH (b) (CUR amount: 10%). Loading efficiency of CMSPs fabricated with various CUR usage (c) (pH 8) and various pH (d) (CUR

amount: 10%). Cumulative release of CUR from CMSPs fabricated with different CUR usage (e) (pH 8) and different pH (f) (CUR amount: 10%). For each experiment, SF concentration was fixed at 5 mg/ml, ionic strength of sodium phosphate solution was fixed at 1.25 M. The results are shown in mean ± SD, n ≥ 3. The statistical significance is expressed as ***p < 0.001, **p < 0.01, *p <0.05.

### 3.2.4. *In vitro* cytotoxicity assay

MTT assay was conducted to investigate the ability of CMSPs to inhibit growth of MDA-MB-231 cells. SFPs and MSPs were used as controls. SFPs, MSPs and CMSPs with 30% CUR were incubated with MDA-MB-231 cells for 3 days before determining the relative cell viabilities. Free CURs with amount equal to that encapsulated by CMSPs were also incubated and the viabilities were compared with that from CMSPs. As illustrated in Fig. 3.8, cell growth was significantly inhibited by either CMSPs or free CUR at higher CUR concentrations. Within the dose range from 3 to100 μg/ml, CMSPs were significantly more cytotoxic to MDA-MB-231 cells than free CUR at equivalent CUR dosage. For instance, the cell viability of MDA-MB-231 cells treated with 60 μg/ml CMSPs for 3 days was 12.2 ± 6.3% and when treated with equivalent CUR, the viability was 46.3 ± 5.2 %, which suggests the inhibition of cancer cell growth was enhanced by CMSPs. The enhanced cytotoxicity of CMSPs could be the result of enhanced uptake of CMSPs by cells and the encapsulated CUR was released via diffusion or the degradation [27] of SF matrix inside the cells, which in turn increased the up take efficiency of CUR, thus decreased the cell viability. SF nanoparticles and MSPs, on the other hand, had very little effect on cell toxicity at lower concentration and relatively low cytotoxicity at higher concentrations, indicating that SF nanoparticles and MSP are non-toxic nanoparticles. Similar studies have been reported and indicated that SF particles also showed no cytotoxicity to many other cell lines [59, 182, 205, 208]. For example, Xie *et al.* have compared the *in vitro* anti-cancer effect of CUR and CUR loaded SF

nanoparticles against HCT-116 cancer cells [208]. It was found that the curcumin-silk fibroin nanofibrous matrix had equivalent anti-cancer effect to the DMSO dissolved CUR.

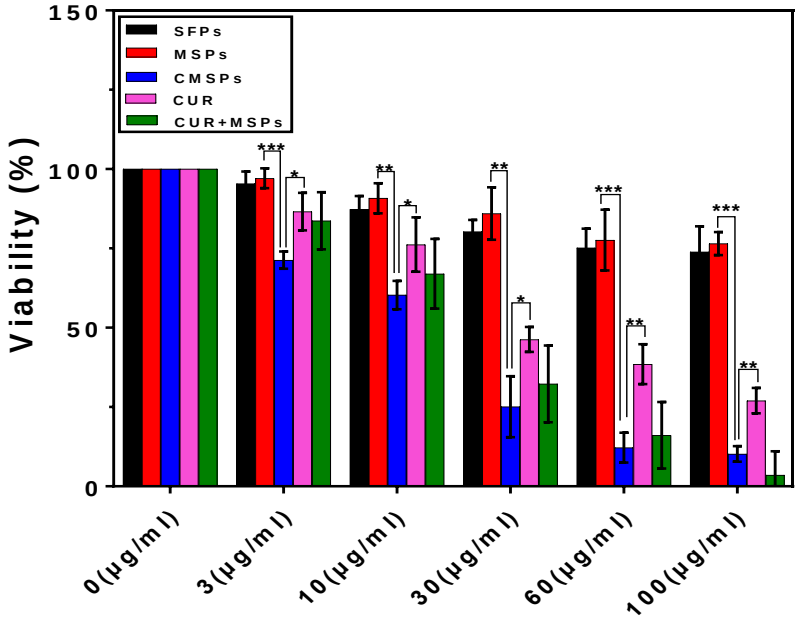


Fig. 3.8. *In vitro* cytotoxicity studies for MDA-MB-231 cells treated with SFPs, MSPs, CMSPs (CUR usage: 30%) and free CUR (amount equivalent to the CUR loaded in CMSPs) for 3 days. Added inhibitions of free CUR and MSPs equivalent to the amount of CUR and MSPs in CMSPs were also compared (CUR + MSPs). The results are shown in mean ± SD, n = 8. The statistical significance is expressed as ***$p < 0.001$, **$p < 0.01$, *$p < 0.05$.

To investigate whether the higher cytotoxicity of CMSPs on MDA-MB-231 cells is a simple addition of CUR and MSPs cytotoxicity or enhanced CUR delivery by the nanoparticles, the growth inhibition result of CMSPs is compared with the added inhibition of corresponding free CUR and MSPs with amounts equal to the amounts of CUR and MSP content in CMSPs. The results are also shown in Fig. 3.8 demonstrated that CMSPs have higher cytotoxicity than the added toxicities of free CUR and MSPs (except the data at 100 µg/ml). Therefore, the enhanced cytotoxicity of CMSPs against MDA-MB 231 cells is expected as a result of enhanced cell internalization of the CUR loaded particles.

### 3.2.5. Cellular uptake assays

To investigate the internalization and intracellular drug release behaviours of CMSPs, MDA-MB-231 cells were treated with different concentrations of CMSPs (with 30% CUR loaded) and free CUR. The amount of free CUR was equal to the CUR content in CMSPs. The percentage of cell uptake of CUR is determined by flow cytometry and the results are shown in Fig. 3.9a. The uptake efficiency of CUR for cells treated with CMSPs is significantly higher than those treated with free CUR at all concentrations and the difference is especially large at lower concentration. This result suggests that the enhanced growth inhibition effect of CMSPs, as illustrated in Section 3.2.4, is a result from higher CMSPs uptake. Since CUR is a highly hydrophobic drug, its dispersion and diffusion in aqueous solution is significantly poor. However, when loaded in CMSPs, CUR was encapsulated within CMSPs and can cross the cell membrane for cell uptake. The results are consistent with the reports that SF particles can be taken up rapidly by cells [72, 182]. To investigate whether the uptake efficiency of CMSPs is significantly affected by the CUR content, MDA-MB-231 cells were incubated with SFPs, MSPs and CMSPs (30% CUR loaded) for 24 h. The SF content of these particles was labelled with Rhodamine B which can be detected by flow cytometry to determine the uptake of these particles. These results are shown in Fig. 3.9b. All three kind of particles displayed similar cellular uptake efficiency and uptake increased with the increasing particle concentration. Considerably high uptake efficiency (nearly 70%) can be reached at lower concentration (e.g.10 μg/ml) which is beneficial to drug delivery.

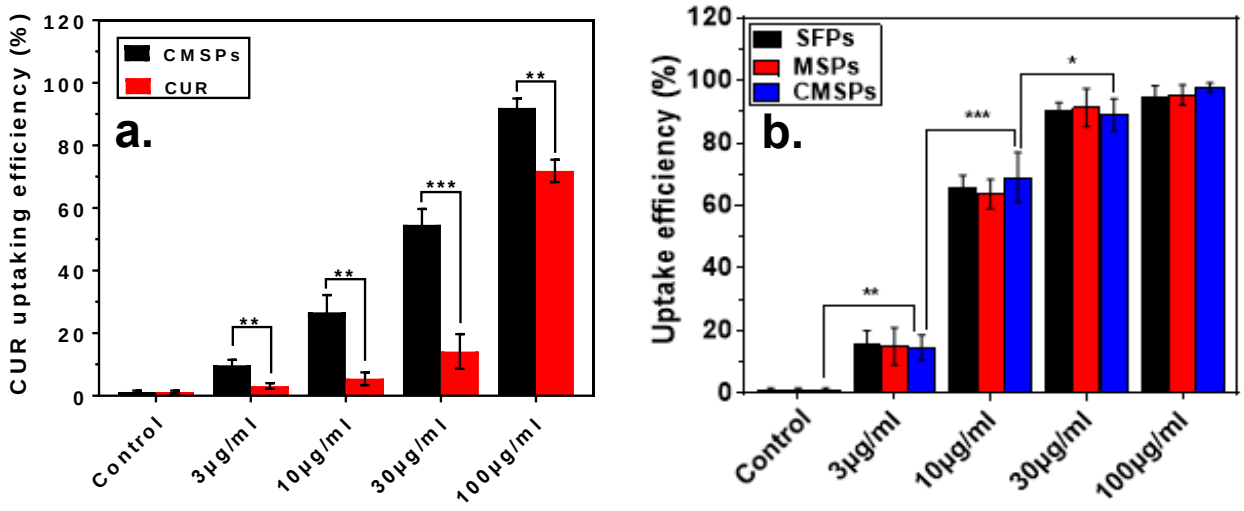


Fig. 3.9. Cellular uptake assays of the different particles. CUR uptake in MDA-MB-231 cells after treated with CMSPs (with 30% CUR loaded) and equivalent amount of free CUR for 24 h (a). Particle uptake efficiency of SFPs, MSPs and CMSPs in MDA-MB-231 cells after incubation for 24 h (b). SF content in these particles was labelled with Rhodamine B and the uptake efficiencies were determined by measuring the cell population containing Rhodamine B fluorescence with flow cytometry. The results are shown in mean ± SD, n = 3. The statistical significance is expressed as ***$p < 0.001$, **$p < 0.01$, *$p < 0.05$. It was found that cells treated with CMSPs had significantly higher uptake efficiency of CUR than those treated with free CUR.

Fig. 3.10 shows the fluorescent microscopic images of CUR uptake by MDA-MB-231 cells after incubation with free CUR (Fig. 3.10a&b) or CMSPs (Fig. 3.10c&d). CUR molecule is auto-fluorescent (Ex 340 nm, Em 530 nm [155]) and was observed with GFP channel. The nucleus and cytoskeleton were stained with DAPI and Texas Red®-X Phalloidin. The enhanced CUR up take effect of CMSPs is confirmed by these images. As shown in Fig. 3.10a&b, the green fluorescence in cells that have been treated the free CUR, is very weak which suggests the uptake efficiency of free CUR is low, consistent with uptake efficiency shown in Fig. 3.9a. In contrast, Fig. 3.10c&d shows that over 90% of the cells incubated with CMSPs have displayed much brighter green fluorescence which appears to be quite uniformly distributed within the cytosol. The

dramatically increased fluorescence intensity suggests that CMSPs can significantly enhance the uptake of CUR for MDA-MB-231 cells. The yellow fluorescence in the merged images indicates the co-localization of the Texas red and CUR fluorescence.

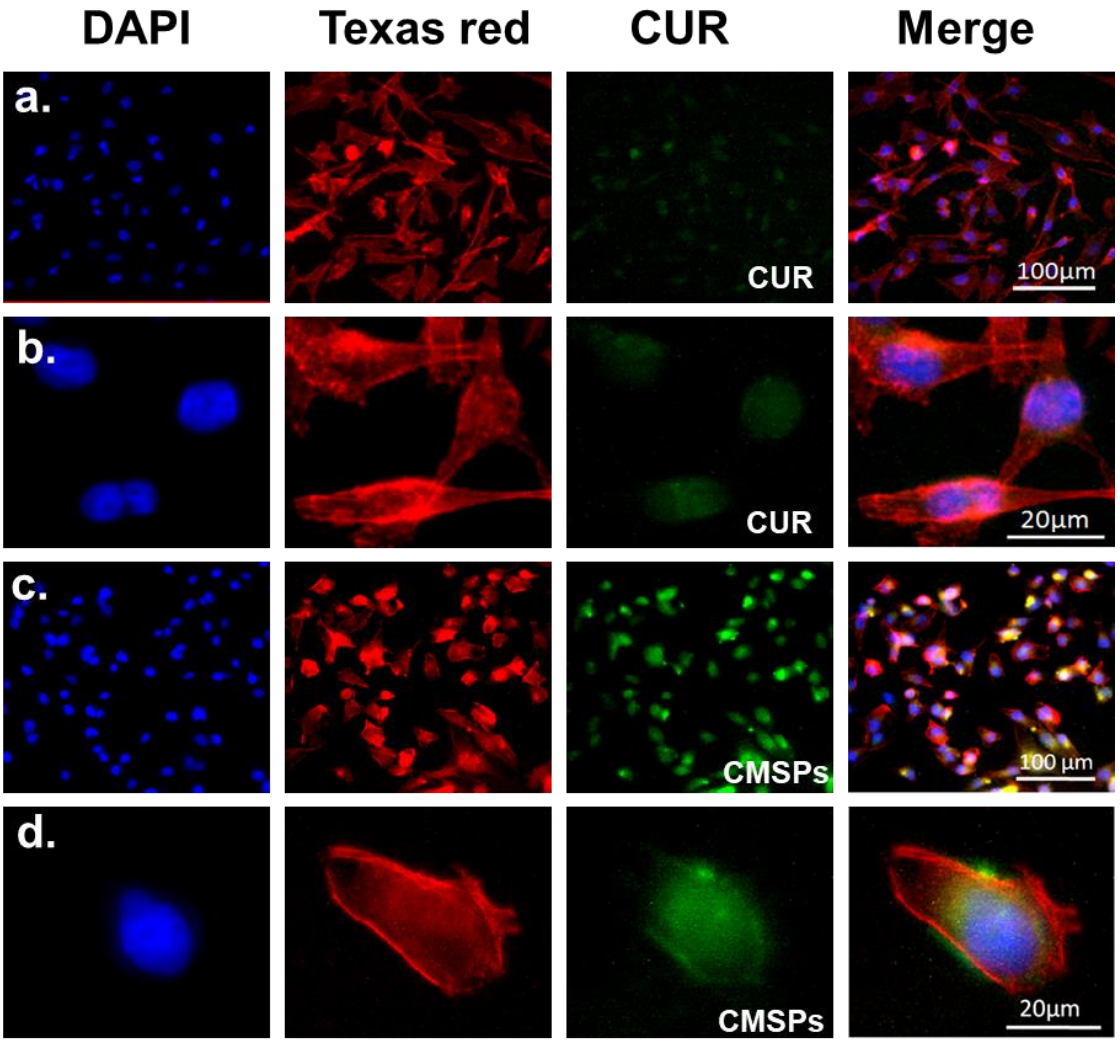


Fig. 3.10. Representative microscopic images of MDA-MB-231 cells incubated with free CUR (a&b), CUR amount (10 μg/ml) equivalent to the CUR loaded in CMSPs (30%) and CMSPs (c&d, 30 μg/ml) for 4 h. Cell nucleus and cytoskeleton were stained with DAPI (blue) and Texas red (red); all images were taken with AF6000 microscope (Leica). Comparing the images in a&b to c&d, it can be seen that CMSPs significantly improve the cellular uptake of the CUR.

To demonstrate the uptake of the nanoparticles, Fig. 3.11 shows the fluorescent microscopic images of FITC-labelled SFPs (Fig. 3.11a&b) and MSPs (Fig. 3.11c&d) uptake by MDA-MB-231

cells. It can be seen from Fig. 3.11a&c that over 90% of the cells have green fluorescence, consistent with uptake efficiency shown in Fig. 3.9b. Fig. 3.11b&d shows the uptake by single cells.

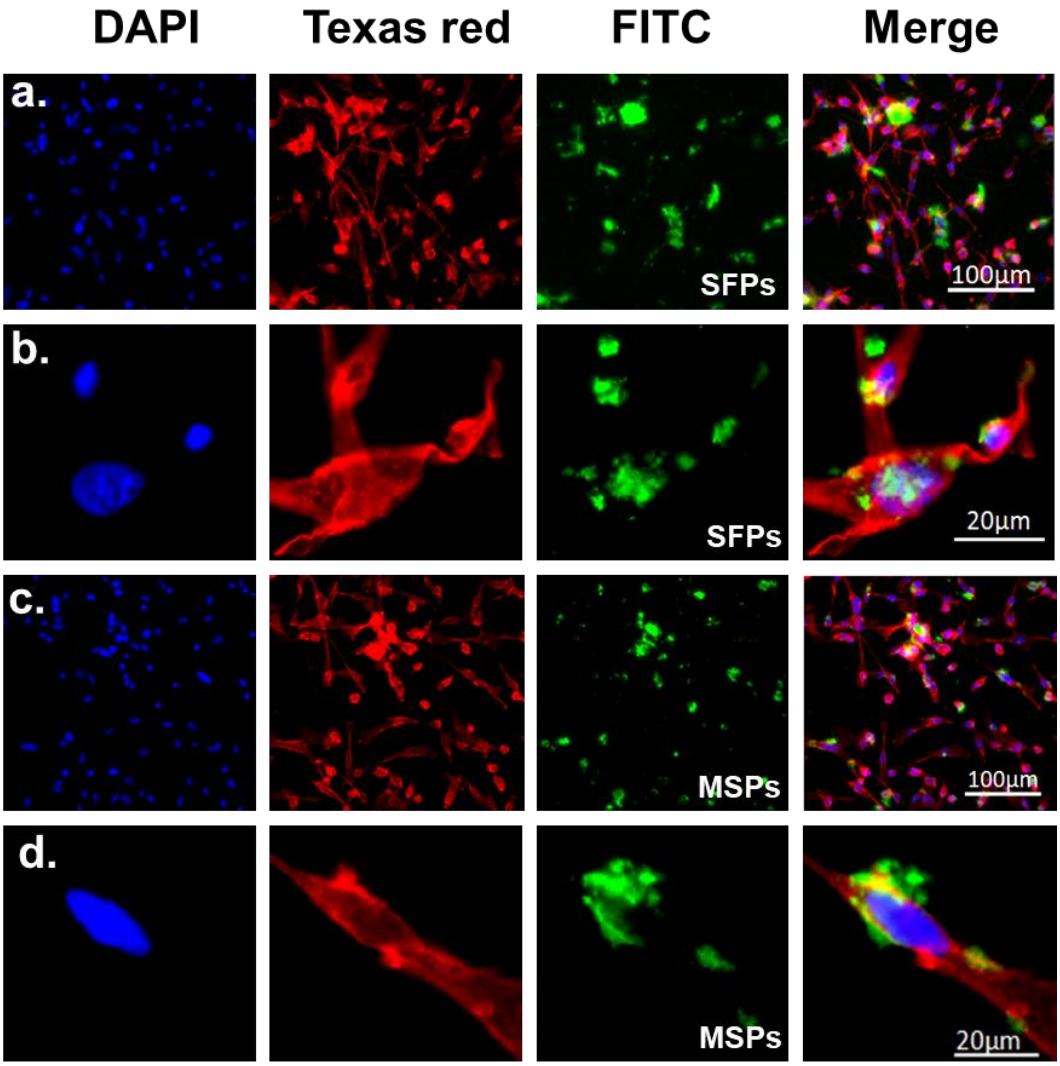


Fig. 3.11. Representative microscopic images of MDA-MB-231 cells incubated with FITC-labelled SFPs (a&b, 30 μg/ml) or FITC labelled MSPs (c&d, 30 μg/ml). Cell nucleus and cytoskeleton were stained with DAPI (blue) and Texas red (red); all images were taken with AF6000 microscope (Leica).

## 3.3. Conclusions

Smaller particles as drug carriers are desired for drug delivery systems. However, SF particles fabricated using potassium phosphate are relatively larger (500 -1200 nm). In this Chapter, a method to fabricate SFPs using sodium phosphate was developed and the results indicated that SFPs fabricated with sodium phosphate possess significantly smaller size than those fabricated using potassium phosphate. This new method provides a simple process allowing the fabrication of smaller SFPs without using any organic solvent. Size and secondary structure of SFPs was controlled by changing SF concentration, the pH and ionic strength of sodium phosphate solutions. The size, zeta potential and drug loading / releasing efficiency of CMSPs was controlled by using different SF concentrations, CUR amounts and pH values of sodium phosphate solutions. Sustained release of CUR from CMSPs was observed for 20 days and CMSPs fabricated at lower pH values showed higher CUR release rate. Enhanced growth inhibition of CMSPs against MDA-MB-231 cells was observed by MTT assay and CUR uptake efficiency was also significantly enhanced due to the better internalization of CMSPs. The effect of particle concentration on cellular uptake efficiency was investigated and the results indicate that uptake efficiency can be increased by increasing particle concentration. In addition, these particles displayed similar uptake efficiency, which suggests the CUR content in CMSPs did not affect the uptake efficiency of particles. Therefore, CMSPs can be used as potential drug delivery system for cancer therapy.

# 4. Preparation of Magnetic Alginate / Chitosan Layer-by-Layer Nanoparticles as Potential Carriers for Targeted Delivery of Curcumin into Human Breast Cancer Cells


## Abstract

Curcumin is a promising anti-cancer drug but its applications in cancer therapy are limited due to its poor solubility, short half-life and low bioavailability. In this study, curcumin loaded magnetic alginate / chitosan nanoparticles were fabricated to improve the bioavailability, uptake efficiency and cytotoxicity of curcumin to MDA-MB-231 breast cancer cells. Alginate and chitosan were deposited on $Fe_3O_4$ magnetic nanoparticles based on their electrostatic properties. The sizes of the nanoparticles were within the optimum size range (50 - 200 nm) for drug delivery. Sustained curcumin release was obtained use the nanoparticles with the ability to control the curcumin release rate by altering the number of chitosan and alginate layers. In addition, the final polymer layer was found strongly affected the drug release. Confocal fluorescence microscopy results showed that targeted delivery of curcumin to desired sites with the aid of an external magnetic field was achieved. The Fluorescence-activated cell sorting (FACS) assay indicated that MDA-MB-231 breast cancer cells treated with curcumin loaded magnetic alginate / chitosan nanoparticles had a 3-6-fold uptake efficiency to those treated with free curcumin. MDA-MB-231 breast cancer cells exhibited significantly higher curcumin uptake efficiency in contrast to normal HDF cells after both been treated with curcumin loaded nanoparticles. The MTT assay indicated that the curcumin loaded nanoparticles exhibited significantly higher cytotoxicity towards MDA-MB-231 cancer cells than HDF cells, which is desired for anticancer drug delivery. The sustained release profiles, enhanced uptake efficiency and cytotoxicity to cancer cells as well as the potential of targeted delivery make

MACPs a promising candidate for targeted anti-cancer drug delivery.

**Keywords**: Alginate, Chitosan, Layer-by-layer, Magnetic nanoparticles, Drug delivery, Cancer, Curcumin

**Abbreviations**: CUR: curcumin; CHI: chitosan; SA: sodium alginate; MNPs: magnetic nanoparticles; MAPs: Magnetic alginate nanoparticles; MACPs: magnetic alginate / CHI layer-by-layer nanoparticles; CMACPs: Curcumin loaded magnetic alginate / chitosan layer-by-layer nanoparticles; CMACPs 1&4: Curcumin loaded magnetic alginate / chitosan layer-by-layer nanoparticles with 1 and 4 layers of polymer coating; HDF: Human Dermal Fibroblasts

## 4.1. Introduction

Curcumin (CUR) is a yellow, hydrophobic, polyphenolic compound of turmeric that is extracted from the rhizomes of *Curcuma longa,* which are widely cultivated in Asian countries such as India and China and have been historically used as a spice [3, 172]. CUR is 'Generally Recognized as Safe (GRAS)' by the Food and Drug Administration (FDA) [3] and has been widely used in medicine due to its anti-oxidant [4-6], anti-inflammatory [7-9], wound-healing [10-11] and anti-bacterial [12-13] properties. Recent research has demonstrated that CUR has the ability to inhibit carcinogenesis in various cell lines including breast, colon and gastric cancer cells, which has resulted in increased interest as a promising anticancer drug [14-17]. However, CUR exhibits poor solubility in aqueous solution, limiting its applications for cancer therapy [18-20].

It has been reported that after an oral administration of 2 g/kg of CUR in humans, an extremely low serum concentration (0.006 ± 0.005 μg/ml) of CUR was observed after 1 h [209]. As a result, the bioavailability and anti-cancer efficiency of CUR is limited by its low solubility [18-20]. In order to

improve the bioavailability, various nanocarriers have been used, including lipid based nanoparticles [21-25], polymer nanoparticles [26-32] and inorganic nanoparticles [33]. The main advantages of the CUR loaded nanocarriers are their small size and large surface area, which enable them to pass through the cell membranes with an enhanced uptake efficiency [3, 30]. Research has increasingly focused on the fabrication of biopolymer nanoparticles for CUR delivery due to advantages of low cytotoxicity, excellent biocompatibility and biodegradability [30]. Two of the most commonly used biopolymers in medical applications are alginate and chitosan (CHI). Alginate is an anionic polysaccharide composed of (1-4)-linked β-D-mannuronate (M) and α -L-guluronate (G) residues while CHI is a cationic polysaccharide composed of N-acetyl-D-glucosamine and D glucosamine [82, 93] and is positively charged below neutral pH, due to the protonation of amino groups [80]. Both alginate and chitosan (CHI) are naturally obtained biopolymers that possess desirable properties such as biocompatibility, biodegradability and are not toxic [82]. Moreover, alginate based nanoparticles can be fabricated by simple processes such as $Ca^{2+}$ cross-linking or altering of pH [92]. CHI based nanoparticles can be prepared by providing polyanion of tripolyphosphate (TPP) without introducing harsh cross-linking agents or organic solvents [88]. Electrostatic interactions between positive CHI chains and negative drugs such as CUR enable the retention of the drugs in CHI based nanoparticles, providing a prolonged drug release profile [85]. These advantages of alginate and CHI make them promising candidates as nanocarriers for drug delivery [82]. Various alginate or CHI based nanoparticles have been developed for the delivery of CUR [32, 90, 210-212]. For example, Anitha *et al*. prepared CUR loaded dextran sulphate–chitosan nanoparticles and reported that a controlled and pH dependent CUR release over a period of one week was achieved [90]. Maghsoudi *et al.* prepared CUR loaded alginate nanoparticles and reported that the CUR loaded nanoparticles exhibited enhanced solubility in aqueous solution comparing

with free CUR [211].

Exploiting the electrostatic properties of alginate and CHI, a layer-by-layer coating method can be employed to prepare multilayer alginate / CHI polyelectrolyte nanoparticles, this method allows simple engineering of desired surface features for specific applications [213]. By altering the number of layers deposited it is possible to control the drug release rate [214-216]. In addition, the use of a noncovalent route for multilayer formation provides a low-cost simple fabrication method [217]. Due to these promising advantages of the layer-by-layer method, it has been widely used to fabricate nanoparticles for drug delivery [213-216, 218]. Apart from engineering the size and surface properties of nanocarriers, incorporation of magnetic nanoparticles (MNPs) enables the targeted delivery of the drug carriers to tumour sites with the help of an external magnetic field [48]. Targeted delivery by MNPs has been reported as a promising strategy for cancer therapy, which possesses the advantages including visualize the targeting process, rapid targeting and accumulation of drug carriers at the tumour sites by magnetic forces, the MNPs can be heated in a magnetic field to promote the drug release and avoid complex chemical modifications of targeting ligands on the surface of nanoparticles [48]. The toxicity of MNPs has been reported very low and can be well tolerated in the human body [219]. The small size and large surface area of MNPs makes them suitable for polyelectrolyte layer-by-layer deposition. Therefore, deposition of alginate / CHI multilayers onto MNPs will enable targeted delivery and controlled released of drugs. In this paper, magnetic alginate / CHI layer-by-layer nanoparticles (MACPs) were fabricated for the delivery of CUR into MDA-MB-231 breast cancer cells and HDF (Human dermal fibroblasts).

## 4.2. Results and discussion

### 4.2.1. Characterization of magnetic alginate / chitosan layer-by-layer nanoparticles and curcumin loaded magnetic alginate / chitosan nanoparticles

#### 4.2.1.1. Zeta potential, size and FTIR spectra

As shown in Fig. 4.1, magnetic alginate particles (MAPs) were prepared via the self-assembly of alginate on the surface of MNPs in $Ca^{2+}$ solution (Stage 1). Following this the formation of MACPs (Stage 2) was done by coating MAPs with CHI. Stage 3: Particles with 1 layer of alginate and CHI were then coated with sodium alginate (SA) again. Stage 2 and 3 were then repeated consecutively for the desired number of layers.

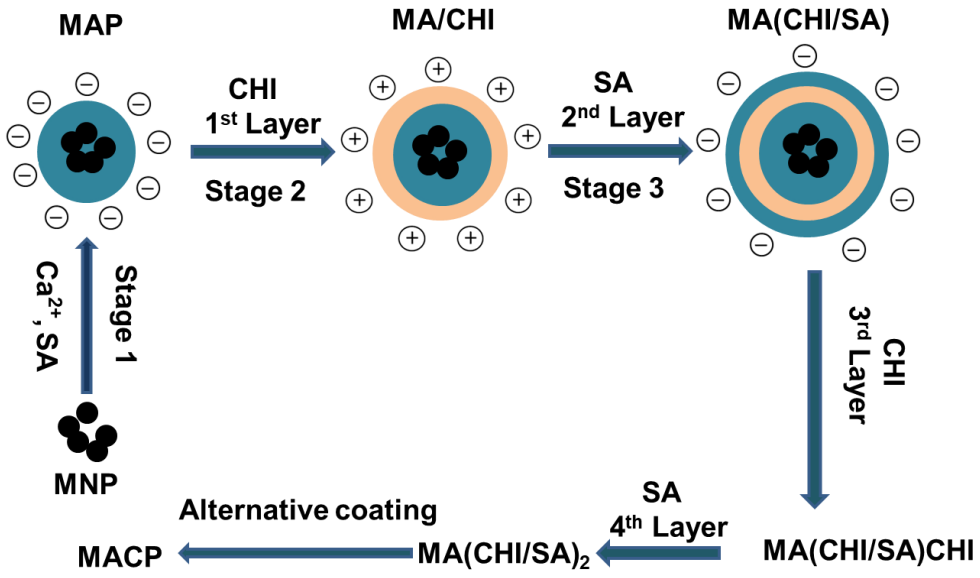


Fig. 4.1.Schematic illustration for the preparation of MAPs and MACPs. MAPs were fabricated by coating cross-linked alginate on MNPs using $Ca^{2+}$ as the cross-linker. MACPs were prepared by alternatively depositing CHI and SA on MAPs based on the electrostatic interaction between the two biopolymers. The alternative coating was repeated until MACPs with desired number of layers were obtained (Stage 2 and 3).

MAPs and MACPs with different number of layers were dispersed in DI water (pH was adjusted to 7 using HCl and NaOH) or sodium phosphate solution (pH 7) and their zeta potential was analysed using DLS. As shown in Fig. 4.2a, the zeta potential of MAPs in water was -21.4 mV which was similar to the results of $Ca^{2+}$ crosslinked alginate particles reported in previous literature [220-221]. The zeta potential of free SA in water has been reported as -50 mV [222]. The reason for the increased zeta potential of MAPs is due to the crosslinking with $Ca^{2+}$. The carboxyl groups contribute to the anionic charge of the alginate polymer [223]. Upon gelation, the negatively charged carboxyl groups from the G blocks in the alginate chains interact with $Ca^{2+}$ ions and form an 'egg-box'-like structure, reducing the density of free carboxyl groups as well as the anionic charges [223]. Therefore, an increase of zeta potential was observed for MAPs. After deposition of the first layer (CHI), zeta potential of particles become positive (+19.2 mV) followed by a reduction to -44.8 mV after the negatively charged alginate polymer was coated as the second layer. Positive charges ranging from +12.1 to +19.2 mV were observed when CHI was coated as the outermost layer and negative charges ranging from -43 to -48.5 mV were associated with alginate coatings as the outermost layer. An oscillation of zeta potential was observed with the alternative deposition of SA and CHI, indicating the successful coating of negative alginate and positive chitosan polymers.

The zeta potential of particles in sodium phosphate solution (10 mM) is also shown in Fig. 4.2a and exhibited a similar oscillation behaviour between coatings. However, negative surface charges were observed for MACPs (layer number: 1, 3, 5, 7, 9) with CHI outermost layer. This phenomenon is due to the adsorption of the phosphate anions onto the surface of the chitosan polymers. Phosphates contain small multivalent anions and therefore, tend to interact or complex with cationic amino groups on CHI surfaces via electrostatic interactions [88]. Therefore, the phosphate anions adsorbed onto CHI layers provided the negative charges on the particles. Similar phenomena have been

reported previously: for example, Swain *et al.* analysed the zeta potential of CHI in both 1 and 10 mM NaCl and found that the zeta potential value decreased as the ionic strength of NaCl increased [84]. The authors suggested the reduced surface charge was attributed to the adsorption of anions onto the surface of CHI polymers [84]. Further to this, Acevedo *et al*. analysed the zeta potential of CHI (5 mg/ml) in water and NaCl solution (0.2 M) and reported the zeta potential value of +72 mV in water and +33 mV in NaCl solution [224]. It was suggested that this reduced absolute zeta potential value was governed by a compression of the electrical double layer due to the electrostatic interactions with $Cl^-$ in the solvent [224]. As shown in Fig. 4.2a, the zeta potential of MACPs with alginate as the outermost layer analysed in phosphate solution exhibited similar values as they were in water, which is in agreement with previously reported data [222]. On the other hand, MAPs exhibited a more negative zeta potential values in phosphate solution (-36 mV) compared to water (-21.4 mV). This is due to reaction between $Ca^{2+}$ and phosphate ions to form insoluble calcium phosphate, which leads to the loss of $Ca^{2+}$ and the increased density of free carboxyl groups thus resulting in an overall increased negative charge. The zeta potential behaviour of drug carriers can be utilized to control the drug loading and release processes. For example, cationic drug carriers such as CHI nanoparticles can be used to improve the loading of anionic drug molecules and prolong their release time based on electrostatic interactions between positive CHI and negative drug molecules [85]. In the case of MACPs, different numbers of polymer layers with different zeta potentials can potentially be used to improve drug loading.

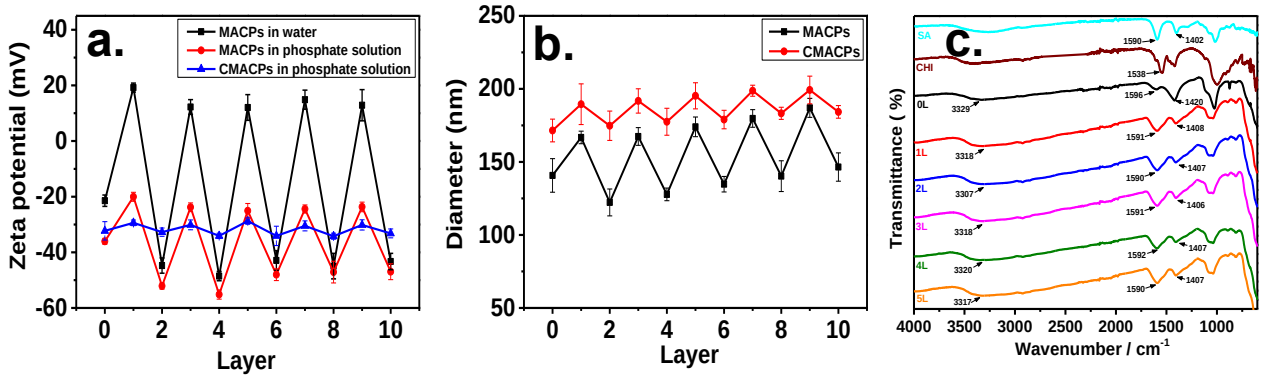


Fig. 4.2. Zeta potential (a) and average diameter (b) of MACPs and CMACPs as a function of the number of coated layers. Zeta potential of particles was analysed in water (pH 7) and phosphate solution (10 mM, pH 7). Particle size was analysed in phosphate solution. Oscillations of zeta potential and average diameter were observed with the alternate coating of SA and CHI. (c) FTIR spectra of MAPs and MACPs with the number of deposited polymer layers from 1 to 5. The results are shown in mean ± SD, n ≥ 3.

The average diameter of MACPs was analysed by NTA as shown in Fig. 4.2b, where the diameter of MAPs was found to be 141 nm which increased to 167 nm after the coating of the first CHI layer. The size of particles increased gradually as the coating of SA / CHI bilayers and reached 187 nm for 9 layers. The growth in particle size is attributed to the deposition of SA and CHI polymers. Size differences were observed depending on the outermost polymer of MACPs were also observed. For example, after coating with the second layer (SA), the average diameter of MACPs decreased from 167 (3 layers) to 128 nm (4 layers) and then increased to 174 nm after the deposition of CHI as the fifth polymer layer. This leaves a mean size difference of ~40 nm between CHI and SA and is most likely due to the different surface charges of the particles. For MACPs with CHI as the outermost layer, the zeta potential ranged from -20 to -25.1 mV in phosphate buffer solutions while the zeta potential for alginate as the outermost layer ranged from -47 to -55.2 mV. Particles with absolute zeta potential values higher than 30 mV can be considered stable in solution [225]. Therefore, MACPs with alginate outermost layers were very stable in solution due to their sufficient surface charges. On the other hand, particles with CHI as the outermost layer were less stable and more likely to

aggregate in aqueous solutions forming larger particles.

The zeta potential of CMACPs in sodium phosphate solution at pH 7 is shown in Fig. 4.2a. A significant change in surface charge was observed for particles after CUR loading. The zeta potential of free CUR sodium phosphate solution was -31.1 mV. In contrast, the zeta potentials of MAPs and MACPs with the outermost layer of alginate (layer number: 0, 2, 4, 6, 8, 10) was within the range from -36 to -55.5 mV (Fig. 4.2a) while the zeta potentials of the particles with CHI outermost layer (layer number: 1, 3, 5, 7, 9) were around -20 mV. After CUR loading, the zeta potentials of CMACPs were found between -28.7 and -34.2 mV suggesting the CUR was encapsulated in or adsorbed onto the particles, reducing the difference of the zeta potentials between MACPs with alginate and CHI outermost layers. Increased particle sizes (between 172 – 199 nm) were observed for CMACPs (Fig. 4.2b) compared to MACPs (122 – 187 nm), which can be attributed to the loading of CUR. For CMACPs with the same outermost polymer (SA or CHI), the average diameter of particles increased as the number of layers increased due to the fact that larger polymer matrixes encapsulate more CUR molecules. Slightly larger particle size was observed for CMACPs with the outermost polymer of CHI compared to those with SA as the outermost layer. This is because CMACPs with SA outermost layers exhibited a higher absolute value of zeta potential than those with CHI. They possessed a greater electrostatic repulsion therefore maintained smaller aggregation sizes. It is worth to note that the size of CMACPs were also within the range of 50 - 200 nm. For the efficient delivery of drug to the cancer sites, the optimum size range of drug carriers is generally accepted to be about 50 - 200 nm [38]. Particles with size less than 50 nm will easily extravasate through the discontinuous endothelium of live, spleen and bone marrow therefore are less likely to accumulated at the desired sites. On the other hand, particle with diameter larger than 200 nm may not pass through the porous vasculature to reach the tumour site and will be eliminated

more easily by the immune system [38]. Therefore, CMACPs are within the optimum size range for the delivery of drugs to the tumour sites.

The chemical compositions and interactions between different polymer layers were analysed by FTIR as shown in Fig. 4.2c. For SA, the peaks at 1590 $cm^{-1}$ and 1402 $cm^{-1}$ were characteristic for the asymmetric stretching and symmetric stretching of -COOH groups respectively [226-227]. In MAPs and MACPs with the number of layers (1, 2, 3, 4 and 5), these two peaks moved towards higher wavenumbers, indicating the formation of $Ca^{2+}$-alginate ionic cross-linking [228]. This is because of the changes in charge density, atom radius and atom weight of the cations [228-229]. For CHI, the peak at 1538 $cm^{-1}$ was characteristic of -$NH_2$ bonds [230]. The presence of CHI in the MACPs was also confirmed by comparing the curves of MAPs (0 L) and MACPs (1 L - 5 L). The broad characteristic adsorption at 3329 $cm^{-1}$ for -OH groups in MAPs shifted to a lower frequency for MACPs (1-5 L), demonstrating the superposition of amine N-H stretching in CHI and -OH groups of alginate and CHI [230-231]. The peak at 1596 $cm^{-1}$ in MAPs became broader, and moved to a lower frequency for MACPs, which can be attributed to the overlapped -$NH_2$ stretching from chitosan and -COOH stretching from alginate [232]. These results confirmed that CHI and alginate chains were successfully incorporated into the MACPs.

#### 4.2.1.2. Morphology characterization

The morphology of MAPs and MACPs were also analysed by AFM and TEM (Fig. 4.3).

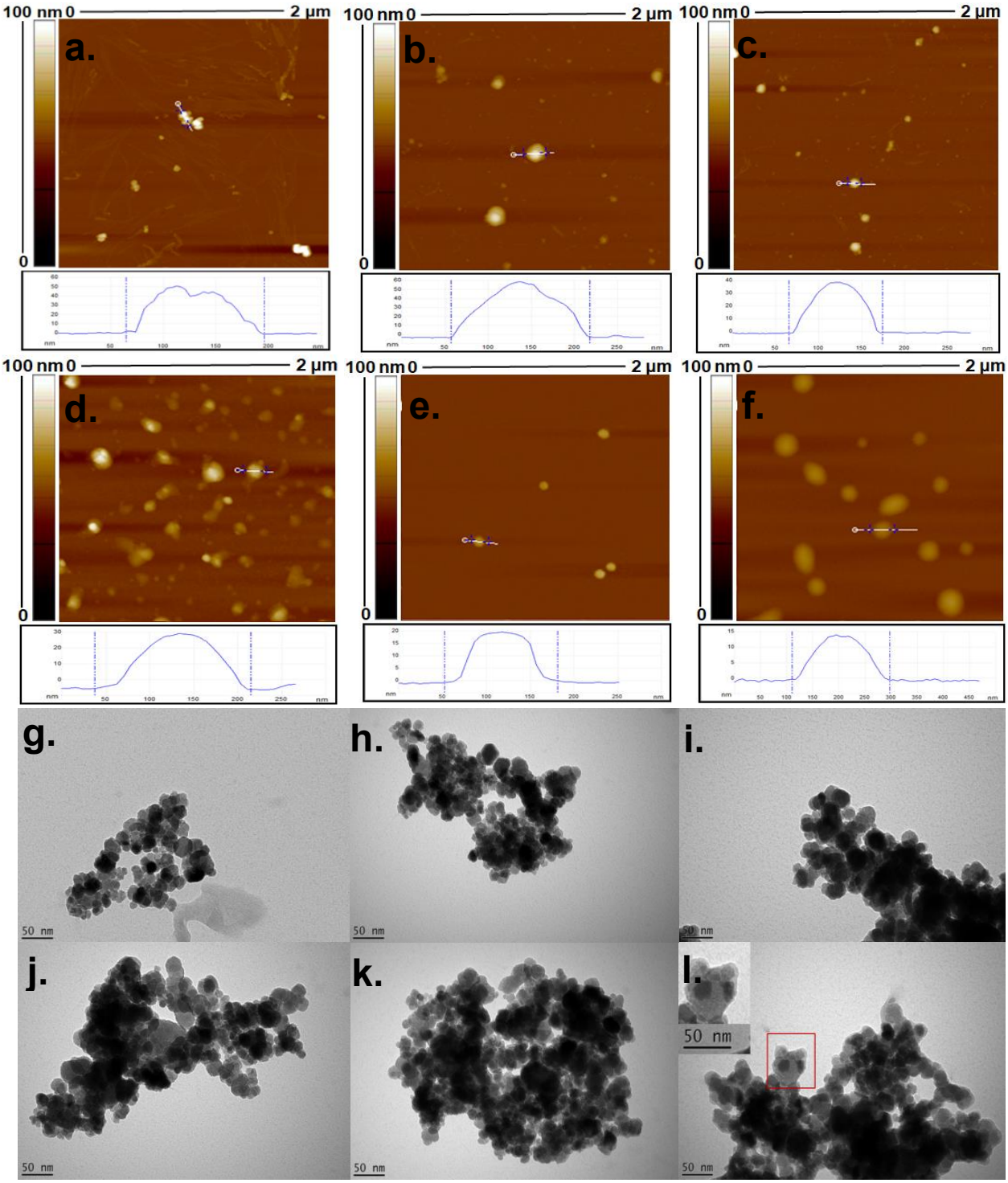


Fig. 4.3. AFM and TEM images of MAPs (a and g) and MACPs with the layer number of 1 (b and h), 4 (c and i), 5 (d and j), 8 (e and k) and 9 (f and l). Smaller particles were observed for MACPs with SA as the outermost layer.

As shown in Fig. 4.3a, particles with diameters around 140 nm were observed and exhibited rough surfaces, which were attributed to the aggregation of small solid MAPs. This finding is consistent with the MAPs size analysed by NTA. After alternate coating with SA and CHI, the resultant MACPs (Fig. 4.3b-f) exhibited more spherical shapes and smooth surfaces, which further confirmed the successful coating of both polymers. For MACPs, inter-digitation among the adjacent CHI / SA layers were constructed due to the existence of surface charges [233]. Therefore, after the removal of excess polymers, stable films were formed by soft polymers of CHI and SA leading to the smooth surface of MACPs.

Moreover, AFM images showed that MACPs with SA as the outermost layer (Fig. 4.3c&e) exhibited smaller sizes, which is consistent with the NTA measurements and confirmed the result that MACPs with SA as the outermost layer are more stable due to their lower zeta potential values. Characterisation of MAPs and MACPs via TEM revealed magnetic cores (dark areas) surrounded by polymer shells, which were the chitosan and alginate layers as shown in Fig. 4.3g-l. The inset in Fig. 4.3l is an enlarged section of the image clearly showing magnetic core particles and the surrounding CHI / SA layers.

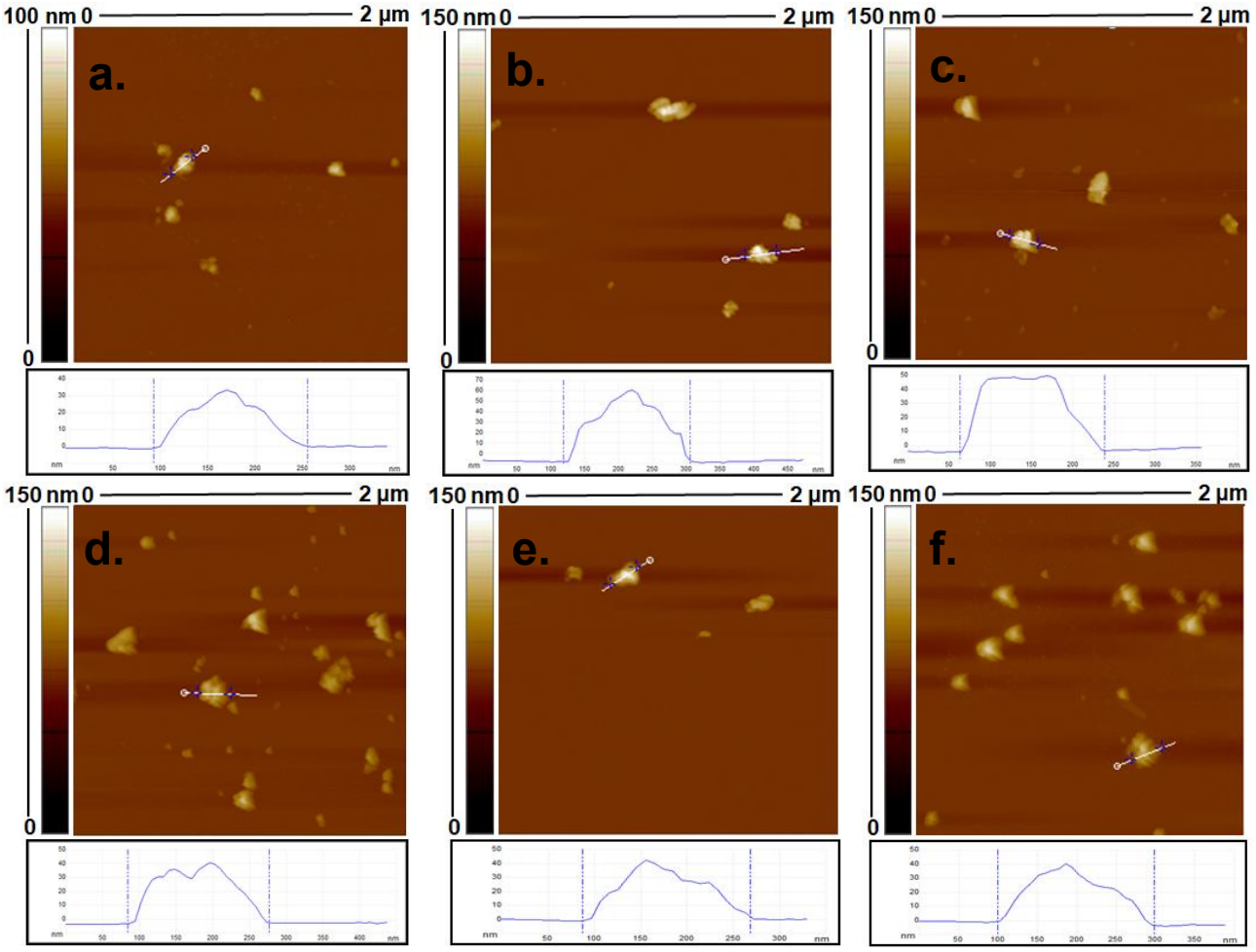


Fig. 4.4. AFM images of CUR loaded MAPs (a) and CUR loaded MACPs (CMACPs) with the layer number of 1 (b), 4 (c), 5 (d), 8 (e) and 9 (f).

AFM was also used to investigate the morphology of CMACPs. As shown in Fig. 4.4a, the diameter of CUR loaded MAPs was ~150 nm and increased as the polymer layer increased, reaching a maximum of ~200 nm for 9 layers (Fig. 4.4f), which is in agreement with the average size analysed by NTA as shown in Fig. 4.2b. However, rougher surface morphology was observed for CMACPs compared to MACPs as shown in Fig. 4.3. CUR is known as a highly hydrophobic drug [234-236] and the loading of CUR into MACPs increased the hydrophobicity of the particles. This meant that the particles rapidly dehydrated during AFM analysis and exhibited rough surfaces, indicating the successful loading of CUR into MACPs.

### 4.2.2. Loading and release of curcumin

CUR loaded MACPs were prepared by dispersing MACPs in CUR water / DMSO solution and incubated under stirring for 24 h. The addition of DMSO increases CUR solubility and its permeability into MACPs. The volume ratio of water : DMSO was 3:2, resulting in a homogeneous CUR solution (3 mg/ml) without sedimentation during the 24 h of incubation.[237] Fig. 4.5a clearly demonstrates that the resulting CMACPs can be collected with a Neodymium magnet while CUR itself in the bulk solution was not affected by the magnetic field. Therefore, MACPs can be potentially used for targeted delivery of CUR via external magnetic fields.

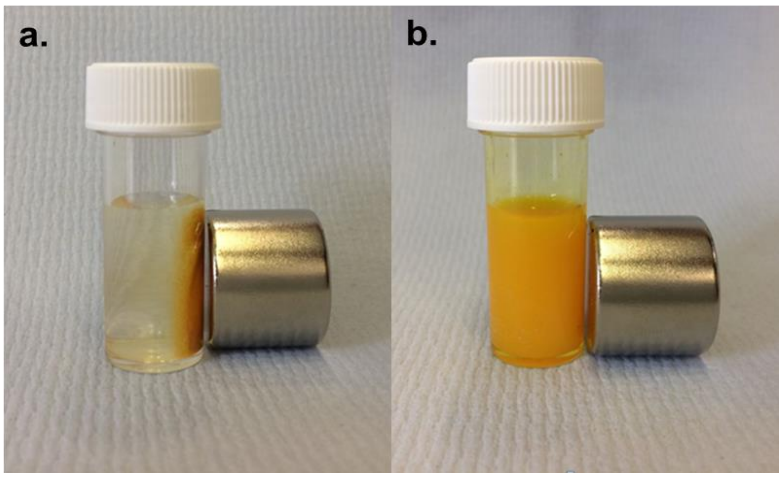


Fig. 4.5. CMACPs were prepared by suspending MACPs in CUR water / DMSO solution and incubating for 24 h under stirring. The resulting CMACPs can be rapidly collected by a Neodymium magnet (pull force 25 Kg, 25.4 mm diameter x 30 mm thick) within 1 min (a). The free CUR in solution on the other hand was not affected by the magnetic force (b).

Encapsulation efficiency results reveal that 49.2% of CUR was loaded into CMAPs and the encapsulation efficiency increased to 67.5% with increasing number of layers of CHI and SA (see Fig. 4.6a). For particles with the same type of polymer (CHI or SA) on the outermost surface an increased trend of encapsulation efficiency was observed with the increase of the layer number. However, as illustrated in Fig. 4.6a, a higher encapsulation efficiency of CUR was observed for

CMACPs with CHI as the outermost layer (layer number: 1, 3, 5, 7 and 9) compared to that use SA as the outermost layer (layer number: 2, 4, 6, 8, 10). The most feasible explanation for this is the different surface charges between the particle outermost layers. As illustrated in Fig. 4.2a, CHI layers exhibited positive surface charges in water while SA layers exhibited negative surface charges. Therefore, the negatively charged CUR molecules are adsorbed on the surface of the CHI layer more readily, facilitating a more efficient and faster encapsulation into polymer matrix. On the other hand, SA layer was negatively charged in water, and thus CUR molecules were less readily to interact with the negatively charged particle surface and enter the polymer matrixes due to the electrostatic repulsion. Moreover, larger amount of CUR molecules was expected on the surface of CHI layer, which also led to a higher encapsulation efficiency. The same hypothesis can be used to explain the loading efficiency of CMAPs and CMACPs. As shown in Fig. 4.6b, a higher loading efficiency of CUR was observed for MACPs with CHI as the outermost layer to those that possessed SA as the outermost layer. Higher loading efficiencies from 54.8% to 64.9% were achieved for CMAPs and CMACPs compared to many previously reported CUR loaded CHI and alginate based particles [26, 29, 90] with loading efficiencies from 2.7 % to 48 %, suggesting CMAPs and CMACPs possess great potential loading CUR into nanoparticles for drug delivery applications.

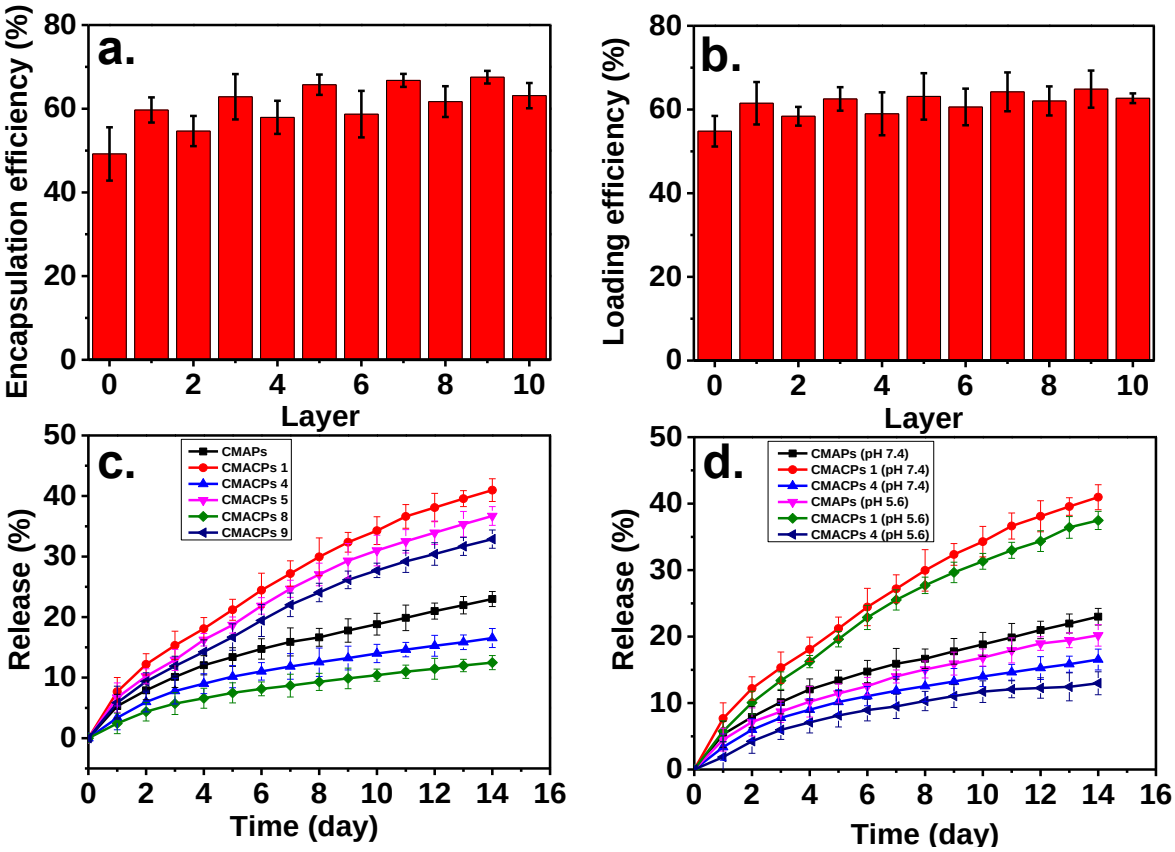


Fig. 4.6. The drug loading and release profiles of the CMAPs and CMACPs are affected by the type of outermost polymers and the number of layers. Encapsulation efficiency of CMAPs and CMACPs (a). Curcumin loading efficiency into CMAPs and CMACPs (b). Curcumin release profile of CMAPs and CMACPs with different layers (1, 4, 5, 8, 9) of deposited polymers (c). Curcumin release profile of CMAPs and CMACPs (layer number: 1&4) in PBS buffer at pH 7.4 and pH 5.6 (d). The results are shown in mean ± SD, n =3.

In order to investigate the release profile of CMAPs and CMACPs, 5 mg of particles were dispersed in 5 ml PBS buffer at pH 7.4 and incubated at 37 °C under shaking (200 rpm). The particles were collected with strong Neodymium magnets at predetermined time intervals and the CUR concentration in supernatants were analysed to obtain the accumulative CUR release profile. As shown in Fig. 4.6c, for all particles, CUR was released more rapidly within the first two days and then released slower but at more sustained rates in PBS for up to 2 weeks. The faster release in the first two days is most likely due to the loss of weakly adsorbed CUR molecules on the surface of the

particles or in the polymer matrix close to particle surfaces. The sustained CUR release after the first two days was then dependent on the diffusion of CUR molecules through the polymer matrixes into the bulk PBS solution, thus exhibiting a slower and more sustained release pattern. No significant burst release was observed during the whole release process most likely due to the poor solubility of hydrophobic CUR into aqueous solution [27, 238]. During drug release, CMACPs with CHI as the outermost layer exhibited a faster CUR release rate than CMAPs and CMACPs with SA as the outermost layer (CMACPs 4 and 8). As mentioned previously in Section 4.2.1.1, CHI is positively charged in water but negatively in phosphate solution due to the adsorption of negative phosphate ions [88], therefore more negatively charged CUR molecules are adsorbed onto the CHI layer surface when these particles were dispersed in CUR water / DMSO solution than on alginate, as illustrated in Fig. 4.6a&b. When CMACPs with layer numbers of 1, 5 and 9 were dispersed in PBS, phosphate ions competed with CUR molecules for the free amino groups on the CHI chains, which in turn facilitated the loss of CUR molecules from the surface of CHI and the diffusion of CUR from inner polymer matrix (where CUR concentration is higher) to the particle surface. Thus, faster CUR release rates were observed for CMACPs with layer numbers of 1, 5 and 9. On the other hand, CMAPs and CMACPs with layer numbers of 4 and 8, where alginate was deposited as the outermost layer, showed similar negative surface charges in water and phosphate solutions, less CUR molecules were adsorbed during the loading process and thus the drug release rate was not promoted in phosphate solutions. For particles with the same type of polymer, reduced release rates were observed as the number of layers increased (release rate: CMACPs 1 > CMACPs 5 > CMACPs 9, CMAPs > CMACPs 4 > CMACPs 8). By increasing the number of polymer layers, it was more difficult for the innermost CUR to permeate out. This is in agreement with previously reported data [214-216], where Chai *et al*. fabricated doxorubicin loaded poly (lactic-co-glycolic acid)

nanoparticles and layer-by-layer coated the particles with CHI and alginate [214]. After comparing the drug release rates of uncoated and polymer coated particles, the authors found that with the CHI / SA coating the initial drug burst release was reduced from 55.1% to 5.8% and the overall drug release rate was also reduced. In another example, Haidar *et al*. prepared bovine serum albumin loaded liposomes and layer-by-layer coated them with CHI / SA [215]. The polymer coated liposomes showed a reduced albumin release rate to the uncoated ones. Further to this, Zhou *et al*. developed polyethyleneimine coated PLGA nanoparticles and reported that the drug release rate reduced with increasing layers [216].

In order to investigate the drug release profile of CMAPs and CMACPs at different pH, CMAPs, CMACPs with 1 and 4 layers were dispersed in PBS at pH 7.4 and pH 5.6. As illustrated in Fig. 4.6d, the release pattern of CUR from particles at pH 5.6 was similar to those at pH 7.4 but slightly slower. In 14 days, about 23%, 41% and 17% of CUR were released from CMAPs, CMACPs 1 and CMACPs 4 at pH 7.4 respectively while about 20%, 37% and 13% of CUR were released at pH 5.6. This data are in agreement with previously published work by Martins *et al*. who investigated the release profiles of CUR from N-trimethyl chitosan / alginate complexes at pH 7.4 and pH 1.2 and reported that 80% of CUR was released at pH 7.4 within the first hour while only 22% of CUR was released at pH 1.2 [212]. The pH dependent release pattern can be attributed to the altered surface charge and hydrophobicity of polymers at different pH values.

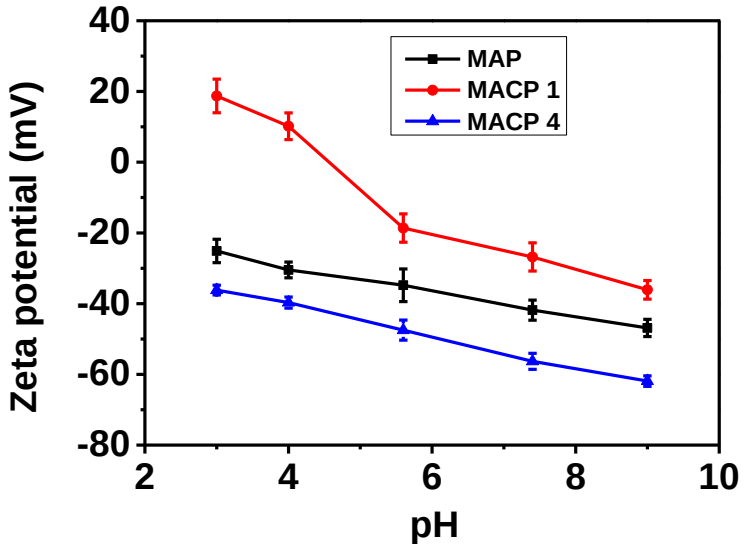


Fig. 4.7. Zeta potential of MAPs, MACPs 1 and MACPs 4 in sodium phosphate solution as a function of pH. Zeta potential of all the particles decreased as the increase of pH. MACPs 1 (with CHI outermost layer) exhibited higher zeta potential than MAPs and MACPs 4, which possess cross-linked or adsorbed SA as the outermost layer. MACPs 1&4 represent MACPs that possess 1&4 layers of polymers coated on MNPs respectively. The results are shown in mean ± SD, n = 3.

The zeta potential of MAPs, MACPs 1 and MACPs 4 in sodium phosphate solution as a function of pH is shown in Fig. 4.7. MACP1 showed positive surface charge under acidic conditions, (at pH ~ 4.3 and lower) this can be explained by the protonation of amino groups from the surface CHI on the particles [80]. In neutral and alkaline conditions the surface charge of MACPs 1 turned negative and an increased negative zeta potential was observed with increasing pH, due to the loss of protons from the amino groups [32]. Therefore, as the pH value of the solution decreased from pH 7.4 to 5.6, more amino groups were protonated and the consequential increased electrostatic interaction between CHI and CUR made the dissociation of CUR molecules more difficult. MAPs and MACPs with SA as the outermost layer showed negative surface charges from pH 3 to 9, however became less negative as the decrease of pH, which was due to the protonation of the carboxyl groups of alginate [224]. Thus, the less negatively charged alginate surface also made the dissociation of CUR

molecules more difficult. Moreover, as the decrease in pH, more protonated carboxyl groups from the alginate surfaces formed hydrogen bonds with each other, reducing the solubility of alginate layers [93]. Therefore, alginate surfaces became more hydrophobic with decreasing pH, which in turn restricted the release of CUR.

### 4.2.3. Cellular uptake assays

#### 4.2.3.1. CUR uptake assay by flow cytometry

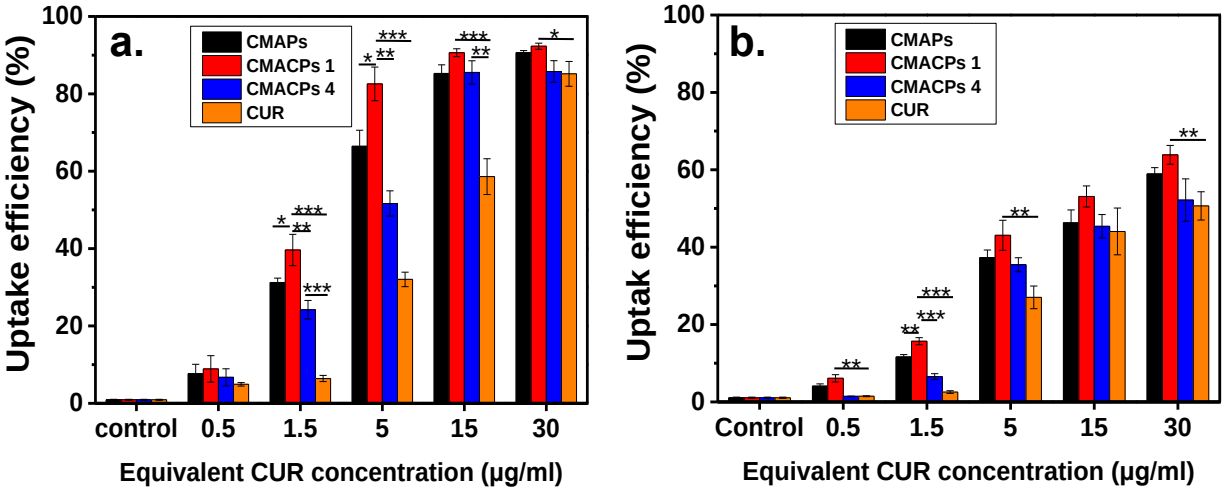


Fig. 4.8. Cellular uptake analysis of CUR in MDA-MB-231 cells (a) and HDF cells (b) after incubation with CMAPs, CMACPs 1&4 and free CUR for 24 h. The CUR uptake was analysed by flow cytometry. The dosages of CUR in particles were equivalent to the amounts of free CUR used. CMACPs 1&4 represent CMACPs that possess 1&4 layers of polymers coated on MNPs respectively. The results are shown in mean ± SD, n = 3. The statistical significance is expressed as *** $p < 0.001$, ** $p < 0.01$, * $p < 0.05$.

To investigate the cellular uptake kinetics of CMAPs and CMACPs, MDA-MB-231 breast cancer cells and HDF cells were incubated with free CUR and particles containing equivalent amount of CUR for 24 h. The resulting cells were analysed by flow cytometry to determine the cellular uptake of CUR by different cells. As shown in Fig. 4.8a, it is evident that the percentage of MDA-MB-231

cells that have taken up CUR was CUR dose dependent. Significant higher uptake efficiency was observed for MDA-MB-231 cells treated with CMAPs and CMACPs than those treated with free CUR, indicating that the nanoparticles can facilitate the CUR uptake. This is in agreement with previously reported data[3, 31, 239-241] that CUR uptake through nanoformulations is at least 2-3-fold greater than free CUR [3]. Here, at a CUR concentration of 1.5 μg/ml, an uptake efficiency of 31.2%, 39.6% and 24.2% was observed for MDA-MB-231 cells treated with CMAPs, CMACPs 1&4 respectively, which is 3-6-fold higher than the uptake efficiency of cells treated with free CUR. The increased CUR uptake of CMAPs can be attributed to the fact that the CUR loaded nanoparticles were more easily taken up by cells via endocytosis due to their smaller size (172 - 199 nm), while highly hydrophobic CUR was insoluble in aqueous solution forming larger aggregates, which are more difficult to be internalized by cells [240, 242]. The order of uptake efficiency of free CUR and CUR loaded particles was CMACPs 1 > CMAPs >CMACPs 4 > free CUR. Particles with CHI as the outermost layers exhibited the highest uptake efficiency (39.6 %). This result is in agreement with the work by Zhou *et al*. who compared the uptake efficiency of CHI / alginate coated poly (lactide-co-glycolide) nanoparticles and observed the uptake efficiency of particles with CHI as the outermost layers was higher than those having alginate as the outermost layer [213]. The promoted CUR uptake by the CHI surface is because of the protonated amino groups, which interact with the negatively charged cell surfaces and promote the accumulation of CMACPs 1 onto the surface of MDA-MB-231 cells. Fig. 4.8b shows the CUR uptake efficiency for HDF cells after being treated with free CUR and CUR loaded particles. HDF cells exhibited a similar uptake pattern but an overall much lower CUR uptake efficiency compared to MDA-MB-231 cells, suggesting CMAPs and CMACPs tend to target cancer cells rather than normal cells. This agrees with many previously published reports that the cancer cells normally exhibit higher uptake efficiencies of CUR and CUR

loaded nanoparticles than normal cells [29, 243-245]. Cancer cells possess a higher metabolic activity to normal cells and their surfaces tend to overexpress various receptors which in turn increase the available binding sites promoting the uptake of particles and drugs [246-248].

#### 4.2.3.2. Magnetically targeted delivery assay

To investigate the potential of CMAPs and CMACPs for magnetically targeted delivery of CUR, free CUR, CMAPs and CMACPs were incubated with MDA-MB-231 cells in glass bottom dishes. A Neodymium magnet was placed under the target area of the dish to allow for the accumulation of magnetic nanoparticles within the selected area. Taking advantage of the auto-fluorescent property of CUR, the confocal fluorescence images show the cellular uptake of CUR in and out of the target (magnet-affected) areas. The overall fluorescent intensity of MDA-MB-231 cells within the target areas that were treated with free CUR (Fig. 4.9a) was lower than cells treated with CUR loaded nanoparticles (Fig. 4.9c, e&g), suggesting CMAPs and CMACPs have enhanced the uptake of CUR. This result is consistent with the uptake efficiency shown in Fig. 4.8. No obvious difference on fluorescent intensities was observed between Fig. 4.9a and b, showing that the free CUR uptake is not affected by the presence of magnetic forces.

In contrast, cells treated with CMAPs (Fig. 4.9c), CMACPs 1 (Fig. 4.9e) and CMACPs 4 (Fig. 4.9g) within the magnet-affected area showed a significant increase of fluorescent intensity compared to the cells treated with same particles but outside of the target areas (Fig. 4.9d, f&h). The enhanced CUR uptake in the target areas was attributed to the accumulation of CUR loaded magnetic nanoparticles to the target areas driven by the magnetic force. On the other hand, the local concentration of CUR loaded magnetic particles outside the target areas was significantly lower, thus showing much lower fluorescent intensities. This result clearly shows that CMAPs and

CMACPs have the potential for targeted drug delivery.

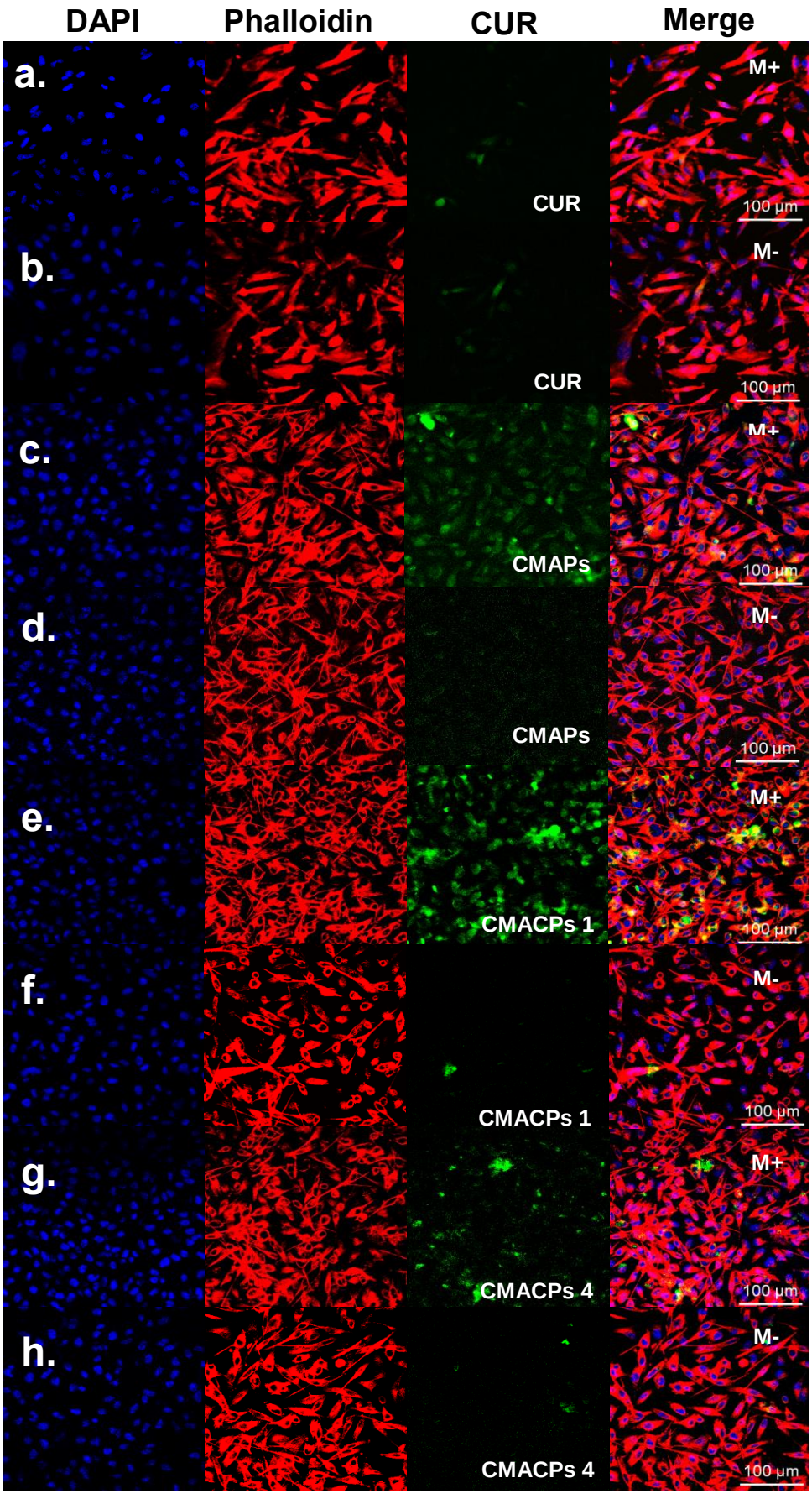

Fig. 4.9. Confocal fluorescence microscopy images of MDA-MB-231 cells incubated with free CUR (a&b), CMAPs (c&d), CMACPs 1 (e&f) and CMACPs 4 (g&h). CMACPs 1&4 represent CMACPs that possess 1 & 4 layers of polymers coated on MNPs respectively. CUR loaded particles contained equivalent amount of drug as free CUR (5 µg/ml). Cell nucleus and cytoskeleton were stained with DAPI (blue) and Alexa Fluor 568 Phalloidin (red). M+ denotes the images taken within the magnet affected target area and M- denotes the images taken outside of the magnet-affected area.

### 4.2.4. *In vitro* cytotoxicity assay

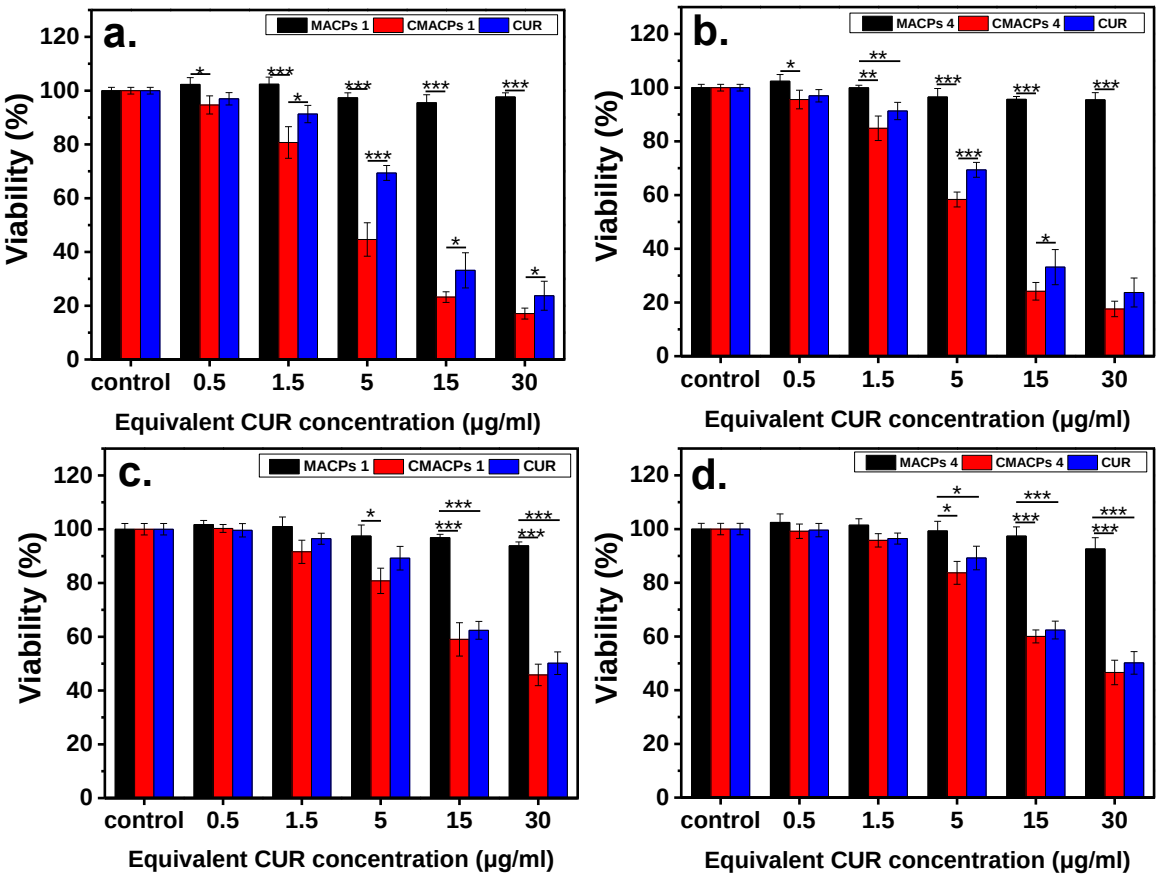


Fig. 4.10. The *in vitro* MTT assay suggested CMACPs exhibited significantly higher cytotoxicitytowards MDA-MB-231 breast cancer cells than HDF cells. MDA-MB-231 cells (a&b) and HDF cells (c&d) were treated with free CUR, CMACPs 1, CMACPs 4 and blank MACPs 1, MACPs 4 for 48 h. CMACPs 1&4 (or MACPs 1&4) represent CMACPs (or MACPs) that possess 1&4 layers of polymers, respectively. The amounts of CUR in CUR loaded nanoparticles were equivalent to the amounts of free CUR (0.5 - 30 µg/ml),

respectively. The results are shown in mean ± SD, n ≥ 3. The statistical significance is expressed as *** $p < 0.001$, ** $p < 0.01$, * $p < 0.05$.

In order to investigate the cytotoxicity of CMACPs towards cancer and normal cells, MDA-MB-231 breast cancer cells and HDF cells were incubated with free CUR, CMACPs 1, CMACPs 4 and blank MACPs for 48 h. The *in vitro* MTT assay results are shown in Fig. 4.10. It can be observed in Fig. 4.10a&b that both free CUR and CMACPs exhibited increased cytotoxicity towards MDA-MB-231 cells with increasing CUR concentration, which was in agreement with previously reported data that indicated CUR possesses dose dependent cytotoxicity towards cancer cells [3, 31, 239-241]. Both CMACPs 1 and 4 showed enhanced cytotoxicity towards MDA-MB-231 cells compared to free CUR, which can be attributed to the enhanced uptake of CMACPs. As discussed in Section 4.2.3.1, the uptake efficiency of MDA-MB-231 cells treated with CMACPs was 3-6-fold greater than those treated with free CUR. It is expected that the sustained release of CUR from internalized CMACPs maintained a high CUR concentration within the MDA-MB-231 cells, thus leading to lower viability of cells. CMACPs 1 were observed to exhibit higher cytotoxicity towards MDA-MB-231 cells than CMACPs 4, which was due to their higher CUR release rate (Fig. 4.6c) and uptake efficiency (Fig. 4.8a). As shown in Fig. 4.10c&d, the viability of HDF normal cells after treatment with free CUR and CMACPs was reduced at higher CUR concentrations (> 15 μg/ml) but significantly less affected at CUR concentrations less than 15 μg/ml compared to MDA-MB-231 cancer cells. This is in agreement with many previously studies, indicating CUR shows specific cytotoxicity towards cancer cells [29, 243-245]. One of the major accepted theories is that cancer cells possess lower glutathione levels than normal cells due to their reprogrammed metabolic pathways [30]. Depletion of glutathione, which is important for the sensitivity of cells to CUR can lead to the enhancement of CUR sensitivity of cancer cells [30, 243, 249]. In addition, most cancer cells, but not normal cells, express constitutively

active NF-KB that mediates their survival. CUR can suppress NF-KB regulated gene products, thus suppressing the proliferation of cancer cells [243, 250]. High viabilities were observed for both MDA-MB-231 cells and HDF cells after they were treated with blank MACPs, demonstrating that MACPs are non-toxic towards these cells.

## 4.3. Conclusions

MACPs were prepared by a layer-by-layer coating of CHI and SA onto the surface of $Fe_3O_4$ nanoparticles. The successful coating of CHI and SA was confirmed by the zeta potential and FTIR spectral measurements of the particles. Incorporation of CUR was confirmed by a change in surface charge and morphology of CMACPs. Meanwhile, the mean diameter of CMACPs was lower than 200 nm and within the optimum size range for drug delivery applications. *In vitro* drug release profiles illustrated the sustained release of CUR from CMACPs and indicated that it was possible to control the release rate by altering the outermost polymer (CHI or SA) as well as by changing the number of layers. More polymer layers resulted in a slower CUR drug release profile, where CHI as the outermost layer showed a faster CUR release. Confocal fluorescence microscopic images confirmed the successful internalization of CUR into MDA-MB-231 breast cancer cells and indicated that rapid and targeted delivery of CUR could be achieved by CMACPs in the presence of an external magnetic field. FACS analysis indicated the CMACPs mediated uptake of CUR by MDA-MB-231 cells was 3-6-fold greater than that of free CUR. MDA-MB-231 cancer cells showed a significantly higher uptake efficiency of CUR than that of HDF normal cells after being treated with CMACPs. The MTT assay indicated that CMACPs exhibited a significantly higher cytotoxicity towards MDA-MB-231 cancer cells than towards HDF cells. In summary, the sustained release profiles, enhanced uptake efficiency and strong cytotoxicity to cancer cells as well as the potential for targeted delivery make MACPs a promising candidate for anti-cancer drug delivery.

# 5. Magnetic-Silk Fibroin / Polyethyleneimine Core-Shell Nanoparticles as Potential Carriers for Cell Transfection


## Abstract

Gene therapy is a promising method for disease treatment. Despite the recent advances, the lack of efficient methods significantly hindered the applications. Polyethyleneimine (PEI) is one of the most efficient non-viral gene delivery agents due to its high cationic charge density and is capable of condensing DNA into nano-sized complexes. However, the high cytotoxicity and lack of targeting have limited its application. In this paper, silk fibroin (SF), a biocompatible and biodegradable protein, was selected to fabricate magnetic-silk / PEI core-shell nanoparticles (MSPPs) and silk-PEI nanoparticles (SPPs) for the delivery of c-myc antisense oligodeoxynucleotides (ODNs) into MDA-MB-231 breast cancer cells. The size and zeta potential of the particles can be controlled by altering the amount of silk fibroin in particle synthesis. Lower surface charges and reduced cytotoxicity were observed for MSPPs compared to PEI coated magnetic nanoparticles (MPPs). Both MSPPs and SPPs were capable of delivering the ODNs into MDA-MB-231 cells and significantly inhibiting the cell growth. With magnetofection, high ODN uptake efficiencies (over 70%) were achieved within 20 min using MSPPs as carriers, exhibiting a significantly enhanced uptake effect compared to the same carriers via non-magnetofection. Both MSPPs and SPPs exhibited higher inhibition effect against MDA-MB-231 breast cancer cells compared to human dermal fibroblast (HDF). Targeted ODN delivery can be achieved using MSPPs with the help of a magnet, making them promising candidates for gene therapy applications.



**Keywords:** Silk, PEI, Magnetic nanoparticles, Gene delivery, Cancer, ODN, Magnetofection


**Abbreviations:**

PEI: polyethyleneimine

SF: silk fibroin

ODN: c-myc antisense oligodeoxynucleotide

HDF: human dermal fibroblasts

MNPs: magnetic nanoparticles

SPPs: silk-PEI nanoparticles

MPPs: PEI coated magnetic nanoparticles

SPPs: silk-PEI nanoparticles

MSPPs: magnetic-silk / PEI core-shell nanoparticles

SPP50: SPPs with 50% of SF

MSPP50: MSPPs with 50% of SF

SPP75: SPPs with 75% of SF

MSPP75: MSPPs with 75% of SF

SPP90: SPPs with 90% of SF

MSPP90: MSPPs with 90% of SF

## 5.1. Introduction

Gene therapy has shown great potential in curing many diseases originating from defective genes [67, 251-252]. Efficient gene therapy demands the delivery of genes to the cell nucleus or cytoplasm replacing or silencing the defective genes [252]. However, genes will have to overcome several intracellular barriers such as cell membrane and endosome membrane [253-254]. Therefore, carriers are needed for the efficient gene delivery [252].

Many gene delivery vectors have been developed including viral and non-viral delivery systems [143, 255-256]. Although viral carriers are known as the most effective gene vectors [252], the application of viral gene delivery systems has been limited by their potential toxicity and immunogenicity concerns [41, 255, 257]. Therefore, non-viral gene delivery systems have been explored as an alternative tool for gene therapy [41, 67, 252]. Apart from non-immunogenicity, non-viral gene delivery systems also

possess advantages including low cost, ease of fabrication and modification and high *in vivo* stability [67]. A variety of non-viral vectors have been developed [41, 258-259]. One of the most efficient non-viral transfection agents is polyethyleneimine (PEI) [41-45]. Once mixed with DNA, PEI will condense them into nanoparticles that are suitable for the internalization into cells through endocytosis [143, 252]. In addition, PEI is able to destabilize the endosomal membrane by the 'proton sponge effect' to protect DNA against degradation and facilitate the release of DNA from endosomes into the cytoplasm [42-43, 143, 252]. Despite its high transfection efficiency, the applications of PEI are still limited by its inherent problems such as high cytotoxicity and lack of targeting [44]. Attempts have been made to improve targeting by developing PEI coated magnetic nanoparticles (MPPs) for gene delivery through a process called 'magnetofection' [67, 252], in which an external magnetic field was used to enhance the transfection efficiencies by rapidly concentrating the magnetic vectors on the cell surface [142]. Moreover, it has been reported that the cytotoxicity of MPPs vectors is lower than that of PEI [143].

However, MPPs still possess significant cytotoxic effects and lead to a decreased viability to many cell lines [260-263]. Hoskins *et al*. investigated this by exposing MCF-7, SH-SY5Y and U937 cells to 100 μg/ml of MPPs and observed cell viability decreased to 50%, 70% and 80% respectively after a 24 h incubation [260]. When the incubation time was increased to 7 days, the cell viability of these cells decreased to 20%, 10% and 30% respectively [260]. To further reduce the cytotoxicity of MPPs, various approaches have been investigated [260-263]. Hoskins *et al*. reported that MCF-7, SH-SY5Y and U937 cells exhibited viabilities over 95% after 24 h incubating with MPPs-PEG and around 90% after 7 days [260]. Strojan *et al.* fabricated glutathione modified PEI coated magnetic nanoparticles (GSH NPs) by adding glutathione during nanoparticle synthesis and reported that glutathione reduced 30% cytotoxic effects to CHO cells and decreased observed oxidative stress response

compared to standard formulation [262]. Another example is Du *et al*., where PEI was modified with lactose at different lactosylation degrees (6.8% and 11.7%) and then coated onto magnetic nanoparticles (MNPs) [263]. The resulting lactose modified MPPs showed reduced cytotoxicity to RAW 264.7 cells compared with unmodified MPPs.

In this work, silk fibroin (SF) was used to reduce the cytotoxicity of MPPs. SF protein from cocoons of *Bombyx mori* is an FDA approved, natural derived material which has been widely used to form various biomaterials including gels, sponges and films for different medical applications such as drug delivery, tissue engineering and wound dressing [64]. Excellent biocompatibility [180], tuneable biodegradability [181] and easy processing [64] of SF has made it a promising biomaterial for drug and gene delivery systems [64, 140, 264-266]. For example , *Antheraea pernyi* silk fibroin (ASF) / PEI / DNA ternary complexes were fabricated by Liu *et al.* by coating PEI / DNA complexes with ASF [140]. Cell viabilities of HEK 293 and HCT 116 cells incubated for 24 h with ASF / PEI / DNA complexes were over 10% higher than those incubated with PEI / DNA complexes. Yu *et al.* synthesized cationized ASF (CASF) nanoparticles by modifying ASF with spermine and suggested that CASF is a potential gene delivery carrier with the advantages of low cytotoxicity and biocompatibility [264]. Although with great potential to be modified or in combination with other transfection agents to form gene delivery carriers with reduced cytotoxicity, the fabrication of magnetic-silk fibroin / polyethyleneimine core-shell nanoparticles (MSPPs) and their performance as gene delivery carriers through magnetofection has not yet been sufficiently reported. Therefore, in this study, MSPPs and SF-polyethyleneimine nanoparticles (SPPs) were fabricated for the transfection of c-myc antisense oligodeoxynucleotides (ODNs) into MDA-MB-231 breast cancer cells and human dermal fibroblast (HDF) cells. The size and zeta potential of SPPs and MSPPs with different SF percentages were analysed with DLS. The morphologies of naked ODNs, MPPs, SPPs, MSPPs, and MSPP-ODN

complexes were determined by AFM. TEM was also used to analyse the morphologies of MPPs, SPPs and MSPPs. Toxicities of MSPPs with different SF percentages and the growth inhibition effects using their ODN complexes against MDA-MB-231 cells and HDF cells were determined through the MTT assay. The uptake profiles of SPP-ODN and MSPP-ODN complexes were investigated by flow cytometry and the localizations of ODNs in MDA-MB-231 cells after treatment with naked ODNs and different transfection complexes were determined by confocal microscopy.

## 5.2. Results and discussion

### 5.2.1. Characterization of silk-polyethyleneimine and magnetic-silk / polyethyleneimine nanoparticles

#### 5.2.1.1. Size, zeta potential and morphology of silk-polyethyleneimine nanoparticles

SF forms aggregates in salt solutions such as sodium phosphate. The salting out associated aggregation of SF in high concentration salt solutions is resulted from the adsorption of counterions to the SF peptides, leading to reduction of their net surface charge. During salting-out, micellar-like structures are first formed due to the enhancement of hydrophobic interactions between SF protein chains, followed by further aggregation and finally particulate SF globules [79].

The addition of salt can also be used to induce the aggregation of PEI [267]. PEI is a cationic polymer with hydrophobic backbones and closely-spaced amines making PEI a highly positive charged polymer [267]. The intra-chain repulsion caused by the amine groups on the same chain keeps the polymer from aggregating [267]. If the charge on the hydrophobic chains is insufficient e.g. by increasing salt concentration, the hydrophobic backbones will collapse and form aggregates [268-269].

Adding a small amount of salt into PEI solution increases the PEI solubility and prevents its aggregations due to the fact that the attractive interactions between hydrophobic chains are counterbalanced by the electrostatic repulsion at low ionic strength [267]. The solubility of PEI reached a maximum at 150 mM NaCl concentration. Further increasing the salt concentration resulted in the salt screening the electrostatic repulsion therefore decreasing intra-chain repulsion, resulting in PEI aggregations via hydrophobic interactions [267].

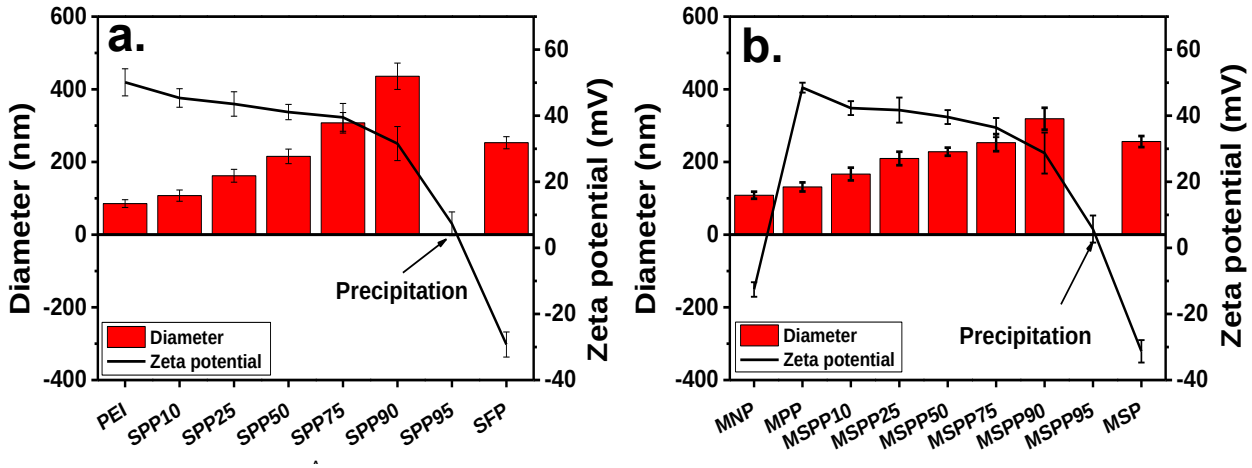


Fig. 5.1. Effect of SF (5 mg/ml) / PEI (5 mg/ml) ratio on the size and zeta potential of SPPs (a), and MSPPs (b). The increase of SF ratio resulted in the increase of the size of SPPs and MSPPs also resulted in the decrease of the zeta potential of SPPs and MSPPs. The results are shown in mean ± SD, $n \geq 3$.

PEI particles were prepared by adding PEI solution (5 mg/ml) into sodium phosphate solution (pH 8) at an ionic strength of 1.25 M. After an incubation time of 6 h at room temperature aggregations were observed. The particle size was then analysed using DLS as shown in Fig. 5.1a, which indicated that the mean diameter of PEI particles was 85 nm. The addition of different ratios of SF into the PEI solution resulted in the increasing of particle size (Fig. 5.1a). Increasing the SF ratio leads to accelerated aggregation of SPPs as well as increased particle yield. When using a mixture containing 90% SF (5 mg/ml) and 10% PEI (5 mg/ml), the SPP aggregation was almost immediate

upon added into salt solution. As shown in Fig. 5.1a, the size of SPPs increased from 107 to 436 nm when increasing SF content from 10% to 90%.

This phenomenon is most likely due to the inter-chain attractions between positively charged PEI chains and negatively charged SF chains. When a small amount of SF was added to PEI solutions, negative SF chains were attracted and electrostatically bound to positive PEI chains, weakening the charge density of PEI chains. With increasing amount of SF, PEI chains are neutralized and the backbone charge becomes insufficient to keep the molecules extended after the mixtures being added into salt solutions [267]. This is supported by the SPPs zeta potential measurements (shown in Fig. 5.1a), where the zeta potential decreases with increasing SF content. A zeta potential of +50 mV was observed for PEI particles. The strong electrostatic repulsions among PEI particles therefore resulted in small particles (85 nm). An addition of 10% SF in PEI solution reduced the zeta potential of SPPs to +45 mV, increasing the mean particle diameter to 107 nm (Fig. 5.1a). Further increasing the SF content lead to lower zeta potentials and larger SPP particle sizes, where 90% SF resulted in a zeta potential of +32 mV. At 95% SF content the SPPs were almost electroneutral (zeta potential: +7.3 mV) and large amount of precipitate was observed. The changes of particle size and zeta potential dependent on the SF/PEI ratio give strong indication of hybrid particle formation.

In addition to DLS analysis the size and morphology of SPPs were also determined using AFM. As shown in Fig. 5.2a-f, spherical particles with smooth surfaces were observed. PEI-only particles (Fig. 5.2a) showed diameters ~ 80 nm, in contrast to SPPs, where particles with diameters of over 400 nm were observed for the highest SF content (90%, Fig. 5.2f), which is consistent with the particle sizes given by DLS.

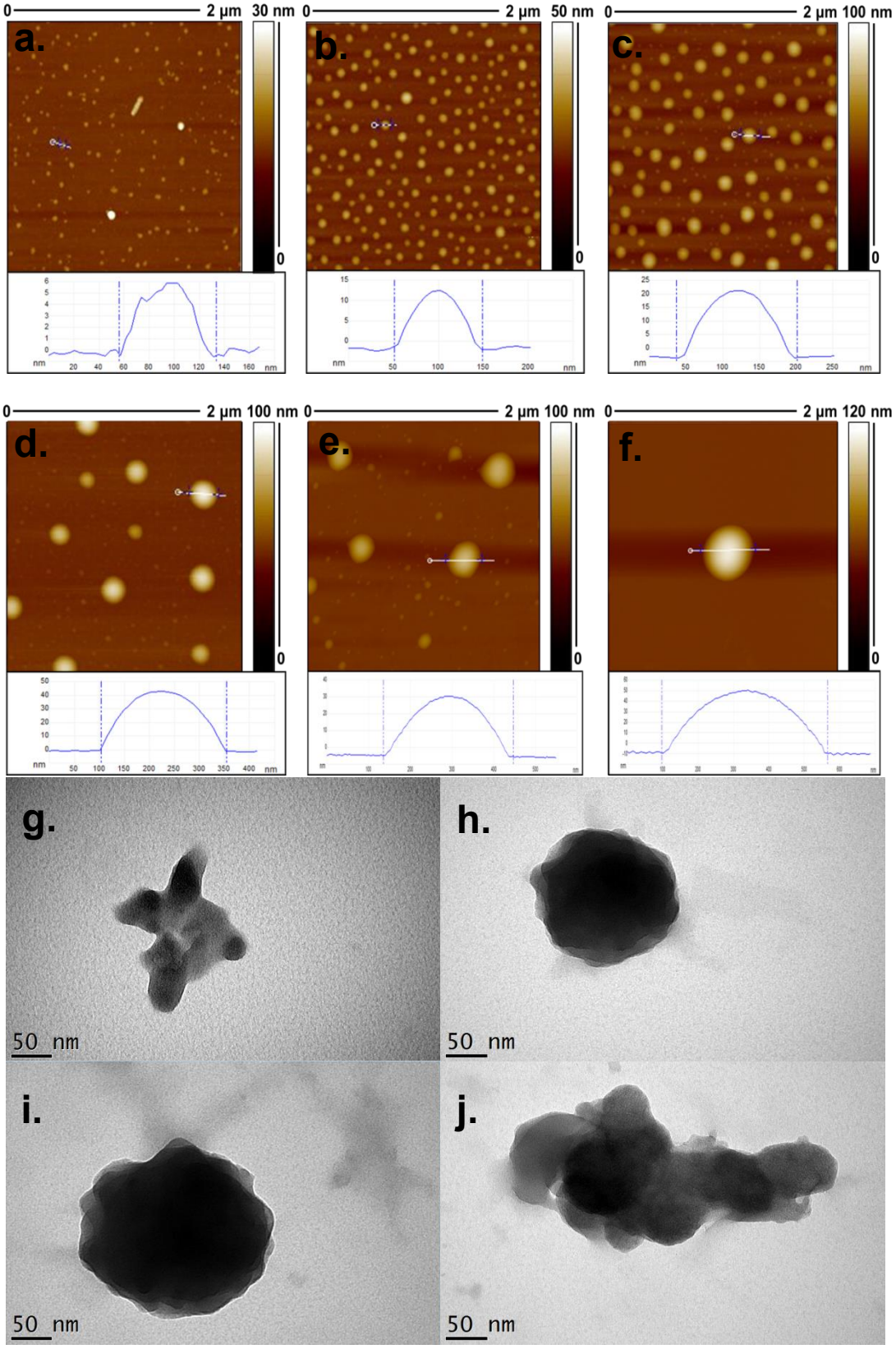


Fig. 5.2. AFM and TEM images of the PEI particles (a&g) and SPPs (b-j) with different amount of SF: 10% (b), 25% (c), 50% (d&h), 75% (e&i) and 90% (f&j).

In order to reveal the structures of the SPPs, TEM analysis was undertaken. Fig. 5.2g shows small

PEI particles with diameters of ~30 nm aggregated to form larger particles (~100 nm). The structures of SPPs with 50%, 75% and 90% of SF are shown in Fig. 5.2h, i&j, respectively. Increasing diameters of ~200 nm, ~260 nm and ~400 nm were observed from these particles respectively, which was consistent with the results given by DLS and AFM. SPPs with 90% of SF (SPP90) shown in Fig. 5.2j clearly show that the particle formed by the aggregation of many smaller particles with diameters ranging from 30 – 100 nm, confirming that increasing SF content resulted in lower surface charge and lead to particle aggregation.

#### 5.2.1.2. Size, zeta potential and morphology of magnetic-silk / polyethyleneimine nanoparticles

MPPs were fabricated by adding PEI (5 mg/ml) to MNPs suspended in sodium phosphate solution. Zeta potential measurements of MNPs revealed negative charges of -12.6 mV and high positive charges of +48.5 mV for MPPs (see Fig. 5.1b), which is in agreement with previously published data by Wang *et al.* and Zhao *et al.* [143,270]. These measurements strongly suggest that negatively charged MNPs have been coated with positive PEI molecules, where PEI molecules would first adsorb onto the surface of MNPs through electrostatic attractions and Van der Waals forces [271] before aggregating and entirely covering the MNP in the final salt solutions [267]. DLS measurements of MNPs revealed average particle diameters of 109 nm and increased to 131 nm after PEI coating (see Fig. 5.1b) , similar to the results reported by Ota *et al.* previously. [61]

The particles were further characterised by AFM to investigate the morphologies of MNPs, MPPs and MSPPs. AFM revealed that the MNPs exhibited rough surfaces with particle sizes ranging between 10 - 30 nm (Fig. 5.3a), while MPPs were ~ 110 nm in diameter as well as showing

smoother surface morphologies (Fig. 5.3b) supporting the conclusion that the MNP surfaces were coated with PEI polymers. It has to be note that MNPs size measurements with AFM show a significantly smaller particle size than DLS measurement, which is most likely due to MNP particle aggregation occurred in the suspensions during the DLS measurement. Further to this, TEM analysis of MPPs reveals a core-shell type structure as shown in Fig. 5.3g. The core phase consisted of $Fe_3O_4$ nanoparticles, represented by the dark regions of the image compared to the shells structure of PEI polymer in grey. TEM images clearly revealed (Fig. 5.3g) that smaller MPPs of the order of ~20 nm aggregated and formed larger aggregated particles of ~100 nm in diameter, consistent with the AFM data. Steitz *et al*. previously reported that coating with PEI polymers can bridge two or more particles together and form larger aggregations through Van der Waals forces [272]. On the other hand, MPPs are strongly positively charged due to a large amount of amine groups in PEI, resulting in strong electrostatic repulsions among MPPs and thus enabling better dispersion of these particles. The balance between Van der Waals forces and electrostatic repulsions resulted in such aggregate size of MPPs. Any change to the electrostatic charges on the surface of the polymer will however change this and lead to different aggregate sizes.

Further to the synthesis of MPPs above, the PEI (5 mg/ml) was mixed with different ratios of SF (5 mg/ml) before they were coated onto MNPs. The resulting particle sizes and zeta potentials measured (by DLS) were also shown in Fig. 5.1b. The mixed polymer shell of SF and PEI resulted in different surface charges and aggregation sizes of MSPPs. The addition of SF reduced the zeta potential of MSPPs compared with MPPs indicating negatively charged SF and positively charged PEI had co-aggregated on the surface of MNPs. By altering the SF / PEI ratio both particle size and zeta potential are controllable as shown in Fig. 5.1b. For example, 10% of SF in PEI resulted in a decreased zeta potential of +42 mV and an increased average diameter of 167 nm for MSPPs.

Increasing the SF to 90% resulted in even lower zeta potential (+29 mV) and larger particle diameter (319 nm). The increased aggregate size can be explained by reduced electrostatic repulsions between particles, causing MSPPs to form aggregates through Van der Waals forces more readily. At a SF content of 95% a near neutral sample was produced having a zeta potential of +5.7 mV with almost all the particles precipitated out, suggesting there was insufficient electrostatic repulsion between particles to keep them from aggregating.

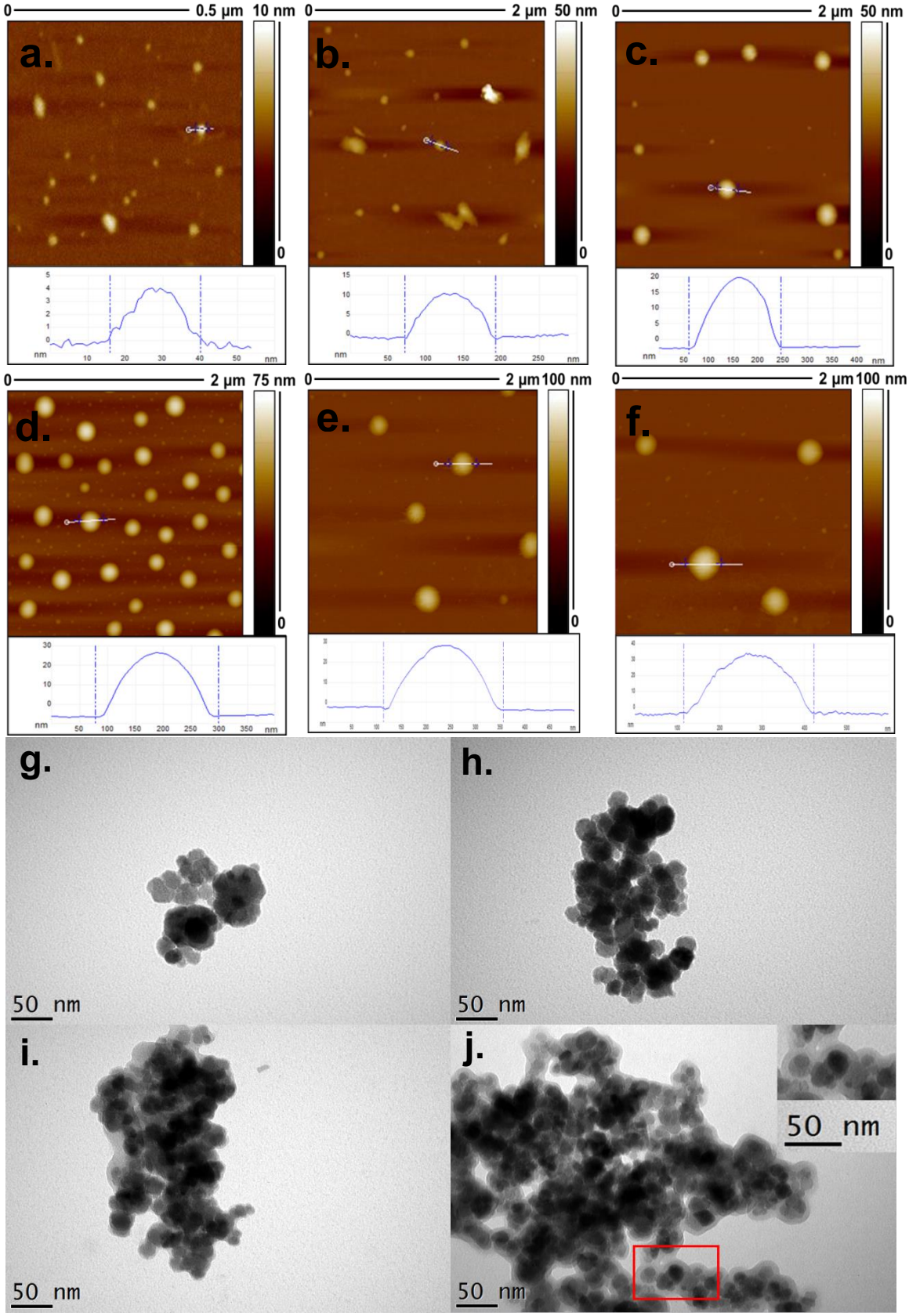


Fig. 5.3. AFM and TEM images of the MNPs (a), MPPs (b&g), and MSPPs with 10% (c), 50% (d&h), 75% (e&i), and 90% (f&j) of SF.

Morphologies of MSPPs were analyzed by AFM and TEM. As shown in Fig. 5.3c-f, the size of MSPPs increased with increasing SF content, which is consistent with measurements by DLS. Spherical and smooth particles were observed, suggesting the surfaces of MNPs were coated by SF-PEI polymer mixture. Similar to SPPs, AFM images for MSPPs revealed smaller particles around larger ones (Fig. 5.3c-f), suggesting the large particles were aggregations of small MSPPs. TEM images of MSPPs (at 50%, 75% and 90%) shown in Fig. 5.3h-j reveal that MSPPs were formed by multiple $Fe_3O_4$ cores covered by SF-PEI shells. The inset in Fig. 5.3j is an enlarged section of the image (red boxed area). Altering the SF content did not show any effect on the size of the smaller core-shell magnetic nanoparticles which is consistently around 20 nm in diameter. However, the increased SF percentage resulted in larger aggregates supporting the previous AFM and DLS data.

Finally, it is worth to note that positive zeta potential in excess of +28 mV were observed even at low PEI contents (10%) in SF-PEI mixtures. This is due to the high charge density of PEI [273]. This phenomenon is favorable for the fabrication of low toxic cationic carriers for DNA transfection. DNA is able to adsorb onto the carrier surface via electrostatic attractions between negatively charged DNA and positively charged carriers, demonstrating the importance of positive charges for DNA adsorption [67, 272]. PEI, as a highly positively charged polymer is known to be efficient for DNA transfection [61, 143, 274], however it is also known to have a high toxicity to cells [275] making PEI generally less favorable. Therefore, a PEI-based transfection carrier system with reduced PEI content but sufficient positive charges is beneficial for transferring DNAs into nucleus while exhibiting much lower toxicity during transfection.

### 5.2.2. Interaction of magnetic-silk fibroin / polyethyleneimine nanoparticles with c-myc antisense oligodeoxynucleotides.

For successful gene transfection, vectors are normally required to condense the DNAs [111-112, 276]. The mechanisms by which DNAs form complexes with transfection vectors has been reported and morphologies of the complexes have been previously characterized by AFM [270, 276-278]. Single stranded ODNs are different to plasmids and long linear DNAs in both molecular weight and topography which may result in different pathways in condensation and forming complexes [279]. It is therefore important to investigate the formation of MSPP-ODN complexes and their assembly mechanism. The morphologies of naked ODNs and the resulting complexes were characterized by AFM. For the naked ODN, spherical structures with diameters ranging from 30 to 40 nm and heights of 2 to 3 nm were observed (see Fig. 5.4a), similar to the ODN self-assembled structures previously reported by Costa *et al.* [280]. Nanowires were also observed, similar to the ones reported by Maria *et al*., having lengths of over 500 nm and heights ranging from 2.5 to 3.5 nm (Fig. 5.4a) [281]. As the ODNs used in this research are small, single stranded human c-myc antisense ODNs made up of only 15 nucleotides (15-nt) in length (5'-AAC-GTT-GAG-GGG-CAT-3'), the large scaled nanostructure is most likely to be a higher order structure of self-assembled ODNs [279-282]. The self-assembly of guanine (G) rich ODNs into higher order nanostructures such as networks and long nanowires [281] has been previously reported [279-282].

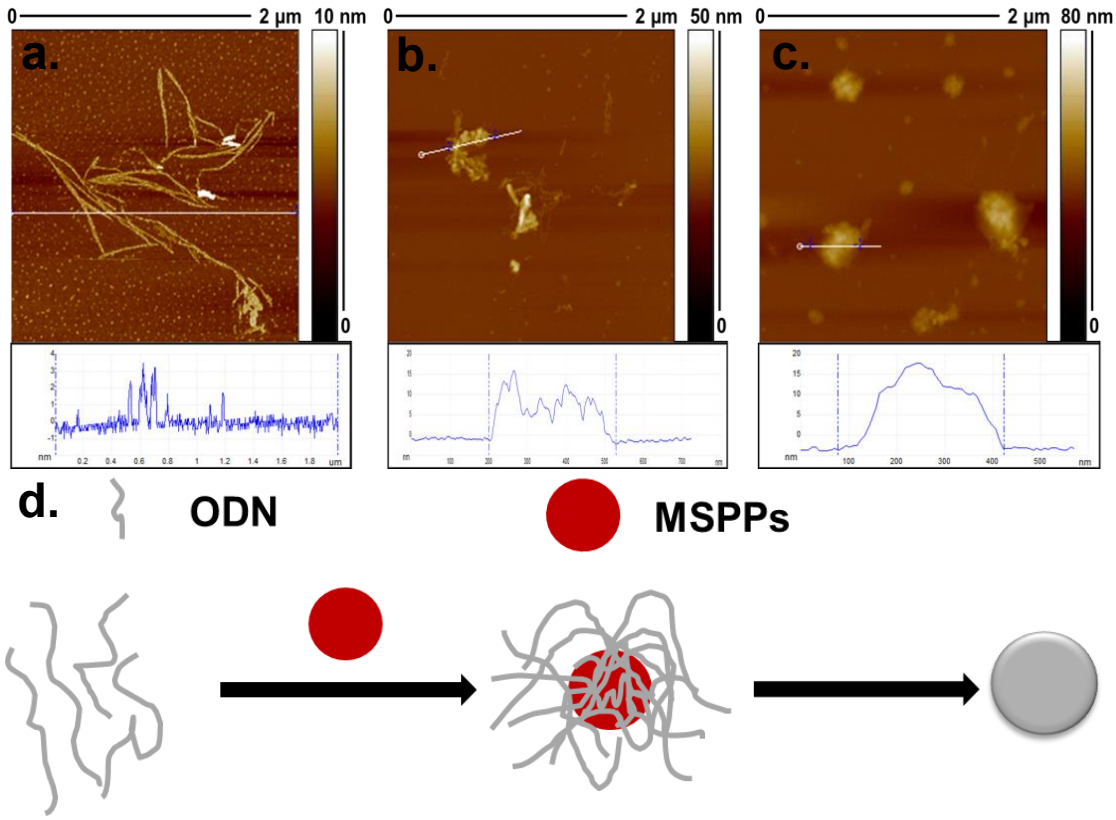


Fig. 5.4. AFM images of ODNs (a) and MSPP90-ODN complexes (b&c). The AFM images were taken after 30 s (b) and 30 min (c) condensation respectively. MSPP90/ODN mass ratio was fixed at 12:1. (d) Schematic representation of the possible mechanism for the condensation of ODNs by MSPPs. ODN chains wrapped around the MSPPs to form spheroidal MSPP-ODN complexes.

Fig. 5.4b&c are representative AFM images of ODNs that were mixed under gentle shaking with MSPPs with 90% SF (MSPP90) at a mass ratio of 12:1 after 30 s (b) and 30 min (c) condensation time. After 30 s, condensed nanofibre-like structures and aggregations of nanowires were observed (Fig. 5.4b), similar to the nanostructures reported by Chen *et al*. who mixed a 21-nt ODN with polypropyleneimine (PPI) followed by a 10 min condensation time [279]. The height of the condensed nanofibres ranged from 2 to 15 nm and diameters of aggregated structures from 80 to 300 nm, suggesting that the free ODNs were condensed by MSPP90. After 30 min condensation time well-condensed MSPP-ODN complexes were formed as shown in Fig. 5.4c, consisting of spheroidal particles with diameters of 100 nm to 350 nm and heights ranging from 10 to 20 nm.

Rough surfaces morphologies were observed as a result of ODN complexation on particle surfaces. Comparable spheroidal condensates have also been reported in previous studies [276-280]. Chen *et al*. analysed the condensates of PPI-ODN, and also observed similar nanofibre-shaped structures at the early stages of condensation and spheroidal particles after long term condensation time [279]. They suggested that the PPI was acting like a 'zipper' in the condensation process. At early stage, the PPI electrostatically interacted with phosphate groups from different ODN chains and helped form end-to-end ODN chains. Dendrimers were then formed by those ODN chains and further aggregated to form nanofibres. Finally the nanofibres interacted with each other and formed spheroidal particles by multi-molecular associations [279]. In our case, ODNs were most likely interacted with MSPPs through electrostatic attractions and produce nanofibres during the initial condensation process Fig. 5.4d. At longer condensation times (30 min), ODN chains tightly wrapped around the MSPPs and spheroidal MSPP-ODN complexes were formed.

### 5.2.3. *In vitro* cytotoxicity assay

#### 5.2.3.1. Inhibition effect of MSPPs and MSPPs-ODN on MDA-MB-231 cells

C-myc oncogene is an evolutionarily conserved gene expressed in many cell types including MDA-MB-231 breast cancer cells [283]. It is often associated with many essential biological processes including cell growth, proliferation, transformation and apoptosis [283-284]. Disordered expression of the c-myc gene will lead to malignant transformation of cells [283]. Down regulation of the expression of c-myc by exposing the cancer cells to c-myc antisense ODN has been reported to be able to inhibit cancer cell growth [283, 285-286]. c-myc antisense ODN is a single-stranded nucleic acid designed to specifically bind to the target mRNA through the Watson-Crick base pair complementarity to form

duplexes [287]. This therefore blocks the translation of the target gene or alternatively, the RNase H can be activated to digest the specific mRNA [251, 287]. High efficacy was expected for antisense ODNs due to its specificity to target mRNAs [287]. However, the application of c-myc antisense ODNs is limited by major hurdles such as poor delivery and cellular uptake of naked ODNs into the target tissue along with their poor *in vivo* stability [251, 287-289]. The inherent hydrophilicity and negative charges of ODNs make it very difficult for them to approach and cross the hydrophobic cell membranes into the cytoplasm or nucleus [290]. Therefore, large amount of ODNs and long incubation times are needed for the observation of any cell growth inhibition effect when the cells are treated with naked ODN [285-286, 291]. For example, in the study by Watson *et al.,* 4 days were required for the observation of initial inhibition for MDA-MB-231 cells exposed to 5 μM c-myc antisense ODN [286]. In another study, Leonetti *et al*. added 100 μg/ml c-myc antisense ODN to M14 cells and only after 4 days growth inhibition could be observed [285]. These illustrate the need for efficient transfection systems for antisense gene delivery to solve the above problems [292]. Various vectors have previously been developed and have shown improved inhibition efficiency at lower ODN dosages [251, 292-294]. However, it is clear that vast improvement is still needed for efficient systems.

In this study, the MTT assay was used to assess the growth inhibition effect of MSPP-ODN and SPP-ODN complexes on MDA-MB-231 and HDF cells. MDA-MB-231 cells were incubated with MPP-ODN, MSPP (50-90% SF)-ODN and SPP90-ODN in serum-free medium for 4 h with naked ODN as a negative control. The MPPs, MSPPs and SPPs were mixed with ODN at the selected mass ratios (1:1 - 100:1). The viabilities of cells after treatment with MSPPs, SPPs and MPPs with the dosages equivalent to the amounts used in complexes were also investigated. The ODN dosage was fixed at the final concentration of 1 μg/ml. All cells were exposed to a magnetic field for the first 20 minutes of the initial 4 h incubation. After the initial incubation, the cells were washed

with PBS buffer before incubated in complete mediums to a final duration of 3 days.

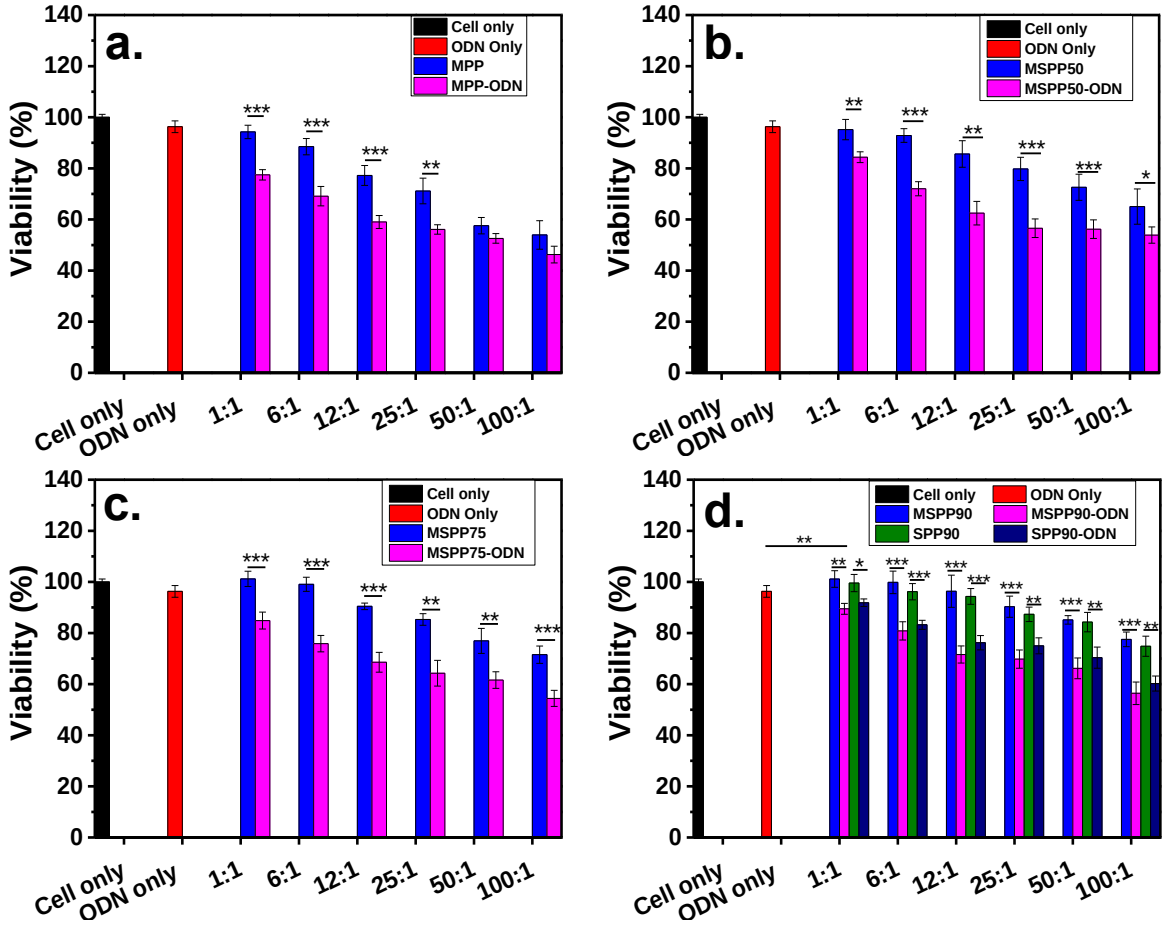


Fig. 5.5. MTT assay of MDA-MB-231 cells after 72 h incubation with different complexes: MPP-ODN (a), MSPP50-ODN (b), MSPP75-ODN (c), SPP90 and MSPP90-ODN (d) at different particle/ODN mass ratios (1:1-100:1). Complexes were added into serum-free MDA-MB-231 cell cultures for a 4 h transfection time, after which cells were washed with PBS and further incubated in complete mediums to a final duration of 3 days. At the beginning of transfection, the cells were exposed to a magnetic field for 20 min. Corresponding carriers and ODN-only with the amounts equivalent to the dosages in complexes were also used as controls to investigate their toxicity to MDA-MD-231 cells. The dosages of ODN were fixed at 1 μg/ml. The results are shown in mean ± SD, n = 4. The statistical significance is expressed as ***$p < 0.001$, **$p < 0.01$, *$p < 0.05$.

MTT assay in Fig. 5.5 shows that negligible growth inhibition was observed for MDA-MB-231 cells treated with naked ODNs (red columns), indicating that efficient transfection was difficult for naked ODNs due to its poor cellular uptake. The increased dosage of MPPs and MSPPs resulted in

decreased viability of MDA-MB-231 cells treated with those particles, indicating that MPPs and MSPPs possessed dose-dependent cytotoxicity to MDA-MB-231 cells. The introduction of SF into the MPPs system reduced the cytotoxicity of MPPs. Cells treated with MSPPs (at 50%-90% SF) showed a higher viability than those treated with MPPs (blue columns). At the same MSPP dose, cell viability increased with the increase of SF content in MSPPs. For example, at the concentration of 50 μg/ml (associated with the MSPP / ODN ratio of 50:1) MDA-MB-231 cells showed the viabilities of 58%, 73%, 77% and 85% after treated with MPPs, and MSPPs with 50%, 75% and 90% of SF respectively, giving strong evidence that the addition of SF resulted in reduced cytotoxicity of MSPPs.

By increasing mass ratios of MPPs / ODN from 1:1 to 100:1 a clear decrease in cell viability can be seen (Fig. 5.5a), where at lower mass ratios from 1:1 to 25:1, cells treated with MPP-ODN exhibited a significantly lower viability to those treated with MPPs. All these lowered cell viabilities indicate that c-myc antisense ODN induced cell growth inhibition occurred. However, at higher ratios (50:1 to 100:1) no significant difference on viabilities were observed between cells treated with MPPs and MPP-ODN, suggests the inhibited cell growth mainly have been a result from the cytotoxicity of MPPs and shield the effect of ODNs. On the other hand, as shown in Fig. 5.5b-d, on average a ~20% lower viability for MDA-MB-231 cells treated with MSPPs (50% - 90% SF)-ODN to those treated with MSPPs (50 - 90% SF) was observed at the whole ratio range investigated, indicating that MSPPs with SF are capable of transfecting the ODN for the inhibition of cell growth. It is important to note that even at higher particle / ODN ratios (50:1 to 100:1) cells showed significantly lower viabilities after treated with MSPP-ODN to those treated with MSPPs (50 - 90% SF), suggesting the reduced viabilities were mainly attributed to the function of ODN instead of toxicity of MSPPs. These results indicated that with reduced cytotoxicity compared to MPPs, MSPPs (50 - 90% SF) allow the

efficient growth inhibition performance of ODN without bringing significant cytotoxicity of carriers to cells, which is desired in gene transfection.

Since MSPP90 showed the lowest toxicity among these particles (MSPPs 50 - 90% SF) and is still capable of transfecting the c-myc antisense ODN to cause the growth inhibition of MDA-MB-231 cells, it is of interest to investigate its optimum mass ratio with ODN to achieve high inhibition effect from ODN while avoid additional cytotoxicity from MSPP90. As shown in Fig. 5.5d, when the MSPP / ODN mass ratio was 1:1, MSPP90-ODN exhibited the lower inhibition effect than other MSPP-ODN complexes, which was most likely because insufficient MSPP90 were provided at such mass ratio. Increased mass ratio from 1:1 to 12:1 resulted in decreased viabilities for cells treated with MSPP90-ODN, suggesting the growth inhibition effect was enhanced with increased amount of MSPPs in MSPP90-ODN, which is most likely because the increased surface charge of complexes making them easier to interact with cell membrane and to be internalized. Further increase the MSPP90 / ODN ratio from 12:1 to 25:1, the viability of cells treated with MSPP90 decreased from 96% to 90% without observation of significant viability decrease for cells treated with MSPP90-ODN complexes (only from 72% to 70%), indicated that the optimum MSPP90-ODN mass ratio for MDA-MB-231 cell growth inhibition at the ODN concentration of 1 μg/ml was 12:1. The further decreased viability of cells treated with MSPP90-ODN complexes at the mass ratio of 25:1 or over was most likely resulted from the cytotoxicity of MSPPs (90% SF) at higher dosages. MDA-MB-231 cells treated with SPP90 and SPP90-ODN showed similar growth inhibition pattern to those treated with MSPP90 and MSPP90-ODN, suggesting both particles possess similar cytotoxicity towards MDA-MB-231 cells. On the other hand, lower viability was observed for cells treated with MSPP90-ODN complexes than those treated with SPP90-ODN complexes due to the higher transfection effect of MSPP90-ODN via magnetofection.

It has been previously reported that the significant cytotoxicity of PEI is thought to be mainly due to its high amine content that resulted in high cationic charge density [45, 136-138]. Free PEI molecules can interact with negatively charged substances such as serum proteins or even red blood cells to form aggregates which can adhere to tissue surfaces to cause significant cell damage [136]. PEI is also able to interact with proteins inside the cell and therefore interfere with critical intracellular processes [44]. Many studies have been conducted to reduce the surface charge of PEI based transfection systems in order to minimum their cytotoxicity. For example, Xue *et al.* encapsulated hexadecylated-PEI polymers / siRNA complexes in negative charged lipids, the resulting surface charge of encapsulated complexes were decreased as well as the cytotoxicity compared with un-encapsulated PEI complexes [139]. In another example, Liu *et al.* designed ASF / PEI / DNA ternary complexes by coating negatively charged *Antheraea pernyi* silk fibroin (ASF) onto the surface of PEI / DNA complexes [140]. The coating of ASF resulted in fewer surface charges and therefore a higher viability of cells transfected with ASF / PEI / DNA ternary complexes was observed compared to those transfected by PEI / DNA complexes. Therefore, it is believed that the reduced cytotoxicity of MSPPs is resulted from the reduced surface charge on these particles.

#### 5.2.3.2. Concentration effect of particles/complexes on MDA-MB-231 and HDF cells

To investigate the inhibition effect of MSPP-ODN and SPP-ODN at different concentrations on cancer and normal cells, MDA-MB-231 breast cancer cells and HDF cells were selected and treated with SPP90-ODN, MSPP90-ODN, SPP90 and MSPP90. MSPP90 was chosen because it exhibited the lowest cytotoxicity among MSPPs with different SF percentages and SPP90 was chosen as a comparison with MSPP90. MSPP90 and SPP90 were mixed with ODN at a mass

ratio of 12:1 before incubating with MDA-MB-231 or HDF cells in serum-free medium for 4 h. The final concentrations of ODN in medium were 1, 5 and 10 µg/ml. A magnet plate was placed below the cells for the first 20 min of the initial incubation. After initial incubation, the cells were washed twice with PBS to remove any un-internalized particles and complexes before incubation in complete medium for a final duration of 3 days.

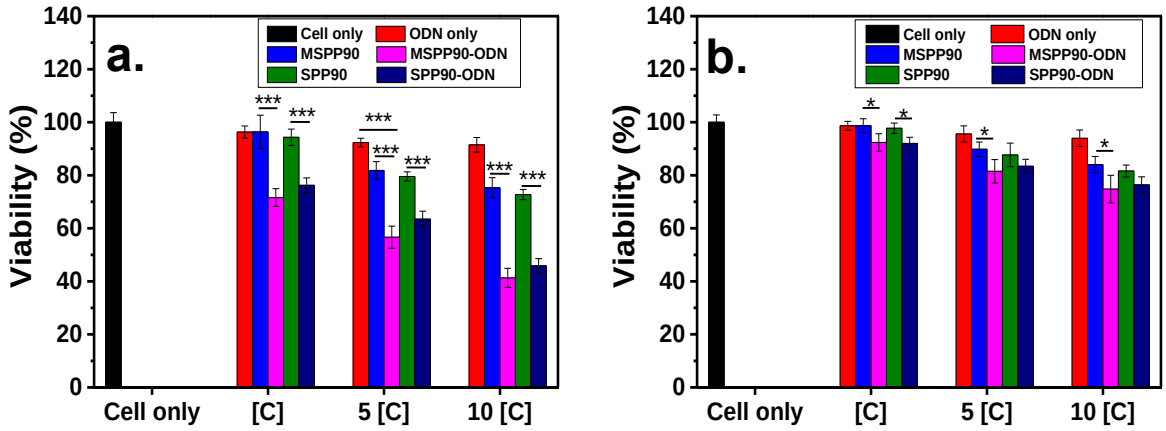


Fig. 5.6. Concentration effect of particles and complexes on breast cancer cells (a) and HDF cells (b). MDA-MB-231 cells and HDF cells were incubated with ODNs, MSPP90, SPP90, MSPP90-ODN, SPP90-ODN complexes for 4 h in serum-free medium. At the beginning, the cells were treated with an external magnetic field for 20 min. After the initial transfection, cells were washed twice with PBS buffer and incubated in complete medium for a final duration of 3 days. [C]= 12 µg/ml MSPP90 or SPP90 + 1 µg/ml ODN. Equivalent amount of ODN, MSPP90 and SPP90 were used as controls. The results are shown in mean ± SD, n = 4. The statistical significance is expressed as ***$p < 0.001$, **$p < 0.01$, *$p < 0.05$.

As shown in Fig. 5.6, naked ODN showed negligible growth inhibition effect on both MDA-MB-231 cells and HDF cells at the concentrations studied, suggesting that the growth inhibition effect of naked ODN was poor to both cells due to its poor internalization properties [251, 287-289]. Increasing the concentration of MSPP90 in medium resulted in decreased viability of MDA-MB-231 cells, which is

consistent with the previous results obtained (see Fig. 5.5). This result strongly suggests that MSPP90 possess dose-dependent cytotoxicity to MDA-MB-231 cancer cells. After treatment with MSPP90-ODN, MDA-MB-231 cells showed significantly lower viability than cells treated with naked ODN and MSPP90, suggesting the complexation with MSPP90 have improved the effect of ODN. With the increased concentration from 1 [C] to 5 [C] and 10 [C], the viability of MDA-MB-231 cells treated with MSPP90-ODN decreased from 72% to 57% and 41%. While cells treated with MSPP90 showed the decreased viability of 96%, 82% and 75%. This result suggested that enhanced growth inhibition effect of MSPP90-ODN can be achieved without brought massive cytotoxicity from MSPP90.

Fig. 5.6b presents the viability of HDF cells after being treated with naked ODNs, MSPP90, SPP90 and their ODN complexes. It was observed that HDF cells were less affected by the particles and complexes. For example, after both cell lines being treated with MSPP90-ODN at the same concentration (1[C]), HDF cells exhibited a higher viability (92%) compared to that of MDA-MB-231 cells (72%). This is because cancer cells tend to exhibit a higher uptake efficiency on particles than normal cells due to the higher metabolic activity of cancer cells [246] which leads to the overexpression of receptors on their surface and increases the available binding sites [246-248]. Furthermore, it has been reported that differences in cell-cell interactions between normal cells and cancer cells can also lead to faster particle uptake for cancer cells than normal cells [295]. Gal *et al.* compared the internalization of polystyrene particle by MDA-MB-231 breast cancer cells and MCF-10A benign cells [295]. The result indicates that cancer cells uniformly internalize particles in larger amounts and higher rate. However, only cells at the edge of a growing colony of benign cells are able to internalize particles [295]. This is due to the fact that normal, adherent cells maintain tight cell-cell connections [296]. In contrast, cell-cell and cell-matrix interactions are less important for

cancer cells, and particles can thus be internalized into any cell on the plate at high rates [295-296]. Therefore, it is fair to assume that MDA-MB-231 cancer cells have taken up more MSPP90-ODN compared to HDF cells, which in turn resulted in the lower viability of MDA-MB-231 cells.

### 5.2.4. Cellular uptake assays

#### 5.2.4.1. Uptake efficiency of MSPPs-ODN and SPP 90-ODN on MDA-MB-231 cells

Slow vector accumulation and the consequently low vector concentration at target tissues is reported as a strong obstacle for efficient gene transfection [297]. By applying a magnetic field, magnetic vectors combining DNAs can be rapidly concentrated onto the surface of target cells which can facilitate complex internalization and enhance transfection efficiency [298]. This is also known as 'magnetofection'. For non-magnetofection vectors, their improved accumulation property is based on their designed biophysical properties or coupling with targeting ligands. However, in practice, it has been proved insufficient for rapid accumulation on target sites [298]. On the other hand, magnetofection has shown outstanding performance in rapid transfection [150-151, 298]. Mykhaylyk *et al.* compared the transfection performance of magnetic and non-magnetic complexes exposed to a magnetic field [150]. Their data showed that the magnetic complexes concentrated onto the surface of target cells and consequently transfection efficiencies were found 1,000-fold higher than the transfections conducted with non-magnetic vectors [150]. Krötz *et al*. reported that magnetic particle-ODN complexes can be transfected into 84% of human umbilical vein endothelial cells within 15 min followed by nuclear accumulation within 2 h when exposed to a magnetic field, this is substantially faster than non-magnetofection methods which generally require 24 h incubation times

[151].

To investigate the uptake kinetics of MPPs, MSPPs and SPPs, particles were complexed with fluorescence labelled ODNs at the mass ratio of 12:1. The final concentration of ODN was fixed at 1 µg/ml. As shown in Fig. 5.7a, with magnetofection, 81% of MDA-MB-231 cells incubated with MPP-ODN took up the complexes with 5 min of incubation which was followed by washing the cells in PBS buffer twice and 24 h of further cultivation in complete medium. This resulted in a 3.1-fold increase of transfected cells (26%) compared with cells treated with MPP-ODN without a magnetic field. This result supports previous studies which claimed that magnetofection can provide outstanding performance in rapid transfection compared to non-magnetofection [150-151, 298]. Increasing magnetofection time to 20 min only resulted in an increased uptake efficiency of 1% (from 81% to 82%). A further increase to the magnetofection to 24 h finally resulted in the highest uptake efficiency of 88%. This indicated that most MPP-ODN complexes were concentrated on the surface of cells within the first 5 min and extending the magnetofection time did not significantly increase the uptake efficiency. The result is in agreement with Krötz *et al*. who found no further enhancement of uptake efficiency was observed when extending the magnetofection time from 15 min to 24 h for human umbilical vein endothelial cells incubated with $p22^{phox}$-antisens ODN containing magnetic vectors [151]. For the MMDA-MB-231 cells treated with MPP-ODN without the presence of a magnetic field, increasing transfection time to 20 min increased the uptake efficiency by 43% (from 26% to 69%) and a further increase to a total of 86% was seen for a transfection time of 24 h, showing a clear time-dependent uptake of complexes through non-magnetofection. This is because the association of vectors to cells is a diffusion-limited process [257], which means only a fraction of the vectors interacted with the cells within the initial short period (e.g. 5 min). Therefore, increasing transfection time resulted in the significantly increase of complex uptake [257].

After 4 h transfection with Oligofectamine-ODN, ODNs uptake was found 58.3% for cells exposed to the magnetic field and 57.5% for cells not exposed to a magnetic field. This clearly suggests that Oligofectamine-ODN transfection is not dependent on the presence of a magnetic field. The uptake efficiency of Oligofectamine-ODN transfection for 4 h is lower than that of MPP-ODN for 4 h without the presence of magnetic field, which is most likely due to the faster sedimentation of MPP-ODN than Oligofectamine-ODN due to the higher mass density of MPPs. No significant differences were observed for cells incubated with naked ODNs with or without the presence of a magnetic field. Only 1.5% (M-) and 1.6% (M+) of total cells took up ODNs after being incubated with naked ODNs for 5 min. The uptake efficiency appeared to be time dependent. However, only 12.3% (M-) and 11.6% (M+) uptake efficiencies were achieved when cells were incubated with naked ODNs for 24 h, indicating that it is difficult for naked ODNs to be taken up by MDA-MB-231 cells. This explains the negligible reduction of cell viability by naked ODNs.

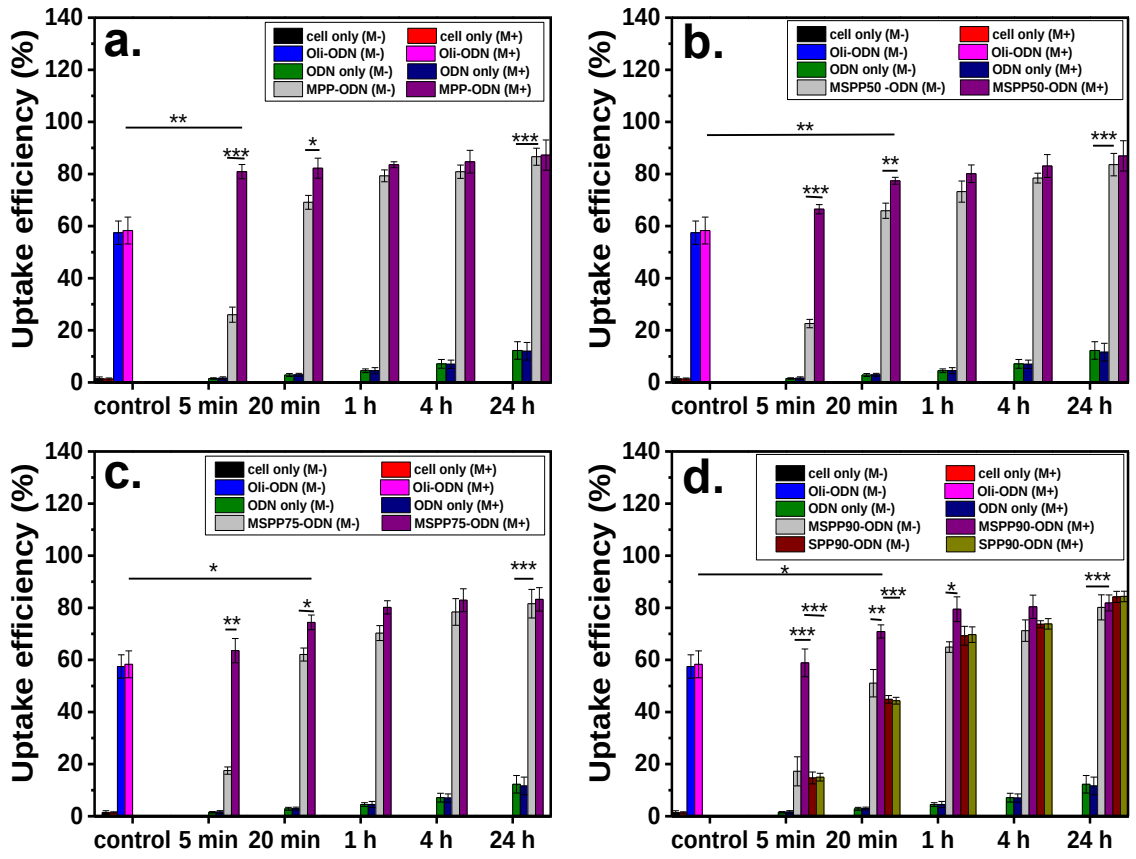


Fig. 5.7. Cellular uptake assays of MPP-ODN (a), MSPP50-ODN (b), MSPP75-ODN (c), MSPP90-ODN and SPP90-ODN (d) complexes for MDA-MB-231 cells. The cell only and ODNs only are used as negative controls with the dosages of ODNs equivalent to the amount of ODNs used for the complexes. Oligofectamine-ODN was used as a positive control with a standard transfection time of 4 h. The concentration of the complexes was fixed at 12 µg/ml MSPPs +1 µg/ml ODN. Cells were incubated with ODN or transfection complexes for 5 min - 24 h with (M+) or without (M-) the presence of an external magnetic field for a maximum of 20 min. The cells were then washed twice with PBS buffer and cultured with complete medium until to a final duration of 24 h before the FACS analysis. The results are shown in mean ± SD, n ≥ 3. The statistical significance is expressed as ***p < 0.001, **p < 0.01, *p <0.05.

The uptake kinetics of MSPP-ODN complexes are represented in Fig. 5.7b-d. With the short magnetofection time of 5 min, 67%, 64% and 59% uptake efficiencies were achieved by MDA-MB-231 cells treated with MSPP50, MSPP75 and MSPP90, respectively. In contrast, only 23%, 18% and 17% of ODN uptake efficiencies were achieved for cells treated with MSPP50,

MSPP75 and MSPP90 through non-magnetofection. This clearly shows that the uptake efficiency of ODNs can be drastically improved by MSPPs trough magnetofection.

On the other hand, Fig. 5.7b-d revealed that the uptake efficiencies of MSPP-ODN were time dependent. With increased magnetofection time from 5 min to 20 min, significant increased uptake efficiencies (over 70%) were observed for MDA-MB-231 cells treated with MSPP-ODN with magnetic field, suggesting longer transfection period helped the accumulation of MSPP-ODN to the cell surface. The difference in uptake over time is presumably due to the difference in positive surface charges between MPPs and MSPPs. As mentioned in Section 5.2.1.2, the positive charges of MSPPs are lower than those of MPPs due to the introduction of negatively charged SF and with the increase of SF the surface charges of MSPPs decrease further. The decreased surface charges of MSPPs may be the reason why longer magnetofection times are required for MSPP-ODN to achieve uptake efficiencies similar to MPP-ODN. However, it is worth to note that considerably high uptake efficiency (over 70% compare to ~ 80% final uptake efficiency at 24 h) was achieved by MSPP-ODN within 20 min. Moreover, when the magnetofection time was increased from 20 min to 1 h, only limited improvements on uptake efficiency were observed for cells treated with MSPP-ODN through magnetofection. The uptake efficiencies obtained from MSPP-ODN were about the same level as those obtained from MPP-ODN, which required 24 h for MSPP-ODN through non-magnetofection. Extended magnetofection time from 1 h to 24 h did not lead to a significant increase of uptake efficiency for MSPP-ODN, suggesting almost all MSPP-ODN had been taken up by cells within 1 h of magnetofection. This result demonstrated that MSPPs were capable of rapidly delivering ODNs into cells through magnetofection.

The uptake kinetics of MDA-MB-231 cells treated with SPP90-ODN was also investigated. As

shown in Fig. 5.7d. No significant differences on uptake efficiencies were observed for cells incubated with SPP90-ODN with or without magnetic field, suggesting a magnetic field had no effect to the performance of non-magnetic SPPs. After 5 and 20 min of transfection time, lower uptake efficiencies were observed for cells treated with SPP90-ODN (49%, 20 min) compared with MSPP90-ODN (51%, 20 min) when there was no magnetic field provided. However, slightly higher uptake efficiencies were obtained by SPP90-ODN (69%, 1 h) than MSPP90 (65%, 1 h) when the transfection time was extended to 1 h or over. This can be attributed to more PEI in SPP90 than that in MSPP90 with the same overall weight, therefore facilitate the internalization over time.

#### 5.2.4.2. Concentration effect on the uptake efficiency of MSPP90-ODN and SPP90-ODN on MDA-MB-231 cells and HDF cells

The ODN uptake efficiency for MDA-MB-231 is shown in Fig. 5.8a. Cells were incubated with naked ODNs and complexes at different concentrations for 20 min before washed and further incubated for a final duration of 24 h. Fig. 5.8a clearly shows that increasing the concentration of MSPP90-ODN and SPP90-ODN lead to the improved uptake efficiencies for MDA-MB-231 cells, which explains why increased concentrations of transfection complexes resulted in decreased viability of cells as shown previously in Section 5.2.3.2. The uptake efficiencies obtained by Oligofectamine-ODN were 2.7, 5.7 and 3.7-fold higher than those obtained by naked ODNs at the concentration [C], 5[C] and 10[C] respectively, suggesting an enhanced uptake efficiency can be achieved by Oligofectamine within a short transfection time of 20 min. However, higher uptake efficiencies were obtained by MSPP90-ODN and SPP90-ODN with or without the presence of a magnetic field. In particular, with a magnetic field the uptake efficiency of MSPP90-ODN is much

higher. The uptake efficiencies by HDFs, as a control of non-cancer cells, are displayed in Fig. 5.8b and are significantly lower than that of MDA-MB-231 breast cancer cells. These results explain why both MSPP90-ODN and SPP90-ODN exhibited a lower growth inhibition effect to HDF cells compared with MDA-MB-231 cells (see Section 5.2.3.2).

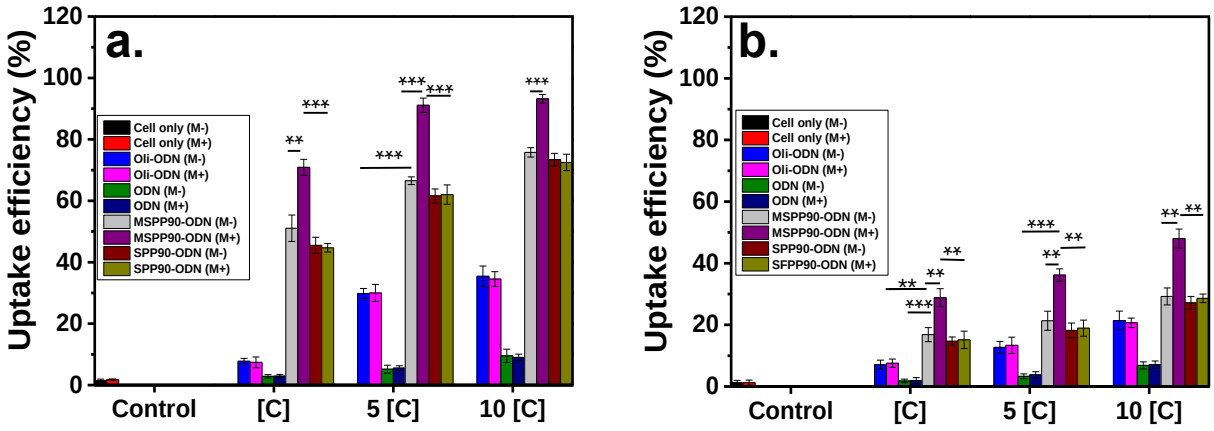


Fig. 5.8. Cellular uptake assays of MDA-MB-231 cells (a) and HDF cells (b) after treated with MSPP90-ODN and SPP90-ODN at different concentrations. The cell-only and ODNs-only are used as negative controls with the ODN dosages equivalent to the amount used for the complexes. Oligofectamine-ODN was used as a positive control. Cells were incubated with ODN or complexes for 20 min with (M+) or without (M-) the presence of an external magnetic field. After the initial transfection, cells were washed twice with PBS and incubated in complete medium to a final duration of 24 h before the FACS analysis. The MSPP90 / ODN and SPP90 / ODN mass ratio was fixed at 12:1. [C]=12 μg/ml MSPP90 or SPP90 + 1 μg/ml ODN. The results are shown in mean ± SD, n = 3. The statistical significance is expressed as ***$p < 0.001$, **$p < 0.01$, *$p < 0.05$.

### 5.2.5. Magnetically targeted delivery assay

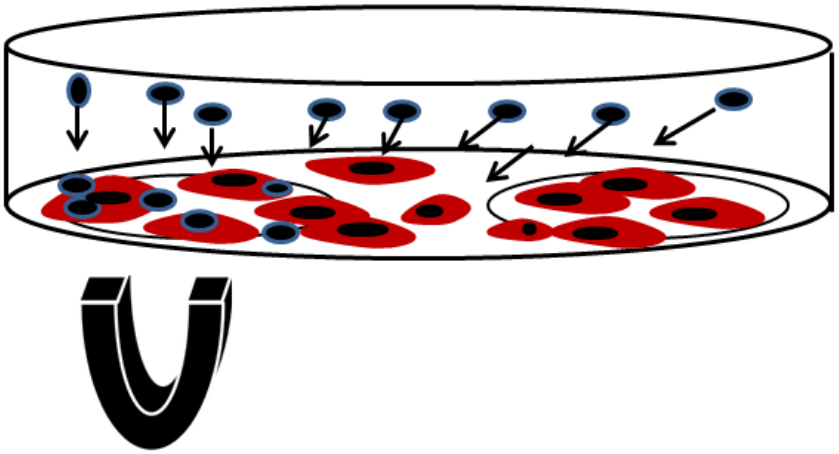

Fig. 5.9. Schematic diagram of magnetically targeted delivery of transfection complexes to MDA-MB-231 cells. Cells were seeded in 6-well plates with 2 coverslips previously placed in each well and incubated for overnight to allow for cell attachment. Next, mediums were removed, and the cells were washed twice with PBS buffer before incubation in serum-free mediums. Naked ODN, Oligofectamine-ODN, SPP 90-ODN and MSPP 90-ODN were added into the serum-free mediums and incubated with cells for 4 h. A magnet was placed under one of the coverslips for the first 20 min of the 4-h initial incubation. After the initial incubation, the serum-free mediums were removed and replaced with complete medium and the cells were further incubated to a final duration of 24 h before analysis with a confocal microscope.

To investigate the potential of MSPPs for magnetically targeted delivery of ODN, MSPP 90-ODN were incubated with MDA-MB-231 cells with or without the presence of a magnet as shown in Fig. 5.9. Naked ODNs, Oligofectamine-ODN and SPP90-ODN were also incubated with cells as negative controls. As shown in Fig. 5.10a&b, fluorescence intensities of cells treated with naked ODNs were seen to be significantly lower than those cells treated with transfection complexes, suggesting naked ODNs were not efficiently internalized by cells, which is consistent with uptake efficiency shown in Fig. 5.7. Moreover, for cells treated with naked ODNs (Fig. 5.10a&b), Oligofectamine-ODN (Fig. 5.10c&d) and SPP90-ODN (Fig. 5.10e&f), the presence of the magnet

did not result in any significant difference to the fluorescence intensities, suggesting that the magnetic field did not change the cellular uptake of these complexes. Fig. 5.10g&h reveals the uptake of MSPP90-ODN without and with a magnet placed under the cells respectively. With the presence of the magnet the ODN uptake was significantly enhanced. The improved ODN uptake is because large amounts of MSPP90-ODN were concentrated at the area with a magnet. On the other hand, the local concentration of MSPP90-ODN at the areas without magnet was significantly reduced, therefore reduced the uptake. This result reveals that MSPPs have great potential to be used for magnetically targeted delivery of ODNs to desired sites.

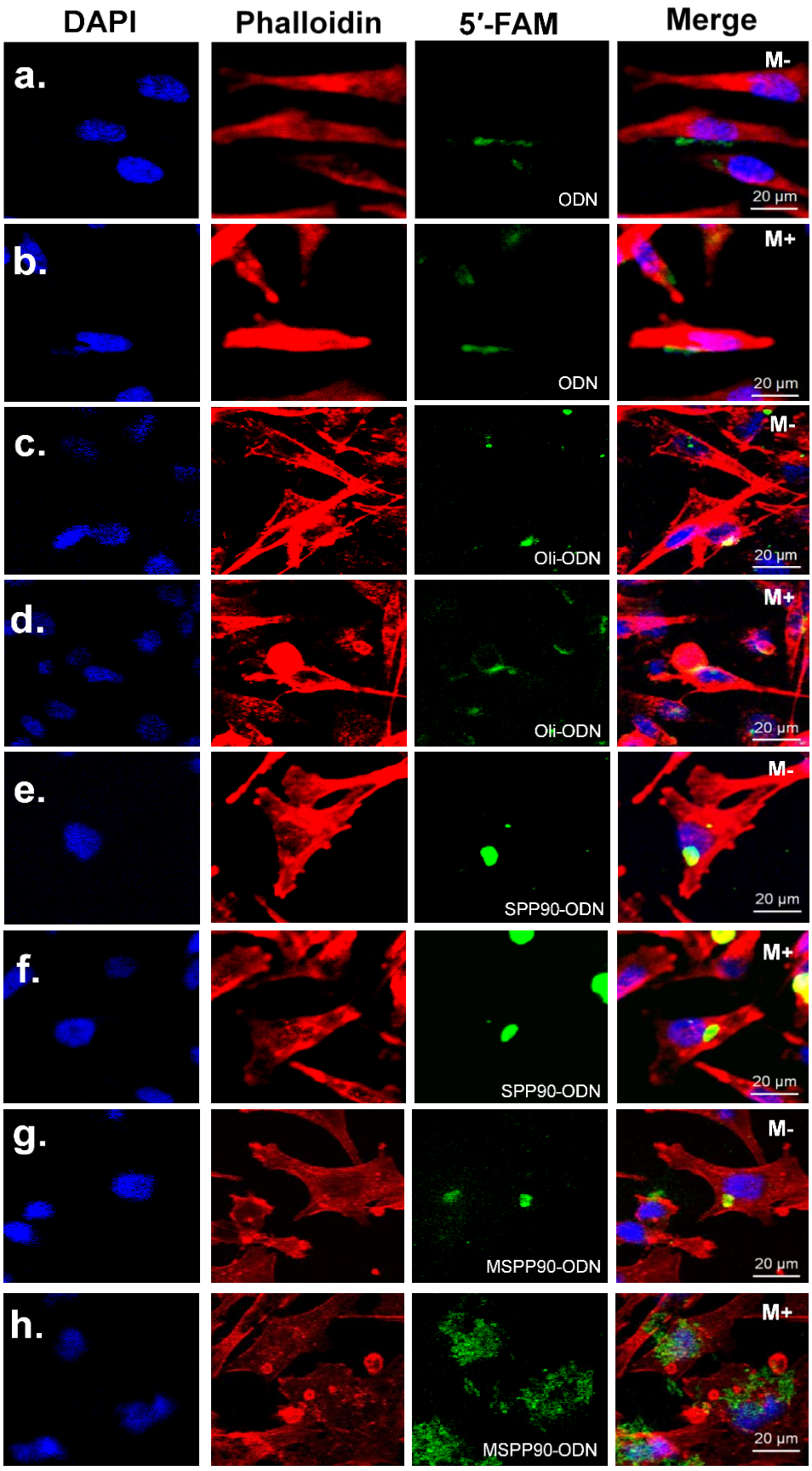


Fig. 5.10. Confocal microscopic images of MDA-MB-231 cells incubated with naked ODNs (a&b), Oligofectamine-ODN (c & d), SPP90-ODN (e&f) and MSPP90-ODN (g&h). ODNs were labelled with

5′-FAM (green). Cell nucleus and cytoskeleton were stained with DAPI (blue) and Alexa Fluor 568 Phalloidin (red); all images were taken with the LSM510 confocal microscope (Zeiss). M+ indicates the presence of a magnet during the incubation and M- indicates the absence of the magnet.

## 5.3. Conclusions

In summary, SPPs and MSPPs with core-shell structures have been fabricated using biocompatible and biodegradable SF biomaterial in conjunction with PEI and MNPs. The particle size and zeta potentials are controllable by changing the percentage of SF during fabrication. SPPs and MSPPs are capable of delivering ODNs into MDA-MB-231 breast cancer cells and significantly inhibiting cell growth. In addition to this, MSPPs and SPPs showed significantly reduced cytotoxicity compared to MPPs. Both SPPs and MSPPs are less toxic to HDF cells than to MDA-MB-231 cancer cells. High uptake efficiency of ODNs (over 70%) can be achieved by MSPPs within a short time (20 min) through magnetofection. Moreover, with the presence of external magnetic fields, MSPPs can target deliver ODNs to the desired areas with reduced ODN concentration at non-targeting areas, thus avoiding undesirable side-effects of MSPPs to healthy tissue. SPPs and MSPPs therefore are promising candidates for targeted gene therapy.

# 6. Conclusions

In this thesis, a variety of nanoparticles (SFPs, MSPs, MAPs, MACPs, SPPs, MPPs and MSPPs) have been fabricated and their performances for drug or gene delivery applications have been studied.

SFPs, MSPs, MAPs and MACPs were used for the delivery of the anticancer model drug CUR. The nanoparticles were observed to be non-cytotoxic, which can be attributed to the selection of non-cytotoxic and biocompatible SF, SA and CHI as the coating materials. What is more, the *in vitro* cytotoxicity assay indicated that MSPPs exhibited significate lower cytotoxicity than MPPs, suggesting that the addition of biocompatible SF successfully reduced the cytotoxicity of MPPs.

Significant higher uptake efficiencies of CUR or ODNs was observed when loaded into carriers (MSPs, MAPs, MACPs, SPPs, MPPs and MSPPs), compared to free CUR or ODNs. This is due to the size range of the nanocarriers (100-360 nm) as well as the fact that free CUR, which is highly hydrophobic, can easily aggregate in aqueous solution and in the case of free ODNs, self-assembled long nanowires formed. Because of the enhanced uptake of CUR or ODNs when they were loaded into nanoparticles, their cellular growth inhibition effect to cancer cells was also Improved.

Moreover, a new method for the preparation of SFPs via salting out was developed in this project. Instead of using the conventional methods of salting out via potassium phosphate, sodium phosphate was employed and the resulting SFPs were observed to be significantly smaller in size (90 - 300 nm) than the SFPs (500 - 12000 nm) fabricated using potassium phosphate. The difference in the particle size is due to the different hydration properties of sodium and potassium ions and their different adsorption behaviour to SF polypeptides. Since smaller carriers (50 – 200

nm) are desired for cancer therapy, this new method is therefore promising for the fabrication of SFPs for future drug delivery applications.

The CUR release rate can be controlled by altering the pH of the sodium phosphate solution for the preparation of CMSFPs. Further to this, the release rate is influenced by the outermost coating layer, suggesting specific drug release profiles can be achieved by carefully designing the drug carriers.

In addition, the *in vitro* magnetically targeted delivery assay of MAPs, MACPs and MSPPs indicated that the magnetic nanocarriers allowed the targeted delivery of cargo to selected areas under a magnetic field, suggesting these nanocarriers are promising for targeted delivery of anticancer drugs or genes to cancer cells.

In summary, in order to fabricate non-cytotoxic nanoparticles, the selection of non-cytotoxic and biocompatible materials in the particle preparation process is required. Smaller particle sizes generally benefit the internalization of the particles into cells. Meanwhile, particles within the optimum size range of 50 – 200 nm can specifically increase the uptake of these particles by cancer cells. Therefore, exploring of methods to prepare particles within the suitable size range is necessary. Moreover, encapsulation of magnetic cores enables the rapid accumulation and targeted delivery of the nanoparticles.

# 7. Future work

The results from the previous experimental Chapters indicated that magnetic core-shell nanoparticles (MAPs, MACPs and MSPPs) are capable of *in vitro* targeted delivery to desired locations. However, the purpose of designing these magnetic nanoparticles is to target deliver anticancer drugs into tumour sites, which are located inside the human body. Therefore, it is required to test their in vivo targeting performance by running animal experiments.

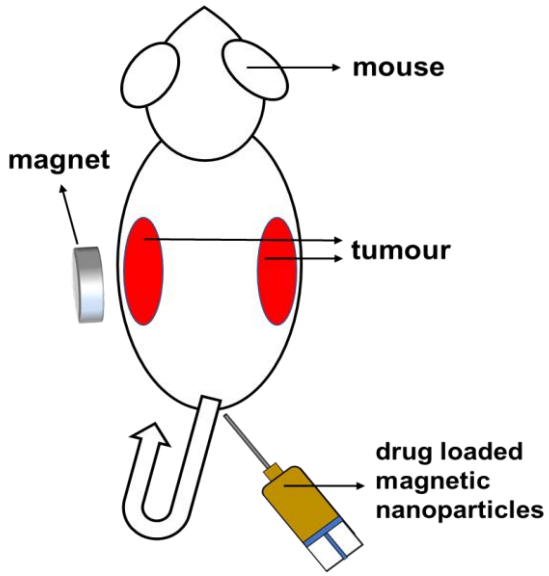


Fig. 7.1. Schematic representation of the experimental plan for the *in vivo* targeting performance of the drug loaded magnetic nanoparticles.

The animal experiment plan is shown in Fig. 7.1. Initially, cancer cells are planted into two different sites of a mouse to allow the growth of tumours. Then, a small magnet is attached next to one of the tumours and an anticancer drug (e.g. CUR) is loaded into the magnetic nanoparticles. These are then injected into the mouse every 24 h. By monitoring the size of the tumours with or without the attached magnet, the targeting effect of the magnetic nanoparticles under a magnetic field can be

observed. Finally, dissect the tumours and analyse the concentration of the anticancer drug in each tumour site to quantitatively analyse the targeting effect of the magnetic nanoparticles under a magnetic field.

In Chapter 3, the different salting out effects of sodium and potassium ions is explained due to the different adsorption behaviours of these ions to negatively charged SF polypeptides. The SF polypeptides are assumed as small, hydrophobic particles and sodium ions, which are more hydrated in aqueous solution than potassium ions, which are assumed less hydrophobic than potassium ions. Therefore, the potassium ions are believed more readily adsorbing onto SF, while sodium ions are more readily to stay closer to bulk of the water, leading to a stronger salting out effect of potassium ions. However, proteins contain both hydrophobic and hydrophilic sites. The hydrophobic amino acids are protected by hydrophilic ones in an aqueous solution. Therefore, it can be assumed that the salting out process of SF is expected to be more complex than the simplified model discussed in Chapter 3. It is likely that sodium ions are more rapidly adsorbed onto the hydrophilic amino acids and reduce their overall net surface charge, leading to the exposure of hydrophobic amino acids. These prefer the adsorption of potassium ions compared to sodium ions. It would therefore be beneficial to design an experiment test this hypothesis.

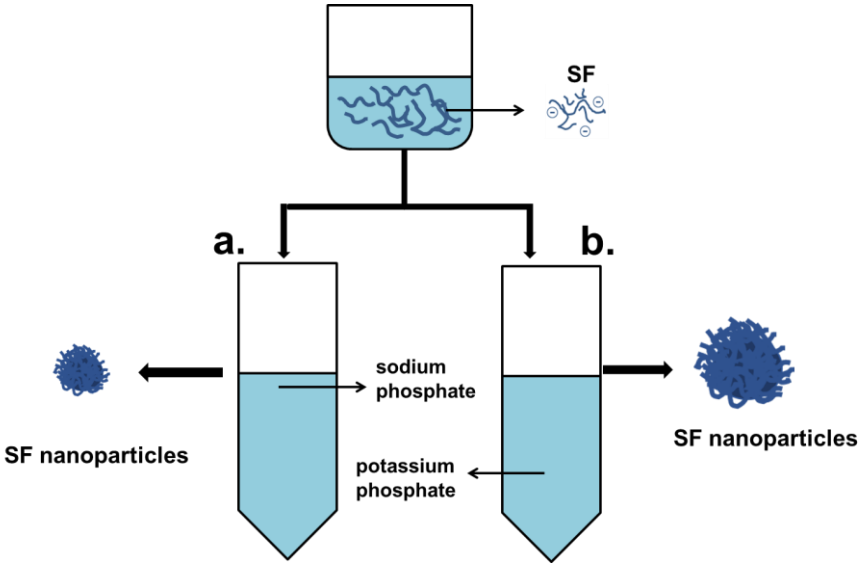


Fig. 7.2. Schematic representation of the experimental plan for the salting out process of SF via sodium (a) and potassium (b) phosphate solutions.

As shown in Fig. 7.2, initially, SF solutions are added into sodium or potassium phosphate solution. Mixed SF / salt solutions are then taken from each tube at preselected time intervals (e.g. 15, 30 min, 1, 2, 4, 8, 12, 24, 48 h). These are then analysed for their SF particle size and the sizes are plotted against time.

If the previously mentioned hypothesis is correct then the initial aggregation of SF polypeptides will be first happening in the sodium phosphate solution, as the sodium ions would be more readily adsorbed onto the hydrophilic amino acids. This in turn would mean that the SF particles fabricated from sodium phosphate solutions would be expected to possess larger sizes than those fabricated from potassium phosphate solutions for the same time intervals. After the exposure of hydrophobic amino acids, potassium ions are expected more readily to adsorb to SF polypeptides, leading to a stronger salting out effect and larger size of SF particles fabricated from potassium phosphate solutions at the latter time intervals, as shown in Fig. 7.3.

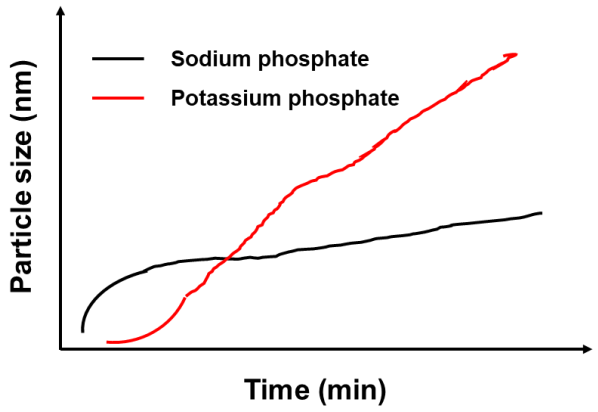


Fig. 7.3. Prognostic graph of the size of SF particles prepared from sodium / potassium phosphate solutions as a function of salting out time.

# 8. References:


1. Cho, K.; Wang, X.; Nie, S.; Shin, D. M., Therapeutic nanoparticles for drug delivery in cancer. *Clin Cancer Res* **2008,** *14* (5), 1310-1316.
2. Allen, T. M.; Cullis, P. R., Drug delivery systems: entering the mainstream. *Science* **2004,** *303* (5665), 1818-1822.
3. M Yallapu, M.; Jaggi, M.; C Chauhan, S., Curcumin nanomedicine: a road to cancer therapeutics. *Curr Pharm Des* **2013,** *19* (11), 1994-2010.
4. Masuda, T.; Hidaka, K.; Shinohara, A.; Maekawa, T.; Takeda, Y.; Yamaguchi, H., Chemical studies on antioxidant mechanism of curcuminoid: analysis of radical reaction products from curcumin and Linoleate. *J. Agric. Food Chem.* **1999,** *47* (1), 71-77.
5. Ruby, A.; Kuttan, G.; Babu, K. D.; Rajasekharan, K.; Kuttan, R., Anti-tumour and antioxidant activity of natural curcuminoids. *Cancer Lett.* **1995,** *94* (1), 79-83.
6. Ak, T.; Gulcin, I., Antioxidant and radical scavenging properties of curcumin. *Chem Biol Interact* **2008,** *174* (1), 27-37.
7. Brouet, I.; Ohshima, H., Curcumin, an anti-tumor promoter and anti-inflammatory agent, inhibits induction of nitric oxide synthase in activated macrophages. *Biochem. Biophys. Res. Commun.* **1995,** *206* (2), 533-540.
8. Kawamori, T.; Lubet, R.; Steele, V. E.; Kelloff, G. J.; Kaskey, R. B.; Rao, C. V.; Reddy, B. S., Chemopreventive effect of curcumin, a naturally occurring anti-inflammatory agent, during the promotion/progression stages of colon cancer. *Cancer Res.* **1999,** *59* (3), 597-601.
9. Aggarwal, B. B.; Harikumar, K. B., Potential therapeutic effects of curcumin, the anti-inflammatory agent, against neurodegenerative, cardiovascular, pulmonary, metabolic, autoimmune and neoplastic diseases. *Int J Biochem Cell Biol* **2009,** *41* (1), 40-59.
10. Sidhu, G. S.; Singh, A. K.; Thaloor, D.; Banaudha, K. K.; Patnaik, G. K.; Srimal, R. C.; Maheshwari, R. K., Enhancement of wound healing by curcumin in animals. *Wound Repair Regen.* **1998,** *6* (2), 167-177.
11. Panchatcharam, M.; Miriyala, S.; Gayathri, V. S.; Suguna, L., Curcumin improves wound healing by modulating collagen and decreasing reactive oxygen species. *Mol Cell Biochem* **2006,** *290* (1), 87-96.
12. Negi, P.; Jayaprakasha, G.; Jagan Mohan Rao, L.; Sakariah, K., Antibacterial activity of turmeric oil: a byproduct from curcumin manufacture. *J. Agric. Food Chem.* **1999,** *47* (10), 4297-4300.
13. Mun, S. H.; Joung, D. K.; Kim, Y. S.; Kang, O. H.; Kim, S. B.; Seo, Y. S.; Kim, Y. C.; Lee, D. S.; Shin, D. W.; Kweon, K. T.; Kwon, D. Y., Synergistic antibacterial effect of curcumin against methicillin-resistant Staphylococcus aureus. *Phytomedicine* **2013,** *20* (8), 714-718.
14. Rezaee, R.; Momtazi, A. A.; Monemi, A.; Sahebkar, A., Curcumin: a potentially powerful tool to reverse cisplatin-induced toxicity. *Pharmacol. Res* **2016,** *117*, 218-227.
15. Wilken, R.; Veena, M. S.; Wang, M. B.; Srivatsan, E. S., Curcumin: A review of anti-cancer properties and therapeutic activity in head and neck squamous cell carcinoma. *Mol Cancer* **2011,** *10* (1), 12.
16. Aggarwal, B. B.; Kumar, A.; Bharti, A. C., Anticancer potential of curcumin: preclinical and clinical studies. *Anticancer res* **2003,** *23* (1A), 363-398.
17. Li, M.; Zhang, Z.; Hill, D. L.; Wang, H.; Zhang, R., Curcumin, a dietary component, has anticancer, chemosensitization, and radiosensitization effects by down-regulating the MDM2 oncogene through the PI3K/mTOR/ETS2 pathway. *Cancer Res* **2007,** *67* (5), 1988-1996.
18. Tapal, A.; Tiku, P. K., Complexation of curcumin with soy protein isolate and its implications on solubility and stability of curcumin. *Food Chem.* **2012,** *130* (4), 960-965.
19. Wan, S.; Sun, Y.; Qi, X.; Tan, F., Improved bioavailability of poorly water-soluble drug curcumin in cellulose acetate solid dispersion. *AAPS PharmSciTech* **2012,** *13* (1), 159-166.

20. Sahu, A.; Bora, U.; Kasoju, N.; Goswami, P., Synthesis of novel biodegradable and self-assembling methoxy poly (ethylene glycol)–palmitate nanocarrier for curcumin delivery to cancer cells. *Acta Biomater* **2008,** *4* (6), 1752-1761.
21. Liu, A.; Lou, H.; Zhao, L.; Fan, P., Validated LC/MS/MS assay for curcumin and tetrahydrocurcumin in rat plasma and application to pharmacokinetic study of phospholipid complex of curcumin. *J Pharm Biomed Anal* **2006,** *40* (3), 720-727.
22. Tiyaboonchai, W.; Tungpradit, W.; Plianbangchang, P., Formulation and characterization of curcuminoids loaded solid lipid nanoparticles. *Int J Pharm* **2007,** *337* (1), 299-306.
23. Li, L.; Braiteh, F. S.; Kurzrock, R., Liposome-encapsulated curcumin: in vitro and in vivo effects on proliferation, apoptosis, signaling, and angiogenesis. *J. Clin. Oncol.* **2005,** *104* (6), 1322-1331.
24. Hajj Ali, H.; Michaux, F.; Ntsama, B.; Sandrine, I.; Durand, P.; Jasniewski, J.; Linder, M., Shea butter solid nanoparticles for curcumin encapsulation: Influence of nanoparticles size on drug loading. *Eur J Lipid Sci Technol* **2016,** *118* (8), 1168-1178.
25. Wang, T.; Ma, X.; Lei, Y.; Luo, Y., Solid lipid nanoparticles coated with cross-linked polymeric double layer for oral delivery of curcumin. *Colloids Surf B Biointerfaces* **2016,** *148*, 1-11.
26. Zhang, J.; Tang, Q.; Xu, X.; Li, N., Development and evaluation of a novel phytosome-loaded chitosan microsphere system for curcumin delivery. *Int. J. Pharm.* **2013,** *448* (1), 168-174.
27. Xie, M.-B.; Li, Y.; Zhao, Z.; Chen, A.-Z.; Li, J.-S.; Hu, J.-Y.; Li, G.; Li, Z., Solubility enhancement of curcumin via supercritical CO 2 based silk fibroin carrier. *J. Supercrit. Fluids* **2015,** *103*, 1-9.
28. Song, W.; Muthana, M.; Mukherjee, J.; Falconer, R. J.; Biggs, C. A.; Zhao, X., Magnetic-Silk Core-Shell Nanoparticles as Potential Carriers for Targeted Delivery of Curcumin into Human Breast Cancer Cells. *ACS Biomater Sci Eng* **2017,** *3* (6), 1027-1038.
29. Anitha, A.; Maya, S.; Deepa, N.; Chennazhi, K.; Nair, S.; Tamura, H.; Jayakumar, R., Efficient water soluble O-carboxymethyl chitosan nanocarrier for the delivery of curcumin to cancer cells. *Carbohydr. Polym.* **2011,** *83* (2), 452-461.
30. Montalbán, M. G.; Coburn, J. M.; Lozano-Pérez, A. A.; Cenis, J. L.; Víllora, G.; Kaplan, D. L., Production of curcumin-loaded silk fibroin nanoparticles for cancer therapy. *Nanomaterials* **2018,** *8* (2), 126.
31. Liu, J.; Xu, L.; Liu, C.; Zhang, D.; Wang, S.; Deng, Z.; Lou, W.; Xu, H.; Bai, Q.; Ma, J., Preparation and characterization of cationic curcumin nanoparticles for improvement of cellular uptake. *Carbohydr. Polym.* **2012,** *90* (1), 16-22.
32. Chuah, L. H.; Billa, N.; Roberts, C. J.; Burley, J. C.; Manickam, S., Curcumin-containing chitosan nanoparticles as a potential mucoadhesive delivery system to the colon. *Pharm Dev Technol* **2013,** *18* (3), 591-599.
33. Bhandari, R.; Gupta, P.; Dziubla, T.; Hilt, J. Z., Single step synthesis, characterization and applications of curcumin functionalized iron oxide magnetic nanoparticles. *Mater Sci Eng C* **2016,** *67*, 59-64.
34. Alexis, F.; Pridgen, E.; Molnar, L. K.; Farokhzad, O. C., Factors affecting the clearance and biodistribution of polymeric nanoparticles. *Mol. Pharmaceutics* **2008,** *5* (4), 505-515.
35. Blanco, E.; Shen, H.; Ferrari, M., Principles of nanoparticle design for overcoming biological barriers to drug delivery. *Nat Biotechnol* **2015,** *33* (9), 941-951.
36. Reddy, L. H.; Murthy, R., Pharmacokinetics and biodistribution studies of doxorubicin loaded poly (butyl cyanoacrylate) nanoparticles synthesized by two different techniques. *Biomed Pap Med Fac Univ Palacky Olomouc Czech Repub* **2004,** *148* (2), 161-166.
37. Gabizon, A. A.; Barenholz, Y.; Bialer, M., Prolongation of the circulation time of doxorubicin encapsulated in liposomes containing a polyethylene glycol-derivatized phospholipid: pharmacokinetic studies in rodents and dogs. *Pharm. Res.* **1993,** *10* (5), 703-708.
38. Wasan, K. M., *Role of lipid excipients in modifying oral and parenteral drug delivery: Basic principles and biological examples*. John Wiley & Sons: 2007.
39. Moghimi, S. M.; Hunter, A. C.; Murray, J. C., Long-circulating and target-specific nanoparticles: theory to practice. *Pharmacol Rev* **2001,** *53* (2), 283-318.

40. Fang, C.; Shi, B.; Pei, Y.-Y.; Hong, M.-H.; Wu, J.; Chen, H.-Z., In vivo tumor targeting of tumor necrosis factor-α-loaded stealth nanoparticles: effect of MePEG molecular weight and particle size. *Eur J Pharm Sci* **2006,** *27* (1), 27-36.

41. Lungwitz, U.; Breunig, M.; Blunk, T.; Göpferich, A., Polyethylenimine-based non-viral gene delivery systems. *Eur J Pharm Biopharm* **2005,** *60* (2), 247-266.

42. Dey, D.; Inayathullah, M.; Lee, A. S.; LeMieux, M. C.; Zhang, X.; Wu, Y.; Nag, D.; De Almeida, P. E.; Han, L.; Rajadas, J., Efficient gene delivery of primary human cells using peptide linked polyethylenimine polymer hybrid. *Biomaterials* **2011,** *32* (20), 4647-4658.

43. Xiang, L.; Bin, W.; Huali, J.; Wei, J.; Jiesheng, T.; Feng, G.; Ying, L., Bacterial magnetic particles (BMPs)–PEI as a novel and efficient non–viral gene delivery system. *J Gene Med* **2007,** *9* (8), 679-690.

44. Forrest, M. L.; Koerber, J. T.; Pack, D. W., A degradable polyethylenimine derivative with low toxicity for highly efficient gene delivery. *Bioconjug Chem* **2003,** *14* (5), 934-940.

45. Seow, W. Y.; Liang, K.; Kurisawa, M.; Hauser, C. A., Oxidation as a facile strategy to reduce the surface charge and toxicity of polyethyleneimine gene carriers. *Biomacromolecules* **2013,** *14* (7), 2340-2346.

46. Yamamoto, Y.; Nagasaki, Y.; Kato, Y.; Sugiyama, Y.; Kataoka, K., Long-circulating poly (ethylene glycol)–poly (d, l-lactide) block copolymer micelles with modulated surface charge. *J Control Release.* **2001,** *77* (1-2), 27-38.

47. Gessner, A.; Waicz, R.; Lieske, A.; Paulke, B.-R.; Mäder, K.; Müller, R., Nanoparticles with decreasing surface hydrophobicities: influence on plasma protein adsorption. *Int. J. Pharm.* **2000,** *196* (2), 245-249.

48. Arruebo, M.; Fernández-Pacheco, R.; Ibarra, M. R.; Santamaría, J., Magnetic nanoparticles for drug delivery. *Nano today* **2007,** *2* (3), 22-32.

49. Wu, M.; Huang, S., Magnetic nanoparticles in cancer diagnosis, drug delivery and treatment. *Mol Clin Oncol* **2017,** *7* (5), 738-746.

50. Markides, H.; Rotherham, M.; El Haj, A., Biocompatibility and toxicity of magnetic nanoparticles in regenerative medicine. *J Nanomater* **2012,** *2012*, 13.

51. Park, J. H.; Saravanakumar, G.; Kim, K.; Kwon, I. C., Targeted delivery of low molecular drugs using chitosan and its derivatives. *Adv. Drug Delivery Rev.* **2010,** *62* (1), 28-41.

52. Colombo, M.; Carregal-Romero, S.; Casula, M. F.; Gutiérrez, L.; Morales, M. P.; Böhm, I. B.; Heverhagen, J. T.; Prosperi, D.; Parak, W. J., Biological applications of magnetic nanoparticles. *Chem Soc Rev* **2012,** *41* (11), 4306-4334.

53. Yellen, B. B.; Forbes, Z. G.; Halverson, D. S.; Fridman, G.; Barbee, K. A.; Chorny, M.; Levy, R.; Friedman, G., Targeted drug delivery to magnetic implants for therapeutic applications. *J Magn Magn Mater* **2005,** *293* (1), 647-654.

54. Widder, K. J.; Senyei, A. E.; Scarpelli, D. G., Magnetic microspheres: a model system for site specific drug delivery in vivo. *Proc Soc Exp Biol Med* **1978,** *158* (2), 141-146.

55. Gupta, P.; Hung, C., Minireview Magnetically controlled targeted micro-carrier systems. *Life Sci.* **1989,** *44* (3), 175-186.

56. Driscoll, C. F.; Morris, R. M.; Senyei, A. E.; Widder, K. J.; Heller, G. S., Magnetic targeting of microspheres in blood flow. *Microvasc Res* **1984,** *27* (3), 353-369.

57. Matsunaga, T.; Kamiya, S., Use of magnetic particles isolated from magnetotactic bacteria for enzyme immobilization. *Appl Microbiol Biotechnol* **1987,** *26* (4), 328-332.

58. Lübbe, A. S.; Bergemann, C.; Riess, H.; Schriever, F.; Reichardt, P.; Possinger, K.; Matthias, M.; Dörken, B.; Herrmann, F.; Gürtler, R., Clinical experiences with magnetic drug targeting: a phase I study with 4′-epidoxorubicin in 14 patients with advanced solid tumors. *Cancer Res.* **1996,** *56* (20), 4686-4693.

59. Tian, Y.; Jiang, X.; Chen, X.; Shao, Z.; Yang, W., Doxorubicin-loaded magnetic silk fibroin nanoparticles for targeted therapy of multidrug-resistant cancer. *Adv Mater* **2014,** *26* (43), 7393-7398.

60. McBain, S. C.; Yiu, H. H.; Dobson, J., Magnetic nanoparticles for gene and drug delivery. *Int. J. Nanomed.* **2008,** *3* (2), 169.

61. Ota, S.; Takahashi, Y.; Tomitaka, A.; Yamada, T.; Kami, D.; Watanabe, M.; Takemura, Y., Transfection efficiency

influenced by aggregation of DNA/polyethylenimine max/magnetic nanoparticle complexes. *J. Nanopart. Res.* **2013,** *15* (5), 1-12.

62. Liu, X.; Chen, X.; Li, Y.; Wang, X.; Peng, X.; Zhu, W., Preparation of superparamagnetic Fe3O4@ alginate/chitosan nanospheres for Candida rugosa lipase immobilization and utilization of layer-by-layer assembly to enhance the stability of immobilized lipase. *ACS Appl. Mater. Interfaces* **2012,** *4* (10), 5169-5178.

63. Qi, Y.; Wang, H.; Wei, K.; Yang, Y.; Zheng, R.-Y.; Kim, I. S.; Zhang, K.-Q., A review of structure construction of silk fibroin biomaterials from single structures to multi-level structures. *Int. J. Mol. Sci.* **2017,** *18* (3), 237.

64. Vepari, C.; Kaplan, D. L., Silk as a Biomaterial. *Prog Polym Sci* **2007,** *32* (8), 991-1007.

65. Kundu, B.; Rajkhowa, R.; Kundu, S. C.; Wang, X., Silk fibroin biomaterials for tissue regenerations. *Adv. Drug Delivery Rev.* **2013,** *65* (4), 457-470.

66. Altman, G. H.; Diaz, F.; Jakuba, C.; Calabro, T.; Horan, R. L.; Chen, J.; Lu, H.; Richmond, J.; Kaplan, D. L., Silk-based biomaterials. *Biomaterials* **2003,** *24* (3), 401-416.

67. Zhang, L.; Li, Y.; Jimmy, C. Y.; Chan, K. M., Redox-responsive controlled DNA transfection and gene silencing based on polymer-conjugated magnetic nanoparticles. *RSC Adv* **2016,** *6* (76), 72155-72164.

68. Li, C.; Vepari, C.; Jin, H.-J.; Kim, H. J.; Kaplan, D. L., Electrospun silk-BMP-2 scaffolds for bone tissue engineering. *Biomaterials* **2006,** *27* (16), 3115-3124.

69. Valluzzi, R.; Gido, S. P.; Muller, W.; Kaplan, D. L., Orientation of silk III at the air-water interface. *International Journal of Biological Macromolecules* **1999,** *24* (2-3), 237-242.

70. Moraes, M. A. d.; Nogueira, G. M.; Weska, R. F.; Beppu, M. M., Preparation and characterization of insoluble silk fibroin/chitosan blend films. *Polymers* **2010,** *2* (4), 719-727.

71. Li, Q.; Qi, N.; Peng, Y.; Zhang, Y.; Shi, L.; Zhang, X.; Lai, Y.; Wei, K.; Kim, I. S.; Zhang, K.-Q., Sub-micron silk fibroin film with high humidity sensibility through color changing. *RSC Adv* **2017,** *7* (29), 17889-17897.

72. Kundu, J.; Chung, Y. I.; Kim, Y. H.; Tae, G.; Kundu, S. C., Silk fibroin nanoparticles for cellular uptake and control release. *Int J Pharm* **2010,** *388* (1), 242-250.

73. Bessa, P. C.; Balmayor, E. R.; Azevedo, H. S.; Nurnberger, S.; Casal, M.; van Griensven, M.; Reis, R. L.; Redl, H., Silk fibroin microparticles as carriers for delivery of human recombinant BMPs. Physical characterization and drug release. *J Tissue Eng Regen Med* **2010,** *4* (5), 349-355.

74. Chen, M.; Shao, Z.; Chen, X., Paclitaxel-loaded silk fibroin nanospheres. *J Biomed Mater Res A* **2012,** *100* (1), 203-210.

75. Wen, X.; Peng, X.; Fu, H.; Dong, Y.; Han, K.; Su, J.; Wang, Z.; Wang, R.; Pan, X.; Huang, L., Preparation and in vitro evaluation of silk fibroin microspheres produced by a novel ultra-fine particle processing system. *Int. J. Pharm.* **2011,** *416* (1), 195-201.

76. Cao, Z.; Chen, X.; Yao, J.; Huang, L.; Shao, Z., The preparation of regenerated silk fibroin microspheres. *Soft Matter* **2007,** *3* (7), 910-915.

77. Imsombut, T.; Srisuwan, Y.; Srihanam, P.; Baimark, Y., Genipin-cross-linked silk fibroin microspheres prepared by the simple water-in-oil emulsion solvent diffusion method. *Powder Technol* **2010,** *203* (3), 603-608.

78. Wang, X.; Yucel, T.; Lu, Q.; Hu, X.; Kaplan, D. L., Silk nanospheres and microspheres from silk/pva blend films for drug delivery. *Biomaterials* **2010,** *31* (6), 1025-1035.

79. Lammel, A. S.; Hu, X.; Park, S. H.; Kaplan, D. L.; Scheibel, T. R., Controlling silk fibroin particle features for drug delivery. *Biomaterials* **2010,** *31* (16), 4583-4591.

80. Agnihotri, S. A.; Mallikarjuna, N. N.; Aminabhavi, T. M., Recent advances on chitosan-based micro-and nanoparticles in drug delivery. *J Control Release.* **2004,** *100* (1), 5-28.

81. Kumar, M. N. R., A review of chitin and chitosan applications. *React Funct Polym* **2000,** *46* (1), 1-27.

82. Bhunchu, S.; Rojsitthisak, P., Biopolymeric alginate-chitosan nanoparticles as drug delivery carriers for cancer therapy. *Pharmazie* **2014,** *69* (8), 563-570.

83. López-Cruz, A.; Barrera, C.; Calero-DdelC, V. L.; Rinaldi, C., Water dispersible iron oxide nanoparticles coated with

covalently linked chitosan. *J Mater Chem* **2009,** *19* (37), 6870-6876.

84. Swain, S.; Dey, R.; Islam, M.; Patel, R.; Jha, U.; Patnaik, T.; Airoldi, C., Removal of fluoride from aqueous solution using aluminum-impregnated chitosan biopolymer. *Sep. Sci.* **2009,** *44* (9), 2096-2116.

85. Bernkop-Schnürch, A.; Dünnhaupt, S., Chitosan-based drug delivery systems. *Eur J Pharm Biopharm* **2012,** *81* (3), 463-469.

86. Akbuğa, J.; Durmaz, G., Preparation and evaluation of cross-linked chitosan microspheres containing furosemide. *Int. J. Pharm.* **1994,** *111* (3), 217-222.

87. Bodmeier, R.; Oh, K.-H.; Pramar, Y., Preparation and evaluation of drug-containing chitosan beads. *Drug Dev Ind Pharm* **1989,** *15* (9), 1475-1494.

88. Rampino, A.; Borgogna, M.; Blasi, P.; Bellich, B.; Cesàro, A., Chitosan nanoparticles: preparation, size evolution and stability. *Int. J. Pharm.* **2013,** *455* (1-2), 219-228.

89. Bhise, K. S.; Dhumal, R. S.; Paradkar, A. R.; Kadam, S. S., Effect of drying methods on swelling, erosion and drug release from chitosan–naproxen sodium complexes. *AAPS PharmSciTech* **2008,** *9* (1), 1-12.

90. Anitha, A.; Deepagan, V.; Rani, V. D.; Menon, D.; Nair, S.; Jayakumar, R., Preparation, characterization, in vitro drug release and biological studies of curcumin loaded dextran sulphate–chitosan nanoparticles. *Carbohydr. Polym.* **2011,** *84* (3), 1158-1164.

91. Tapia, C.; Corbalan, V.; Costa, E.; Gai, M.; Yazdani-Pedram, M., Study of the release mechanism of diltiazem hydrochloride from matrices based on chitosan− alginate and chitosan− carrageenan mixtures. *Biomacromolecules* **2005,** *6* (5), 2389-2395.

92. Ching, S. H.; Bansal, N.; Bhandari, B., Alginate gel particles–A review of production techniques and physical properties. *Crit Rev Food Sci Nutr* **2017,** *57* (6), 1133-1152.

93. Lee, K. Y.; Mooney, D. J., Alginate: properties and biomedical applications. *Prog. Polym. Sci.* **2012,** *37* (1), 106-126.

94. Tønnesen, H. H.; Karlsen, J., Alginate in drug delivery systems. *Drug Dev Ind Pharm* **2002,** *28* (6), 621-630.

95. Chen, S.-C.; Wu, Y.-C.; Mi, F.-L.; Lin, Y.-H.; Yu, L.-C.; Sung, H.-W., A novel pH-sensitive hydrogel composed of N, O-carboxymethyl chitosan and alginate cross-linked by genipin for protein drug delivery. *J Control Release.* **2004,** *96* (2), 285-300.

96. George, M.; Abraham, T. E., Polyionic hydrocolloids for the intestinal delivery of protein drugs: alginate and chitosan—a review. *J Control Release.* **2006,** *114* (1), 1-14.

97. Choi, B.; Park, H.; Hwang, S.; Park, J., Preparation of alginate beads for floating drug delivery system: effects of CO2 gas-forming agents. *Int. J. Pharm.* **2002,** *239* (1-2), 81-91.

98. Kuo, C. K.; Ma, P. X., Ionically crosslinked alginate hydrogels as scaffolds for tissue engineering: Part 1. Structure, gelation rate and mechanical properties. *Biomaterials* **2001,** *22* (6), 511-521.

99. Phillips, G. O.; Williams, P. A., *Handbook of hydrocolloids*. Elsevier: 2009.

100. Draget, K. I.; Skjåk-Bræk, G.; Stokke, B. T., Similarities and differences between alginic acid gels and ionically crosslinked alginate gels. *Food Hydrocoll* **2006,** *20* (2-3), 170-175.

101. Draget, K.; Bræk, G. S.; Smidsrød, O., Alginic acid gels: the effect of alginate chemical composition and molecular weight. *Carbohydr. Polym.* **1994,** *25* (1), 31-38.

102. Cevher, E.; Sezer, A. D.; Çağlar, E. S. e., Gene delivery systems: recent progress in viral and non-viral therapy. In *Recent Advances in Novel Drug Carrier Systems*, InTech: 2012.

103. Moss, J. A., Gene therapy review. *Radiol Technol* **2014,** *86* (2), 155-180.

104. Stone, D., Novel viral vector systems for gene therapy. Molecular Diversity Preservation International: 2010.

105. Friedmann, T.; Roblin, R., Gene therapy for human genetic disease? *Science* **1972,** *175* (4025), 949-955.

106. Rosenberg, S. A.; Aebersold, P.; Cornetta, K.; Kasid, A.; Morgan, R. A.; Moen, R.; Karson, E. M.; Lotze, M. T.; Yang, J. C.; Topalian, S. L., Gene transfer into humans—immunotherapy of patients with advanced melanoma, using tumor-infiltrating lymphocytes modified by retroviral gene transduction. *N Engl J Med* **1990,** *323* (9), 570-578.

107. Blaese, R. M.; Culver, K. W.; Miller, A. D.; Carter, C. S.; Fleisher, T.; Clerici, M.; Shearer, G.; Chang, L.; Chiang, Y.;

Tolstoshev, P., T lymphocyte-directed gene therapy for ADA− SCID: initial trial results after 4 years. *Science* **1995,** *270* (5235), 475-480.
108. Ibraheem, D.; Elaissari, A.; Fessi, H., Gene therapy and DNA delivery systems. *Int. J. Pharm.* **2014,** *459* (1-2), 70-83.
109. Naldini, L., Gene therapy returns to centre stage. *Nature* **2015,** *526* (7573), 351.
110. Wong, S. Y.; Pelet, J. M.; Putnam, D., Polymer systems for gene delivery—past, present, and future. *Prog. Polym. Sci.* **2007,** *32* (8-9), 799-837.
111. Arscott, P. G.; Li, A. Z.; Bloomfield, V. A., Condensation of DNA by trivalent cations. 1. Effects of DNA length and topology on the size and shape of condensed particles. *Biopolymers* **1990,** *30* (5‐6), 619-630.
112. Ono, M. Y.; Spain, E. M., Dynamics of DNA condensates at the solid− liquid interface by atomic force microscopy. *J Am Chem Soc* **1999,** *121* (32), 7330-7334.
113. Luo, D.; Saltzman, W. M., Synthetic DNA delivery systems. *Nat. Biotechnol.* **2000,** *18* (1), 33.
114. Gao, X.; Kim, K.-S.; Liu, D., Nonviral gene delivery: what we know and what is next. *AAPS J* **2007,** *9* (1), E92-E104.
115. Schatzlein, A., Non-viral vectors in cancer gene therapy: principles and progress. *Anticancer Drugs* **2001,** *12* (4), 275-304.
116. Mady, M. M., Cationic liposomes as gene delivery system. *Afr J Pharm Pharmacol* **2011,** *5* (17), 2007-2012.
117. Labhasetwar, V., Nanotechnology for drug and gene therapy: the importance of understanding molecular mechanisms of delivery. *Curr Opin Biotechnol* **2005,** *16* (6), 674-680.
118. Nayerossadat, N.; Maedeh, T.; Ali, P. A., Viral and nonviral delivery systems for gene delivery. *Adv Biomed Res* **2012,** *1*.
119. Boulaiz, H.; Marchal, J. A.; Prados, J.; Melguizo, C.; Aranega, A., Non-viral and viral vectors for gene therapy. *Cell Mol Biol* **2005,** *51* (1), 3-22.
120. Kay, M. A.; Glorioso, J. C.; Naldini, L., Viral vectors for gene therapy: the art of turning infectious agents into vehicles of therapeutics. *Nat Med* **2001,** *7* (1), 33.
121. Bouard, D.; Alazard‐Dany, N.; Cosset, F. L., Viral vectors: from virology to transgene expression. *Br J Pharmacol* **2009,** *157* (2), 153-165.
122. Munier, S.; Messai, I.; Delair, T.; Verrier, B.; Ataman-Önal, Y., Cationic PLA nanoparticles for DNA delivery: comparison of three surface polycations for DNA binding, protection and transfection properties. *Colloids Surf B Biointerfaces* **2005,** *43* (3-4), 163-173.
123. Nagasaki, T.; Shinkai, S., The concept of molecular machinery is useful for design of stimuli-responsive gene delivery systems in the mammalian cell. *J Incl Phenom Macrocycl Chem* **2007,** *58* (3-4), 205-219.
124. Stone, D.; David, A.; Bolognani, F.; Lowenstein, P.; Castro, M., Viral vectors for gene delivery and gene therapy within the endocrine system. *J Endocrinol* **2000,** *164* (2), 103-118.
125. Bordignon, C.; Notarangelo, L. D.; Nobili, N.; Ferrari, G.; Casorati, G.; Panina, P.; Mazzolari, E.; Maggioni, D.; Rossi, C.; Servida, P., Gene therapy in peripheral blood lymphocytes and bone marrow for ADA− immunodeficient patients. *Science* **1995,** *270* (5235), 470-475.
126. Vorburger, S. A.; Hunt, K. K., Adenoviral gene therapy. *oncologist* **2002,** *7* (1), 46-59.
127. Thrasher, A. J.; Gaspar, H. B.; Baum, C.; Modlich, U.; Schambach, A.; Candotti, F.; Otsu, M.; Sorrentino, B.; Scobie, L.; Cameron, E., Gene therapy: X-SCID transgene leukaemogenicity. *Nature* **2006,** *443* (7109), E5.
128. Teramato, S.; Ishii, T.; Matsuse, T., Crisis of adenoviruses in human gene therapy. *Lancet* **2000,** *355* (9218), 1911-1912.
129. Al-Dosari, M. S.; Gao, X., Nonviral gene delivery: principle, limitations, and recent progress. *AAPS J* **2009,** *11* (4), 671.
130. Jones, C. H.; Chen, C.-K.; Ravikrishnan, A.; Rane, S.; Pfeifer, B. A., Overcoming nonviral gene delivery barriers: perspective and future. *Mol. Pharmaceutics* **2013,** *10* (11), 4082-4098.
131. Bhattacharya, S.; Bajaj, A., Advances in gene delivery through molecular design of cationic lipids. *Chem Commun* **2009,** (31), 4632-4656.

132. Xu, Y.; Szoka, F. C., Mechanism of DNA release from cationic liposome/DNA complexes used in cell transfection. *Biochem* **1996,** *35* (18), 5616-5623.
133. Liu, D.; Ren, T.; Gao, X., Cationic transfection lipids. *Curr Med Chem* **2003,** *10* (14), 1307-1315.
134. Song, Y. K.; Liu, F.; Chu, S.; Liu, D., Characterization of cationic liposome-mediated gene transfer in vivo by intravenous administration. *Hum Gene Ther* **1997,** *8* (13), 1585-1594.
135. Wu, G. Y.; Wu, C. H., Receptor-mediated in vitro gene transformation by a soluble DNA carrier system. *J Biol Chem* **1987,** *262* (10), 4429-4432.
136. Xue, H. Y.; Liu, S.; Wong, H. L., Nanotoxicity: a key obstacle to clinical translation of siRNA-based nanomedicine. *Nanomedicine* **2014,** *9* (2), 295-312.
137. Bansal, R.; Kiran, P.; Kumar, P., Synthesis, characterization and evaluation of diglycidyl-1, 2-cyclohexanedicarboxylate crosslinked polyethylenimine nanoparticles as efficient carriers of DNA. *NEW J CHEM* **2016,** *40* (6), 5044-5052.
138. Ghiamkazemi, S.; Amanzadeh, A.; Dinarvand, R.; Rafiee-Tehrani, M.; Amini, M., Synthesis, and characterization, and evaluation of cellular effects of the FOL-PEG-g-PEI-GAL nanoparticles as a potential non-viral vector for gene delivery. *J Nanomater* **2010,** *12*, 5511-5523.
139. Xue, H. Y.; Narvikar, M.; Zhao, J.-B.; Wong, H. L., Lipid encapsulation of cationic polymers in hybrid nanocarriers reduces their non-specific toxicity to breast epithelial cells. *Pharm. Res.* **2013,** *30* (2), 572-583.
140. Liu, Y.; You, R.; Liu, G.; Li, X.; Sheng, W.; Yang, J.; Li, M., Antheraea pernyi silk fibroin-coated PEI/DNA complexes for targeted gene delivery in HEK 293 and HCT 116 cells. *Int. J. Mol. Sci.* **2014,** *15* (5), 7049-7063.
141. Ogris, M.; Brunner, S.; Schüller, S.; Kircheis, R.; Wagner, E., PEGylated DNA/transferrin–PEI complexes: reduced interaction with blood components, extended circulation in blood and potential for systemic gene delivery. *Gene Ther* **1999,** *6* (4), 595.
142. Huth, S.; Lausier, J.; Gersting, S. W.; Rudolph, C.; Plank, C.; Welsch, U.; Rosenecker, J., Insights into the mechanism of magnetofection using PEI‐based magnetofectins for gene transfer. *J Gene Med* **2004,** *6* (8), 923-936.
143. Wang, X.; Zhou, L.; Ma, Y.; Li, X.; Gu, H., Control of aggregate size of polyethyleneimine-coated magnetic nanoparticles for magnetofection. *Nano Res* **2009,** *2* (5), 365-372.
144. Schillinger, U.; Brill, T.; Rudolph, C.; Huth, S.; Gersting, S.; Krötz, F.; Hirschberger, J.; Bergemann, C.; Plank, C., Advances in magnetofection—magnetically guided nucleic acid delivery. *J Magn Magn Mater* **2005,** *293* (1), 501-508.
145. Plank, C.; Zelphati, O.; Mykhaylyk, O., Magnetically enhanced nucleic acid delivery. Ten years of magnetofection—Progress and prospects. *Adv. Drug Delivery Rev.* **2011,** *63* (14-15), 1300-1331.
146. Kuehnle, A. R.; Kuehnle, M. R., Magnetophoretic particle delivery method and apparatus for the treatment of cells. Google Patents: 1996.
147. Mah, C.; Zolotukhin, I.; Fraites, T.; Dobson, J.; Batich, C.; Byrne, B., Microsphere-mediated delivery of recombinant AAV vectors in vitro and in vivo. *Mol Ther* **2000,** *1*, S239.
148. Plank, C.; Scherer, F.; Schillinger, U.; Anton, M., Magnetofection: enhancement and localization of gene delivery with magnetic particles under the influence of a magnetic field. *J Gene Med* **2000,** *2* (5).
149. Hughes, C.; Galea-Lauri, J.; Farzaneh, F.; Darling, D., Streptavidin paramagnetic particles provide a choice of three affinity-based capture and magnetic concentration strategies for retroviral vectors. *Mol Ther* **2001,** *3* (4), 623-630.
150. Mykhaylyk, O.; Antequera, Y. S.; Vlaskou, D.; Plank, C., Generation of magnetic nonviral gene transfer agents and magnetofection in vitro. *Nat Protoc* **2007,** *2* (10), 2391-2411.
151. Krötz, F.; De Wit, C.; Sohn, H.-Y.; Zahler, S.; Gloe, T.; Pohl, U.; Plank, C., Magnetofection—a highly efficient tool for antisense oligonucleotide delivery in vitro and in vivo. *Mol Ther* **2003,** *7* (5), 700-710.
152. Lammel, A. S.; Hu, X.; Park, S.-H.; Kaplan, D. L.; Scheibel, T. R., Controlling silk fibroin particle features for drug delivery. *Biomaterials* **2010,** *31* (16), 4583-4591.
153. Kherb, J.; Flores, S. C.; Cremer, P. S., Role of carboxylate side chains in the cation Hofmeister series. *The Journal of Physical Chemistry B* **2012,** *116* (25), 7389-7397.

154. Haider, Z. A.; Arai, M.; Hirabayashi, K., Mechanism of the gelation of fibroin solution. *Biosci Biotechnol Biochem* **1993,** *57* (11), 1910-1912.
155. Crivello, J. V.; Bulut, U., Curcumin: A naturally occurring long-wavelength photosensitizer for diaryliodonium salts. *Poly.Chem.* **2005,** *43* (21), 5217-5231.
156. Pecora, R., Dynamic light scattering measurement of nanometer particles in liquids. *J. Nanopart. Res.* **2000,** *2* (2), 123-131.
157. Bhattacharjee, S., DLS and zeta potential–What they are and what they are not? *J Control Release.* **2016,** *235*, 337-351.
158. Dragovic, R. A.; Gardiner, C.; Brooks, A. S.; Tannetta, D. S.; Ferguson, D. J.; Hole, P.; Carr, B.; Redman, C. W.; Harris, A. L.; Dobson, P. J., Sizing and phenotyping of cellular vesicles using Nanoparticle Tracking Analysis. *Nanomedicine* **2011,** *7* (6), 780-788.
159. Filipe, V.; Hawe, A.; Jiskoot, W., Critical evaluation of Nanoparticle Tracking Analysis (NTA) by NanoSight for the measurement of nanoparticles and protein aggregates. *Pharm. Res.* **2010,** *27* (5), 796-810.
160. Meyer, E., Atomic force microscopy. *Prog Surf Sci* **1992,** *41* (1), 3-49.
161. Zhong, Q.; Inniss, D.; Kjoller, K.; Elings, V., Fractured polymer/silica fiber surface studied by tapping mode atomic force microscopy. *Surf. Sci* **1993,** *290* (1-2), L688-L692.
162. Gołek, F.; Mazur, P.; Ryszka, Z.; Zuber, S., AFM image artifacts. *Appl. Surf. Sci.* **2014,** *304*, 11-19.
163. Williams, D. B.; Carter, C. B., The transmission electron microscope. In *Transmission electron microscopy*, Springer: 1996; pp 3-17.
164. Bozzola, J. J., *Electron microscopy*. Wiley Online Library: 1992.
165. van Meerloo, J.; Kaspers, G. J.; Cloos, J., Cell sensitivity assays: the MTT assay. In *Cancer cell culture*, Springer: 2011; pp 237-245.
166. Adan, A.; Alizada, G.; Kiraz, Y.; Baran, Y.; Nalbant, A., Flow cytometry: basic principles and applications. *Crit Rev Biotechnol* **2017,** *37* (2), 163-176.
167. Semwogerere, D.; Weeks, E. R., Confocal microscopy. *Encyclopedia of Biomaterials and Biomedical Engineering* **2005,** *23*, 1-10.
168. Paddock, S. W., Principles and practices of laser scanning confocal microscopy. *Mol Biotechnol* **2000,** *16* (2), 127-149.
169. Prasad, V.; Semwogerere, D.; Weeks, E. R., Confocal microscopy of colloids. *J Phys Condens Matter* **2007,** *19* (11), 113102.
170. Birkner, N.; Wang, Q., How an FTIR Spectrometer Operates. *UC Davis ChemWiki* **2014**.
171. Amand, L.-E.; Tullin, C. J., The Theory Behind FTIR analysis. *Dep. Of Energy Conversion, Chalmers University of Technology, Sweden* **1996**.
172. Chattopadhyay, I.; Biswas, K.; Bandyopadhyay, U.; Banerjee, R. K., Turmeric and curcumin: Biological actions and medicinal applications. *Curr. Sci.(Bangalore)* **2004,** *87* (1), 44-53.
173. Ammon, H. P.; Wahl, M. A., Pharmacology of Curcuma longa. *Planta Med.* **1991,** *57* (01), 1-7.
174. Ganjali, S.; Blesso, C. N.; Banach, M.; Pirro, M.; Majeed, M.; Sahebkar, A., Effects of curcumin on HDL functionality. *Pharmacol. Res* **2017,** *119*, 208-218.
175. Bisht, S.; Maitra, A., Systemic delivery of curcumin: 21st century solutions for an ancient conundrum. *Curr. Drug Discovery Technol.* **2009,** *6* (3), 192-199.
176. Anand, P.; Kunnumakkara, A. B.; Newman, R. A.; Aggarwal, B. B., Bioavailability of curcumin: problems and promises. *Mol Pharm* **2007,** *4* (6), 807-818.
177. Rahimi, H. R.; Nedaeinia, R.; Shamloo, A. S.; Nikdoust, S.; Oskuee, R. K., Novel delivery system for natural products: Nano-curcumin formulations. *AJP* **2016,** *6* (4), 383-398.
178. Shehzad, A.; Khan, S.; Shehzad, O.; Lee, Y. S., Curcumin therapeutic promises and bioavailability in colorectal cancer. *Drugs Today (Barc)* **2010,** *46* (7), 523-532.

179. Cruz-Correa, M.; Shoskes, D. A.; Sanchez, P.; Zhao, R.; Hylind, L. M.; Wexner, S. D.; Giardiello, F. M., Combination treatment with curcumin and quercetin of adenomas in familial adenomatous polyposis. *Clin Gastroenterol Hepatol* **2006,** *4* (8), 1035-1038.
180. Dal Pra, I.; Freddi, G.; Minic, J.; Chiarini, A.; Armato, U., De novo engineering of reticular connective tissue in vivo by silk fibroin nonwoven materials. *Biomaterials* **2005,** *26* (14), 1987-1999.
181. Horan, R. L.; Antle, K.; Collette, A. L.; Wang, Y.; Huang, J.; Moreau, J. E.; Volloch, V.; Kaplan, D. L.; Altman, G. H., In vitro degradation of silk fibroin. *Biomaterials* **2005,** *26* (17), 3385-3393.
182. Gupta, V.; Aseh, A.; Rios, C. N.; Aggarwal, B. B.; Mathur, A. B., Fabrication and characterization of silk fibroin-derived curcumin nanoparticles for cancer therapy. *Int J Nanomedicine* **2009,** *4* (1), 115-122.
183. Shi, P.; Goh, J. C., Release and cellular acceptance of multiple drugs loaded silk fibroin particles. *Int J Pharm* **2011,** *420* (2), 282-289.
184. Zhao, Z.; Li, Y.; Chen, A.-Z.; Zheng, Z.-J.; Hu, J.-Y.; Li, J.-S.; Li, G., Generation of Silk Fibroin Nanoparticles via Solution-Enhanced Dispersion by Supercritical CO2. *Ind. Eng. Chem. Res.* **2013,** *52* (10), 3752-3761.
185. Zhao, Z.; Li, Y.; Xie, M. B., Silk fibroin-based nanoparticles for drug delivery. *Int J Mol Sci* **2015,** *16* (3), 4880-4903.
186. Zhang, Y.-Q.; Shen, W.-D.; Xiang, R.-L.; Zhuge, L.-J.; Gao, W.-J.; Wang, W.-B., Formation of silk fibroin nanoparticles in water-miscible organic solvent and their characterization. *J. Nanopart. Res.* **2006,** *9* (5), 885-900.
187. Collins, K. D., Ions from the Hofmeister series and osmolytes: effects on proteins in solution and in the crystallization process. *Methods* **2004,** *34* (3), 300-311.
188. Persson, I., Hydrated metal ions in aqueous solution: How regular are their structures? *Pure and Applied Chemistry* **2010,** *82* (10), 1901-1917.
189. Vrbka, L.; Vondrášek, J.; Jagoda-Cwiklik, B.; Vácha, R.; Jungwirth, P., Quantification and rationalization of the higher affinity of sodium over potassium to protein surfaces. *Proceedings of the National Academy of Sciences* **2006,** *103* (42), 15440-15444.
190. Salis, A.; Ninham, B. W., Models and mechanisms of Hofmeister effects in electrolyte solutions, and colloid and protein systems revisited. *Chemical Society Reviews* **2014,** *43* (21), 7358-7377.
191. Yang, Z.-H., The size and structure of selected hydrated ions and implications for ion channel selectivity. *RSC Advances* **2015,** *5* (2), 1213-1219.
192. Hu, X.; Kaplan, D.; Cebe, P., Determining Beta-Sheet Crystallinity in Fibrous Proteins by Thermal Analysis and Infrared Spectroscopy. *Macromolecules* **2006,** *39* (18), 6161-6170.
193. Priyadarsini, K. I., The chemistry of curcumin: from extraction to therapeutic agent. *Molecules* **2014,** *19* (12), 20091-20112.
194. Indira Priyadarsini, K., Chemical and structural features influencing the biological activity of curcumin. *Current pharmaceutical design* **2013,** *19* (11), 2093-2100.
195. LiAl, S., General chemistry. **1999**.
196. Tønnesen, H. H.; Másson, M.; Loftsson, T., Studies of curcumin and curcuminoids. XXVII. Cyclodextrin complexation: solubility, chemical and photochemical stability. *International Journal of Pharmaceutics* **2002,** *244* (1-2), 127-135.
197. Patel, A.; Hu, Y.; Tiwari, J. K.; Velikov, K. P., Synthesis and characterisation of zein–curcumin colloidal particles. *Soft Matter* **2010,** *6* (24), 6192-6199.
198. Hu, D.; Lin, C.; Liu, L.; Li, S.; Zhao, Y., Preparation, characterization, and in vitro release investigation of lutein/zein nanoparticles via solution enhanced dispersion by supercritical fluids. *J. Food Eng.* **2012,** *109* (3), 545-552.
199. Luo, Y.; Teng, Z.; Wang, Q., Development of zein nanoparticles coated with carboxymethyl chitosan for encapsulation and controlled release of vitamin D3. *J. Agric. Food Chem.* **2012,** *60* (3), 836-843.
200. Chen, J.; Zheng, J.; McClements, D. J.; Xiao, H., Tangeretin-loaded protein nanoparticles fabricated from zein/β-lactoglobulin: Preparation, characterization, and functional performance. *Food Chem.* **2014,** *158*, 466-472.
201. Maghsoudi, A.; Shojaosadati, S. A.; Farahani, E. V., 5-Fluorouracil-loaded BSA nanoparticles: formulation

optimization and in vitro release study. *AAPS PharmSciTech* **2008,** *9* (4), 1092-1096.
202. Lian, Y.; Zhan, J.-C.; Zhang, K.-H.; Mo, X.-M., Fabrication and characterization of curcumin-loaded silk fibroin/P (LLA-CL) nanofibrous scaffold. *Front Mater Sci* **2014,** *8* (4), 354-362.
203. Li, H.; Tian, J.; Wu, A.; Wang, J.; Ge, C.; Sun, Z., Self-assembled silk fibroin nanoparticles loaded with binary drugs in the treatment of breast carcinoma. *Int. J. Nanomed.* **2016,** *11*, 4373-4380.
204. Perteghella, S.; Crivelli, B.; Catenacci, L.; Sorrenti, M.; Bruni, G.; Necchi, V.; Vigani, B.; Sorlini, M.; Torre, M. L.; Chlapanidas, T., Stem cell-extracellular vesicles as drug delivery systems: New frontiers for silk/curcumin nanoparticles. *Int. J. Pharm.* **2017,** *520* (1), 86-97.
205. Wu, P.; Liu, Q.; Li, R.; Wang, J.; Zhen, X.; Yue, G.; Wang, H.; Cui, F.; Wu, F.; Yang, M., Facile preparation of paclitaxel loaded silk fibroin nanoparticles for enhanced antitumor efficacy by locoregional drug delivery. *ACS Appl. Mater. Interfaces* **2013,** *5* (23), 12638-12645.
206. Kumari, A.; Yadav, S. K.; Yadav, S. C., Biodegradable polymeric nanoparticles based drug delivery systems. *Colloids Surf., B* **2010,** *75* (1), 1-18.
207. Huang, X.; Brazel, C. S., On the importance and mechanisms of burst release in matrix-controlled drug delivery systems. *J Control Release.* **2001,** *73* (2), 121-136.
208. Xie, M.; Fan, D.; Chen, Y.; Zhao, Z.; He, X.; Li, G.; Chen, A.; Wu, X.; Li, J.; Li, Z., An implantable and controlled drug-release silk fibroin nanofibrous matrix to advance the treatment of solid tumour cancers. *Biomaterials* **2016,** *103*, 33-43.
209. Shoba, G.; Joy, D.; Joseph, T.; Majeed, M.; Rajendran, R.; Srinivas, P., Influence of piperine on the pharmacokinetics of curcumin in animals and human volunteers. *Planta Med.* **1998,** *64* (04), 353-356.
210. Ahmadi, F.; Ghasemi-Kasman, M.; Ghasemi, S.; Tabari, M. G.; Pourbagher, R.; Kazemi, S.; Alinejad-Mir, A., Induction of apoptosis in hela cancer cells by an ultrasonic-mediated synthesis of curcumin-loaded chitosan–alginate–sTPP nanoparticles. *Int. J. Nanomed.* **2017,** *12*, 8545-8556.
211. Maghsoudi, A.; Yazdian, F.; Shahmoradi, S.; Ghaderi, L.; Hemati, M.; Amoabediny, G., Curcumin-loaded polysaccharide nanoparticles: optimization and anticariogenic activity against Streptococcus mutans. *Mater Sci Eng C* **2017,** *75*, 1259-1267.
212. Martins, A. F.; Bueno, P. V.; Almeida, E. A.; Rodrigues, F. H.; Rubira, A. F.; Muniz, E. C., Characterization of N-trimethyl chitosan/alginate complexes and curcumin release. *Int J Biol Macromol* **2013,** *57*, 174-184.
213. Zhou, J.; Romero, G.; Rojas, E.; Ma, L.; Moya, S.; Gao, C., Layer by layer chitosan/alginate coatings on poly (lactide-co-glycolide) nanoparticles for antifouling protection and Folic acid binding to achieve selective cell targeting. *J Colloid Interface Sci* **2010,** *345* (2), 241-247.
214. Chai, F.; Sun, L.; He, X.; Li, J.; Liu, Y.; Xiong, F.; Ge, L.; Webster, T. J.; Zheng, C., Doxorubicin-loaded poly (lactic-co-glycolic acid) nanoparticles coated with chitosan/alginate by layer by layer technology for antitumor applications. *Int. J. Nanomed.* **2017,** *12*, 1791.
215. Haidar, Z. S.; Hamdy, R. C.; Tabrizian, M., Protein release kinetics for core–shell hybrid nanoparticles based on the layer-by-layer assembly of alginate and chitosan on liposomes. *Biomaterials* **2008,** *29* (9), 1207-1215.
216. Zhou, J.; Moya, S.; Ma, L.; Gao, C.; Shen, J., Polyelectrolyte coated PLGA nanoparticles: templation and release behavior. *Macromol Biosci* **2009,** *9* (4), 326-335.
217. Wang, Z.; Zhang, X.; Gu, J.; Yang, H.; Nie, J.; Ma, G., Electrodeposition of alginate/chitosan layer-by-layer composite coatings on titanium substrates. *Carbohydr. Polym.* **2014,** *103*, 38-45.
218. Zhou, G.; Lu, Y.; Zhang, H.; Chen, Y.; Yu, Y.; Gao, J.; Sun, D.; Zhang, G.; Zou, H.; Zhong, Y., A novel pulsed drug-delivery system: polyelectrolyte layer-by-layer coating of chitosan–alginate microgels. *Int. J. Nanomed.* **2013,** *8*, 877-887.
219. Iannone, A.; Magin, R.; Walczak, T.; Federico, M.; Swartz, H.; Tomasi, A.; Vannini, V., Blood clearance of dextran magnetite particles determined by a noninvasive in vivo ESR method. *Magn Reson Med* **1991,** *22* (2), 435-442.
220. Ching, S. H.; Bhandari, B.; Webb, R.; Bansal, N., Visualizing the interaction between sodium caseinate and calcium

alginate microgel particles. *Food Hydrocoll* **2015,** *43*, 165-171.
221. dos Santos Silva, M.; Cocenza, D. S.; Grillo, R.; de Melo, N. F. S.; Tonello, P. S.; de Oliveira, L. C.; Cassimiro, D. L.; Rosa, A. H.; Fraceto, L. F., Paraquat-loaded alginate/chitosan nanoparticles: preparation, characterization and soil sorption studies. *J Hazard Mater* **2011,** *190* (1-3), 366-374.
222. Maldonado, L., and J. Kokini., An optimal window for the fabrication of Edible Polyelectrolyte Complex Nanotubes (EPCNs) from bovine serum albumin (BSA) and sodium alginate. *Food Hydrocoll* **2017**.
223. Donati, I.; Paoletti, S., Material properties of alginates. In *Alginates: Biology and applications*, Springer: 2009; pp 1-53.
224. Acevedo-Fani, A.; Salvia-Trujillo, L.; Soliva-Fortuny, R.; Martín-Belloso, O., Layer-by-Layer Assembly of Food-Grade Alginate/Chitosan Nanolaminates: Formation and Physicochemical Characterization. *Food Biophys* **2017,** *12* (3), 299-308.
225. Rivera, M. C.; Pinheiro, A. C.; Bourbon, A. I.; Cerqueira, M. A.; Vicente, A. A., Hollow chitosan/alginate nanocapsules for bioactive compound delivery. *Int J Biol Macromol* **2015,** *79*, 95-102.
226. Qiu, H.; Qiu, Z.; Wang, J.; Zhang, R.; Zheng, F., Enhanced swelling and methylene blue adsorption of polyacrylamide‐based superabsorbents using alginate modified montmorillonite. *J Appl Polym Sci* **2014,** *131* (6).
227. Kevadiya, B. D.; Joshi, G. V.; Patel, H. A.; Ingole, P. G.; Mody, H. M.; Bajaj, H. C., Montmorillonite-alginate nanocomposites as a drug delivery system: Intercalation and in vitro release of vitamin B1 and vitamin B6. *J Biomater Appl* **2010,** *25* (2), 161-177.
228. Sartori, C.; Finch, D. S.; Ralph, B.; Gilding, K., Determination of the cation content of alginate thin films by FTi. r. spectroscopy. *Polymer* **1997,** *38* (1), 43-51.
229. Daemi, H.; Barikani, M., Synthesis and characterization of calcium alginate nanoparticles, sodium homopolymannuronate salt and its calcium nanoparticles. *Sci Iran* **2012,** *19* (6), 2023-2028.
230. Zeng, M.; Feng, Z.; Huang, Y.; Liu, J.; Ren, J.; Xu, Q.; Fan, L., Chemical structure and remarkably enhanced mechanical properties of chitosan-graft-poly (acrylic acid)/polyacrylamide double-network hydrogels. *Polym Bull* **2017,** *74* (1), 55-74.
231. Su, X.; Mahalingam, S.; Edirisinghe, M.; Chen, B., Highly Stretchable and Highly Resilient Polymer–Clay Nanocomposite Hydrogels with Low Hysteresis. *ACS Appl. Mater. Interfaces* **2017,** *9* (27), 22223-22234.
232. Liu, X.; Chen, X.; Li, Y.; Wang, X.; Peng, X.; Zhu, W., Preparation of Superparamagnetic Fe3O4@Alginate/Chitosan Nanospheres for Candida rugosa lipase Immobilization and Utilization of Layer-by-Layer Assembly to Enhance the Stability of Immobilized Lipase. *ACS Appl. Mater. Interfaces* **2012,** *4* (10), 5169-5178.
233. Tiwari, S.; Mishra, B., Multilayered membrane-controlled microcapsules for controlled delivery of isoniazid. *Daru* **2011,** *19* (1), 41-46.
234. Aditya, N.; Aditya, S.; Yang, H.; Kim, H. W.; Park, S. O.; Ko, S., Co-delivery of hydrophobic curcumin and hydrophilic catechin by a water-in-oil-in-water double emulsion. *Food Chem.* **2015,** *173*, 7-13.
235. Altunbas, A.; Lee, S. J.; Rajasekaran, S. A.; Schneider, J. P.; Pochan, D. J., Encapsulation of curcumin in self-assembling peptide hydrogels as injectable drug delivery vehicles. *Biomaterials* **2011,** *32* (25), 5906-5914.
236. Yang, F.; Lim, G. P.; Begum, A. N.; Ubeda, O. J.; Simmons, M. R.; Ambegaokar, S. S.; Chen, P. P.; Kayed, R.; Glabe, C. G.; Frautschy, S. A., Curcumin inhibits formation of amyloid β oligomers and fibrils, binds plaques, and reduces amyloid in vivo. *J Biol Chem* **2005,** *280* (7), 5892-5901.
237. Manju, S.; Sreenivasan, K., Conjugation of curcumin onto hyaluronic acid enhances its aqueous solubility and stability. *J Colloid Interface Sci* **2011,** *359* (1), 318-325.
238. Cui, J.; Yu, B.; Zhao, Y.; Zhu, W.; Li, H.; Lou, H.; Zhai, G., Enhancement of oral absorption of curcumin by self-microemulsifying drug delivery systems. *Int. J. Pharm.* **2009,** *371* (1-2), 148-155.
239. Mohanty, C.; Acharya, S.; Mohanty, A. K.; Dilnawaz, F.; Sahoo, S. K., Curcumin-encapsulated MePEG/PCL diblock copolymeric micelles: a novel controlled delivery vehicle for cancer therapy. *Nanomedicine* **2010,** *5* (3), 433-449.
240. Zaman, M. S.; Chauhan, N.; Yallapu, M. M.; Gara, R. K.; Maher, D. M.; Kumari, S.; Sikander, M.; Khan, S.; Zafar, N.;

Jaggi, M., Curcumin nanoformulation for cervical cancer treatment. *Sci Rep* **2016,** *6*, 20051.
241. Mohan Yallapu, M.; Ray Dobberpuhl, M.; Michele Maher, D.; Jaggi, M.; Chand Chauhan, S., Design of curcumin loaded cellulose nanoparticles for prostate cancer. *Curr Drug Metab* **2012,** *13* (1), 120-128.
242. Jagannathan, R.; Abraham, P. M.; Poddar, P., Temperature-dependent spectroscopic evidences of curcumin in aqueous medium: a mechanistic study of its solubility and stability. *J Phys Chem B* **2012,** *116* (50), 14533-14540.
243. Mangalathillam, S.; Rejinold, N. S.; Nair, A.; Lakshmanan, V.-K.; Nair, S. V.; Jayakumar, R., Curcumin loaded chitin nanogels for skin cancer treatment via the transdermal route. *Nanoscale* **2012,** *4* (1), 239-250.
244. Rejinold, N. S.; Sreerekha, P.; Chennazhi, K.; Nair, S.; Jayakumar, R., Biocompatible, biodegradable and thermo-sensitive chitosan-g-poly (N-isopropylacrylamide) nanocarrier for curcumin drug delivery. *Int J Biol Macromol* **2011,** *49* (2), 161-172.
245. Kunwar, A.; Barik, A.; Mishra, B.; Rathinasamy, K.; Pandey, R.; Priyadarsini, K., Quantitative cellular uptake, localization and cytotoxicity of curcumin in normal and tumor cells. *Biochim Biophys Acta Gen Subj* **2008,** *1780* (4), 673-679.
246. Chaves, N. L.; Estrela-Lopis, I.; Böttner, J.; Lopes, C. A.; Guido, B. C.; de Sousa, A. R.; Báo, S. N., Exploring cellular uptake of iron oxide nanoparticles associated with rhodium citrate in breast cancer cells. *Int. J. Nanomed.* **2017,** *12*, 5511-5523.
247. Kettler, K.; Veltman, K.; van de Meent, D.; van Wezel, A.; Hendriks, A. J., Cellular uptake of nanoparticles as determined by particle properties, experimental conditions, and cell type. *Environ Toxicol Chem* **2014,** *33* (3), 481-492.
248. Kohler, N.; Sun, C.; Wang, J.; Zhang, M., Methotrexate-modified superparamagnetic nanoparticles and their intracellular uptake into human cancer cells. *Langmuir* **2005,** *21* (19), 8858-8864.
249. Syng-ai, C.; Kumari, A. L.; Khar, A., Effect of curcumin on normal and tumor cells: role of glutathione and bcl-2. *Mol Cancer Ther* **2004,** *3* (9), 1101-1108.
250. Shishodia, S.; Amin, H. M.; Lai, R.; Aggarwal, B. B., Curcumin (diferuloylmethane) inhibits constitutive NF-κB activation, induces G1/S arrest, suppresses proliferation, and induces apoptosis in mantle cell lymphoma. *Biochem Pharmacol* **2005,** *70* (5), 700-713.
251. Zhao, X.; Pan, F.; Zhang, Z.; Grant, C.; Ma, Y.; Armes, S. P.; Tang, Y.; Lewis, A. L.; Waigh, T.; Lu, J. R., Nanostructure of polyplexes formed between cationic diblock copolymer and antisense oligodeoxynucleotide and its influence on cell transfection efficiency. *Biomacromolecules* **2007,** *8* (11), 3493-3502.
252. Zhang, L.; Li, Y.; Jimmy, C. Y.; Chen, Y. Y.; Chan, K. M., Assembly of polyethylenimine-functionalized iron oxide nanoparticles as agents for DNA transfection with magnetofection technique. *J. Mater. Chem. B* **2014,** *2* (45), 7936-7944.
253. De Smedt, S.; Remaut, K.; Lucas, B.; Braeckmans, K.; Sanders, N.; Demeester, J., Studying biophysical barriers to DNA delivery by advanced light microscopy. *Adv. Drug Delivery Rev.* **2005,** *57* (1), 191-210.
254. Pack, D. W.; Hoffman, A. S.; Pun, S.; Stayton, P. S., Design and development of polymers for gene delivery. *Nat Rev Drug Discov* **2005,** *4* (7), 581-593.
255. El-Aneed, A., An overview of current delivery systems in cancer gene therapy. *J Control Release.* **2004,** *94* (1), 1-14.
256. Nayerossadat, N.; Maedeh, T.; Ali, P. A., Viral and nonviral delivery systems for gene delivery. *Adv Biomed Res* **2012,** *1* (1), 27-27.
257. Plank, C.; Schillinger, U.; Scherer, F.; Bergemann, C.; Rémy, J.-S.; Krötz, F.; Anton, M.; Lausier, J.; Rosenecker, J., The magnetofection method: using magnetic force to enhance gene delivery. *J. Biol. Chem* **2003,** *384* (5), 737-747.
258. Kean, T.; Roth, S.; Thanou, M., Trimethylated chitosans as non-viral gene delivery vectors: cytotoxicity and transfection efficiency. *J Control Release.* **2005,** *103* (3), 643-653.
259. Thomas, M.; Klibanov, A., Non-viral gene therapy: polycation-mediated DNA delivery. *Appl Microbiol Biotechnol* **2003,** *62* (1), 27-34.
260. Hoskins, C.; Cuschieri, A.; Wang, L., The cytotoxicity of polycationic iron oxide nanoparticles: common endpoint

assays and alternative approaches for improved understanding of cellular response mechanism. *J Nanobiotechnology* **2012,** *10* (1), 15.
261. Hoskins, C.; Wang, L.; Cheng, W. P.; Cuschieri, A., Dilemmas in the reliable estimation of the in-vitro cell viability in magnetic nanoparticle engineering: which tests and what protocols? *Nanoscale Res Lett* **2012,** *7* (1), 1-12.
262. Strojan, K.; Lojk, J.; Bregar, V. B.; Veranič, P.; Pavlin, M., Glutathione reduces cytotoxicity of polyethyleneimine coated magnetic nanoparticles in CHO cells. *Toxicol In Vitro* **2017,** *41*, 12-20.
263. Du, J.; Zhu, W.; Yang, L.; Wu, C.; Lin, B.; Wu, J.; Jin, R.; Shen, T.; Ai, H., Reduction of polyethylenimine-coated iron oxide nanoparticles induced autophagy and cytotoxicity by lactosylation. *Regen Biomater* **2016,** *3* (4), 223-229.
264. Yu, Y.; Hu, Y.; Li, X.; Liu, Y.; Li, M.; Yang, J.; Sheng, W., Spermine-modified Antheraea pernyi silk fibroin as a gene delivery carrier. *Int. J. Nanomed.* **2016,** *11*, 1013-1023.
265. Li, L.; Puhl, S.; Meinel, L.; Germershaus, O., Silk fibroin layer-by-layer microcapsules for localized gene delivery. *Biomaterials* **2014,** *35* (27), 7929-7939.
266. Mathur, A. B.; Gupta, V., Silk fibroin-derived nanoparticles for biomedical applications. *Nanomedicine* **2010,** *5* (5), 807-820.
267. Curtis, K. A.; Miller, D.; Millard, P.; Basu, S.; Horkay, F.; Chandran, P. L., Unusual Salt and pH Induced Changes in Polyethylenimine Solutions. *PLoS ONE* **2016,** *11* (9), e0158147.
268. Dobrynin, A. V.; Rubinstein, M., Hydrophobic polyelectrolytes. *Macromolecules* **1999,** *32* (3), 915-922.
269. Chandler, D., Interfaces and the driving force of hydrophobic assembly. *Nature* **2005,** *437* (7059), 640-647.
270. Zhao, X.; Cui, H.; Chen, W.; Wang, Y.; Cui, B.; Sun, C.; Meng, Z.; Liu, G., Morphology, structure and function characterization of PEI modified magnetic nanoparticles gene delivery system. *PLoS ONE* **2014,** *9* (6), e98919.
271. McBain, S.; Yiu, H.; El Haj, A.; Dobson, J., Polyethyleneimine functionalized iron oxide nanoparticles as agents for DNA delivery and transfection. *J Mater Chem* **2007,** *17* (24), 2561-2565.
272. Steitz, B.; Hofmann, H.; Kamau, S. W.; Hassa, P. O.; Hottiger, M. O.; von Rechenberg, B.; Hofmann-Amtenbrink, M.; Petri-Fink, A., Characterization of PEI-coated superparamagnetic iron oxide nanoparticles for transfection: Size distribution, colloidal properties and DNA interaction. *J Magn Magn Mater* **2007,** *311* (1), 300-305.
273. Smits, R.; Koper, G.; Mandel, M., The influence of nearest-and next-nearest-neighbor interactions on the potentiometric titration of linear poly (ethylenimine). *J Phys Chem* **1993,** *97* (21), 5745-5751.
274. Namgung, R.; Singha, K.; Yu, M. K.; Jon, S.; Kim, Y. S.; Ahn, Y.; Park, I.-K.; Kim, W. J., Hybrid superparamagnetic iron oxide nanoparticle-branched polyethylenimine magnetoplexes for gene transfection of vascular endothelial cells. *Biomaterials* **2010,** *31* (14), 4204-4213.
275. Florea, B. I.; Meaney, C.; Junginger, H. E.; Borchard, G., Transfection efficiency and toxicity of polyethylenimine in differentiated Calu-3 and nondifferentiated COS-1 cell cultures. *AAPS PharmSci* **2002,** *4* (3), 1-11.
276. Andrushchenko, V.; Leonenko, Z.; Cramb, D.; van de Sande, H.; Wieser, H., Vibrational CD (VCD) and atomic force microscopy (AFM) study of DNA interaction with Cr3+ ions: VCD and AFM evidence of DNA condensation. *Biopolymers* **2002,** *61* (4), 243-260.
277. Danielsen, S.; Vårum, K. M.; Stokke, B. T., Structural analysis of chitosan mediated DNA condensation by AFM: influence of chitosan molecular parameters. *Biomacromolecules* **2004,** *5* (3), 928-936.
278. Volcke, C.; Pirotton, S.; Grandfils, C.; Humbert, C.; Thiry, P.; Ydens, I.; Dubois, P.; Raes, M., Influence of DNA condensation state on transfection efficiency in DNA/polymer complexes: an AFM and DLS comparative study. *J. Biotechnol* **2006,** *125* (1), 11-21.
279. Chen, A. M.; Santhakumaran, L. M.; Nair, S. K.; Amenta, P. S.; Thomas, T.; He, H.; Thomas, T., Oligodeoxynucleotide nanostructure formation in the presence of polypropyleneimine dendrimers and their uptake in breast cancer cells. *Nanotechnology* **2006,** *17* (21), 5449-5460.
280. Costa, L.; Kerkmann, M.; Hartmann, G.; Endres, S.; Bisch, P.; Heckl, W.; Thalhammer, S., Structural studies of oligonucleotides containing G-quadruplex motifs using AFM. *Biochem. Biophys. Res. Commun.* **2004,** *313* (4), 1065-1072.

281. Chiorcea-Paquim, A.-M.; Santos, P. V.; Eritja, R.; Oliveira-Brett, A. M., Self-assembled G-quadruplex nanostructures: AFM and voltammetric characterization. *Phys Chem Chem Phys* **2013,** *15* (23), 9117-9124.
282. Chiorcea-Paquim, A.-M.; Santos, P. V.; Oliveira-Brett, A. M., Atomic force microscopy and voltammetric characterisation of synthetic homo-oligodeoxynucleotides. *Electrochim Acta* **2013,** *110*, 599-607.
283. Junghans, M.; Kreuter, J.; Zimmer, A., Antisense delivery using protamine–oligonucleotide particles. *Nucleic Acids Res* **2000,** *28* (10), e45-e45.
284. Gu, Y.; Zhang, J.; Ma, X.; Kim, B.-w.; Wang, H.; Li, J.; Pan, Y.; Xu, Y.; Ding, L.; Yang, L., Stabilization of the c-Myc protein by CAMKIIγ promotes T cell lymphoma. *Cancer Cell* **2017,** *32* (1), 115-128. e7.
285. Leonetti, C.; D'Agnano, I.; Lozupone, F.; Valentini, A.; Geiser, T.; Zon, G.; Calabretta, B.; Citro, G.; Zupi, G., Antitumor effect of c-myc antisense phosphorothioate oligodeoxynucleotides on human melanoma cells in vitro and in mice. *JNCI* **1996,** *88* (7), 419-429.
286. Watson, P. H.; Pon, R. T.; Shiu, R. P., Inhibition of c-myc expression by phosphorothioate antisense oligonucleotide identifies a critical role for c-myc in the growth of human breast cancer. *Cancer Res.* **1991,** *51* (15), 3996-4000.
287. Santhakumaran, L. M.; Thomas, T.; Thomas, T., Enhanced cellular uptake of a triplex‐forming oligonucleotide by nanoparticle formation in the presence of polypropylenimine dendrimers. *Nucleic Acids Res* **2004,** *32* (7), 2102-2112.
288. Mumcuoglu, D.; Ekiz, M. S.; Gunay, G.; Tekinay, T.; Tekinay, A. B.; Guler, M. O., Cellular internalization of therapeutic oligonucleotides by peptide amphiphile nanofibers and nanospheres. *ACS Appl. Mater. Interfaces* **2016,** *8* (18), 11280-11287.
289. Petrilli, R.; O Eloy, J.; M Marchetti, J.; FV Lopez, R.; J Lee, R., Targeted lipid nanoparticles for antisense oligonucleotide delivery. *Curr Pharm Biotechnol* **2014,** *15* (9), 847-855.
290. Gangar, A.; Fegan, A.; Kumarapperuma, S. C.; Huynh, P.; Benyumov, A.; Wagner, C. R., Targeted delivery of antisense oligonucleotides by chemically self-assembled nanostructures. *Mol. Pharmaceutics* **2013,** *10* (9), 3514-3518.
291. Balaji, K.; Koul, H.; Mitra, S.; Maramag, C.; Reddy, P.; Menon, M.; Malhotra, R. K.; Laxmanan, S., Antiproliferative effects of c-myc antisense oligonucleotide in prostate cancer cells: a novel therapy in prostate cancer. *J Urol* **1997,** *50* (6), 1007-1015.
292. Pan, B.; Cui, D.; Sheng, Y.; Ozkan, C.; Gao, F.; He, R.; Li, Q.; Xu, P.; Huang, T., Dendrimer-modified magnetic nanoparticles enhance efficiency of gene delivery system. *Cancer Res.* **2007,** *67* (17), 8156-8163.
293. Sarkar, T.; Conwell, C. C.; Harvey, L. C.; Santai, C. T.; Hud, N. V., Condensation of oligonucleotides assembled into nicked and gapped duplexes: potential structures for oligonucleotide delivery. *Nucleic Acids Res* **2005,** *33* (1), 143-151.
294. Pan, B.; Cui, D.; Xu, P.; Ozkan, C.; Feng, G.; Ozkan, M.; Huang, T.; Chu, B.; Li, Q.; He, R., Synthesis and characterization of polyamidoamine dendrimer-coated multi-walled carbon nanotubes and their application in gene delivery systems. *Nanotechnology* **2009,** *20* (12), 125101-125109.
295. Gal, N.; Massalha, S.; Samuelly-Nafta, O.; Weihs, D., Effects of particle uptake, encapsulation, and localization in cancer cells on intracellular applications. *Med Eng Phys* **2015,** *37* (5), 478-483.
296. Hazan, R. B.; Phillips, G. R.; Qiao, R. F.; Norton, L.; Aaronson, S. A., Exogenous expression of N-cadherin in breast cancer cells induces cell migration, invasion, and metastasis. *J Cell Biol* **2000,** *148* (4), 779-790.
297. Luo, D.; Saltzman, W. M., Enhancement of transfection by physical concentration of DNA at the cell surface. *Nat. Biotechnol.* **2000,** *18* (8), 893-895.
298. Ma, Y.; Zhang, Z.; Wang, X.; Xia, W.; Gu, H., Insights into the mechanism of magnetofection using MNPs-PEI/pDNA/free PEI magnetofectins. *Int. J. Pharm.* **2011,** *419* (1), 247-254.